Information Content of Halo Displays for Remote Sensing of Ice Crystal Properties

Linda Forster

München 2017

Information Content of Halo Displays for Remote Sensing of Ice Crystal Properties

Linda Forster

Dissertation
an der Fakultät für Physik
der Ludwig–Maximilians–Universität
München

vorgelegt von
Linda Forster
aus Starnberg

München, den Abgabedatum

Erstgutachter: Prof. Dr. Bernhard Mayer
Zweitgutachter: Prof. Dr. Markus Rapp
Tag der mündlichen Prüfung: Prüfungsdatum

Inhaltsverzeichnis

Zusammenfassung

Zirren haben mit einem globalen Bedeckungsgrad von etwa 30% (Wylie and Menzel, 1999, Stubenrauch et al., 2006) einen wichtigen Einfluss auf die Energiebilanz der Erde und Erdatmosphäre. Die Balance zwischen der reflektierten Solarstrahlung und der absorbierten thermischen Strahlung hängt stark von den optischen Eigenschaften der Wolkenpartikel ab. Zirren bestehen aus kleinen asphärischen Eiskristallen, die zu komplexen Formen anwachsen können und häufig orientiert sind. Das spiegelt sich auch in einer großen Variabilität der optischen Eigenschaften wider. Um den Effekt von Eiswolken auf die Strahlungsbilanz besser quantifizieren zu können, ist es deshalb wichtig die Kenntnis von typischen Eiskristallformen und -orientierungen zu verbessern.

Ziel dieser Arbeit ist es zu untersuchen, ob Beobachtungen von Haloerscheinungen Informationen liefern können um die Komplexität der Eiskristalleigenschaften einzugrenzen. Zu diesen Eigenschaften zählen die Eiskristallform, -oberflächenrauhigkeit, -größe und -orientierung. Haloerscheinungen entstehen durch Brechung und Reflexion von Licht an glatten Prismenflächen von hexagonalen Eiskristallen. Diese optischen Phänomene werden hauptsächlich durch verschiedene Eiskristallformen und -orientierung hervorgerufen und könnten deshalb wichtige Informationen über diese Eiskristalleigenschaften liefern. Der 22° Halo, eine der häufigsten Haloerscheinungen, entsteht durch zufällig orientierte Hexagone. Nebensonnen treten auf bei Lichtbrechung an orientierten Eiskristallplättchen und die Berührungsbögen zum 22° Halo entstehen durch orientierte Säulen.

Zur kontinuierlichen Beobachtung von Haloerscheinungen wurde das wetterfeste Kamerasystem HaloCam auf der Messplattform des Meteorologischen Instituts München aufgebaut. Zusammen mit dem automatischen Haloerkennungsalgorithmus HaloForest liefert HaloCam einen konsistenten Datensatz von Langzeit-Halobeobachtungen. Eine Auswertung der Häufigkeit von 22° Halos im Zeitraum zwischen Januar 2014 und Juni 2016 mit HaloForest ergab einen Anteil von etwa 2% relativ zur gesamten Beobachtungszeit. Mit Hilfe von parallel gesammelten Ceilometerdaten konnte abgeleitet werden, dass etwa 25% der Eiswolken einen sichtbaren 22° Halo erzeugten. Eine visuelle Auswertung der HaloCam Daten während der 6-wöchigen ACCEPT Messkampagne in den Niederlanden zeigte dass Nebensonnen mit einer relativen Häufigkeit von 70% öfter zu sehen waren als 22° Halos mit 60%, gefolgt von oberen Berührungsbögen mit 30%. Der Anteil der Halo-produzierenden Zirren konnte für diesen Datensatz ebenfalls visuell auf 27% bestimmt werden.

Das Ableitungsverfahren RICO wurde entwickelt um aus kalibrierten Strahldichtemessungen von 22° Halos mit Hilfe von Strahlungstransportsimulationen Eiskristallgröße, -form und Anteil der glatten Kristalle zu bestimmen. Die Analyse von HaloCam Daten im Zeitraum zwischen September 2015 und November 2016 ergab effektive Eiskristallradien von etwa 18 µm im Mittel mit einer Streuung zwischen 5 und 38 µm, die nahezu unabhängig von Form und Rauhigkeit ist. Um die 22° Halos aus den HaloCam Beobachtungen zu reproduzieren, wurden für säulenförmige Kristalle ein mittlerer Anteil von 30% glatten Kristallen, für hohle Säulen ein Anteil von 60%

und für plättchenförmige Kristalle ein mittlerer Anteil von 80% glatten Kristallen benötigt. Die optischen Eigenschaften von Eiskristallplättchen konnten die HaloCam Beobachtungen im Bereich des 22° Halos insgesamt am besten reproduzieren, gefolgt von Eiskristallsäulen. Eiskristallplättchen erzeugen allerdings bis etwa 50 µm zusätzlich zum 22° auch einen 46° Halo. Da die ausgewerteten HaloCam Daten ausschließlich 22° Halos ohne 46° Halo zeigten, müssen die Plättchen ausgeschlossen werden. Folglich sind Eiskristallsäulen die dominierende Eiskristallform in diesem Datensatz. Während der ML-CIRRUS Messkampagne (Voigt et al., 2016) konnte ein einzigartiger Datensatz aufenommen werden, der HaloCam Beobachtungen ~~mehrerer Haloerscheinungen~~ mit in-situ Messungen des Forschungsflugzeugs HALO kombiniert. Zur Strahlungstransportmodellierung von orientierten Eiskristallen wurde das Monte Carlo Strahlungstransportmodell MYSTIC (Mayer, 2009) mit dem speziell dafür entwickelten Raytracing Algorithmus CrystalTrace erweitert. Mit CrystalTrace wurde eine Methode demonstriert, die erlaubt aus gleichzeitigen Beobachtungen eines 22° Halo und Nebensonnen oder einem oberen Berührungsbogen den Anteil orientierter Kristalle zu bestimmen.

Kapitel 1

Introduction

Cirrus clouds cover about 30% of the globe (Wylie and Menzel, 1999, Stubenrauch et al., 2006) and play an important role in the Earth's energy budget. They consist of small non-spherical ice crystals, which scatter and absorb solar radiation and emit thermal infrared radiation. Depending on which of the two effects dominates, cirrus clouds have either a cooling or a warming effect on climate. The amount of transmitted and reflected light by cirrus clouds is governed by the optical thickness, the ice crystal size, habit, surface roughness and orientation. Ice crystals can grow to different habits depending on temperature and relative humidity of their environment including hexagonal columns and plates or arbitrarily complex habits as bullet-rosettes, aggregates of crystals and dendrites (Bailey and Hallett, 2004, 2009).

Passive remote sensing of ice cloud optical thickness and effective radius is operationally performed by using a two-channel inversion technique from spectral reflectance measurements. This retrieval technique makes use of the principle that cloud reflection at a non-absorbing wavelength in the visible spectrum is primarily a function of cloud optical thickness, whereas cloud reflection at an absorbing wavelength in the near IR is mainly determined by the particle size (e.g. King et al. (1997)). Originally developed for the retrieval of water cloud properties by Nakajima and King (1990), the two-channel retrieval has been applied to ice clouds by Ou et al. (1999), Rolland et al. (2000), Rolland and Liou (2001), King et al. (2004). Zinner et al. (2016) adapted the two-channel method to ground-based observations using the specMACS hyperspectral imager. In contrast to spherical water droplets the radiative properties of non-spherical ice crystals depend crucially on the ice crystal shape, surface roughness and orientation (e.g. Liou (1986), Wielicki et al. (1995), Wendisch et al. (2007), Yi et al. (2013)). Wrong assumptions of the ice crystal shape can result in significant errors in retrievals of optical thickness or cloud microphysical properties (Mishchenko et al., 1996, Baran et al., 1999). Key et al. (2002), Eichler et al. (2009) and Zinner et al. (2016) estimate the uncertainty of the cirrus optical thickness and effective radius to >50% and >20%, respectively. Better knowledge of shape, surface roughness, and orientation of ice crystals in cirrus clouds would therefore help to improve estimates of the radiative forcing of cirrus clouds as well as satellite retrievals of cirrus optical properties as discussed by Yang et al. (2015), Liou and Yang (2016) and references therein. Moreover, Yang et al. (2015) highlight the importance of the assumed ice crystal habit and surface roughness also for numerical weather prediction and general circulation models. Yang et al. (2015) report differences in the net cloud radiative effect at the top of the atmosphere of up to $3.54\,\mathrm{W\,m^{-2}}$ globally for ice crystal spheres in comparison to hexagonal particles. Ice crystal orientation can also have strong effects on the global radiative budget as pointed out by Noel and Sassen (2005).

Halo displays are produced by hexagonal ice crystals with smooth faces via refraction and

Abbildung 1.1: *Examples of halo displays observed at the Meteorological Institute of the LMU in Munich. The sun is blocked by a black circular shade to avoid stray light and saturation of the camera sensor. Top left: a bright 22° halo. Top right: right 22° parhelia or sundog. Bottom left: a faint 22° halo with upper and lower tangent arc. Bottom right: 22° halo with circumscribed halo.*

reflection of light. The formation of halo displays has already been described by Wegener (1925) and by a number of later publications (Greenler, 1980, Minnaert, 1993, Tape, 1994). More than 30 different halo displays have been observed. The optical phenomena are formed by different ice crystal shapes and orientations and might therefore contain information about these ice crystal properties. This study aims at investigating whether observations of halo displays can provide information about ice crystal shape and orientation and can thus contribute to a better understanding of the ice crystal microphysical and optical properties. Figure 1.1 shows examples of the most frequent halo displays: the 22° halo (top left) is formed by randomly oriented hexagonal ice crystals and appears as a bright ring around the sun at a scattering angle of about 22°. Further frequently observed halo displays are 22° parhelia, commonly called sundogs, which are caused by light refracted by horizontally oriented hexagonal plates. The top right image in Fig. 1.1 shows a bright sundog on the right side of the sun. Upper and lower tangent arcs, presented on the lower left in Fig. 1.1, can also be quite frequently observed. Their shape depends on the solar elevation. For small solar elevations the upper and lower tangent arcs are separated while they merge for larger solar elevations as depicted on the lower right image in Fig. 1.1. As the sun is approaching the zenith they are almost indistinguishable from the 22° halo. Halos are not only beautiful optical displays but also contain valuable information about ice particle shape and orientation (Lynch and Schwartz, 1985, Sassen et al., 1994, van Diedenhoven, 2014). Recent publications showed that the brightness contrast of the 22° halo in ice crystal scattering phase functions is related to the aspect ratio and surface roughness of

the crystals (van Diedenhoven, 2014). Quantitative analysis of the frequency of occurrence or brightness contrast of halo displays can therefore help to determine ice crystal properties, such as habit, surface roughness and orientation in cirrus clouds.

Probably the first reported photometric measurements of halo displays were performed by Lynch and Schwartz (1985) who took a photo of a 22° halo around the moon with a Kodak Plus-X pan film camera. After digitizing the photo, the halo brightness and width was analyzed and compared with theoretical values to infer information about ice crystal size and shape. In order to exploit the information content of halo displays, continuous long-term observations of cirrus clouds are required. In the 1990's many observations have been collected by amateur halo-observing networks (Pekkola, 1991, Verschure, 1998) which is work-intensive and requires a lot of personnel. The largest dataset of halo observations has been collected by the German "Arbeitskreis Meteore e.V. Sektion Halobeobachtungen" (AKM, `https://www.meteoros.de`). The community was founded in 1990 and consists of a network of about 80 volunteers who collect halo observations on a monthly basis throughout Germany, Austria, Romania and the UK. Since 1986 more than 150 000 observations of halo displays have been reported. The AKM collects information about the halo type and its duration, the type of cloud producing the halo, the weather situation during the observation (frontal system, precipitation) and more. These observations are valuable for obtaining an average frequency of the different halo displays in Europe. However, for a systematic comparison with other measurement data, continuous observations at a specific location for a long period of time are required. An extensive long-term observation study of high-level clouds and halo displays was performed by Sassen et al. (2003b), who evaluated a ∼10 year record of photographic halo observations together with measurements with a polarization lidar and other remote sensing instruments at the Facility for Atmospheric Remote Sensing (FARS) in Salt Lake City, Utah. This study is also based on visually collected halo observations. A fisheye camera, which took pictures every 20 min, was used in this study in combination with field notes and extra photographs to monitor optical displays. Sassen et al. (2003b) pointed out that their optical display statistics are representative only for the observation area at FARS and that a common format for reporting atmospheric optical displays is needed to allow comparison of data from different locations.

The aim of this study is to investigate the information content of halo displays regarding ice crystal properties, which comprise ice crystal size, habit, surface roughness, and orientation in cirrus clouds.

To answer this question, continuous long-term observations of halo displays are necessary. To perform automated halo observations, the weather-proof camera system HaloCam was designed with a sun-tracking mount and a wide-angle lens to provide images with high temporal and spatial resolution.

This study presents, to the author's knowledge, the first automated, continuous and long-term camera observations of halo displays. Together with HaloForest, the newly developed automated detection algorithm for halo displays, the HaloCam system provides a consistent long-term dataset of halo displays as suggested by Sassen et al. (2003b). Both the HaloCam camera system and the halo detection algorithm are described in Forster et al. (2017). Furthermore, this study uses for the first time calibrated radiance observations of 22° halos and systematically investigates the ice crystal optical and microphysical properties of the halo-producing cirrus clouds with radiative transfer models. To investigate the information content of halo displays regarding ice crystal orientation, the raytracing algorithm CrystalTrace was developed and implemented

in the radiative transfer model MYSTIC (Mayer, 2009) which is part of the radiative transfer library libRadtran (Mayer and Kylling, 2005). This combination of CrystalTrace and MYSTIC allows to perform radiative transfer simulations with oriented ice crystals accounting for multiple scattering and interaction with aerosol, surface albedo.

After providing a brief overview over the underlying theoretical concepts and equations, the methods which were developed and used in this study will be presented. First, ice crystal single scattering properties were investigated and suitable parameters were determined to retrieve information about ice crystal microphysical properties. In next chapter all methods and tools which were developed and used in this study are presented. Except for the radiative transfer library libRadtran with the MYSTIC and DISORT solvers, the ice crystal optical properties and the specMACS instrument, all presented tools and methods were developed within this study. The results present statistics of halo displays during the ACCEPT campaign and a long-term statistic of 22° halos in Munich. Using calibrated radiance measurements the retrieval of ice crystal properties is applied to specMACS observations for two case studies and to long-term HaloCam observations. Using CrystalTrace a method is proposed to retrieve the fraction of oriented ice crystals from observations of upper tangent arcs and sundogs together with 22° halos.

Kapitel 2

Theory

This chapter provides the theoretical basis required for the further understanding of this study which focuses on the remote sensing of cirrus clouds and halo displays. Halo displays are produced by refraction and reflection of light by ice crystals. The formation of ice crystals and cirrus clouds and their microphysical properties, which are a prerequisite for the formation of halo displays, are described in the first part of the theory chapter. The second chapter presents the basic radiative laws used in this study including the radiative transfer equation following Thomas and Stamnes (1999) and Zinth and Zinth (2005). The optical properties of molecules, aerosol and ice crystals are described which are necessary for radiative transfer simulations. Combining the radiative with the ice crystal microphysical principles the final section of this chapter explains the formation of halo displays.

2.1 Ice crystals and cirrus clouds

The following sections provide a description of the formation of cirrus clouds which consist primarily of ice crystals. The description of their macro- and microphysical properties mainly follows Rogers and Yau (1996), Wallace and Hobbs (2006), Lynch et al. (2002), Lamb and Verlinde (2011), and Liou and Yang (2016).

2.1.1 Formation of cirrus clouds

Clouds in the atmosphere form when the air becomes supersaturated with respect to liquid or ice water and water vapor condenses. The most frequent way of reaching a state of supersaturation is the rise of an air parcel accompanied by adiabatic cooling. In the upper troposphere where the temperatures are well below 0 °C, ice clouds form. If the temperature falls below −41 °C, the homogeneous freezing level of water, the cloud consists entirely of ice crystals (Wallace and Hobbs, 2006). This study focuses on the properties of thin high-level clouds, which are separated by the World Meteorological Organization (WMO, 1983) into three types according to their morphology: cirrus, cirrocumulus and cirrostratus. Cirrus clouds tend to be transparent and wispy and are composed of ice crystals. They typically occur in altitudes greater than 6 km and consist entirely of ice crystals for temperatures less than about −38 °C. Sassen and Campbell (2001) evaluated cirrus observations over a period of 10 years in Salt Lake City which reveal an average cloud base/top height of 8.79 km/11.02 km with cloud base/top temperatures around −37.4 °C/−53.9 °C. A typical example of a cirrus cloud is displayed in Fig. 2.1. Subvisual cirrus, i.e. cirrus with optical depths lower than 0.03, and contrail cirrus are not yet included in the WMO classification although recognized well in meteorology. As described in (Liou and Yang,

Abbildung 2.1: *Example of a cirrus cloud from WMO (1983).*

2016) cirrus clouds mainly form by synoptic-scale disturbances as e.g. jet streams, closed upper-levels lows, frontal overriding, etc. with relatively weak mean vertical lifting rates and usually develop from top to lower levels. Cirrus clouds can be generated by injection or by strong thunderstorm updrafts producing anvil-cirrus. Another formation mechanism are orographic processes and contrail-cirrus produced by the rapid cooling of aircraft exhausts. Ice clouds have also been observed in the middle atmosphere: polar stratospheric clouds (PSC) between 15 km to 20 km, the so-called mother-of-pearl (nacreous) clouds (20–30 km height) and between 50–55 km the noctilucent clouds (Liou and Yang, 2016).
Having outlined the macrophysical formation of cirrus clouds their microphysics will be described in the following in terms of the formation and growth of ice crystals.

2.1.2 Formation and growth of ice crystals

The water molecule can exist in three thermodynamic states: vapor, liquid, and ice. Essentially all ice in the Earth's biosphere is ice *Ih*, the hexagonal crystal form of ordinary ice. Stable down to −200 °C it has a density of $0.917\,\mathrm{g\,cm^{-3}}$ (Liou and Yang, 2016). In rare cases the structure of ice can exhibit dodecagonal, bullet pyramidal and pyramidal shape. The majority of ice crystals owe their hexagonal shape to the hexagonal molecular symmetry within the crystal. Ice crystals in the atmosphere can form either by homogeneous or heterogeneous nucleation. Homogeneous freezing or sublimation occurs when the water molecules produce a stable ice-like structure by statistical fluctuations which can serve as an ice nucleus. However, extremely high supersaturation is required for homogeneous freezing which rarely occurs in the atmosphere: at temperatures slightly below 0 °C supersaturation of more than a factor of 20 with respect to ice is necessary for homogeneous nucleation. Liou and Yang (2016) state that droplets smaller than 5 µm freeze homogeneously only at temperatures of −40 °C or lower.
In the atmosphere clouds at a temperature of −15 °C already contain a significant amount of ice crystals. These ice crystals are formed by heterogeneous nucleation. Ice crystals form either by contact freezing or deposition on most materials. The required supersaturation and supercooling for contact freezing or deposition, i.e. heterogeneous nucleation, is less than for homogeneous nucleation. Supersaturation together with supercooling and the material properties influence the probability of heterogeneous nucleation. Common materials for ice nuclei are clay materials, especially kaolinite, bacteria, and meteoric material. Since the concentration of ice nuclei

is decreasing with height, supercooled water droplets at −15 °C and below are not uncommon. Hogan et al. (2004) found that supercooled water clouds are rarely found below −35 °C, which was confirmed by Hu et al. (2010). At −20 °C some liquid droplets can still exist in ice clouds. Secondary ice crystals can be produced by shattering of ice crystals when they collide with large graupel particles. Another formation mechanism for secondary ice crystals is splintering of freezing water droplets.

The mass increase of a growing ice particle is governed by the diffusion process. How the saturation vapor pressure e_s changes with temperature T is described by the Clausius-Clapeyron equation

$$\frac{de_s}{dT} = \frac{Le_s}{R_v T^2} \,, \tag{2.1}$$

with the latent heat L and R_v the gas constant for water vapor. Its integrated form gives the exponential increase of the saturation vapor pressure with temperature:

$$\frac{e_s(T)}{e_0} = \exp\left[L\,\frac{1/T_0 - 1/T}{R_v}\right] \,, \tag{2.2}$$

where $e_0 (= 6.11\,\text{hPa})$ is the value at the triple point with a temperature of $T_0 (= 273.15\,\text{K})$ at which vapor, liquid, and ice phase can coexist Fig. 2.2. The saturation vapor pressure over

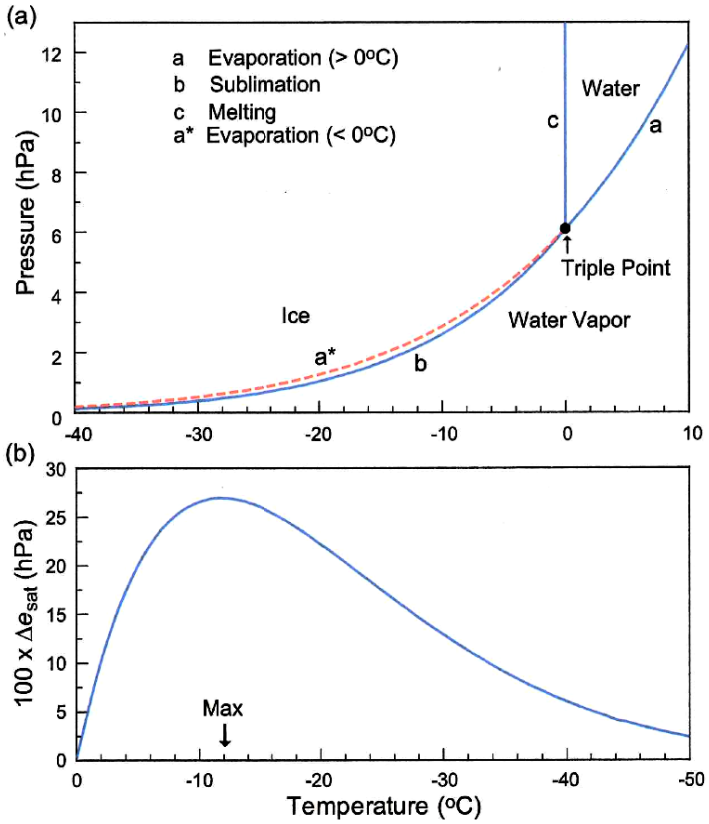

Abbildung 2.2: *Figure adopted from Liou and Yang (2016). (a) Phase diagram of water illustrating the saturation vapor pressure as a function of temperature for the vapor, water and ice phase of the water molecules. The triple point is indicated by a heavy dot and the solid and dashed lines below 0 °C represent ice and water, respectively. (b) Differences of saturation vapor pressure between water and ice as a function of temperature with a maximum at about −12 °C.*

ice is smaller than over supercooled water at the same temperature (dashed line in Fig. 2.2a) due to the different latent heat at the transition. With help of the time-dependent second-order

diffusion equation

$$\frac{\partial n}{\partial t} = D\,\nabla^2\, n \tag{2.3}$$

the concentration of molecules n can be described at any point in the water vapor field with the molecular diffusion coefficient D. Under the assumption that the system is in equilibrium and imposing boundary conditions at the positions of the ice particle ($\rho_\mathrm{v}(s)$) and ambient air ($\rho_\mathrm{v}(\infty)$) the growth equation for an ice crystal can be described by

$$\frac{dm}{dt} = 4\pi\, C\, D\, [\rho_\mathrm{v}(\infty) - \rho_\mathrm{v}(s)]\ . \tag{2.4}$$

The non-sphericity of ice crystals is accounted for by the parameter C which depends on the size and shape of the ice crystal. For a spherical particle $C = r$. For a circular disk of radius r the capacitance can be parameterized by $C = 2r/\pi$ which can be used for the approximation of ice crystal plates. The shape of needles can be approximated by prolate spheroids. Using the Clausius-Clapeyron equation and the definition of the saturation ratio with respect to ice, $S_\mathrm{i} = e/e_\mathrm{i}$, where e is the water vapor pressure of the ambient air and e_i is the saturation pressure over ice, an analytical expression for crystal growth can be derived:

$$\frac{dm}{dt} = \frac{4\pi C(S_\mathrm{i} - 1)}{(f_\mathrm{k} + f_\mathrm{D})}\ , \tag{2.5}$$

where

$$f_\mathrm{k} = L^2/(K R_\mathrm{v} T^2) \,\text{and}\, f_\mathrm{D} = R_\mathrm{v} T/[D e_\mathrm{i}(T)]\ , \tag{2.6}$$

with ambient temperature T, the thermal conductivity K and latent heat L. The growth rate is a function of temperature and inversely proportional to pressure. In a cloud containing supercooled water droplets the air is saturated with respect to liquid water and therefore supersaturated with respect to ice (cf. Fig. 2.2a). Supersaturation ranges from 10 % at −10 °C to 21 % at −20 °C (Wallace and Hobbs, 2006). This allows ice particles to grow by sublimation from the vapor phase at the expense of the water droplets, which is called Wegener-Bergeron-Findeisen process (Wegener, 1926, Bergeron, 1935, Findeisen, 1938). Liou and Yang (2016) state that the growth rate of ice crystals by this process is maximum at a temperature of about −12 °C, as shown in Fig. 2.2b. A contribution to the different morphology of ice and water clouds is the lower equilibrium vapor pressure over ice compared to water at the same temperature (cf. Fig. 2.2). This enables ice particles to survive longer in the non-saturated air surrounding the cloud producing the feather-like appearance of ice clouds as well as fallstreaks or virga (Wallace and Hobbs, 2006).

Ice crystals are formed by diffusion of water vapor and grow further by accretion, which consists of collision and coalescence. Growth by collision is determined by the ice crystal fall speed. For ice crystal aggregation the collection efficiency strongly depends on the ice crystal shape, since dendrites are more likely to stick together than compact particles. Moreover, it is favored by warmer temperatures, particularly above about −5 °C where the ice surfaces become sticky. In a mixed phase cloud ice particles grow by riming which describes the process of an ice crystal capturing supercooled water droplets which freeze upon them. Particles occur like rimed needles, columns, plates, and stellars which will finally loose their shape and turn into graupel particles.

2.1.3 Ice crystal shape

Ice crystals have a common shape with a six-fold (hexagonal) symmetry which can be realized in a range of different axis ratios. Growing ice crystals exhibit non-spherical shapes due to non-uniform deposition coefficients which affect the growth rates across the crystal surface. Their specific shape depends on temperature and ice supersaturation (e.g. Magono and Lee (1966)).

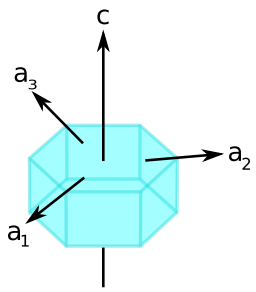

Abbildung 2.3: *Ice crystal geometry. Following the definition in Liou and Yang (2016) the c-axis is perpendicular to the base and top faces of the ice crystal, whereas the three a_i-axes are defined by the intersection of two crystal faces perpendicular to the c-axis.*

Despite the complexity in ice crystal shapes they can be separated into "plates" and "columns", which are called "primary habits" and provide a first-order category for the classification of ice crystal shapes (Lamb and Verlinde, 2011). The crystals have two basal faces and six prism faces as shown in Fig. 2.3. The hexagonal axes a_1, a_2, a_3, and c in Fig. 2.3 define the orientation of the crystal lattice. This primary ice crystal habit is mainly determined by the ambient temperature (cf. Fig. 2.4). Bailey and Hallett (2009) presented a comprehensive ice crystal habit diagram based on both laboratory studies and field observations using the Cloud Particle Imager (CPI) as shown in Fig. 2.4. They report plate-like shapes from $-20\,°C$ to $-40\,°C$ and columnar from $-40\,°C$ to $-70\,°C$. At temperatures below $-20\,°C$ mostly polycrystalline particles occurred. The spatial distribution of water vapor and temperature will be modified by the primary crystal habit and influence the shape of the further growing ice crystal. Between $-10\,°C$ to $-20\,°C$ above ice saturation hollow columns form. With increasing supersaturation pristine plates occur in this temperature region, followed by thick plates of skeleton forms and crystals with broad and sector-like branches below water saturation. Hollow column, solid thick plate, solid bullet and long solid needle exist below water saturation as well. Above water saturation solid long needles, hollow columns, sheath form. Between $-10\,°C$ to $-20\,°C$ a variety of plate types, crystals with sector-like branches, fern-like, ordinary dendritic, and stellar crystals as well as hexagonal plate are observed. For temperatures between $-20\,°C$ to $-40\,°C$, hollow columns, hollow bullet rosette and aggregates occur. Bailey and Hallett (2009) stated that most ice crystals are defective and irregular in shape to varying degrees. They also found that most individual crystals are complex, irregular, and imperfect including single crystals such as plates and columns. It was also pointed out that very small ice crystals growing at low ice supersaturation are mainly compact faceted polycrystals, not spheroids, as suggested in previous publications.

Ice crystal size in cirrus clouds spans values from a few to thousands of micrometers. Figure 2.5 shows the definition of the ice crystal dimensions for columnar (a) and plate-like crystals (b). The maximum dimension L is represents the length of the c-axis, while the maximum diameter of the ice crystal top and base faces is denoted by $2a$. For certain ice crystal types maximum dimension, L, and maximum diameter, $d = 2a$, are related which was found in laboratory and field observations (Auer and Veal, 1970, Heymsfield, 1972). From this data Mitchell and Arnott

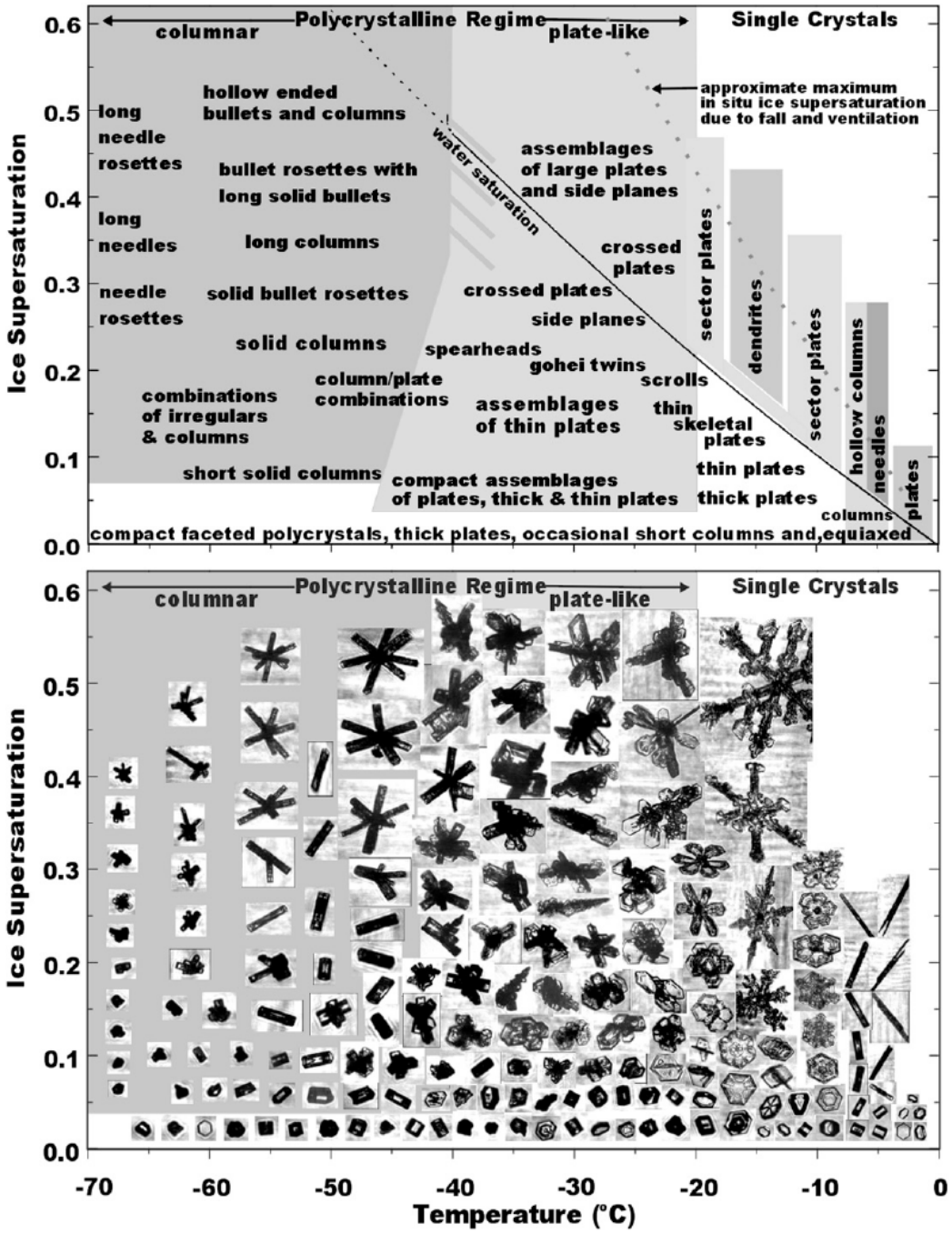

Abbildung 2.4: *Ice crystal morphology as a function of temperature and supersaturation (Bailey and Hallett, 2009).*

(1994) derived the following empirical relationship for columns:

$$d = 0.7000L^{1.0} \qquad \text{for } L \leq 100\,\mu\text{m, and} \tag{2.7}$$

$$d = 0.0696L^{0.5} \qquad \text{for } L > 100\,\mu\text{m}\,. \tag{2.8}$$

In synoptically generated cirrus, which is typical for the mid-latitudes, or in-situ cirrus the ice crystal size tends to increase with cloud depth (Lynch et al., 2002, Baran, 2012). Ice production occurs in the top-most layer, called nucleation layer, which is supersaturated with respect to ice and contains small, single ice crystals. While sedimenting into the deeper cloud layers, the ice

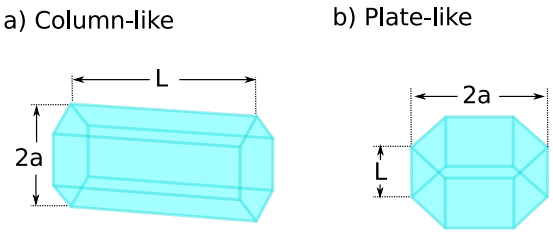

Abbildung 2.5: *Definition of ice crystal dimensions. The length of the c-axis is represented by the maximum dimension L. The maximum diameter of the ice crystal top and base is defined by $2a$.*

crystals can grow from tens of microns up to several cm in size (Heymsfield and Miloshevich, 2003). The ice crystals grow mainly due to deposition of water vapor and aggregation. At the cirrus cloud base sublimation takes place due to the dry air below and leads to rounded crystal edges.

Larger ice crystals tend to take preferred orientations while falling. Jayaweera and Mason (1965) found that cylinders tend to fall with their long axes horizontal in a viscous fluid if the ratio of diameter to maximum dimension is less than 1, i.e. $2a < L$. Ono (1969) observed freely falling columnar and plate crystals in natural ice clouds. The author confirmed that columnar crystals are oriented with their c-axis horizontally, whereas plates are oriented with their main faces horizontally while falling. Platt (1978) performed lidar backscatter measurements and found predominantly plate-shaped ice crystals which were oriented horizontally in cirrus clouds at approximately $-15\,°\mathrm{C}$.

2.1.4 Cirrus microphysical properties

Depending on the excess of water vapor and temperature the ice crystals grow to slightly different sizes within a certain cloud volume. This ensemble of ice crystals can be described by a size distribution, relating the particle size with the number concentration. The size distribution of ice crystals is typically parameterized by a gamma distribution (Heymsfield et al., 2013)

$$N(D) = N_0\, D^{\mu}\, \exp\left(-\lambda D\right), \tag{2.9}$$

with the intercept N_0, the dispersion μ and the slope λ. According to Heymsfield et al. (2013) μ typically takes values between about 0 and 2, whereas λ ranges between about $10\,\mathrm{cm}^{-1}$ to $100\,\mathrm{cm}^{-1}$ for stratiform clouds and temperatures between $0\,°\mathrm{C}$ to $-50\,°\mathrm{C}$. The dispersion (μ) decreases, i.e. the particle size distribution broadens with increasing temperature. Assuming a certain particle size distribution N, the total projected area A_{tot} and total volume of ice per unit volume of air V_{tot} is determined by

$$A_{\mathrm{tot}} = \int_{\mathrm{D_{min}}}^{\mathrm{D_{max}}} A(D)\, N(D)\, dD\,, \tag{2.10}$$

and

$$V_{\mathrm{tot}} = \int_{\mathrm{D_{min}}}^{\mathrm{D_{max}}} V(D)\, N(D)\, dD\,, \tag{2.11}$$

where D_{min} and D_{max} describe the minimum and maximum particle size, N is the number concentration for size D and $A(D)$ and $V(D)$ are the projected area and volume of a specific particle of size D. As discussed by McFarquhar and Heymsfield (1998) there are different ways

to define the effective radius r_{eff}. Throughout this study the following definition will be used

$$r_{\text{eff}} = \frac{3}{4} \frac{V_{\text{tot}}}{A_{\text{tot}}} \, . \tag{2.12}$$

In general, the particle size distribution evolves from cloud top to cloud base: ice crystal size increases and ice crystal shapes become increasingly more complex towards cloud base (Baran (2012) and references therein).

2.2 Radiation and atmospheric radiative transfer

In order to provide a basis for the understanding of the following study on ground-based remote sensing of halo displays, this section will give an overview over the characteristics of light and basic radiation laws, as well as its interactions with atmospheric constituents. Finally, these mechanisms are brought together in the radiative transfer equation, which describes the emission, absorption and scattering of photons traveling through the atmosphere.

2.2.1 Characterization and properties of light

Solar and thermal spectrum

Subregion	Range	Description
X rays	$\lambda < 10\,\mathrm{nm}$	Gamma radiation
UV	$10 < \lambda < 400\,\mathrm{nm}$	Ultra visible light
VIS	$400 < \lambda < 700\,\mathrm{nm}$	Visible light
Near IR	$0.7 < \lambda < 3.5\,\mu\mathrm{m}$	Near infrared light
Thermal IR	$3.5 < \lambda < 100\,\mu\mathrm{m}$	Thermal infrared light

Tabelle 2.1: *Classification of electromagnetic radiation for the solar and thermal spectrum adapted from Thomas and Stamnes (1999).*

Table 2.1 describes the classification of the electromagnetic spectrum in the specific regimes, where the wavelength of the radiation λ is defined as $\lambda = \frac{c}{\nu} = \frac{2\pi c}{\omega}$ with c, the speed of light, and ν (ω) the (angular) frequency. For most of the remote sensing applications it is convenient to separate the spectrum of the light according to its wavelength into two main regimes: the solar and the thermal/terrestrial spectrum, where the transition between both of them is at a wavelength of about 3.5 µm according to Thomas and Stamnes (1999) and 4 µm according to Liou (1992). This study focuses on the solar spectrum and mainly on the visible spectral range between 400 nm and 800 nm.

Radiative quantities

Throughout this study two radiative quantities are commonly used: the irradiance E, defined as the variation of the radiating energy Q by unit area A and time t and the radiance L which additionally takes into account the direction of the incident radiation as an element of the unit solid angle Ω. The quantities in Table 2.2 are spectrally integrated. The spectrally dependent notation of the radiance is defined by $L_\lambda = \mathrm{dQ}/(\mathrm{dA}\cos\theta\,\mathrm{d}\Omega\,\mathrm{d}\lambda\,\mathrm{dt})$ with the unit $[\mathrm{W\,m^{-2}\,nm^{-1}\,sr^{-1}}]$, and similarly the spectral irradiance E_λ measured in $[\mathrm{W\,m^{-2}\,nm^{-1}}]$. Subsequently, an introduction to some fundamental radiative laws is provided following primarily Thomas and Stamnes (1999)

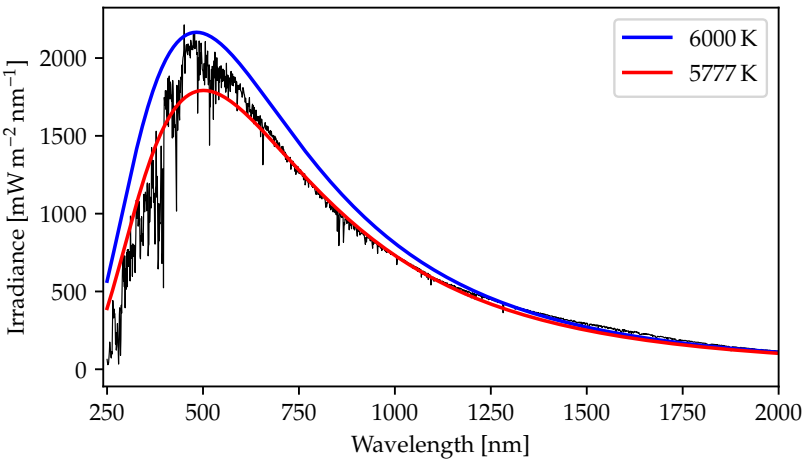

Abbildung 2.6: *Spectrum of the solar radiation at top of the atmosphere (black) based on data from Kurucz (1992). The blue and red curves represent emission from an ideal blackbody at* 6000 K *and* 5777 K, *respectively.*

Quantity	Symbol	Definition	Unit
Radiating energy	Q		J
Radiating power	Φ	$\frac{\mathrm{dQ}}{\mathrm{dt}}$	W
Irradiance	E	$\frac{\mathrm{dQ}}{\mathrm{dA}\cos\theta\,\mathrm{dt}}$	$\mathrm{W\,m^{-2}}$
Radiance	L	$\frac{\mathrm{dQ}}{\mathrm{dA}\cos\theta\,\mathrm{d\Omega}\,\mathrm{dt}}$	$\mathrm{W\,m^{-2}\,sr^{-1}}$

Tabelle 2.2: *Definition of the main radiative quantities used in this study.*

and Zinth and Zinth (2005). If not explicitly stated, the following equations are provided in the spectrally integrated notation only, but are applicable to the spectral quantities in the same way.

Basic radiative laws

The solar spectrum, measured at the top of the atmosphere, is very similar to the radiation spectrum of a blackbody with a temperature of 5778 K (Thomas and Stamnes, 1999). The red and blue curves in Fig. 2.6 result from **Planck's radiation law**, describing the spectral radiance of a blackbody as a function of its temperature:

$$B_{\mathrm{Planck}}(\lambda, T) = \frac{2hc^2}{\lambda^5}\left[\exp\left(\frac{hc}{\lambda k_{\mathrm{B}} T}\right) - 1\right]^{-1}. \tag{2.13}$$

with Planck's constant h, the speed of light in vacuum c and Boltzmann's constant k_{B}. Integrating Planck's radiation law over the half space gives the irradiance as a function of the blackbody

temperature, known as **Stefan-Boltzmann's law**:

$$E_{\text{Planck}}(T) = \pi \cdot \int_0^\infty B_{\text{Planck}}(\lambda, T)\, d\lambda = \sigma_{\text{B}}\, T^4\,, \tag{2.14}$$

where $\sigma_{\text{B}} = 2\pi^5 k_{\text{B}}^4 / 15 h^3 c^2$ is called Stefan-Boltzmann's constant.

Bouguer-Lambert-Beer's law describes the attenuation of the radiance dL along the path length ds through an extincting substance of concentration n with the extinction cross section $\sigma_{\text{ext}} = \sigma_{\text{abs}} + \sigma_{\text{sca}}$, which is the sum of the absorption and the scattering cross section:

$$dL = -L \cdot n \cdot \sigma_{\text{ext}}\, ds\,. \tag{2.15}$$

The optical depth along the path of light s' is defined by

$$\tau_{\text{s}} = \int_0^s k_{\text{ext}}(s')\, ds'\,, \tag{2.16}$$

with the extinction coefficient $k_{\text{ext}} = n \cdot \sigma_{\text{ext}}$. Integrating equation (2.15) over ds, results in the integrated form of Bouguer-Lambert-Beer's law:

$$L(s) = L(0) \cdot \exp(-\tau_{\text{s}})\,, \tag{2.17}$$

Extinction and optical depth are commonly measured along the vertical axis from the top of the atmosphere downward. A path element ds tilted by the zenith angle θ with respect to dz, can be calculated by $ds = dz/\cos\theta = dz/\mu$, where $\mu < 0$ for upward and $\mu > 0$ for downward directed radiances. For such a plane-parallel atmosphere the optical depth τ for a tilted path of the radiation through the atmosphere ds can be calculated as follows:

$$\tau = \int_z^\infty k_{\text{ext}}(z')\, dz' = \int_s^\infty k_{\text{ext}}(s') \cdot \cos\,\theta\, ds' = \cos\,\theta \cdot \tau_{\text{s}} = \tau_{\text{s}} \cdot \mu\,. \tag{2.18}$$

Thereby Bouguer-Lambert-Beer's law can be written as:

$$L(\tau) = L(0) \cdot \exp(-\tau/\mu)\,, \qquad \text{with } \mu > 0, \tag{2.19}$$

where $L(0)$ is the extraterrestrial radiance at the top of the atmosphere.

2.2.2 Radiative transfer equation

One major focus of this study is the transfer of light through the atmosphere and its interaction with atmospheric components such as clouds, molecules and aerosol particles. Chandrasekhar (1960) was the first to develop a radiative transfer equation and to show how to accurately compute the intensity and polarization of radiation in case of multiple Rayleigh scattering (Zdunkowski et al., 2007). His work was extended notably by Sekera and co-workers.
Following Zdunkowski et al. (2007) the radiative transfer equation (RTE) in a three-dimensional medium can be expressed as

$$\boldsymbol{\Omega} \cdot \nabla L = -k_{\text{ext},\lambda} L + \frac{k_{\text{sca},\lambda}}{4\pi} \int_{4\pi} \mathcal{P}(\boldsymbol{\Omega}' \cdot \boldsymbol{\Omega})\, L(\boldsymbol{\Omega}')\, d\boldsymbol{\Omega}' + J^e\,. \tag{2.20}$$

The RTE in plane-parallel (one-dimensional) geometry yields

$$\mu \frac{d}{d\tau} L(\tau, \mu, \phi) = \overbrace{L(\tau, \mu, \phi)}^{(1)} - \overbrace{\frac{\omega_0}{4\pi} \int_0^{2\pi} \int_{-1}^{1} \mathcal{P}(\cos\Theta)\, L(\tau, \mu', \phi') d\mu' d\phi'}^{(2)} - \overbrace{(1-\omega_0) B_{\text{Planck}}(T)}^{(3)}, \tag{2.21}$$

using $\mathbf{\Omega} \cdot \nabla L = dL/ds$ and $ds = dz/\mu$ with $\mu = \cos\theta$. The term $\cos\Theta = \mathbf{\Omega'} \cdot \mathbf{\Omega}$ is the cosine of the scattering angle, which is a function of $\theta', \phi', \theta, \phi$. The four angles denote the zenith and azimuth angle of the incoming direction (θ', ϕ') and the scattered direction (θ, ϕ). $B_{\text{Planck}}(T)$ is the Planckian emission (cf. Eq. (2.13)). Further variables in the radiative transfer equation are: $\omega_0 = k_{\text{sca}}/k_{\text{ext}}$, the single-scattering albedo, τ the optical depth, $\mu = \cos\theta$ the cosine of the zenith angle, and ϕ the azimuth angle.
In the following, the individual parts of the radiative transfer equation will be explained:

Together with the left hand side of Eq. (2.21),

- (1) represents the reduction of radiation due to extinction by atmospheric constituents according to Lambert-Beer's law (Eq. (2.19)),
- (2) characterizes the scattering of the radiation from the direction (θ', ϕ') into the new direction (θ, ϕ), which is determined by the scattering phase function,
- (3) is the contribution of thermal emission to the radiation from the volume element along the propagation direction of the photons, following Planck's law (Eq. (2.13)).

2.2.3 Light scattering by atmospheric particles

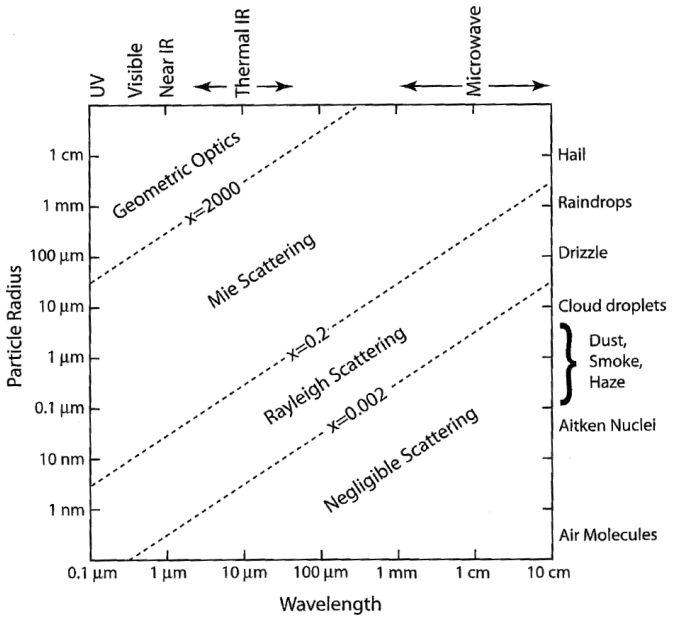

Abbildung 2.7: *Relationship between particle size, radiation wavelength and scattering behavior for atmospheric particles. Diagonal dashed lines represent rough boundaries between scattering regimes (Petty, 2006).*

The method to describe and calculate the optical properties of scattering particles in the atmosphere depends crucially on the relationship between the size of a particle and the wavelength

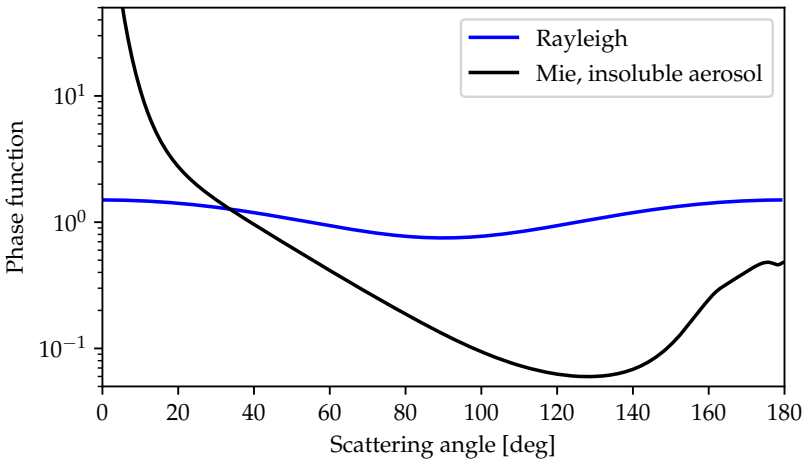

Abbildung 2.8: *Phase functions for Rayleigh scattering (blue) and Lorentz-Mie theory for an insoluble aerosol (black) at a wavelength of* 550 nm.

of the radiation, which is expressed by the size parameter X:

$$X = \frac{2\pi r}{\lambda}\,, \tag{2.22}$$

with wavelength λ and particle radius r. For non-spherical particles the size parameter is calculated by using the maximum dimension instead of the radius. As depicted in Figure 2.7 there are basically three main scattering regimes:

1. Rayleigh or molecular scattering ((Strutt, 1871), $X \ll 1$)
2. Lorentz-Mie theory (Mie (1908), $X \approx 1$, only valid for spherical particles)
3. Geometric optics ($X \gg 1$)

Molecular and aerosol optical properties

For ground-based remote sensing of cirrus clouds, molecular and aerosol optical properties have to be considered and will shortly be explained in the following. For very small particles in the atmosphere, like e.g. molecules, with radii much smaller than the wavelength ($r \ll \lambda$), the size parameter $X \ll 1$ and Rayleigh scattering is valid (cf. Fig. 2.7). Named after Lord Rayleigh, who explained 1871 successfully the color and polarization of skylight. The phase function for Rayleigh scattering is defined as

$$\mathcal{P}(\cos\Theta) = \frac{3}{4}(1 + \cos^2\Theta) \tag{2.23}$$

and depicted in Fig. 2.8 with a blue line. The scattering probability is equally maximal in the forward and backward direction and decreasing towards the sides with a minimum at a scattering angle of $\Theta = 90°$. A measure for the strength of forward scattering is given by the asymmetry factor, which is the first moment of the phase function. The asymmetry factor can be calculated by

$$g = \frac{1}{2}\int_{-1}^{1} \mathcal{P}(\cos\Theta)\,\cos\Theta\; d\cos\Theta\,, \tag{2.24}$$

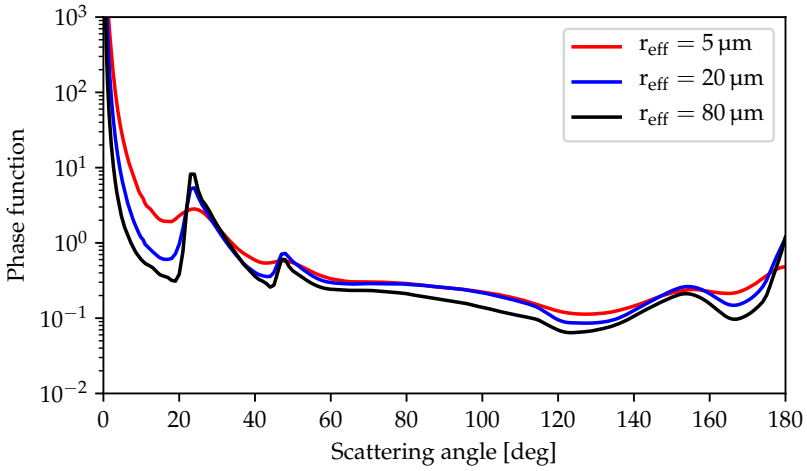

Abbildung 2.9: *Ice crystal phase functions of smooth solid columns for effective radii of 5 (red), 20 (blue), and 80 µm (black) and a wavelength of 550 nm from the database of Yang et al. (2013). The 22° and 46° halo at the respective scattering angles are a geometric optics phenomenon and thus become more pronounced for larger ice crystals.*

where $\mathcal{P}(\Theta)$ is the normalized phase function. For Rayleigh scattering $g = 0$, which is equivalent to symmetric scattering. For complete forward or backward scattering the asymmetry factor would be $g = 1$ and $g = -1$, respectively. The scattering cross section for Rayleigh scattering is inversely proportional to the 4th power of the wavelength λ (Thomas and Stamnes, 1999):

$$\sigma_{\text{sca}} \propto 1/\lambda^4 \,. \tag{2.25}$$

Equation (2.25) explains for example the blue sky: the scattering cross section strongly increases for smaller wavelengths. Blue light ($\lambda = 420$ nm) is scattered 10 times stronger than red light at 720 nm. During dusk and dawn, light travels much longer distances through the atmosphere, and only the longer wavelengths of the solar radiation reach the observer causing the reddish light of the rising or setting sun. In the Mie regime (cf. Fig. 2.7) the size parameter X is close to 1. Small aerosol particles have size parameters of $X \sim 1$ and a pronounced forward scattering compared to molecules, as shown in Fig. 2.8 by the black line for a insoluble aerosol at a wavelength of 550 nm. In this case the asymmetry factor takes values $g > 0$.

Ice crystal optical properties

Mie theory is only applicable to spherical particles, thus different methods have to be use to calculate the optical properties of non-spherical ice crystals. Liou and Yang (2016) give detailed explanations of available methods for different size parameters, such as the Finite-difference time domain (FDTD) method, the T-matrix method or the discrete dipole approximation. For ice crystals much larger than the wavelength, the size parameter is $X \gg 1$, scattering is predominantly in the forward direction and the geometric optics principles can be applied. Figure 2.9 shows three phase functions of solid ice crystal columns with smooth surface, which are averaged over a size distribution with effective radii of 5 µm (red), 20 µm (blue), and 80 µm (black) at a wavelength of 550 nm. The phase functions exhibit a large forward scattering peak and show the 22° and 46° halo at the respective scattering angles. For larger effective radii with constant wavelength the size parameter increases and the halo peaks become more pronounced. Since halo displays are, as rainbows, a geometric optics phenomenon, the optical properties of large

ice crystals can be calculated in the geometric optics approximation. According to Liou and Yang (2016) The phase function of an ensemble of non-spherical ice particles of the same size and randomly oriented can be expressed as

$$\mathcal{P}(\Theta) = \frac{1}{2\pi\sigma_s} \int_0^{2\pi} \int_0^{\pi/2} \mathcal{P}'(\alpha', \gamma')\sigma_s'(\alpha', \gamma') \sin\alpha' d\alpha' d\gamma' \,, \tag{2.26}$$

where α' and γ' are the orientation angles relative to the direction of the incident light beam and $\mathcal{P}'$ is the scattering phase function for a single particle. For randomly oriented particles the phase function depends solely on the scattering angle Θ. The scattering phase function is normalized to unity:

$$\int_0^{2\pi} \int_0^{\pi} \frac{\mathcal{P}(\Theta)}{4\pi} \sin\Theta \, d\Theta d\phi = 1 \,. \tag{2.27}$$

In the case of horizontally oriented ice crystals (cf. Section 2.1.3) the scattering phase function can be written as

$$\mathcal{P}(\alpha, \gamma; \mu', \phi'; \mu, \phi) = \mathcal{P}(\alpha', \gamma'; \cos\Theta, \Delta\phi) \,, \tag{2.28}$$

with $\Delta\phi = \phi - \phi'$. The phase function depends on the directions of the incident and the scattered beams as well as the orientation of the non-spherical ice crystal. The extinction and scattering cross-sections, however, depend only on the direction of the incident light and the ice crystal orientation.

For a symmetric hexagonal ice crystal two orientation angles can be defined with respect to the direction of incident light: α the complement of the zenith angle and β the angle mapped on the x-y plane relative to the incident beam. The surface area of the ice crystal basal face is $3\sqrt{3}D^2/8$ and $D\,L$ for the prism faces. The cross-sectional area for the basal plane mapped along the light beam is $3\sqrt{3}D^2/8 \sin\alpha$. For the prism plane the cross-sectional area also depends on the angle of the light beam relative to the six prime planes, which should be maximum for $\beta = \pi/6$. This yields $DL \cos\alpha \cos(\pi/6 - \beta)$. Thus the geometric cross-section for the entire hexagonal crystal can be written as

$$G(\alpha, \beta) = \frac{3\sqrt{3}}{8} D^2 \sin\alpha + DL \cos\alpha \cos(\pi/6 - \beta) \,. \tag{2.29}$$

To obtain the average cross-section for randomly oriented ice crystals the previous equation is integrated over α and β:

$$\bar{G} = \frac{6}{\pi} \int_0^{\pi/6} \int_0^{\pi/2} G(\alpha, \beta) \cos\alpha \, d\alpha d\beta = \frac{3}{4}(\sqrt{3}D^2/4 + DL) \,. \tag{2.30}$$

The surface of a hexagonal ice crystal is $S = 3(\sqrt{3}D^2/4 + DL)$. The extinction efficiency is defined as $Q_{\text{ext}} = \sigma_e/G$ and approaches 2 in the geometric optics approximation, which is called the optical extinction theorem. In the geometric optics limit the extinction cross-section is $\sigma_e = 2\bar{G} = S/2$ and thus the average geometric cross-section for randomly oriented hexagonal ice crystals (plates, columns) $\bar{G} = 1/4\,S$.

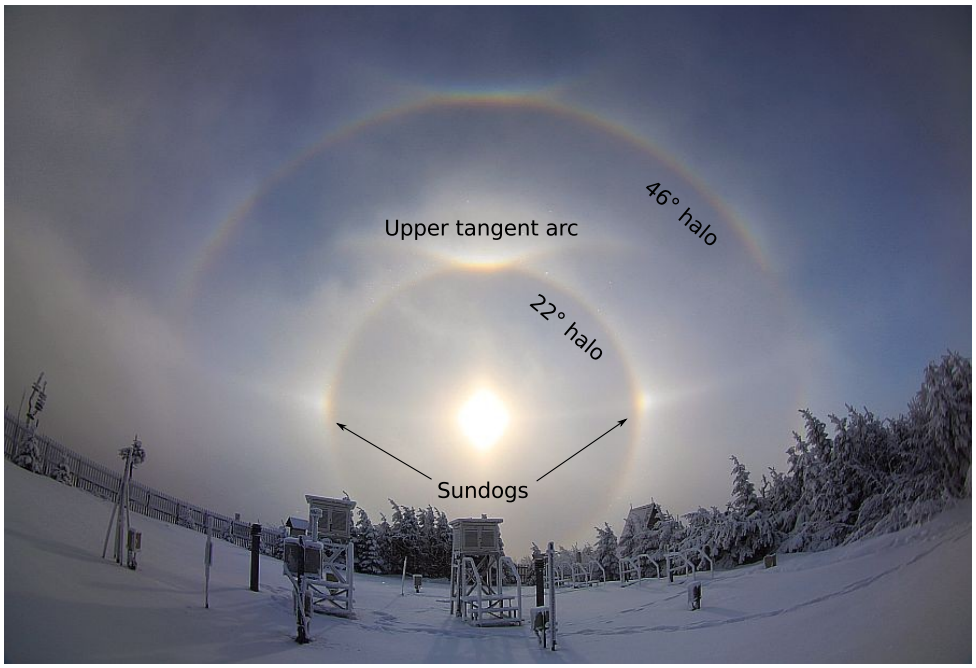

Abbildung 2.10: *Halo displays in ice fog photographed by Claudia Hinz on Mount Fichtelberg, 21 January 2015. The 22° halo, both sundogs, the upper tangent arc and the rare 46° halo are visible.*

2.3 Halo displays

The formation of halo displays, which are produced by refraction and reflection of light by ice crystals, is presented in this section. Figure 2.10 shows different halo displays which are formed by hexagonal crystals in ice fog on Mount Fichtelberg. While the 22° and 46° halo are produced by randomly oriented hexagonal crystals, the upper tangent arc is formed by ice crystal columns, which are oriented with their c-axis horizontally. The sundogs are caused by ice crystal plates which are oriented with their c-axis vertically. According to AKM (http://meteoros.de) 22° halos can be observed on 80 to 120 days per year, sundogs on 60 to 80 days per year, and upper tangent arcs on 20 to 30 days per year. These three halo displays can be spotted most frequently, whereas the 46° halo is visible on only 4 to 10 days per year. An overview over the basic physical principles will be provided, which explain the formation of these halo displays in the geometric optics approximation.

2.3.1 Reflection and refraction laws

The refraction and reflection of light by ice crystals depends mainly on the refractive index, which is primarily a function of the wavelength. The temperature dependence of the refractive index is negligible for $\lambda < 20\,\mu\text{m}$ (Liou and Yang, 2016). The index of refraction is defined as the ratio of the velocity of light c_0 in vacuum to that in the medium

$$n = c_0/c \approx \sqrt{\epsilon} \tag{2.31}$$

and can be expressed with the permittivity ϵ for frequencies in a small range far apart from resonance frequencies. The refractive index consists of a real part n_{Re} and an imaginary part n_{Im}

$$n = n_{\text{Re}} - i\, n_{\text{Im}}\,. \tag{2.32}$$

While the real part describes refraction, absorption is determined by the imaginary part of the refractive index. Figure 2.11 shows the real part of the refractive index of ice for wavelengths

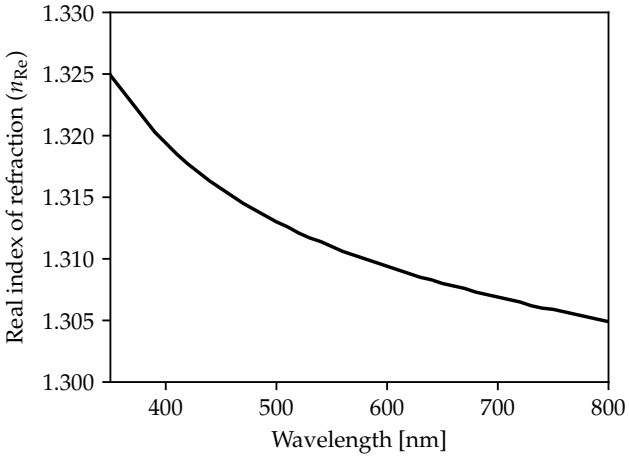

Abbildung 2.11: *Real refractive index of ice in the visible spectral range (data from Warren and Brandt (2008)).*

in the visible spectral range based on the data from Warren and Brandt (2008) for a nominal temperature of 266 K. The real refractive index takes values of about $n_{\mathrm{Re}} \approx 1.31$, whereas the imaginary part is small with $n_{\mathrm{Re}} < 2e^{-7}$ in this wavelength region.

The propagation of light in inhomogeneous media can be described using Fermat's Principle in the geometric optics approximation. Fermat's Principle states that the light propagates such that the optical path W on the traveled path S_0 is maximum or minimum compared to neighboring paths S_{i}. The optical path W is defined as

$$W(S) = \int_{S(Q->P)} n(\vec{x})\, dS \tag{2.33}$$

for light propagating from the source Q to the point of observation P with the refractive index n, which depends on the location $\vec{x}$. For the light path which exhibits an extreme value the condition

$$\left(\frac{dW(S)}{dS}\right)_{S_0} = 0 \tag{2.34}$$

has to be fulfilled. **Snell's law** can be derived using Eq. (2.34). Figure 2.12 shows schematically

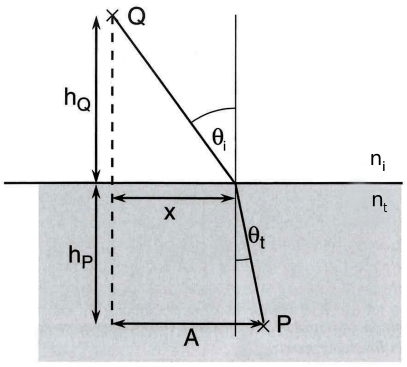

Abbildung 2.12: *Schematic drawing of the light path geometry for refraction at a boundary, adapted from Zinth and Zinth (2005).*

the geometry of a refracted light path. The refractive index of the medium of the incident light n_i is smaller than the refractive index of the medium of the transmitted light n_t. Using the Pythagorean theorem, the optical path W can be calculated from P to Q.

$$W = n_\mathrm{i}\sqrt{h_Q^2 + x^2} + n_\mathrm{t}\sqrt{h_P^2 + (A-x)^2}\,. \tag{2.35}$$

With $dW/dx = 0$ we obtain

$$\frac{dW}{dx} = n_\mathrm{i}\frac{x}{\sqrt{h_Q^2 + x^2}} - n_\mathrm{t}\frac{A-x}{\sqrt{h_P^2 + (A-x)^2}} = 0 \tag{2.36}$$

and finally **Snell's law**

$$n_\mathrm{i}\,\sin\theta_\mathrm{i} = n_\mathrm{t}\,\sin\theta_\mathrm{t}\,. \tag{2.37}$$

Snell's law describes the relation between the angle of incidence in a medium with refractive index n and the angle of refraction in a medium with refractive index n_t.

To calculate the intensity of the reflected and transmitted light the electric and magnetic fields have to be decomposed into their components parallel and perpendicular to the plane of incidence and apply the continuity conditions. The reflection coefficients of the field components parallel ($\vec{r_\parallel}$) and perpendicular ($\vec{r_\perp}$) with respect to the plane of incidence, called **Fresnel Equations**:

$$\vec{r_\perp} = \frac{E_{r\perp}}{E_{i\perp}} = -\frac{\sin(\theta_\mathrm{i} - \theta_\mathrm{t})}{\sin(\theta_\mathrm{i} + \theta_\mathrm{t})}\,, \tag{2.38}$$

$$\vec{r_\parallel} = \frac{E_{r\parallel}}{E_{i\parallel}} = -\frac{\tan(\theta_\mathrm{i} - \theta_\mathrm{t})}{\tan(\theta_\mathrm{i} + \theta_\mathrm{t})}\,. \tag{2.39}$$

2.3.2 Formation of halo displays

According to the long-term observations of Sassen et al. (2003b) and the AKM the most frequently observed halo displays are the 22° halo, the sundogs, and the upper and lower tangent arc. The scattering geometry of 22° halos and sundogs can be calculated with simple analytical equations and will be explained in the following. Although rarely observed, the formation of the 46° halo will be explained together with the 22° halo due to the similarity of the raypaths forming the two halo types.

The 22° and 46° halo

The scattering phase functions in Fig. 2.9 feature both the 22° and 46° halo, which are formed by two refractions in a randomly oriented hexagonal prism as depicted in Fig. 2.13a. An example of a 22° halo and 46° halo is presented in Fig. 2.10. While the formation of the 22° requires refraction through two side faces of the hexagon enclosing a 60°-angle, the 46° forms by refraction through a base and a side face with a wedge angle of 90°. Using Snell's law from Eq. (2.37), the scattering angle of a prism with opening angle Δ can be calculated as a function of the incident angle:

$$\Theta = (\theta_\mathrm{i} - \theta_\mathrm{t}) + (\theta_\mathrm{i}' - \theta_\mathrm{t}') = 2\theta_\mathrm{i}' - \Delta\,. \tag{2.40}$$

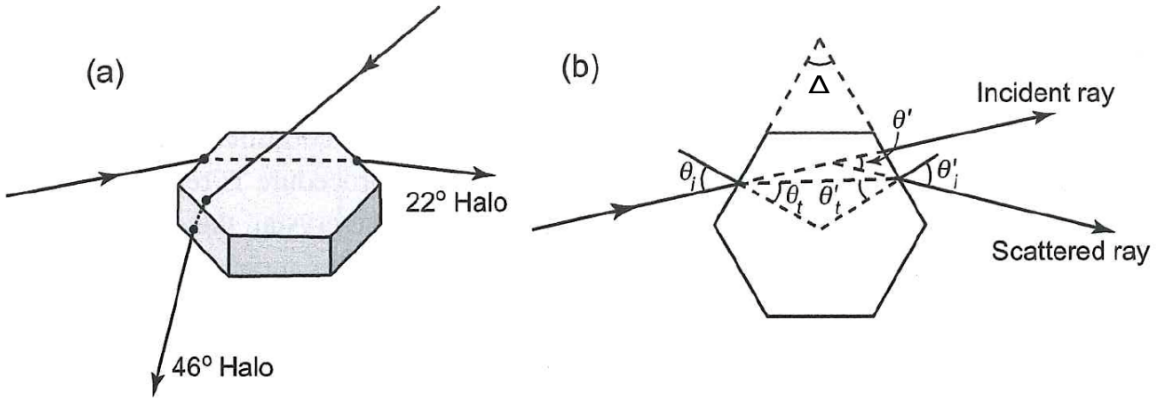

Abbildung 2.13: *Ray paths of the 22° and 46° halo through an ice crystal (adapted from Liou and Yang (2016)).*

Assuming $n_\mathrm{i} = 1$ for air and $n = n_\mathrm{t}$ the refractive index of ice, the scattering angle can be calculated as a function of the incident angle θ_i:

$$\Theta = \theta_\mathrm{i} - \Delta + \arcsin\left(\sin\Delta\sqrt{n^2 - \sin^2\theta_\mathrm{i}} - \sin\theta_\mathrm{i}\ \cos\Delta\right)\ . \tag{2.41}$$

Figure 2.14 shows a schematic plot of the raypaths from Fig. 2.13b for different incident angles, which is realized here by rotating the hexagon relative to the incident direction. Hexagon and raypath are displayed in blue with increasing opacity for smaller scattering angles. If the raypath

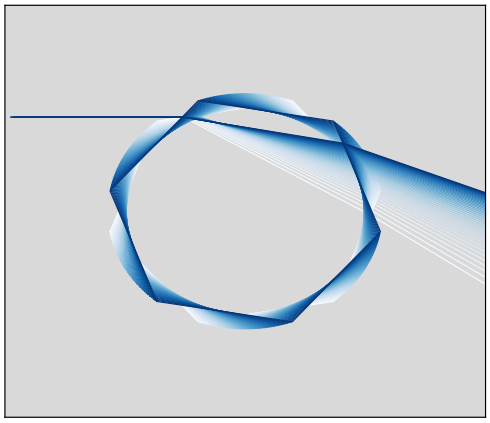

Abbildung 2.14: *Schematic plot of 22° halo raypaths for different incident angles, realized here by different rotation angles of the ice crystal. The calculations were performed using Eq. (2.41). The opacity of the raypaths depicted in blue increases for smaller scattering angles and is represented in dark blue for the minimum scattering angle at 22.1° for a wavelength of 500 nm.*

through the prism is symmetric, i.e. for $\theta_\mathrm{i} = \theta'_\mathrm{t}$, the scattering angle Θ reaches a minimum $\Theta = \Theta_\mathrm{min}$. Using $\Theta_\mathrm{min} = 2\theta_\mathrm{i} - \Delta$ Eq. (2.41) becomes

$$\Theta_\mathrm{min} = 2\arcsin\left(n\ \sin\left(\frac{\Delta}{2}\right)\right) - \Delta\,, \tag{2.42}$$

or

$$n = \frac{\sin\left(\frac{\Theta_{min}+\Delta}{2}\right)}{\sin\left(\frac{\Delta}{2}\right)}\,. \tag{2.43}$$

The dark blue raypath and hexagon in Fig. 2.14 correspond to the minimum scattering angle of 22.1° at a wavelength of 500 nm. The scattering angles for a 60° and 90° prism are presented in Fig. 2.15 as a function of the incident angle for 400 nm (blue) and 800 nm (red). The incident angle is varied between about 15° and 90°, which is perpendicular to the crystal face. For the 60° prism the minimum scattering angles result in 21.5° for 800 nm and 22.6° for 400 nm which are the theoretical values for the 22° halo. Since the refractive index is smaller for larger wavelength the minimum scattering angle for 800 nm is smaller than for 400 nm, which explains the reddish inner edge of the 22° halo. Minimum scattering angles of 47.8° (400 nm) and 44.7° (800 nm) are found for the 90° prism and represent the 46° halo.

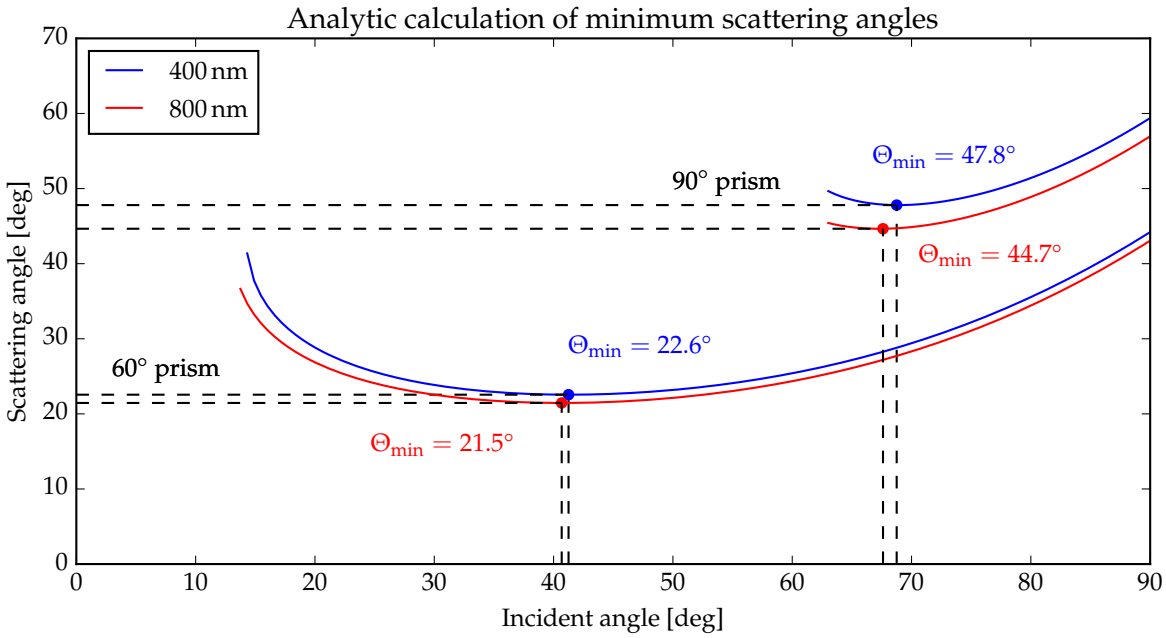

Abbildung 2.15: *Scattering angle as a function of the incident angle for a* 60° *and* 90° *prism using the refractive index for wavelengths of* 400 nm *(blue) and* 800 nm *(red). The calculations were performed using Eq.* (2.41)*. The red and blue dots indicate the minimum scattering angles with the corresponding incident angles.*

The 22° parhelia or sundogs

Another frequently observed halo type are the parhelia of the 22° halo, which are commonly called sundogs (cf. Fig. 2.10). Sundogs form by refraction through two crystal side faces of horizontally oriented ice crystal plates (i.e. with their c-axis vertical). This halo type is not visible in the phase functions in Fig. 2.9 since they assume randomly oriented ice crystals. The raypath responsible for the formation of sundogs can be calculated analytically which was already presented by Wegener (1925) and Minnaert (1937). For a solar elevation of 0° the raypath for sundogs is the same as for 22° halos. For larger solar elevations the light rays cannot follow the path of minimum deviation since the scattering plane is not perpendicular to the c-axis as shown in Fig. 2.16. An equation for the minimum scattering angle of the sundogs can be derived as

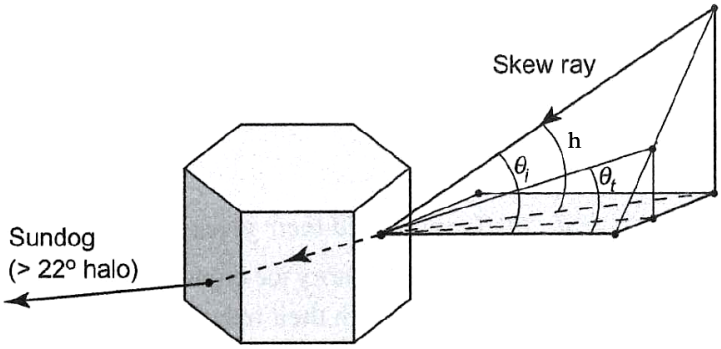

Abbildung 2.16: *The geometry of a skew ray producing a sundog in a 3-D ice crystal plate. The solar elevation angle is denoted with h (adapted from Liou and Yang (2016)).*

outlined in Minnaert (1993).

$$\Theta'_{\text{min}} = 2 \arcsin \left(\sqrt{\frac{n^2 - \sin^2 h}{1 - \sin^2 h}} \, \sin \frac{\Delta}{2} \right) - \Delta \,, \tag{2.44}$$

where h is the solar elevation. Δ is the opening angle of the prism, which is 60° in the case of sundogs as for the 22° halo. Introducing an "effective refractive index"

$$n' = \sqrt{\frac{n^2 - \sin^2 h}{1 - \sin^2 h}} \tag{2.45}$$

the minimum scattering angle for sundogs can be written with similar to Eq. (2.42)

$$\Theta'_{\text{min}} = 2 \arcsin \left(n' \, \sin \frac{\Delta}{2} \right) - \Delta \,, \tag{2.46}$$

with the effective refractive index n' which is increasing with solar elevation. Figure 2.17 shows the minimum scattering angle Θ'_{min} as a function of the solar elevations h. For a solar elevation of $h = 0°$ sundogs and 22° halo are located at the same scattering angle. As the solar elevation increases, the sundogs move further away from the 22° halo to larger scattering angles. The solar elevation at which sundogs can still form is limited. For $h > 60°$ the arcsin in Eq. (2.46) is not defined anymore since its argument takes values > 1. According to Minnaert (1993) for solar elevations larger than 40° no sundogs have been observed. The scattering angles at larger wavelengths are larger than for shorter wavelengths so that the sundogs have a reddish inner edge, similar to the 22° halo. The scattering angle difference between 400 nm and 800 nm is about 1.1° at a solar elevation of 0° and increases to $> 2°$ for solar elevation larger than 55°.

The upper and lower tangent arcs and the circumscribed halo

Upper and lower tangent arcs form by ice crystal columns which are oriented with their c-axis horizontally. Light is refracted through two crystal side faces, similar as for the 22° halo and the sundogs. As their names suggest, these arcs are located tangential to the 22° halo. The shape of the upper and lower tangent arc depends strongly on the solar elevation as illustrated in Fig. 2.18. For solar elevations lower than ∼29° the upper and lower tangent arcs are separated. As the solar elevation is further decreasing the wings of the upper/lower tangent arc are bending more

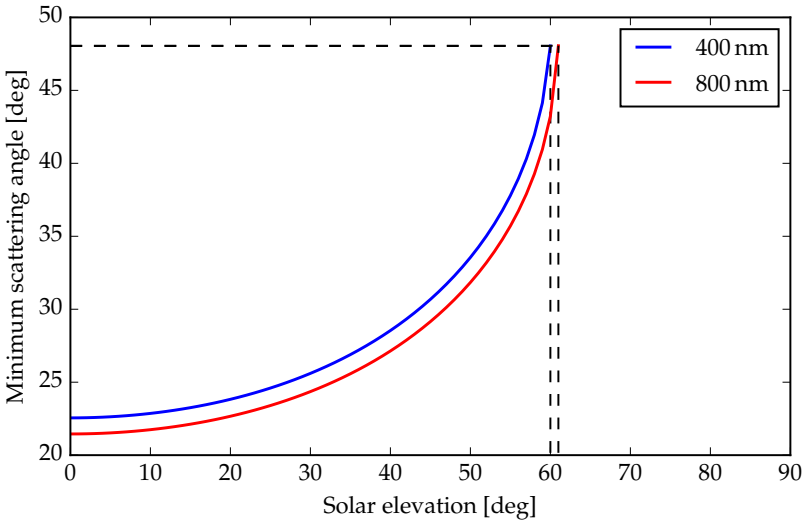

Abbildung 2.17: *Minimum scattering angle of the 22° parhelia or sundogs Θ'_{min} as a function of the solar elevation h for a wavelength of 400 nm and 800 nm. For a solar elevation of 0° the raypath is the same as for the 22° halo resulting in the same scattering angles as in Fig. 2.15: 22.6° and 21.5° for 400 nm and 800 nm, respectively. For solar elevations larger than about 60° ($\Theta'_{\text{min}} \approx 48°$) Eq. (2.46) cannot be solved and sundogs cannot form.*

and more upwards/downwards from the 22° halo. When the solar elevation is smaller than 22° only the upper tangent arc is visible since the lower tangent arc is below the horizon. For solar elevations larger than about 29° the upper and lower tangent arcs merge to form the so-called circumscribed halo as shown in Fig. 2.18. With increasing solar elevation the circumscribed halo is approaching the 22° halo until the two halos merge when the sun is at the zenith. Since the scattering geometry of the tangent arcs and the circumscribed halo is very complex, further investigations of this type of halo will be performed with the help of raytracing simulations and presented in Sections 3.8 and 4.4.

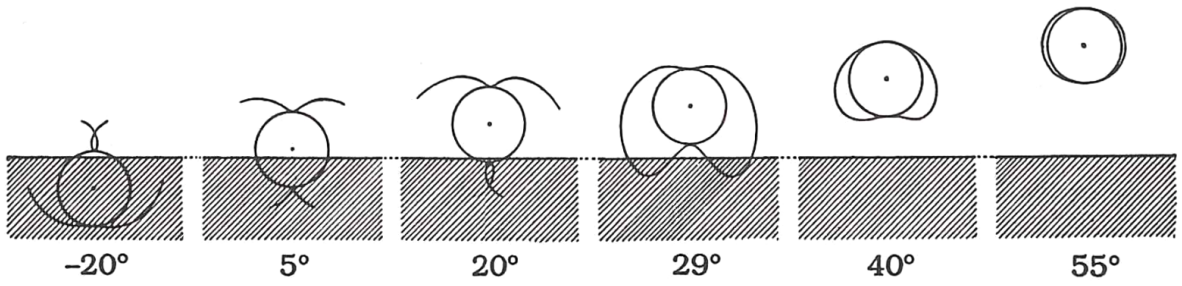

Abbildung 2.18: *Shape of the circumscribed halo at increasing solar elevation (Figure adapted from Minnaert (1993)).*

Kapitel 3

Methods

Sections 3.5.1, 3.5.2 and 3.6 contain parts of the publication by Forster et al. (2017):
Forster, L., M. Seefeldner, M. Wiegner, and B. Mayer, 2017: Ice crystal characterization in cirrus clouds: a sun-tracking camera system and automated detection algorithm for halo displays. *Atmospheric Measurement Techniques*, **10 (7)**, 2499–2516, 10.5194/amt-10-2499-2017, `https://www.atmos-meas-tech.net/10/2499/2017`.

3.1 Radiative transfer simulations

Radiative transfer simulations were performed using the *libRadtran* radiative transfer package (Mayer and Kylling, 2005, Emde et al., 2016). This library provides different solvers for the radiative transfer equation. *libRadtran* allows for an accurate simulation of Rayleigh scattering, molecular absorption, aerosols, surface albedo as well as water and ice clouds. In this study the DISORT and MYSTIC solvers were used for radiative transfer simulations of the 22° halo and will be explained in the following.

3.1.1 MYSTIC

MYSTIC (Emde and Mayer, 2007, Mayer, 2009, Emde et al., 2011, Buras et al., 2011), which stands for "Monte Carlo code for the physically correct tracing of photons in cloudy atmospheres", was used in this study for radiative transfer simulations in the vicinity of the sun with the correct representation of the sunshape which was implemented by Reinhardt et al. (2014). Furthermore, MYSTIC was extended with the ray-tracing algorithm CrystalTrace to perform radiative transfer simulations of oriented ice crystals, which will be explained in Section 3.8.

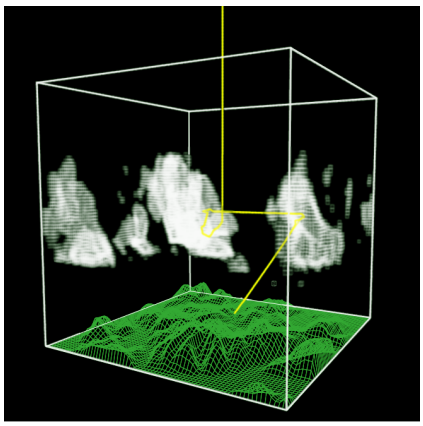

Abbildung 3.1: *Online visualization of a MYSTIC simulation (Mayer, 2009).*

The principle of the Monte Carlo solver MYSTIC is the tracing of individual photons through the atmosphere from the source to their final point. Sampling a large number of photons allows for an accurate simulation of radiances and irradiances and their interaction with inhomogeneous clouds, surface albedo, BRDF[1], and topography without explicit

[1]The "Bi-Directional Polarized Reflectance Function" is a 4D function, describing the reflection of light from

konwledge of the radiative transfer equation. The model domain consists of a one-dimensional (1D) grid, on which the concentrations of molecules and aerosols are defined, and on a three-dimensional (3D) grid for the cloud cells. A visualized example of a MYSTIC simulation is shown in Fig. 3.1. This procedure is outlined in the following for the solar spectrum, i.e. assuming the sun as photon source which is quantified by the extraterrestrial solar irradiance. In MYSTIC, photons are defined by a location and direction in 3D space and are assigned with a weight w_a, which equals to 1 at the source. With the sun as source, the photon's initial direction is defined by the solar zenith angle θ_0 and azimuth angle ϕ_0. The photons are traced through the atmosphere from one scattering event to the other. The photon's free path length to the next scattering event is sampled according to the probability density function (PDF):

$$P_\mathrm{s} = \exp\left(-\int_0^s k_\mathrm{sca}\, ds'\right) \tag{3.1}$$

with the total scattering coefficient $k_\mathrm{sca} = \sum_{i=1}^{N} k_\mathrm{sca,i}$, which is the sum of the scattering coefficient $k_\mathrm{sca,i}$ for N interacting particles and molecules. The decision, which interaction takes place is made by drawing a random number $r \in [0, 1)$. The photon interacts with the jth particle type if the random number fulfills the condition

$$\frac{\sum_{i=1}^{j-1} k_\mathrm{sca,i}}{k_\mathrm{sca}} < r \leq \frac{\sum_{i=1}^{j} k_\mathrm{sca,i}}{k_\mathrm{sca}}\ . \tag{3.2}$$

For sampling the scattering direction the phase function is used as PDF for the scattering angle and a random number between 0 and 2π for the azimuth angle. Since loosing photons is computationally inefficient, absorption is treated implicitly by reducing the photon's weight w_a according to Bouguer-Lambert-Beer's law (Eq. (2.17)).

$$w_\mathrm{a} = \exp\left(-\int k_\mathrm{abs}\, ds\right). \tag{3.3}$$

Here, ds is the element of the photon path s and k_abs is the total absorption coefficient including molecules, aerosols, water and ice clouds. Photons which are absorbed by the earth's surface, are scattered and weighted with the Lambertian albedo or the BRDF. In case a photon exits the sides of the domain, the periodic boundary conditions ensure that it re-enters the domain from the opposite side. The path of the photon terminates if it hits the detector or exits the atmosphere at the top. Another way to save computational time is the backward tracing method, which calculates the photon's path backward from the final point to the source of the radiation (Emde and Mayer, 2007). This technique refers to the Helmholtz reciprocity principle, which states that the path of light from A to B is reversible (von Helmholtz and König, 1896). The backward tracing method is especially powerful for the simulation of radiances, measured by remote sensing instruments with a small field of view (FOV), since only a very small amount of the photons started in the beginning are finally detected by the sensor (cf. Fig. 3.2b). For backward tracing, the probability that a photon is scattered towards the source is calculated at every scattering event. To obtain a better sampling statistic, the photon follows the direct path to the source at each scattering event weighted by the probability for the respective scattering angle, which is given by the scattering phase function. This method is called *local estimate* (Davis et al., 1985, Kunkel and Weinma, 1976) and is illustrated by the dash-dotted lines in Fig. 3.2. For the radiative transfer simulations in clouds, the extremely efficient Variance Reduction

an opaque surface (Mayer, 2009)

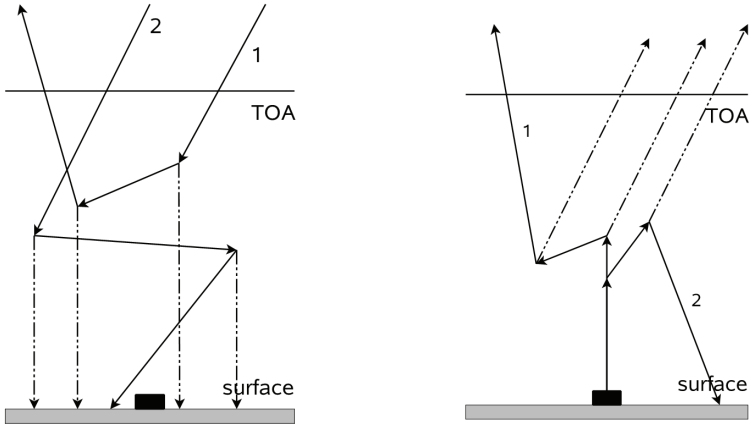

(a) Forward tracing *(b) Backward tracing*

Abbildung 3.2: *MYSTIC forward (a) and backward tracing mode (b), from Mayer (2009).*

"Optimal Options" Method vroom (Buras et al., 2011) was used. This method enables radiance calculations without the need to truncate the forward peak of the scattering phase functions.

3.1.2 DISORT

DISORT stands for "discrete ordinate technique" and was developed by Stamnes et al. (1988) to calculate the angular variation of the radiance. This 1D solver treats the atmosphere as a number of homogeneous, plane-parallel layers. The single terms of the RTE can be represented by Fourier and Legendre moments and the integral over the scattering phase function can be approximated by a sum over discrete angles. This differential equation system can be solved to calculate the radiance at $2n$ "discrete ordinates" or "streams". One advantage of the DISORT solver are that the solution of the RTE can be derived in a completely explicit form. The computational effort for each individual layer is independent of its optical depth. Furthermore, the method is accurate enough to perform benchmark calculations. DISORT is used in this study to calculate the radiance distribution in the region of the 22° halo with 16 streams, which is the default value for radiances in *libRadtran*. These simulations could also be performed with the MYSTIC solver but with much higher computational effort. Since cirrus clouds, especially during the presence of halo displays, are rather homogeneous, 3D effects are negligible in this case and the radiative transfer simulations can be performed with the DISORT solver. Another advantage of DISORT is the noise-free result. A comparison of a radiance simulation using DISORT and MYSTIC is shown in Fig. 3.3. As illustrated by Fig. 3.3 the difference between the simulation performed with DISORT and MYSTIC is small and amounts to about $(1.4 \pm 2.3)\,\%$ for a cirrus cloud with optical thickness COT $= 0.5$, consisting of smooth solid columns with $r_{\text{eff}} = 80\,\mu\text{m}$.

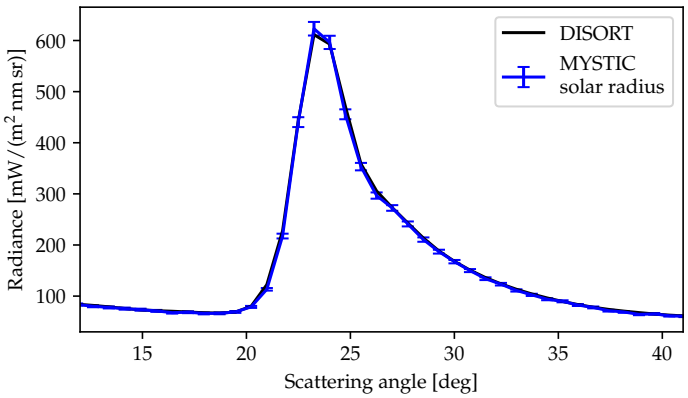

Abbildung 3.3: *Radiative transfer simulations with DISORT and MYSTIC in the almucantar plane, i.e. at a zenith angle of $\theta = \theta_0 = 50°$, for scattering angles between $10° < \phi < 42°$. The cirrus cloud is defined with optical thickness 0.5 containing smooth solid columns with effective radius $r_{\text{eff}} = 80\,\mu\text{m}$ for a wavelength of 550 nm. The MYSTIC simulations were performed for $10e^4$ photons considering the finite opening angle of the sun with 0.5°, whereas the sun is considered a point source for the DISORT simulation.*

3.2 Optical properties

3.2.1 Aerosol optical properties

Throughout this study the aerosol optical properties of the OPAC database are used which are described in Hess et al. (1998). Figure 3.4 shows radiative transfer simulations with DISORT using 4 different aerosol types of the OPAC database: continental clean, average, polluted, and urban represented by the blue, orange, green and red curve respectively. The optical properties consist of different concentrations of insoluble and water-soluble aerosol, soot and sulfate aerosol. Their concentrations vary with height and the differences between the aerosol types is confined to the lowest level between the surface and 1 km height. The continental clean aerosol type does not contain soot in the lowest level. For the continental average and polluted and urban aerosol type the concentrations of the insoluble, water-soluble and soot component increase slightly in this order. If not stated otherwise, the continental average aerosol type is used throughout this study.

3.2.2 Ice crystal optical properties

Two different parameterizations of ice crystal optical properties were used in this study. The first is based on the database of Yang et al. (2013) who use different methods to calculate the single scattering properties for different particle sizes. The second database of optical properties is compiled using the raytracing technique, which will be further explained in Section 3.8, and calculated with the freely available code presented by Macke et al. (1996). The optical properties of these two parameterizations will be described in the following.

Optical properties based on Yang et al. (2013)

Based on the Amsterdam Discrete Dipole Approximation (ADDA) and Improved Geometric Optics Method (IGOM) Yang et al. (2013) provide an extensive database of ice crystal optical properties for 11 different habits assuming random orientation. The database covers a wavelength range between 0.2 µm to 100 µm, maximum diameters from 2 µm to 10 000 µm and three

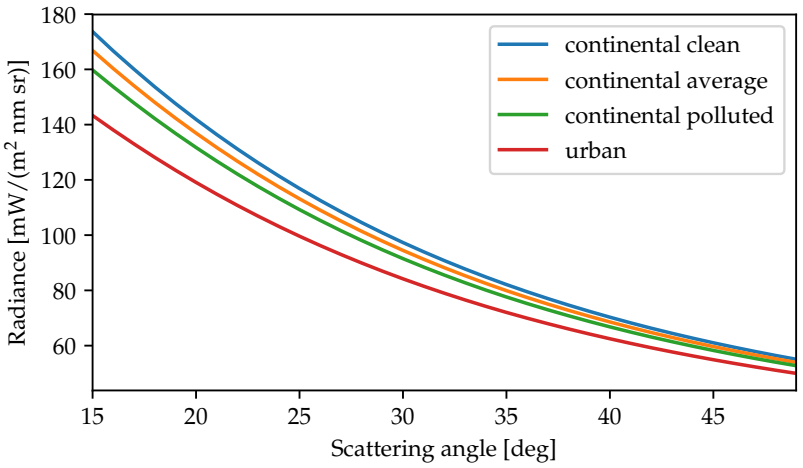

Abbildung 3.4: *Radiative transfer simulations with DISORT using the continental clean (blue), average (orange), polluted (green) and urban (red) aerosol type of the OPAC database. An aerosol optical thickness of 0.1 was chosen at a wavelength of* 500 nm. *The simulation was performed for a SZA of* 45° *in the almucantar plane.*

roughness levels for the ice crystal surface (smooth, moderately and severely roughened). The database contains optical properties for solid and hollow columns, aggregated columns consisting of 8 elements, plates and aggregates of plates with 5 and 10 elements, droxtals and solid and hollow bullet rosettes. Prolate and oblate spheroids are not used in this study. The optical properties for the single ice crystals were averaged over gamma size distributions assuming $N_0 = 1$ and an exponential distribution with $\mu = 1$ in Eq. (2.9) (personal communication with C. Emde). According to Heymsfield and Miloshevich (2003) these values are a reasonable assumption for mid-latitude cirrus clouds. With $N_0 = 1$ and $\mu = 1$ the gamma distribution results in an exponential distribution

$$N(D) = D\ \exp(-\lambda D). \tag{3.4}$$

The slope λ was chosen such that the size distribution results in prescribed effective radii between $r_{\text{eff}} = 5\,\mu\text{m}$ to $90\,\mu\text{m}$. Based on these size distributions the bulk optical properties were calculated according to Eq. (2.12). Henceforth, these optical properties will be referred to as YANG. Figure 3.5 shows scattering phase functions for each of the 9 habits organized in four panels for solid column-, hollow column- and plate-like crystals and droxtals. These ice crystal groups favor the formation of similar halo types: solid columns, aggregates of columns with 8 elements and solid bullet rosettes form both a 22° and 46° halo, whereas the 22° halo is much more pronounced than the 46° halo. A special feature of the solid bullet rosette's phase function is a small peak at a scattering angle of about 10°. Columnar crystals with hollow ends, such as hollow columns and hollow bullet rosettes exhibit a 22° halo but cannot produce a 46° halo since they lack the 90° prism between the crystal base and side faces. For the phase functions of plate-shaped crystals the 46° halo is almost as pronounced as the 22° halo. Surface roughness is parameterized similar to the approach by Cox and Munk (1954) who defined the roughness conditions of the sea surface. The normal distribution of the slope of the ice crystal surface is defined by

$$P(Z_\text{x}, Z_\text{y}) = \frac{1}{\sigma^2\pi} \exp\left(-\frac{Z_\text{x}^2 + Z_\text{y}^2}{\sigma^2}\right), \tag{3.5}$$

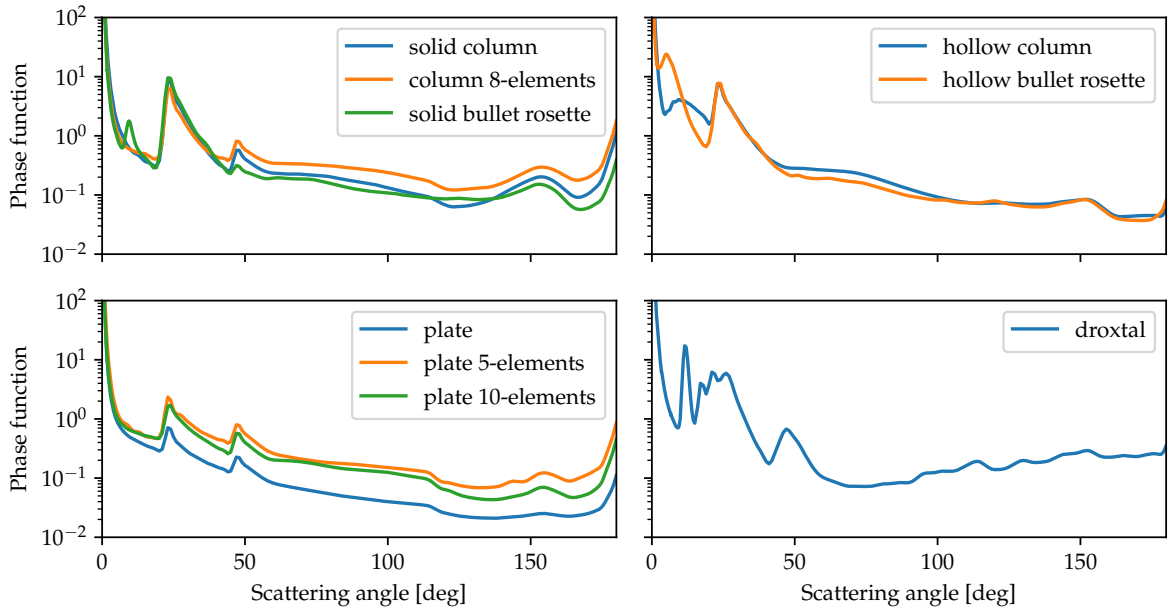

Abbildung 3.5: *Phase functions for 9 different ice crystal habits with smooth surface for a wavelength of* 550 nm *and an effective radius of* $r_{\text{eff}} = 90\,\mu\text{m}$ *from the database of Yang et al. (2013). The phase functions are grouped for column-like crystals with solid and hollow ends, plate-like ice crystals and droxtals. The column- and plate-like crystals comprise single crystals, aggregates, and bullet rosettes.*

with Z_x and Z_y representing the slope variations of the crystal's surface along the two orthogonal directions x and y. The parameter σ is a measure of the degree of surface roughness and takes values of $\sigma = 0$ for a smooth, $\sigma = 0.03$ for a moderately roughened and $\sigma = 0.50$ for a severely roughened surface. The effect of surface roughness is displayed in Fig. 3.6 for solid columns with $r_{\text{eff}} = 90\,\mu\text{m}$ and a wavelength of 550 nm. While for smooth crystals both the 22° and the 46° halo are visible (blue curve), increasing the surface roughness of the ice crystals has the effect of smoothing out the halo features. For moderately rough ice crystals, indicated by the red curve, the 46° halo already disappeared while the brighter 22° halo is still visible. Both halo features are washed out for severely roughened ice crystals, represented by the black curve.

The aspect ratio of the ice crystal habits is defined by the diameter of the hexagonal base $2a$ divided by the length of the side faces L which is by definition the maximum dimension of the ice crystal

$$\text{AR} = 2a/L\,. \tag{3.6}$$

Here, the maximum dimension of the ice crystal $D_{\text{max}} \equiv L$ by definition. Figure 3.7 displays the aspect ratio AR as a function of the maximum dimension L for solid columns and plates, based on the the findings of Arnott et al. (1994), Auer and Veal (1970), Yang et al. (2003), Zhang et al. (2004). For crystal sizes up to 100 µm the solid columns have a constant aspect ratio of AR = 0.7 which is decreasing for larger crystals according to $6.96\sqrt{L}$. Thus, solid columns become more elongated with increasing size. The opposite holds for ice crystal plates. Starting from compact particles for radii of the basal face $a \leq 2\,\mu\text{m}$ with AR = 1, the basal faces of the plates grow faster than their side faces resulting in very thin and wide plates.

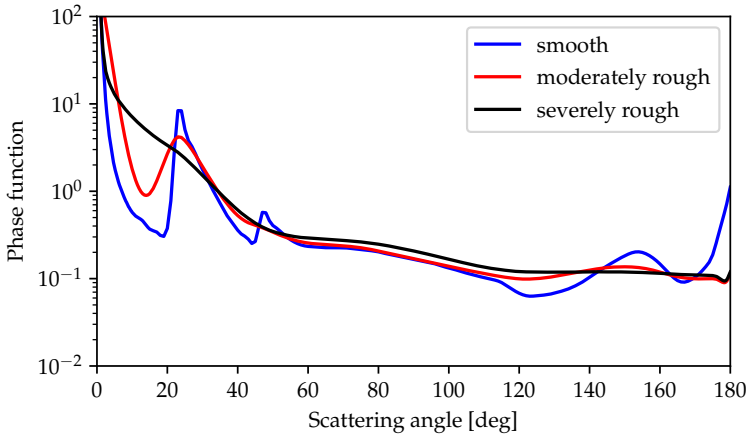

Abbildung 3.6: *Phase functions for solid columns with three different levels of surface roughness: smooth (blue), moderately (red), and severely (black) roughened. Phase functions for an effective radius of* 90 µm *and a wavelength of* 550 nm *are chosen.*

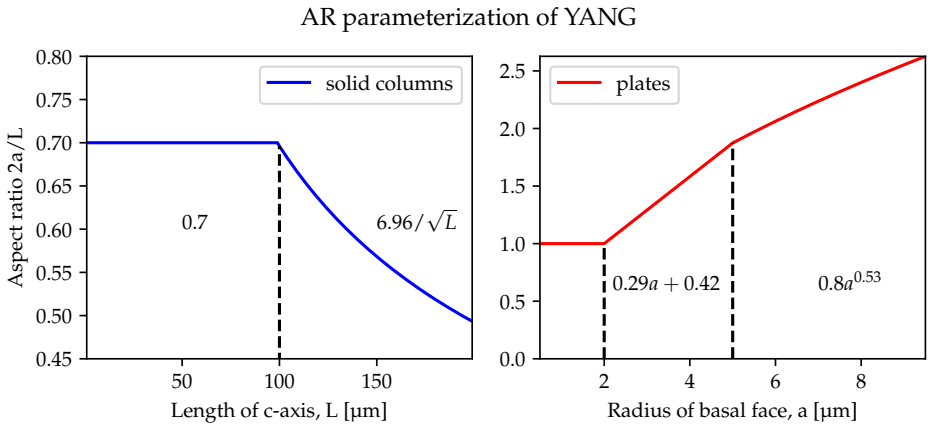

Abbildung 3.7: *Parameterization of the ice crystal aspect ratio of the YANG optical properties for solid columns (blue) on the left and plates (red) on the right.*

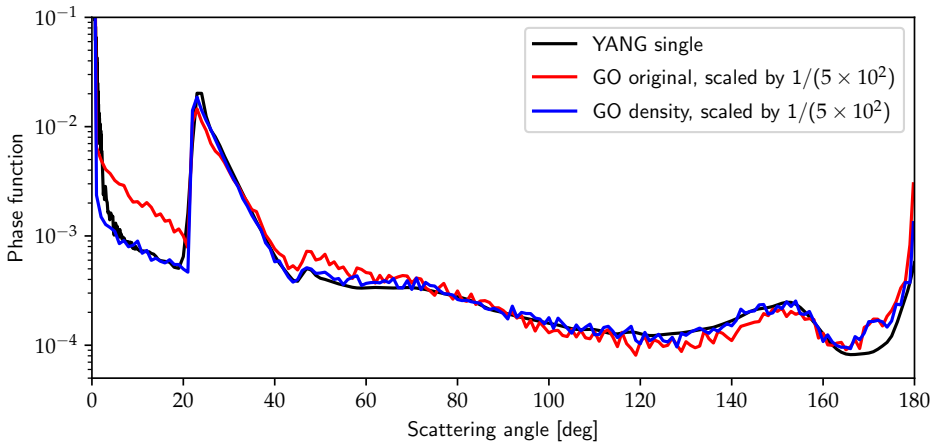

Abbildung 3.8: *Phase functions calculated with Macke et al. (1996) raytracing code using the original version (red) and the version with photon density instead of photon number. In comparison the phase function of the YANG database (black) is shown for a single smooth ice crystal with the same size* $D_{max} = 1 \times 10^4$ µm *and aspect ratio* AR = 0.07.

Optical properties based on raytracing calculations

The second parameterization of ice crystal optical properties used in this study is based on the freely available raytracing code developed by Macke et al. (1996). This parameterization will be referred to as GO in the following. Comparing the results of the original code with the phase function of the YANG database for solid columns of the same size and aspect ratio, shows good agreement between the phase functions for compact solid columns. For long columns (AR $\ll 1$) however, GO shows larger values for scattering angles inside the 22° halo than YANG for an identical ice crystal as displayed in Fig. 3.8 by the black (YANG) and red (GO) line. For a wavelength of 550 nm and assuming a solid ice crystal column with maximum dimension $D_{max} = 1 \times 10^4$ µm and AR = 0.07 (i.e. a long solid column), the offset between the black and blue curve at scattering angles of around 19° is visible. The bug was identified by Konoshonkin et al. (2016): "incident rays are emitted from a rectangular bounded the particle projection. With a change of particle orientation, the area of the rectangular is variable. This area variation must be taken into account." In correspondence with A. Macke the bug was fixed by providing the photon density as a constant instead of the number of photons to trace. For every orientation of the crystal the number of photons is calculated from the photon density multiplied by the area of the bounding rectangle of the projected ice crystal. The blue line in Fig. 3.8 shows the result of the corrected GO code using a constant photon density as input parameter and the resulting phase functions agree well.

The raytracing code described in Macke et al. (1996) models surface roughness by introducing random distortions of the crystal's surface normal following a uniform distribution. This leads to a random distortion of the outgoing ray after a reflection or refraction event. Neshyba et al. (2013) measured single ice crystals in natural conditions during the South Pole Ice Crystal Experiment with the polar nephelometer instrument (Gayet et al., 1997, 1998) and compared the angular scattering intensities with simulations using the GO raytracing code. They found better agreement with the observations when assuming a Weibull distribution instead of the uniform roughness model. Thus, the GO code was slightly modified for this study by replacing the uniform by a Weibull distribution as described in Geogdzhayev and van Diedenhoven (2016).

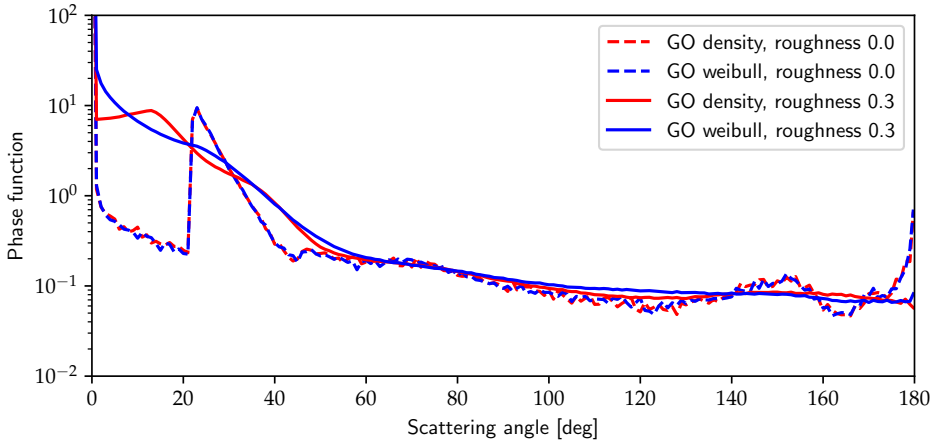

Abbildung 3.9: *Phase functions calculated with Macke et al. (1996) raytracing code using a uniform distribution to parameterize surface roughness (red) and a Weibull distribution with* $\eta = 0.75$ *(blue) shown here for a wavelength of* 550 nm*. A single ice crystal with the size* $D_{max} = 1 \times 10^4$ µm *and aspect ratio AR = 0.07 was chosen with a smooth surface (roughness 0.0, dashed lines) and a roughened surface (roughness 0.3, solid lines).*

For this new roughness model the cosine of the zenith tilt angle μ is calculated by

$$\mu = 1/\left[1 + \sigma^2(-\ln t)^{1/\eta}\right]^{1/2}. \tag{3.7}$$

Here, t is a random number uniformly distributed in the interval [0,1) and the roughness value σ determines the height of the distribution. For the parameter governing the shape of the distribution η a value of 0.75 was chosen which Neshyba et al. (2013) found to best match the observations. Geogdzhayev and van Diedenhoven (2016) also found that the phase functions calculated with $\eta = 0.75$ produce asymmetry factors comparable to the model based on a uniform distribution for different roughness levels. Figure 3.9 illustrates the effect of a Weibull instead of a uniform distribution on the phase function for the same ice crystal geometry as in Fig. 3.8 (solid column) and a wavelength of 550 nm. For smooth crystals (dashed lines) there is no difference between the phase functions since $\mu = 1$ for $\sigma = 0$. For a roughness value of $\sigma = 0.3$ it is clearly visible that the phase function based on a uniform distribution features an artificial plateau at about 19° scattering angle. Performing the calculations with an underlying Weibull distribution with $\eta = 0.75$ yields a smooth phase function without 22° halo.

The raytracing code allows to perform simulations with arbitrary ice crystal aspect ratios, ranging from thin plates (AR $<$ 1) over compact crystals (AR $=$ 1) to long columns (AR $>$ 1) with surface roughness parameters from $\sigma = 0$ (smooth) to $\sigma = 0.7$ (rough). Roughness parameters are limited to values $\sigma \leq 0.7$ since the code does not handle the shadowing and re-entry effects correctly which occur for highly tilted facets (Geogdzhayev and van Diedenhoven, 2016). It is further possible to perform the simulations for arbitrary wavelengths associated with different refractive indices, which have to be provided as input parameter.

In the subsequent section the information content of the ice crystal phase functions presented in the previous sections regarding ice crystal microphysical and optical properties will be analyzed using the 22° and 46° features.

3.3 Information content of the 22° and 46° halo

Halo displays can be analyzed regarding three features: the angular position of the halo, its brightness contrast relative to the background, and the angular width of the halo. The angular position of the halo can help to identify the type of halo display. For example, Eq. (2.41) can be used to calculate the angular position of the brightness peak of the 22° halo and Eq. (2.46) for sundogs. This feature depends on the refractive index and thus the wavelength of the light and provides basic information about ice crystal geometry in terms of the prism angle of the responsible ray path and the ice crystal orientation. For example, 22° halos indicate the presence of ice crystals containing 60° prisms, i.e. hexagonal particles, which are randomly oriented. Sundogs are an indication for hexagonal ice crystals with a 60° prism angle and a vertically oriented *c*-axis. In the following sections the brightness contrast and the angular width of the halo will be investigated regarding their information content about ice crystal properties. Exploiting the fact that halo displays are single scattering phenomena, these features will be analyzed using ice crystal scattering phase functions.

3.3.1 The halo ratio

In previous publications (Gayet et al., 2011, Shcherbakov, 2013, van Diedenhoven, 2014) the halo ratio (HR) was introduced as a measure for the brightness contrast of the 22° and 46° halo in the scattering phase function. Here, the HR is calculated by

$$\mathrm{HR} = \mathcal{P}(\Theta_{\mathrm{max}})/\mathcal{P}(\Theta_{\mathrm{min}})\,, \tag{3.8}$$

with $\Theta_{\mathrm{max}} = 23°$ and $\Theta_{\mathrm{min}} = 21°$ for the 22° halo and $\Theta_{\mathrm{max}} = 47°$ and $\Theta_{\mathrm{min}} = 45°$ for the 46° halo at 500 nm. The effect of the ice crystal aspect ratio on the halo ratio of the 22° and 46° halo is demonstrated by Fig. 3.10 with fixed ice crystal maximum dimension of 320 µm. The HR of the 22° halo increases from thin plates (AR < 1) over compact crystals (AR $= 1$) to long ice crystal columns (AR > 1). This behavior can be explained by the ice crystal geometry changing with the AR. The raypath of the 22° halo passes through two side faces as explained in Section 2.3.2. For an increasing area of the side faces compared to the basal faces these raypaths are favored and the 22° halo becomes more pronounced. The 46° HR shows a maximum for compact crystals with ARs slightly larger than 1 with decreasing values for thin plates and long columns. Recalling the raypath of the 46° halo from Section 2.3.2 explains this relationship. The probability of a path passing through one base and one side face of the crystal is maximum for a compact particle with equal areas of the side and basal face. This behavior can be demonstrated analytically using the geometric cross section of an hexagonal ice crystal as shown in Fig. 3.11. The left panel displays the fraction of the geometric cross section of the crystal's side faces relative to the total geometric cross section, derived from Eq. (2.30):

$$\frac{DL}{\sqrt{3}D^2/4 + DL}\,. \tag{3.9}$$

The right panel shows the geometric cross section of the sum of the crystal side faces and the basal faces:

$$3/4(\sqrt{3}D^2/4 + DL)\,, \tag{3.10}$$

which peaks at an aspect ratio of slightly larger than 1 since the surface area of the basal face is larger than the quadratic side face for the same diameter. The geometric cross section can be

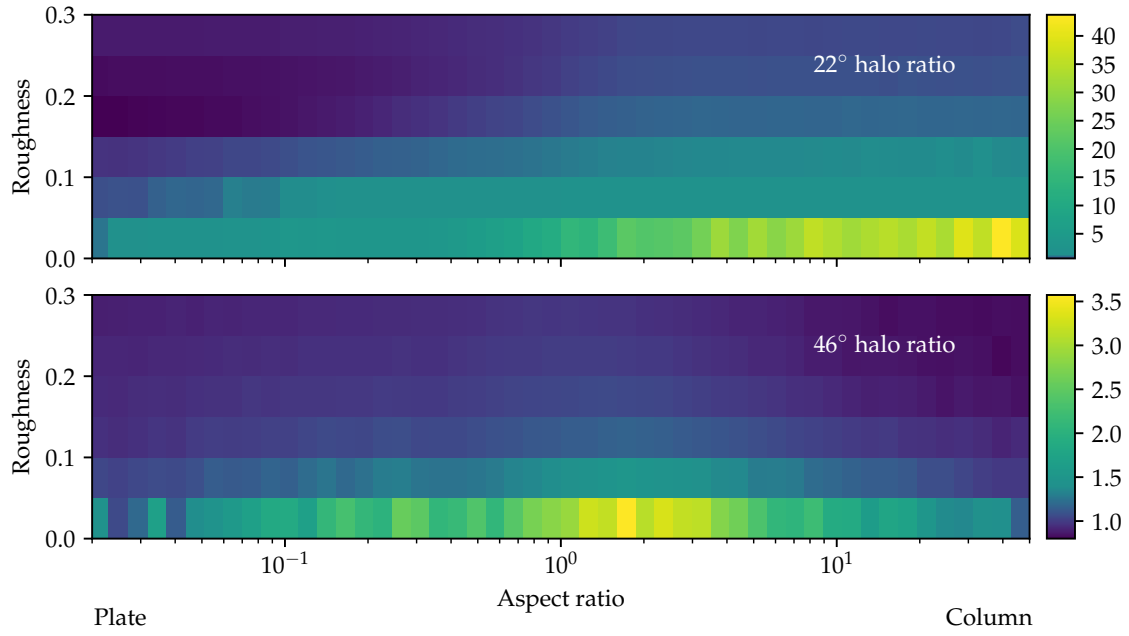

Abbildung 3.10: *22° (top) and 46° halo ratio (bottom) as a function of the ice crystal aspect ratio and surface roughness, calculated with fixed version of the GO raytracing code. The ice crystal aspect ratios range from 0.02 (plate) over 1 (compact particle) to 50 (column) and surface roughness values increase from $\sigma = 0$ (smooth) to $\sigma = 0.3$ (rough). A maximum dimension of 320 µm and a wavelength of 500 nm was chosen.*

used as a rough estimate of the number of ray paths between the faces which depends on the aspect ratio of the crystal. For increasing surface roughness of the ice crystals both the 22° and the 46° HR are decreasing. It can be concluded that the HR contains information about the aspect ratio of the ice crystal. The 22° HR, however, exhibits an ambiguity for smooth plates and rough columns which can result in the same HR. In other words, smooth plates can produce an equally bright 22° halo as rough columns. The presence of a 46° halo indicates smooth compact ice crystals.

The asymmetry factor as a function of the ice crystal aspect ratio is displayed in Fig. 3.12 for and equivalent diameter De of 320 µm. The distribution of the asymmetry factor appears u-shaped with a minimum asymmetry factor of around 0.7 for columns with AR slightly larger than 1. The largest asymmetry factors occur for thin plates with values larger than 0.95.

Figure 3.13 shows the relationship between the HR of the 22° halo and the asymmetry factor. The dashed black line indicates the threshold for the visibility of a 22° halo at HR = 1. It is visible that the HR can help to constrain the asymmetry factor only for smooth ice crystals ($\sigma = 0$, blue curve) for HR $\gg 1$. For small HRs there is no unambiguous relationship between the 22° HR and the asymmetry factor.

3.3.2 The power spillover index and FWHM of the 22°

Flatau and Draine (2014) introduce the so-called "power spillover index" Ψ as a measure of the amount of light scattered into the shadow region inside the 22° halo. The authors suggest that this parameter may be used for constraining the ice crystal size. Figure 3.14a shows the power spillover index for effective radii ranging from 5 to 90 µm at a wavelength of 500 nm using phase functions of the YANG database. Here, the power spillover index is calculated by

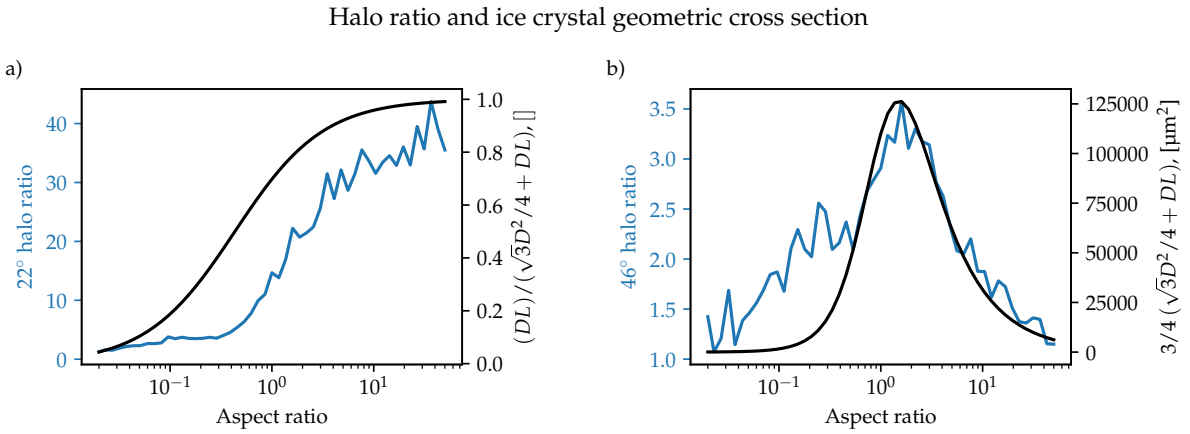

Abbildung 3.11: *(a) 22° halo ratio in comparison with the geometric cross section for the crystal side faces divided by the basal faces (Eq. (3.9)). (b) 46° halo ratio in comparison with the sum of the geometric cross section for the crystal side and basal faces (Eq. (3.10)). The of the 22° and 46° HR is noisy due the scattering phase functions which were calculated for a finite number of rays (cf. Fig. 3.8). This noise increases when calculating the ratio between the halo maximum and minimum.*

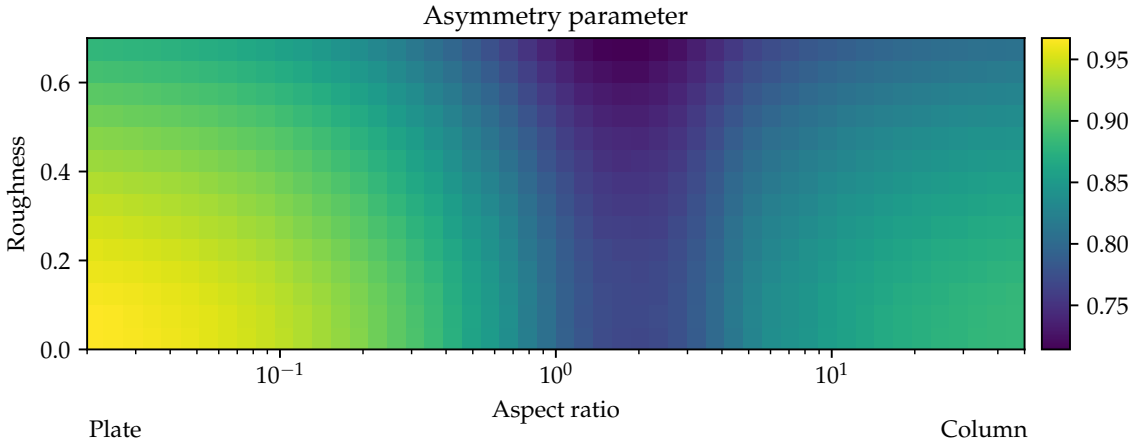

Abbildung 3.12: *Asymmetry factor as a function of ice crystal aspect ratio and surface roughness for the same parameter range as in Fig. 3.10 and a wavelength of* 500 nm.

$$\Psi = \frac{\int_{19^\circ}^{\Theta_{\max}} (\mathcal{P}(\Theta)/d\Theta) d\Theta}{\int_{19^\circ}^{25^\circ} (\mathcal{P}(\Theta)/d\Theta) d\Theta}, \tag{3.11}$$

with $\Theta_{\max}$ the scattering angle of the halo maximum, which is determined using Eq. (2.42) and amounts to 22.1° for 500 nm. Similar to the findings of Flatau and Draine (2014) the spillover index strongly decreases with increasing effective radius. Thus, for larger ice crystal sizes the amount of light scattered into the "shadow region" at scattering angles smaller than the position of the 22° halo decreases. However, the power spillover index is not very useful to derive ice crystal size from halo observations in the atmosphere. As shown in Fig. 3.14b increasing the cirrus optical thickness has a similar effect on the power spillover index as decreasing the effective radius.

Flatau and Draine (2014) also suggest that the full width at half maximum (FWHM) of the 22° halo is related to ice crystal size. However, fitting a Gaussian distribution to the single

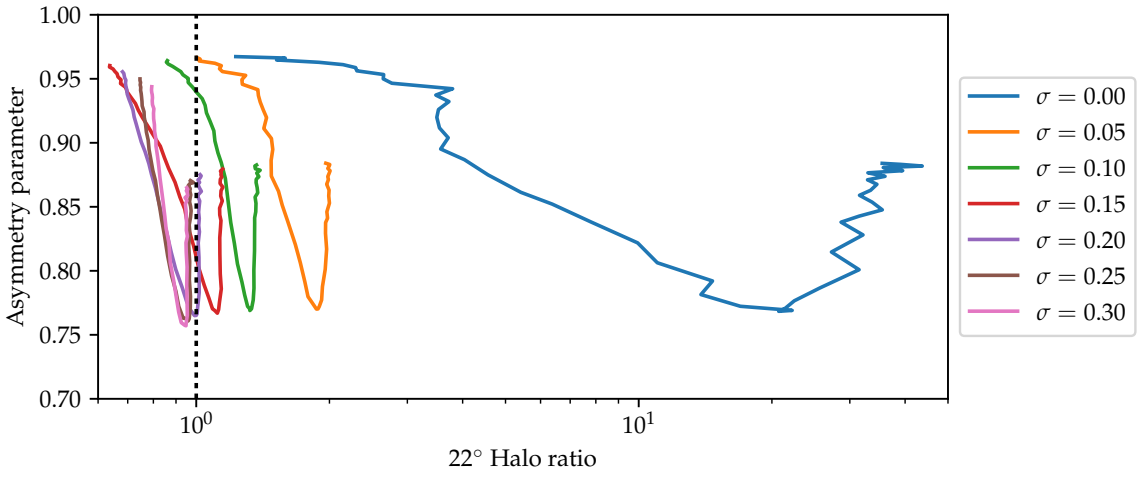

Abbildung 3.13: *Asymmetry factor as a function of the 22° halo ratio for a wavelength of 500 nm and different surface roughness values ranging from $\sigma = 0$ (smooth) to $\sigma = 0.3$ (rough). The black dashed line indicates HR = 1, the threshold for the visibility of the 22° halo. For HR < 1 no 22° halo is visible.*

scattering phase functions was not stable enough to determine a reliable value for the FWHM due to the large forward scattering peak. Thus, for phase functions the power spillover index seems a more suitable measure of the 22° halo width.

This section demonstrates that the shape of the 22° halo peak contains information about ice crystal shape (i.e. aspect ratio) and surface roughness, as well as particle size. The HR, which depends on the height of the halo peak, is sensitive to ice crystal aspect ratio and surface roughness, whereas the spillover index is mainly determined by the size of the ice crystals. While the GO optical properties allow to define different ice crystal aspect ratios and surface roughness levels, they do not account for the physical optics effects responsible for the increase of the spillover index and halo width for small particles. The YANG optical properties, in contrast, are suitable also for small ice crystals, but their aspect ratios are coupled with the ice crystal size and only three different roughness values are available. In Chapter 4 both parameterizations will be applied to measured radiance distributions across the 22° halo and their suitability to represent optical properties of realistic ice clouds will be investigated.

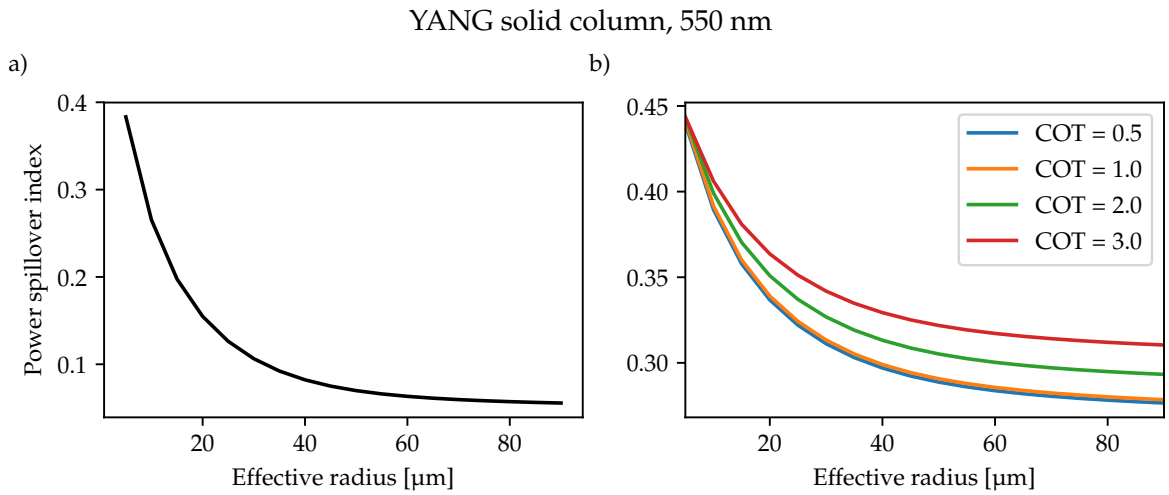

Abbildung 3.14: *Power spillover index of the 22° halo as a function of the effective ice crystal radius for solid columns (YANG) and a wavelength of 550 nm. a) Power spillover index calculated using the phase function and b) radiative transfer simulations with DISORT for different COTs.*

3.4 specMACS – the cloud and sky hyperspectral imaging spectrometer

Measurements of halo displays were performed with the multipurpose hyperspectral cloud and sky imaging spectrometer specMACS which is part of the Munich Aerosol Cloud Scanner (MACS). The characterization and calibration of specMACS is described in detail in Ewald et al. (2015). Designed to measure solar radiation transmitted and reflected by clouds and aerosol, specMACS covers a wavelength range between 400 nm and 2.5 µm with a spectral bandwidth between 2.5 µm and 12.0 nm. The instrument consists of two cameras, the VNIR (visible near-infrared) spectrometer with a wavelength range of 400 nm to 1000 nm, and the SWIR (shortwave infrared) spectrometer with a wavelength range of 1.0 µm to 2.5 µm. A scanning strategy was performed to cover the angular region of the complete 22° halo as well as both sundogs. Figu-

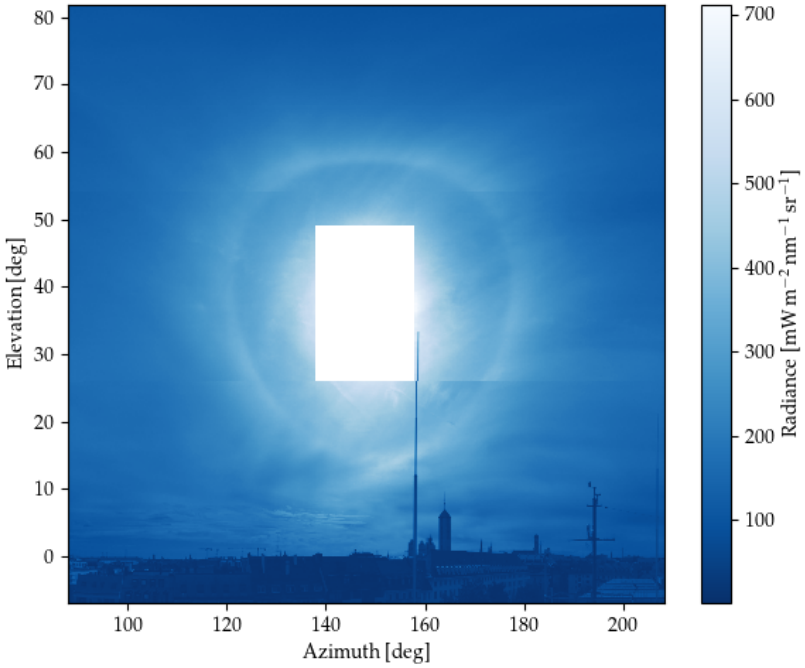

Abbildung 3.15: *specMACS scan of a 22° halo from 22 September 2015 showing the radiance in* $\mathrm{mW\,m^{-2}\,nm^{-1}\,sr^{-1}}$ *for a wavelength of* 550 nm. *Note that the 22° halo deviates from the circular shape due to the representation in an azimuth-elevation grid.*

re 3.15 displays specMACS measurements of a 22° halo, which deviates from the circular shape due to the representation in an azimuth-elevation grid. The scan starts above the sun and is performed horizontally at 3 different elevations across spatial line, i.e. with the camera line sensor oriented vertically. To avoid stray light and saturation of the sensor the shutter of the camera was closed when the scattering angle between sun and camera was smaller than 10°. Scanning across spatial line, stray light can be assumed negligible at this angular distance from the sun the influence of stray light is negligible wich is blocked by the shielding baffles of specMACS (personal communication with F. Ewald and T. Kölling).

The measurement error was calculated as described in Ewald et al. (2015) taking into account the radiometric signal S_0, the dark signal S_d and the temporal noise $\mathcal{N}$

$$S = S_0 + S_\mathrm{d} + \mathcal{N}\,. \tag{3.12}$$

The noise $\mathcal{N}$ consists of the shot noise $\mathcal{N}_{\text{shot}}$, the dark noise $\mathcal{N}_{\text{dc}}$ and the read noise $\mathcal{N}_{\text{read}}$ with a joint standard deviation of

$$\sigma_{\mathcal{N}} = \sqrt{\sigma_{\text{shot}}^2 + \sigma_{\text{dc}}^2 + \sigma_{\text{read}}^2}\,. \tag{3.13}$$

The SWIR noise standard deviation $\sigma_{\mathcal{N}}$ can be represented by a Poisson model and can be parameterized by

$$\sigma_{\mathcal{N},\text{SWIR}} = \sqrt{0.015\,S_0 + 4.77^2}, [\text{DN}] \tag{3.14}$$

between 0 and 12000 DN, whereas for larger values it shows a linear dependence with $k = 0.015$ [DN] until saturation is reached. The VNIR noise standard deviation can be modeled by

$$\sigma_{\mathcal{N},\text{VNIR}} = \sqrt{-4.98e^{-6}\,S_0^2 + 5.22e^{-2}\,S_0 + 24.5}\,, \tag{3.15}$$

which accounts for the non-linearity of the signal noise for large signals (cf. Fig. 13 in Ewald et al. (2015)). The dark signal uncertainty is interpolated between the dark signal before and after the measurement

$$\sigma_{\text{dark}}(t_0) = \sqrt{\sigma_{\text{dark}}^2(t_{0-})\,(1-w)^2 + \sigma_{\text{dark}}^2(t_{0+})\,w^2}\,, \tag{3.16}$$

where $\sigma_{\text{dark}}(t_{0-})$ ($\sigma_{\text{dark}}(t_{0+})$) results from the standard deviation $\sigma_{\text{dark}}(t_{-1})$ ($\sigma_{\text{dark}}(t_{+1})$) of the dark signal average at t_{-1} (t_{+1}) in combination with an upper estimate of the dark signal drift $\Delta\overline{S_{\text{dark}}}$ projected forward from t_{-1} (backward from t_{+1}) to t_0:

$$\begin{aligned}\sigma_{\text{dark}}^2(t_{0,-}) &= \sigma_{\text{dark}}^2(t_{-1}) + 1/2\,(\Delta\overline{S_{\text{dark}}}(t_0 - t_{-1}))^2\,,\\ \sigma_{\text{dark}}^2(t_{0,+}) &= \sigma_{\text{dark}}^2(t_{+1}) + 1/2\,(\Delta\overline{S_{\text{dark}}}(t_{+1} - t_0))^2\,.\end{aligned} \tag{3.17}$$

Since $\Delta\overline{S_{\text{dark}}}$ can not be treated as Gaussian error, the 2σ percentile of σ_{dark} is used to combine the errors. The normalized signal accounting for the photo response nonlinearity can be modeled by

$$s_n = \frac{\sqrt{4\gamma(S - S_{\text{dark}}) + 1} - 1}{2\gamma(t_{set} + t_{ofs})}\,, \tag{3.18}$$

with $\gamma_{\text{VNIR}} = (-2.3 \pm 0.3) \times 10^{-5}$ DN^{-1} and $t_{\text{ofs,VNIR}} = (-0.001 \pm 0.010)$ ms and $\gamma_{\text{SWIR}} = 0$ DN^{-1} and $t_{\text{ofs,SWIR}} = (0.055 \pm 0.001)$ ms. The remaining uncertainty of the sensor's nonlinearity is estimated by

$$\sigma_{\text{nonlin}} = 1/2(s_{\text{n,max}} - s_{\text{n,min}})/s_{\text{n,mean}} \cdot S_0\,. \tag{3.19}$$

In addition, the signal measured by the optical components can be polarization sensitive. This is accounted for by

$$\sigma_{\text{pol}} = 1/2 p_{\text{tot}}(1 + p_{\text{tot}})/(1 - p_{\text{tot}})\,, \tag{3.20}$$

where $p_{\text{tot}} = P \cdot p_{\text{max}}$ with the sensor polarization sensitivity P and the maximum radiance polarization p_{max}. The sensor polarization is composed of a polarization insensitive part O and a polarization sensitive part with partial response $2A$. Then, the polarization sensitivity P is

$$P = \frac{A}{A + O} \cdot 100\%\,. \tag{3.21}$$

For a linear sensor the normalized signal s_{n} scales linearly with the radiance L

$$s_{\text{n}} = R\,L\,, \tag{3.22}$$

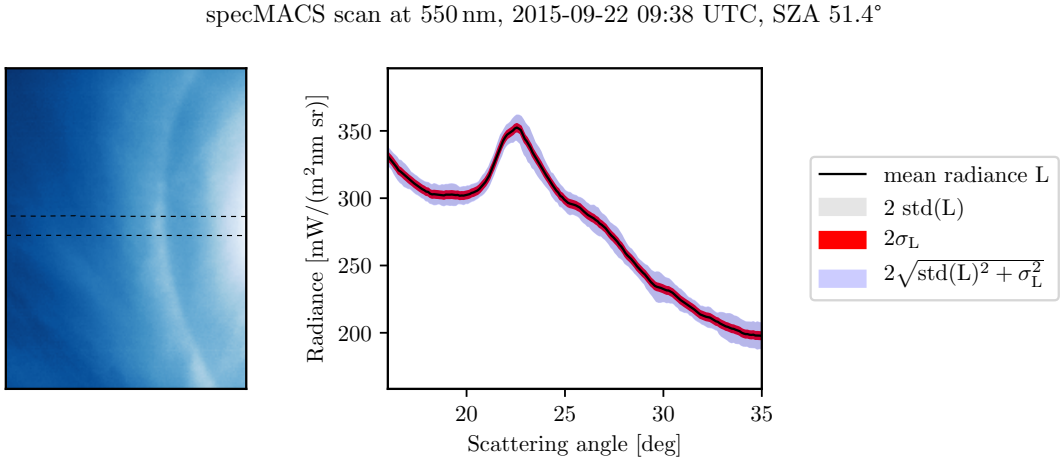

Abbildung 3.16: *a) specMACS scan across the left side of the 22° halo on 22 September 2015, 9:38 UTC displayed at a wavelength of* 550 nm*. The black dashed lines indicate the region centered around the almucantar plane (at the elevation of the sun) with an angular width of* 2°*. b) Radiance distribution across the* 22° *halo as a function of the scattering angle which is obtained by averaging the radiance over the* 2° *bins with a resolution of* 0.1°*. The shaded region around the mean radiance in panel b) represents the the measurement error (red)* σ_L *and combined with the standard deviation of the radiance within the angular region marked in panel a). Both values are provided within a* 2σ *confidence interval.*

with the radiometric response R. For an unknown degree of polarization $p > 0$ the error of the measured normalized signal s_n relative to the normalized polarization insensitive signal s_n^P is defined by $\Delta s_n^P = |s_n - s_n^P|$.

Following Ewald et al. (2015), the total error of the photoelectric signal S_0 is calculated by

$$2\sigma_{S_0} = 2\sqrt{\sigma_{dark}^2 + \sigma_{\mathcal{N}}^2}\,. \tag{3.23}$$

Then, the error of the normalized signal s_n is composed of the relative errors of the photoelectric signal σ_{S_0}, the non-linearity error σ_{nonlin} and the polarization error Δs_n^P

$$\frac{2\sigma_{s_n}}{s_n} = \sqrt{\left(\frac{2\sigma_{S_0}}{S_0}\right)^2 + \left(\frac{2\sigma_{nonlin}}{s_n}\right)^2 + \left(\frac{\Delta s_n^P}{s_n^P}\right)^2}\,, \tag{3.24}$$

where s_n^P is the polarization dependent normalized photoelectric signal. Finally, the total error of the measured radiance L is calculated by

$$\frac{2\sigma_L}{L} = \sqrt{\left(\frac{2\sigma_{s_n}}{s_n}\right)^2 + \left(\frac{2\sigma_R}{R}\right)^2}\,. \tag{3.25}$$

To extract radiance distributions across the 22° halo, the specMACS measurements were binned over a certain interval of the elevation angle and averaged. Figure 3.16 shows an example of a specMACS scan of a 22° halo. The left part of the picture highlights the angular region which is used to calculate the angular dependence of the radiance across the halo. In this case a binwidth of 2° was chosen in the elevation angle, centered around the solar elevation, i.e. in

the almucantar plane. To obtain the radiance distribution in the right panel of Figure 3.16, the data was interpolated to a scattering angle grid with 0.1° resolution ranging from 10° to 35° and averaged over the angular bins. The averaged radiance distribution across the 22° halo L is represented by the black line in Fig. 3.16b. The region aournd the mean radiance shaded in red displays the measurement error $2\sigma_{\mathrm{L}}$. The total error of the measurement uncertainty and the variability of the radiance within the masked angular region is represented by the blue shaded area in Fig. 3.16b and was obtained by Gaussian error propagation assuming the measurements of the individual pixels are independent.

3.5 HaloCam – an automated sun-tracking halo observation system

3.5.1 System description

To collect halo observations automatically, the sun-tracking camera system HaloCam was developed at the Meteorological Institute Munich (MIM) of the Ludwig-Maximilians University (LMU), and installed on the rooftop platform. HaloCam consists of two weather-proof, wide-

Abbildung 3.17: *HaloCam-setup with different wide-angle cameras: HaloCam$_{JPG}$ represents the Mobotix S14D camera model which consists of one camera body and two lenses with* 4 mm *focal length. One lens is centered relative to the sun, the other lens is pointing to the zenith and is not used for this study. This camera records pictures only in the compressed JPEG format. HaloCam$_{RAW}$ represents the Allied Vision Manta G-235 C camera model with a Kowa wide-angle lens with* 6 mm *focal length, which provides the uncompressed "raw" signal measured at the sensor.*

angle cameras which are mounted on a sun-tracking system as shown in Fig. 3.17. Detailed specifications are provided in Table 3.1. HaloCam$_{JPG}$ (Mobotix S14D) is a light-weight modular camera with an RGB CMOS sensor of 1/2" size and two lenses with the same specifications: each lens has a focal length of 4 mm and provides a horizontal and vertical field of view (FOV) of 90° and 67°, respectively. As visible in Fig. 3.17, one lens is pointing to the sun, the other one to the zenith. In this study only the sun-centered lens is used and is, together with the camera body, referred to as HaloCam$_{JPG}$. This very robust and easy-to-operate camera records images in the compressed JPEG format, hence the notation HaloCam$_{JPG}$. The large temperature range from −30 °C to 60 °C allows HaloCam$_{JPG}$ to be operated all year without external heating or cooling. However, due to on-chip post-processing and JPEG compression the images cannot be used for a quantitative analysis.

Therefore, HaloCam$_{RAW}$ was additionally installed which provides the "raw", i.e. un-processed and un-compressed, signal from the sensor. HaloCam$_{RAW}$ consists of an Allied Vision Manta G-235C camera and a Kowa LM6HC wide-angle lens with 6 mm focal length. The camera features a Sony IMX174 CMOS sensor with 1936×1216 squared pixels, which uses a Bayer color filter array (CFA, Bayer (1975)) for spectral measurements (cf. Table 3.1). The color information is captured by the sensor via so-called primary color (RGB) filters, which are located over the individual pixels and arranged in a Bayer mosaic pattern. For HaloCam$_{RAW}$ the Bayer pattern starts with a red pixel (Allied Vision Technologies GmbH, 2015) and a Bayer demosaicing al-

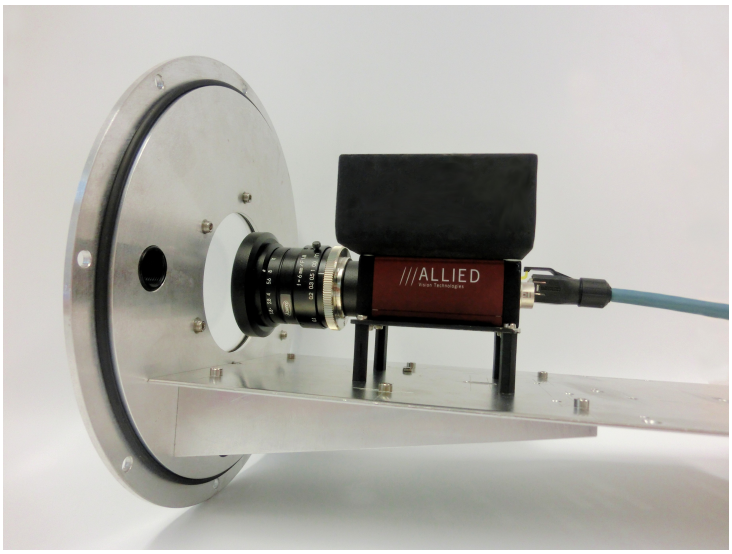

Abbildung 3.18: *Interior of HaloCam$_{\mathrm{RAW}}$'s weather-proof casing. HaloCam$_{\mathrm{RAW}}$ consists of an Allied Vision Manta G-235C camera with a Kowa lens of* 6 mm *focal length. The camera is fixed on a drawer, which is attached to the circular front lid of the cylindric weather-proof casing shown in Fig. 3.17. A sheet metal is attached on the top of the camera body with thermal compound to support the cooling of the camera. For the window of the camera casing, a Heliopan UV-filter was used with anti-reflection coating. The PoE cable is guided inside the camera casing via a water-proof connecting plug through the circular lid just below the window (cf. Fig. 3.17).*

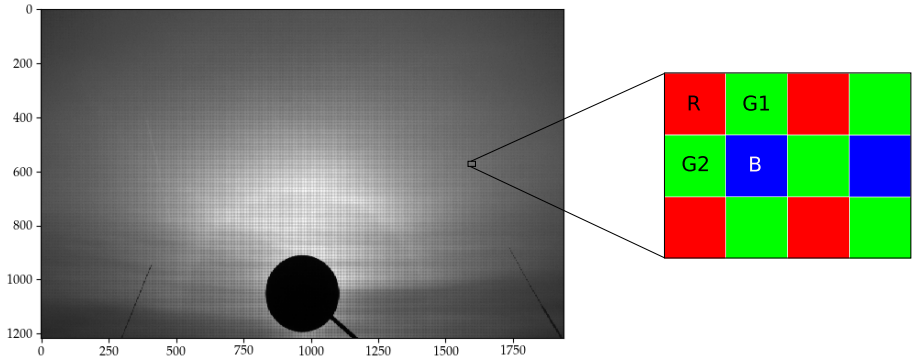

Abbildung 3.19: *HaloCam$_{\mathrm{RAW}}$ raw-image as detected by the sensor. The image exhibits the superimposed checkerboard pattern of the Bayer color filter array (CFA, Bayer (1975)) which is shown schematically to the right of the raw-image for the red (R), the 2 green (G1, G2), and the blue (B) channels.*

gorithm (Allied Vision proprietary) is used to determine a red, green and blue value for each pixel. For this study, HaloCam$_{\mathrm{RAW}}$ is used in the raw-mode, i.e. the signal measured by the camera sensor is directly used without (color) processing. This provides monochrome images with superimposed Bayer checkerboard pattern as shown in Fig. 3.19. A schematic illustration of the Bayer CFA layout with the red (R), blue (B) and two green (G1, G2) channels is displayed as magnified detail of Fig. 3.19.

Since HaloCam$_{\mathrm{RAW}}$ itself is not protected, a weather-proof aluminum casing was built at the Meteorological Institute at LMU (cf. Fig. 3.17). The casing has a cylindric shape and the camera is fixed on a drawer which is attached to the circular front lid as shown in Fig. 3.18. An anti-reflection coated UV-filter from the manufacturer Heliopan is used as window for the

casing. The PoE (Power over Ethernet) cable is guided inside the casing through the circular lid just below the window via a water-proof connecting plug visible in Fig. 3.17. Both HaloCam cameras are operated in an automatic exposure mode. For $\text{HaloCam}_{\text{JPG}}$ the image region used to determine the optimum exposure time is confined to the region where the 22° halo occurs, which ensures that the pixels around the 22° halo are not saturated. $\text{HaloCam}_{\text{RAW}}$ measures the histogram of the current image to adjust the exposure time of the next image so that bright areas are not saturated. In addition, an upper limit for the exposure time of 50 ms is selected since the automatic exposure for $\text{HaloCam}_{\text{RAW}}$ sometimes escalates to very large values resulting in overexposed images. In the following, the term HaloCam refers to the camera system including the suntracking mount and both cameras, whereas the terms $\text{HaloCam}_{\text{JPG}}$ and $\text{HaloCam}_{\text{RAW}}$ will be used for the specific camera.

Using a sun-tracking mount is very suitable for the observation of halo displays and later image processing since it allows to align the center of the camera with the sun. This implies that also the recorded halo displays are centered on the camera pictures. With this setup a small fixed shade is sufficient to protect the camera lens from direct solar radiation and to avoid overexposed pixels and stray light (cf. Fig. 3.17). The mount features two stepping motors with gear boxes for adjusting the azimuth and elevation angles of the camera position as described in Seefeldner et al. (2004) with an incremental positioning of 2.16 arcmin per step. The positioning of the mount is performed by passively tracking the sun: an algorithm calculates the current position of the sun which is converted to incremental motor steps and moves the two motors accordingly. The pointing accuracy of the mount can be roughly estimated to about $\pm 0.5°$ (2σ confidence interval) which will be explained in more detail in Section 3.6.1. The camera FOV and the sensor resolution were chosen to optimize the trade-off between a large coverage of the sky with high spatial resolution and low image distortion. $\text{HaloCam}_{\text{JPG}}$ allows to observe the 22° halo, sundogs, upper/lower tangent arc or circumscribed halo, which are the most frequent halo displays according to Sassen et al. (2003b) and the results of the AKM.

The HaloCam observations aim at gaining a better understanding of the relationship between halo displays and typical ice crystal properties in cirrus clouds. Hence, the observations can be limited to the most frequent halo displays without loosing relevant information about ice crystal shape and orientation while achieving a high spatial and temporal resolution of the scene. Since the presence/absence of the rare 46° halo might add information, as discussed in Section 3.3, $\text{HaloCam}_{\text{RAW}}$ was tilted upwards by 26° compared to $\text{HaloCam}_{\text{JPG}}$ to observe the upper part of both the 22° and 46° halo. Every 10 s HaloCam's position relative to the sun is updated and a picture is recorded. The HaloCam system was installed in September 2013 on the rooftop platform of MIM (LMU) in Munich, first with $\text{HaloCam}_{\text{JPG}}$ only and since September 2015 extended by $\text{HaloCam}_{\text{RAW}}$. On the rooftop platform operational measurements are performed in addition by a MIRA-35 cloud radar (Görsdorf et al., 2015), a CHM15kx ceilometer (Wiegner et al., 2014) and a sunphotometer, which is part of the part of the AERONET (Aerosol Robotic Network) network (Holben et al., 1998), as well as with the institute's own sun-photometer SSARA (Sun–Sky Automatic Radiometer, Toledano et al. (2009, 2011)). HaloCam observations ideally complement these measurements to retrieve more detailed information about ice crystal properties.

Tabelle 3.1: *HaloCam specifications*

Camera system	**HaloCam**$_{\mathrm{JPG}}$	**HaloCam**$_{\mathrm{RAW}}$
Lens	Mobotix L22	Kowa LM6HC
Focal length	4 mm (22 mm)	6 mm
Aperture	F2.0	F1.8 - F16.0 (manual)
Horizontal field of view[2]	93°	87°
Vertical field of view[3]	70°	65°
Camera	Mobotix S14D flexmount	Allied Vision, Manta G-235C
Interface	IEEE 802.3af (PoE)	IEEE 802.3af (PoE)
Protection class	IP65	None
Operating (ambient) temperature	−30 °C to 60 °C	5 °C to 45 °C
Sensor	1/2“ CMOS, RGB	1/1.2“ CMOS, RGB Sony IMX174LQJ
Maximum bit depth	8 bit	12 bit
Sensor resolution	3 MPixel	2.4 MPixel
Sensor pixels	2048×1536	1936×1216
Shutter type	not specified	global shutter
Image formats	JPEG (8 bit)	Bayer (8 or 12 bit) Mono (8 or 12 bit) RGB (8 bit), YUV
Measures $w \times h \times d$	115 × 130 × 33 mm	86.4 × 44 × 29 mm
Weight (camera body + lens)	444 g + 2×159 g	200 g + 215 g

For analyzing the halo displays on the HaloCam images it is necessary to map the pixel location on the sensor to the spherical world coordinates. This can be achieved by a geometric calibration of the camera. Furthermore, if the measured pixel intensities should be compared with radiative transfer simulations, a radiometric calibration is required to convert the measured intensities to radiance values. The geometric calibration is performed for both cameras of the HaloCam system, whereas the radiometric calibration is applied only for HaloCam$_{\mathrm{RAW}}$.

3.5.2 Geometric calibration

Halo displays are single scattering phenomena and thus are directly linked to the optical properties of the ice crystals producing them. The ice crystal phase function predicts the scattering angle Θ of the 22° halo relative to the sun. Thus, the analysis of the HaloCam images can be simplified significantly by mapping the image pixels to scattering angles. This means the camera has to be calibrated in order to determine the parameters for mapping the camera pixels to the real world spherical coordinate system. For this mapping the intrinsic camera parameters have

[2]The horizontal and vertical FOV for both camera systems are the result of the geometric calibration in Section 3.5.2.

[3]See footnote 2.

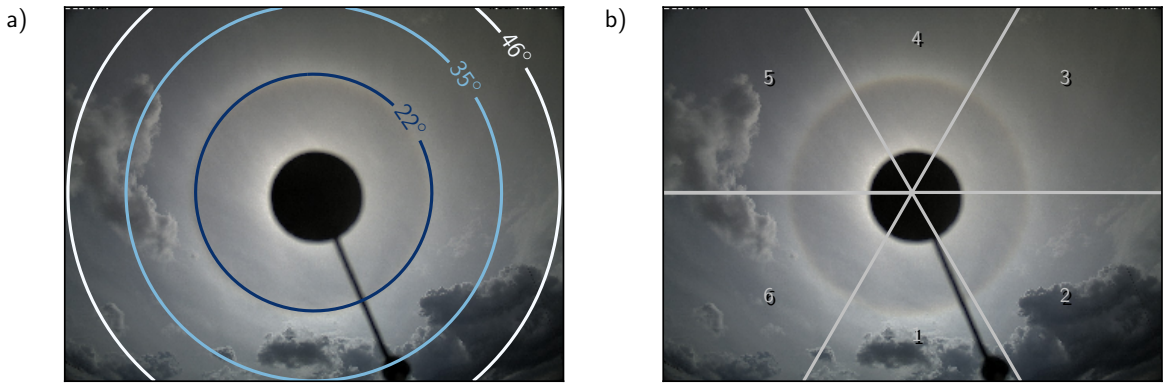

Abbildung 3.20: *a) HaloCam$_{\mathrm{JPG}}$ image from 2014-05-12, 13:52 UTC with corresponding scattering angle (ϑ) grid and representative contour lines at 22°, 35° and 46°, b) shows the relative azimuth (φ) grid with numbered labels for the 6 image segments.*

to be determined, which are the focal lengths f_x, f_y and image center coordinates c_x, c_y, as well as the distortion coefficients of the camera lens.
Different methods exist for the geometric calibration. Here, the method described by Zhang (2000) was used, which is based on Heikkilä and Silvén (1997), to estimate the intrinsic camera parameters as well as the radial and tangential distortion parameters of the lens. This method requires several pictures of a planar pattern, for example a chessboard pattern with known dimensions, taken with different orientations. The calibration method using a chessboard pattern was implemented in OpenCV by Itseez (2015) and is described in detail by Bradski and Kaehler (2008). Using the distortion coefficients and intrinsic parameters, the camera pixels can be undistorted and mapped to the world coordinate system. Thereby a zenith (ϑ) and azimuth angle (φ) can be assigned to each pixel relative to the center of the sun. In this case the relative zenith angle ϑ corresponds to the scattering angle Θ.

An overlay of the scattering angle grid onto a HaloCam$_{\mathrm{JPG}}$ picture is shown in Fig. 3.20a with representative contour lines at $\vartheta = 22°$, 35° and 46°. From the scattering angle grid the horizontal and vertical FOV can be calculated to ∼93° and ∼70°, respectively. HaloCam$_{\mathrm{JPG}}$ images are recorded with a resolution of 1280×960 quadratic pixels which results in an angular resolution of ∼0.07° for both the horizontal and the vertical direction. Figure 3.20b shows the relative azimuth angle grid which is chosen such that the image is separated into 6 segments.

For HaloCam$_{\mathrm{RAW}}$ the geometric calibration was performed with the same method but for the raw-image as shown in Fig. 3.19. The relative zenith (ϑ) and azimuth (φ) for the HaloCam$_{\mathrm{RAW}}$ R-channel are displayed in Figure 3.21. As shown in Fig. 3.21a both the 22° and 46° halo are close to the image center when the elevation of the camera is tilted upwards by 26° compared to HaloCam$_{\mathrm{JPG}}$ where the sun is at the center of the image. This setup allows to observe only the upper part of the 22° and 46° halo, which is more suitable for a quantitative analysis anyway. The lower part of the halo is often obstructed by the horizon (during sunrise and sunset) and usually less pronounced than the upper part due to increased multiple scattering. The horizontal and vertical FOV for HaloCam$_{\mathrm{RAW}}$ can be estimated from the calculated scattering angle grid to ∼87° and ∼65°, respectively. With a resolution of 608×968 quadratic pixels the angular resolution of each of the 4 color channels amounts to about 0.1°. As for HaloCam$_{\mathrm{JPG}}$, the HaloCam$_{\mathrm{RAW}}$ image is separated into segments using the relative azimuth angle φ. Figure 3.21b indicates the 5 azimuth segments defined to obtain a detailed sampling of the 22° halo. For

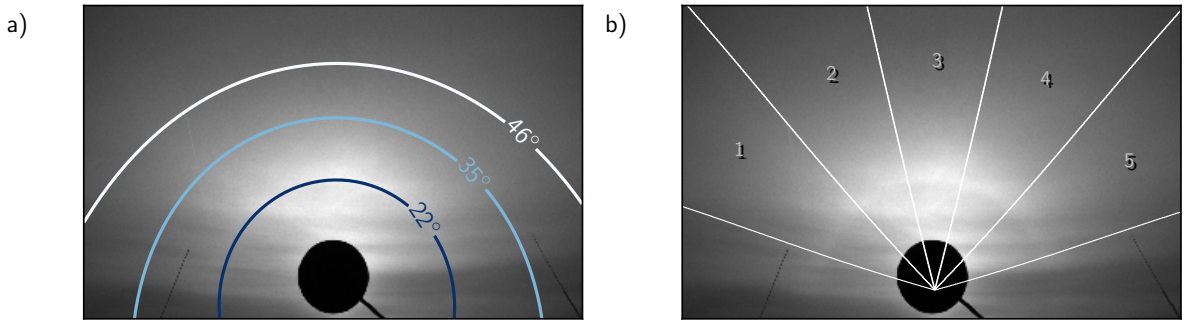

Abbildung 3.21: *a) HaloCam$_{\mathrm{RAW}}$ image (R-channel) from 2016-02-02, 9:42 UTC with corresponding scattering angle (ϑ) grid and representative contour lines at 22°, 35° and 46°, b) displays the relative azimuth (φ) grid for 5 image segments.*

further analysis and feature extraction each of these segments is averaged in direction of the relative azimuth φ.

3.5.3 Radiometric characterization

Each sensor pixel is a semiconductive device which converts light into electrical charge and can be treated as an independent radiometric sensor. The charge collected on a pixel is converted to a voltage and then to a digital value by the A/D converters, which introduces noise at each step. The signal measured by the sensor can be expressed as

$$S = S_0 + S_\mathrm{d} + \mathcal{N} \tag{3.26}$$

with S_d the dark signal, S_0 the radiometric signal, and the measurement noise $\mathcal{N}$, as presented in Ewald et al. (2015). The measurement noise $\mathcal{N}$ is the sum of the radiometric signal noise $\mathcal{N}_0$ and the dark signal noise $\mathcal{N}_\mathrm{d}$.
In the following sections the components of the measured signal S will be characterized and their sensitivity on the camera settings and ambient conditions will be investigated. The dark signal measurements were performed in the optics laboratory of the Meteorological Institute at LMU on 16 July 2015. The measurements at the Large Integrating Sphere (LIS) and the spectral response of the sensor were performed at the Calibration Home Base (CHB) (Gege et al., 2009) of the Remote Sensing Technology Institute at the German Aerospace Center in Oberpfaffenhofen on 28 June 2016 in close cooperation with A. Baumgartner. In the subsequent sections, temporally averaged values are indicated by angle brackets while spatial averages are denoted by an overbar. If not stated differently all variables are defined pixel-wise.

Dark response

The dark signal $\mathrm{S_d}$ can be measured when no light is entering the camera, i.e. the shutter is closed. This implies $S_0 = 0$ and Eq. (3.26) becomes

$$S = S_\mathrm{d} + \mathcal{N}_\mathrm{d}\,. \tag{3.27}$$

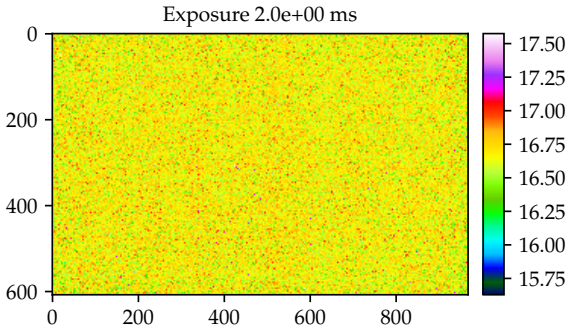

Abbildung 3.22: *HaloCam$_{\mathrm{RAW}}$ dark signal of the R-channel, averaged over 100 images. An exposure time of $t_{\mathrm{expos}} = 2.0\,\mathrm{ms}$ was chosen and a temperature of 45 °C was measured inside the camera.*

For an averaged dark image $\langle S \rangle$ the remaining noise becomes very small $\langle \mathcal{N}_{\mathrm{d}} \rangle \to 0$ and the dark signal S_{d} can directly be measured. The dark signal consists of the dark current s_{dc}, which is caused by thermally generated electrons and holes within the semiconductor material of the sensor, and the read-out offset of the A/D converters S_{read}

$$S_{\mathrm{d}}(T) = s_{\mathrm{dc}}(T)\, t_{\mathrm{expos}} + S_{\mathrm{read}}\,. \tag{3.28}$$

The dark current s_{dc} depends on the temperature T and the exposure time t_{expos}. Thermal electrons are generated randomly over time with an increasing rate as the temperature rises. Furthermore, the dark signal has a spatial component which is called fixed pattern noise (FPN). Since HaloCam$_{\mathrm{RAW}}$ has no external shutter, the dark signal during operation has to be estimated from the laboratory characterization. The following experiments were performed in a dark room and the camera lens was covered with an opaque cloth.

Figure 3.22 displays the dark signal $\langle S_{\mathrm{d}} \rangle$ averaged over 100 images for an exposure time of $t_{\mathrm{expos}} = 2.0\,\mathrm{ms}$ and a device temperature of 45 °C for the R-channel. The temporally and spatially averaged dark signal amounts to about $\overline{\langle S_{\mathrm{d}} \rangle} = (16.7 \pm 0.2)\,\mathrm{DN}$. For this number of averaged images, the dark signal in Fig. 3.22 does not show a significant spatial pattern. The same is true for the G1-, G2-, and B-channel. Thus, it can be assumed that the FPN is smaller than the dark signal noise of 0.02 DN or 0.1 % and is considered negligible for the following analysis and later image processing. Figure 3.23 shows how the dark signal changes with exposure time for a constant temperature inside the camera of about 45 °C. In operational mode and under daylight conditions typical exposure times of 1 to 3 ms are used. For exposure times up to 50 ms the dark signal changes less than 0.02 DN (0.1 %). As observed by Urquhart et al. (2015) and Ewald et al. (2015) (VNIR camera of specMACS), the dark signal appears to be independent of the exposure time. For larger exposure times, which are shaded gray in Fig. 3.23, a significant increase of the dark signal and especially the dark signal noise occurs. This behavior is most likely a combination of the increasing dark current signal due to a longer exposure time but also an increase of the read noise signal S_{read} caused by the A/D converters. To investigate how the dark signal of the camera depends on temperature, measurements were performed with the camera set-up inside a climate chamber (Weiss[4], SB11/160/40) in a dark room and with the

[4]Weiss Klimatechnik GmbH, Greizer Straße 41-49, D-35447 Reiskirchen-Lindenstruth

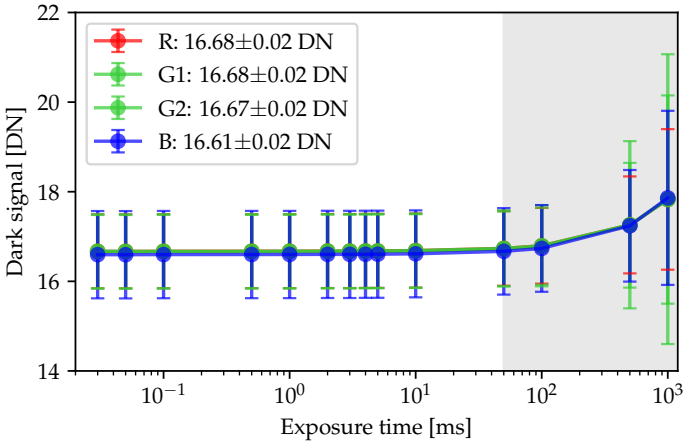

Abbildung 3.23: *HaloCam$_{\mathrm{RAW}}$ dark signal and dark signal noise of all 4 channels (R, G1, G2, B) for different exposure times ranging from* 0.03 ms *to* 1000 ms*. The camera's internal temperature was constant at* 45 °C*. The dark signal average and the standard deviation were evaluated over 100 images for each exposure time.*

camera lens covered as described above. The temperature inside the climate chamber can be adjusted between −40 °C to 180 °C with increments of 0.1 °C. Thus, the estimated accuracy is about 0.05 K. The climate chamber temperature was controlled using the software described in Grob (2015) which is part of the runMACS software suite. For the dark measurements with HaloCam$_{\mathrm{RAW}}$ the temperature was varied between 10 °C and 50 °C in steps of 5 °C. Within this temperature range the averaged dark signal varied less than 0.5 DN. To obtain an estimate for the temporal drift of the dark signal, the standard deviation was calculated using all recorded dark images for the different camera temperatures and exposure times and results to about 2.2 DN for the 4 channels. For the dark signal correction of the HaloCam$_{\mathrm{RAW}}$ data, for each of the 4 channels the respective mean value from Fig. 3.23 is used: 16.68 DN, 16.68 DN, 16.67 DN, and 16.61 DN for the R-, G1-, G2-, and B-channel, respectively.

Sensor photoresponse non-uniformity correction

The radiometric signal S_0 differs from pixel to pixel due to different gains on each photodetector in the focal plane array, called photoresponse non-uniformity (PRNU). Furthermore, the wide-angle lens of HaloCam$_{\mathrm{RAW}}$ causes a decreasing brightness on the sensor for raypaths farther away from the optical axis of the lens which is due to optical vignetting and natural illumination falloff. Optical vignetting occurs when the ray bundle, which forms the image, is truncated by two or more physical structures in different planes (Bass, 2010). Typically, one is the nominal aperture and another is the edge of a lens or a multiple element lens. Natural illumination falloff, or natural vignetting, describes the effect that for off-axis image points the illumination is usually lower than for the image point on the optical axis, which can be approximated by the "cosine-to-the-fourth" relationship (Bass, 2010). The image irradiance of a distant, planar, uniform Lambertian object varies approximately with the object space field angle ϑ according to

$$E = E_0 \cos^4 \vartheta \,, \tag{3.29}$$

where E_0 is the axial irradiance. Three effects contribute to this approximation:

1. The angular distribution of a Lambertian emitter varies with $\cos \vartheta$.

2. The relationship between the distance from the field point and the entrance pupil is $1/d^2 \propto \cos^2 \vartheta$.

3. If the entrance pupil can be approximately by a circle, its projected solid angle varies approximately with $\cos \vartheta$.

However, this relationship should only be used as a guideline. As stated by Bass (2010) wide-angle lenses are usually designed to compensate for effects (1) and (2) by increasing the angular size of the pupil with the field angle. Vignetting and the cosine-to-the-fourth effect can be diminished by reducing the entrance pupil, i.e. the aperture by increasing the f-number. According to Bass (2010) the f-number is defined by

$$f\text{-number} = \frac{\text{focal length}}{\text{entrance pupil diameter}}\,. \tag{3.30}$$

For the Kowa lens of $\text{HaloCam}_{\text{RAW}}$ the f-number can be adjusted mechanically between 1.8 and 11 by a screw. A fixed value of f-number = 8 was chosen for all measurements and the calibration. For the observation of halo displays close to the sun this is a good trade-off between a small aperture and short exposure times.
To obtain a model for the non-uniformity of the sensor response as a function of the pixel location, flat-field measurements were performed at the LIS at CHB. For this experiment the camera was set-up on top of the LIS and several measurements were performed with the same exposure time. To minimize the impact of inhomogeneities in the brightness of the sphere images were recorded at 6 different orientations by rotating the camera around its own axis, i.e. with the center of the camera roughly pointing to the center of the sphere. For each orientation 40 images were recorded, dark signal corrected and averaged. The measurements averaged over the rotation angles of the camera relative to the sphere are shown in Fig. 3.24a with the signal normalized to 1. The spherical patches visible in the figure are due to a hole in the sphere, which allows to inject a laser as light source for specific experiments. The hole occurs at different locations on the image due to the different rotation angles of the camera. Owing to the large field of view of the camera, the rim of the two hemispheric components of the LIS is visible. For fitting a model to the flat-field measurements these two regions were masked out as displayed in Fig. 3.24b. The flat-field model correcting for the PRNU was determined by fitting a 2-dimensional (2D) second order polynomial to the averaged and masked measurements.

$$F(r_{\text{ij}}) = a \cdot r_{\text{ij}}^2 + b \cdot r_{\text{ij}} + c\,. \tag{3.31}$$

Here, the 2D vector r_{ij} contains the radii of the sensor pixels $r_{\text{ij}}^2 = (x_{\text{ij}} - x_0)^2 + (y_{\text{ij}} - y_0)^2$, where x_{ij} and y_{ij} are 2D vectors of the pixel coordinates in x- and y-direction and x_0 and y_0 are the center coordinates. The result is depicted in Fig. 3.24c for the R-channel with the following parameterization:

$$F(r_{\text{ij}}) = -1.23 \times 10^{-6} \cdot r_{\text{ij}}^2 + -4.31 \times 10^{-6} \cdot r_{\text{ij}} + 0.99\,, \tag{3.32}$$

with $y_0 = 297.2$ and $x_0 = 473.8$. Finally, Fig. 3.24d shows the relative difference between the flat-field model and the measurements in percent. The fluctuations of the signal difference are due to inhomogeneities of the integrating sphere (and the FPN of the camera sensor). However, these inhomogeneities are negligible for the image processing procedure since the flat-field model is used to correct the camera measurements. The average difference between model and measurement amounts to $(0.0 \pm 0.5)\,\%$ for the R-channel with similar values for the remaining

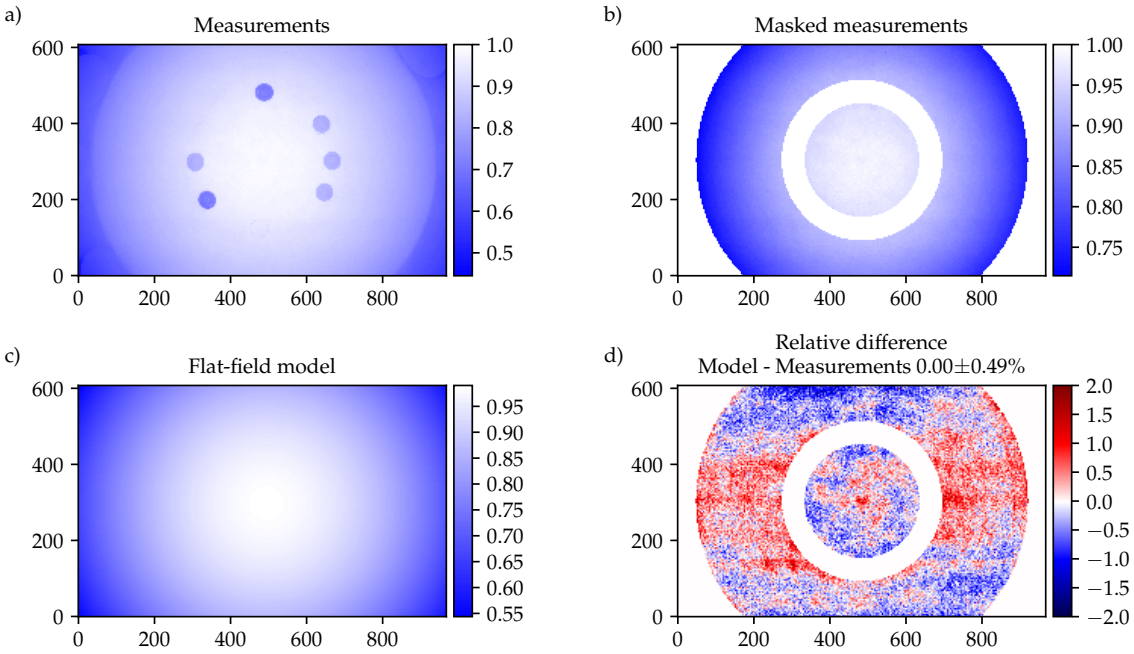

Abbildung 3.24: *(a) HaloCam$_{\mathrm{RAW}}$ dark signal corrected measurements S_0 (R-channel), which are normalized to 1, of the LIS averaged over 6 different camera orientations. (b) S_0, normalized to 1, as in (a) with a mask applied to the areas where the holes and the rim of the LIS is visible. (c) Flat-field model for HaloCam$_{\mathrm{RAW}}$ R-channel fitted against the measurements with a 2-dimensional 2nd order polynomial. (d) Relative difference between flat-field model and measurements.*

channels. The PRNU correction is applied to the dark signal corrected red, green and blue channel separately. Correcting for the PRNU the flat-field corrected signal S_{F} is defined by

$$S_{\mathrm{F}} = S_0 / F \,, \tag{3.33}$$

with the radiometric signal S_0 and the flat-field correction F.

Linearity of radiometric response

Similar to Ewald et al. (2015) the linearity of the CMOS sensor of HaloCam$_{\mathrm{RAW}}$ was investigated by measuring a temporally stable light source with different exposure times. This experiment was performed at the large integrating sphere (LIS) at the CHB, DLR. Baumgartner (2013) characterized the output stability of the LIS to better than $\sigma = 0.02\%$ over a time range of 330 s. For a perfectly linear sensor with response R, the photoelectric signal $\widetilde{S_0}$ should increase linearly with exposure time t_{expos} and radiance L.

$$\widetilde{S_0} = R\,L\,t_{\mathrm{expos}} = s_{\mathrm{n}}\,t_{\mathrm{expos}} \,, \tag{3.34}$$

with the normalized signal s_{n} defined by

$$s_{\mathrm{n}} = R\,L \,. \tag{3.35}$$

The deviation of the actually observed signal S_0 from the linear relationship of $\widetilde{S_0}$ is called photo response non-linearity. The acutally observed signal S_0 can be written as

$$S_0 = F\, s_\mathrm{n}\, t_\mathrm{expos} = F\, R\, L\, t_\mathrm{expos} \tag{3.36}$$

and it follows that the normalized signal can be obtained by

$$s_\mathrm{n} = S_0/(F\, t_\mathrm{expos})\,. \tag{3.37}$$

Figure 3.25 shows the measured radiometric signal S_0 for exposure times t_expos ranging from

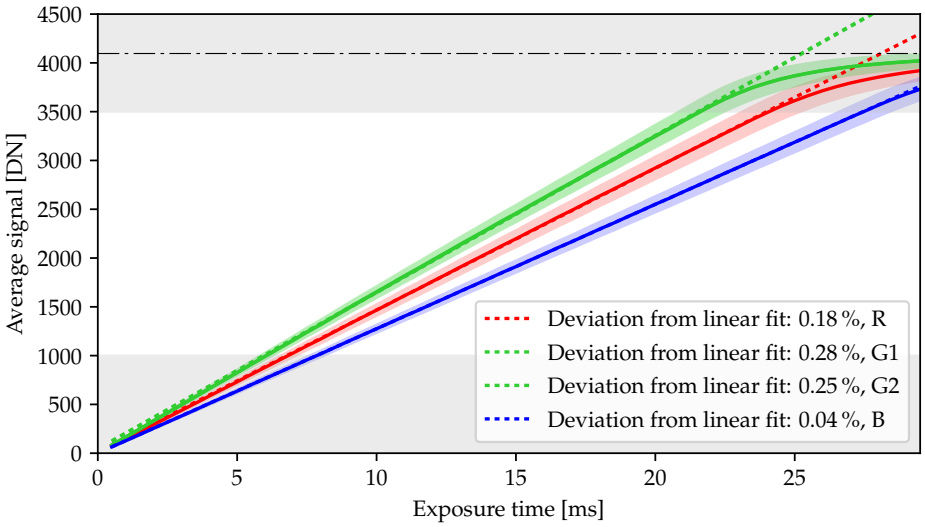

Abbildung 3.25: *HaloCam$_\mathrm{RAW}$ average radiometric signal S_0 as a function of exposure time t_expos for the 4 channels. In operational mode the automatic exposure settings ensure that the measured signal ranges between 1000 and* 3500 DN*, where the averaged signal deviates from a linear behavior between 0.04% for the B-channel and 0.28% for the G1-channel. Signals below and above this range are shaded in gray. For signals close to saturation (4096 DN, black line) the signal deviates clearly from a linear behavior.*

0.5 ms to 29.5 ms, averaged over 5 images for each exposure time. The measured signal ranges between 100 and 4037 DN for the G1 and G2 channels. For the data analysis of the HaloCam$_\mathrm{RAW}$ images, the measured signals range between 1000 and 3500 DN, where the mean deviation from a perfectly linear sensor amounts to 0.18%, 0.28%, 0.25%, and 0.04% for the R-, G1-, G2-, and B-channel, respectively. For signals close to saturation (4096 DN) the sensor becomes strongly non-linear. Thus, signals $S_0 > 3500$ DN are excluded from the analysis.

Spectral response

The spectral response of HaloCam$_\mathrm{RAW}$ was characterized in a similar way as described in Gege et al. (2009) and Baumgartner et al. (2012) using a collimated beam of the monochromator (Oriel MS257) at CHB. The monochromator has an absolute uncertainty of ±0.1 nm $\lambda \leq 1000$ nm, and ±0.25 nm for $\lambda > 1000$ nm with a spectral bandwidth of 0.65 nm and 1.3 nm, respectively. To keep the total time of the calibration procedure short, only a small region of 8×8 pixels (per channel) on the camera sensor was illuminated by the monochromator via a parabolic mirror. Measurements were performed over a wavelength range of 350 nm to 900 nm with steps of 5 nm together with the window of the camera casing shown in Fig. 3.18. Figure 3.26 displays the result

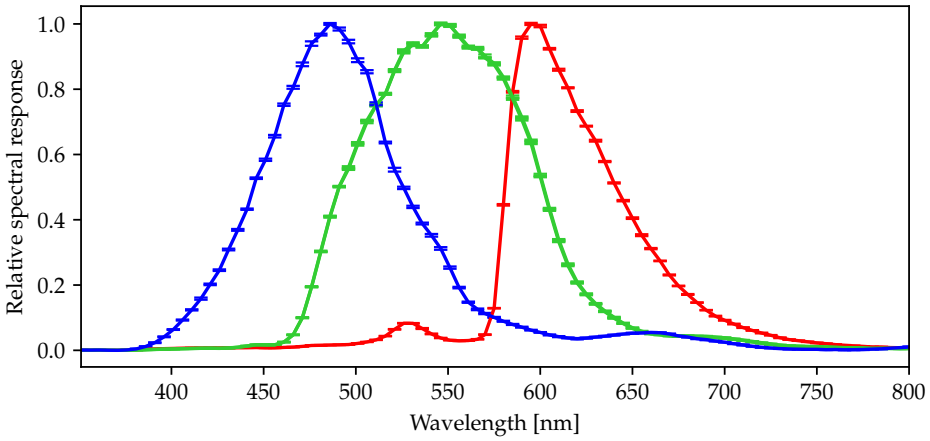

Abbildung 3.26: *HaloCam$_{\mathrm{RAW}}$ relative spectral response for the R-, G1-, G2-, and the B-channel, measured at the CHB at DLR, Oberpfaffenhofen.*

of the spectral calibration for the red, blue and the two green channels. To obtain the spectral sensitivity curves, the raw images were averaged over the pixel region enclosing the light patch of the monochromator and over a set of 10 images per wavelength. Afterwards the dark signal was subtracted and the spectral response for each channel was normalized to 1.

Absolute radiometric response

To obtain an estimate for the absolute radiometric response of HaloCam$_{\mathrm{RAW}}$ the images recorded on 22 September 2015 were cross-calibrated against simultaneous specMACS measurements. For 7 different specMACS scans the HaloCam$_{\mathrm{RAW}}$ image which was recorded closest to the time of the specMACS scan was chosen. The absolute radiometric response of HaloCam$_{\mathrm{RAW}}$ can be determined by dividing the normalized and flat-field corrected signal s_{n} in [DN/ms] by radiance values L in [mW m^{-2} nm^{-1} sr^{-1}].

$$R = s_{\mathrm{n}}/L \tag{3.38}$$

Here, one radiometric response R for all sensor pixels is determined under the assumption that the PRNU is already accounted for by the flat-field correction. Figure 3.27a shows the calibration factor C [DN mW^{-1} m^2 nm sr], which is calculated by the HaloCam$_{\mathrm{RAW}}$ radiometric signal S_0 divided by the specMACS radiance L and scales linearly with the exposure time t_{expos}

$$C = S_0/(L\,F) = s_{\mathrm{n}}/(L\,F) \cdot t_{\mathrm{expos}}\,. \tag{3.39}$$

The errors are provided within the 1σ-confidence interval and consist of the specMACS measurement error, which is calculated for each pixel as described in Section 3.4, and the standard deviation of the calculated calibration factor over all considered pixels. It should be noted that the measurement error of specMACS which amounts to about 5% is responsible for a large part of the uncertainty of the estimated radiometric response. The exposure times range between 1.2 ms and 2.0 ms, which are typical values for HaloCam$_{\mathrm{RAW}}$ measurements of thin cirrus clouds in the vicinity of the sun. Figure 3.27b shows the radiometric response R [DN ms^{-1} mW^{-1} m^2 nm sr] as defined in Ewald et al. (2015) for the 7 evaluated scenes. The radiometric response is independent of the exposure time t_{expos}. The resulting radiometric response for the R-, G1-, G2-, and B-channel is provided in the legend of Fig. 3.27. These values were derived using the upper part of the

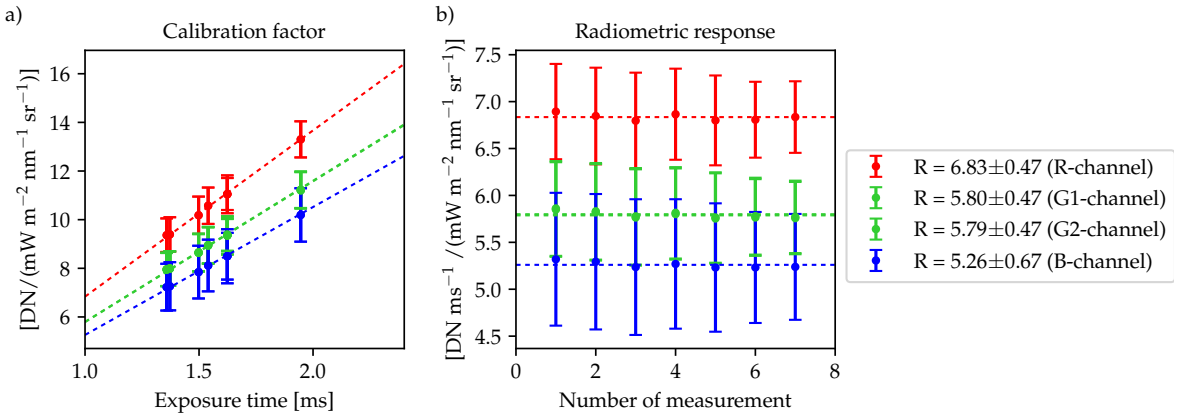

Abbildung 3.27: *Calibration factors (a) and radiometric response (b) for the 4 HaloCam$_{\mathrm{RAW}}$ channels. The values are derived from cross-calibration of HaloCam$_{\mathrm{RAW}}$ against specMACS for 7 different scenes measured simultaneously on 22 September 2015. The legend on the right provides the absolute radiometric response for HaloCam$_{\mathrm{RAW}}$ with 1σ uncertainty evaluated over the 7 measurements.*

specMACS scan above the sun. An additional test using the middle part of the specMACS scan to both sides of the sun revealed very similar values for the response with slightly larger uncertainties: 6.83 ± 0.56, 5.81 ± 0.56, 5.79 ± 0.56, and 5.28 ± 0.78 DN ms^{-1}/(mW m^{-2} nm^{-1} sr^{-1}). The larger uncertainty of the response in the second evaluation is due to larger variabilities in the scenes used for the evaluation. Since the mean values of both evaluations are very similar, it can be argued that the results shown in Fig. 3.27 are a better estimate of the true response values. Therefore, the results shown in Fig. 3.27 will be used in the following.

Signal noise

The measurements of the LIS can also be used to estimate the noise $\mathcal{N}$ of the measured signal as described in Ewald et al. (2015). The noise consists of the dark noise $\mathcal{N}_{\mathrm{d}}$ and the photon shot noise $\mathcal{N}_{\mathrm{shot}}$. Thus, the standard deviation of the signal noise can be calculated by

$$\sigma_{\mathcal{N}} = \sqrt{\sigma_{\mathrm{shot}}^2 + \sigma_{\mathrm{d}}^2}\,, \tag{3.40}$$

As argued by Ewald et al. (2015), the number of photons N detected over a time interval t_{expos} can be estimated by a Poisson distribution. A Poisson distribution with expectation value N has a standard deviation of $\sigma_{\mathrm{N}} \propto \sqrt{N}$. Thus, the variance of the photon shot noise σ_{shot}^2 should scale linearly with the number of detected photoelectrons N and the squared conversion gain k^2 [DN^2] and $\sigma_{\mathcal{N}}$ can be written as

$$\sigma_{\mathcal{N}} = \sqrt{k^2 N + \sigma_{\mathrm{d}}^2}\,. \tag{3.41}$$

Figure 3.28 shows the variance $\sigma_{\mathcal{N}}^2$ (a) and the standard deviation $\sigma_{\mathcal{N}}$ (b) of the measured signal of each sensor pixel, evaluated over 5 images, for all exposure times (0.5 to 9.5 ms). The results are shown for the R-channel here, but are very similar for the other 3 channels. The variance of the measured signal by each pixel should scale linearly with the signal itself (Fig. 3.28a), whereas the standard deviation should scale with the square root of the signal (Fig. 3.28b). The signal noise ranges from about 10 DN for signals of about 100 DN to about 40 DN for signals of about 1500 DN.

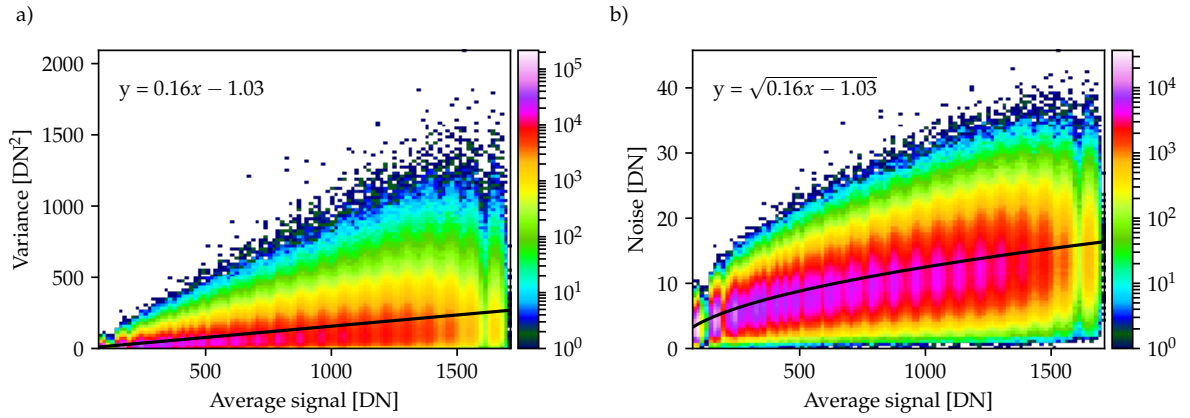

Abbildung 3.28: *2-dimensional histograms of the variance [DN²] (a) and the noise [DN] (b) of the measured signal as a function of the averaged signal of the R-channel.*

HaloCam$_{\mathrm{RAW}}$ total radiometric uncertainty

The total radiometric uncertainty of HaloCam$_{\mathrm{RAW}}$ was estimated by applying Gaussian error propagation to the equations describing the measured signal with the respective errors. Similar to the description in Ewald et al. (2015), the calculation of the total radiometric uncertainty will be outlined in the following. According to Eq. (3.26) the error of the radiometric signal S_0 is computed by combining the absolute errors of the dark signal $\sigma_{\mathrm{d}}(t_{\mathrm{expos}}, T)$ and the instantaneous noise $\sigma_{\mathcal{N}}(S_0)$

$$2\sigma_{\mathrm{S}_0} = \sqrt{(2\sigma_{\mathrm{d}}(t_{\mathrm{expos}}, T))^2 + (2\sigma_{\mathcal{N}}(S_0))^2}\,. \tag{3.42}$$

As defined by Eq. (3.37) the uncertainty of the normalized signal s_{n} consists of the relative error of the photoelectric signal σ_{S_0}, the relative error of the flat-field calibration σ_{F}, and the non-linearity error σ_{nonlin} according to

$$\frac{2\sigma_{s_{\mathrm{n}}}}{s_{\mathrm{n}}} = \sqrt{\left(\frac{2\sigma_{\mathrm{S}_0}}{S_0}\right)^2 + \left(\frac{2\sigma_{\mathrm{F}}}{F}\right)^2 + \left(\frac{2\sigma_{\mathrm{nonlin}}}{s_{\mathrm{n}}}\right)^2}\,. \tag{3.43}$$

Uncertainties due to polarization of light by components of the camera or the casing were not determined for HaloCam$_{\mathrm{RAW}}$. However, according to Ewald et al. (2015) the largest part of the polarization sensitivity of specMACS is introduced by the transmission grating which adds the spectral dimension to the measurements. Since HaloCam$_{\mathrm{RAW}}$ is not equipped with a transmission grating, it is assumed that its polarization sensitivity is lower than for specMACS. According to Hansen and Travis (1974) the direct sunlight is unpolarized and the degree of polarization is increasing towards larger scattering angles. Thus, it can be argued that the degree of polarization for transmitted light in region of the 22° halo is lower than for observations of reflected light from cloud sides, especially in the rainbow scattering region, which is the focus of Ewald (2016). In the final step the radiometric calibration introduces the error of the sensor response σ_{R}, which was estimated from cross-calibration between HaloCam$_{\mathrm{RAW}}$ and specMACS

$$\frac{2\sigma_{\mathrm{L}}}{L} = \sqrt{\left(\frac{2\sigma_{s_{\mathrm{n}}}}{s_{\mathrm{n}}}\right)^2 + \left(\frac{2\sigma_{\mathrm{R}}}{R}\right)^2}\,. \tag{3.44}$$

Tabelle 3.2: *HaloCam$_{\mathrm{RAW}}$ total radiometric uncertainty with a 2σ confidence interval.*

	Signal S	R-channel	G1-channel	G2-channel	B-channel
Relative radiometric uncertainty ($2\sigma_{s_n}$)	1000 DN	2.8 %	2.3 %	2.3 %	3.3 %
	3000 DN	1.8 %	1.6 %	1.6 %	2.1 %
Absolute radiometric uncertainty ($2\sigma_L$)	1000 DN	14.0 %	16.4 %	16.4 %	25.6 %
	3000 DN	13.9 %	16.3 %	16.3 %	25.5 %

Table 3.2 provides the total relative and absolute radiometric uncertainty for the 4 channels of HaloCam$_{\mathrm{RAW}}$ for two typical signals of 1000 and 3000 DN. The relative radiometric uncertainty is the error of the normalized signal s_n (Eq. (3.43)) which is smaller than 3% for all channels. For larger signals the relative 2σ error is smaller since the absolute error is divided by a larger number (cf. Eq. (3.44)). This uncertainty is valid for signal ratios which are independent of the sensor response R. For measurements of spectral radiance, however, the uncertainty increases significantly by the contribution of the uncertainty of the estimated sensor response σ_R. For the R-channel the total absolute uncertainty amounts to about 14% and about 16% for the two green channels. The uncertainty is largest for the B-channel with about 25.5%. Since the radiometric response for HaloCam$_{\mathrm{RAW}}$ was cross-calibrated against specMACS, the relative radiometric uncertainty has to be combined with the measurement uncertainty of specMACS. This method has some issues which potentially increase the uncertainty of the estimated radiometric response in addition: first, the HaloCam$_{\mathrm{RAW}}$ images are recorded every 10 s, so the temporal offset between the specMACS and HaloCam$_{\mathrm{RAW}}$ measurements amount to about 5 s. Second, a slight misalignment between the specMACS and HaloCam$_{\mathrm{RAW}}$ images exists, since they cannot be brought to an exact overlap due to the temporal offset. Third, for comparing the measurements, the specMACS observations have to be convolved with the spectral response of the 4 channels of HaloCam$_{\mathrm{RAW}}$. For wavelengths at the edge of the sensitivity of the specMACS sensor the measurement uncertainty increases strongly introducing additional uncertainty in the estimated radiometric response for the HaloCam$_{\mathrm{RAW}}$ measurements. This effect is responsible for the large uncertainty of the blue channel, which has a spectral response centered at much shorter wavelengths compared to the red and green channels where specMACS has a larger measurement uncertainty.

3.6 HaloForest – an automated halo detection algorithm

3.6.1 Image processing and feature extraction

For processing the HaloCam images, they can be decomposed in their red, green, and blue color channels. The brightness I of each pixel, provided in digital numbers [DN], can then be represented as a data array of the size 1280×960. As an example the HaloCam$_{\mathrm{JPG}}$ image of Fig. 3.20 is used to demonstrate how the images are processed in case of a 22° halo. Figure 3.29 depicts the brightness distributions of the red, green and blue channel as a function of the scattering angle, averaged azimuthally over the uppermost image segment (no. 4 in Fig. 3.20b). The shaded areas around the lines in Fig. 3.29 represent twice the standard deviation of the averaged image region.

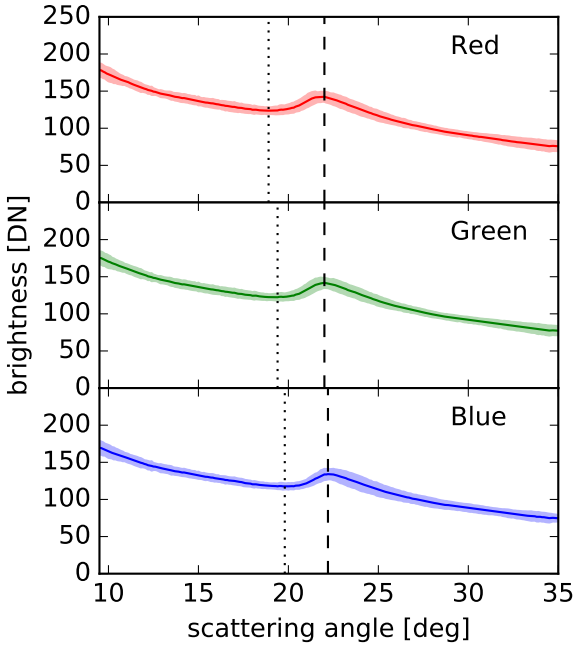

Abbildung 3.29: *HaloCam$_{\mathrm{JPG}}$ image processing demonstrated for the measurements shown in Fig. 3.20, segment no. 4. The three panels show the brightness distributions (in digital numbers [DN]) for the red, green and blue image channel as a function of the scattering angle. The solid line represents the brightness averaged azimuthally over the image segment, whereas the shading indicates the 2σ confidence interval. The vertical lines pinpoint the scattering angles of the 22° halo minimum (dotted) and maximum (dashed) for the RGB channels.*

For analyzing the HaloCam observations several features can be extracted from the brightness distribution across the 22° halo: the scattering angle position of the brightness maximum and minimum, which are indicated in Fig. 3.29 by vertical dashed and dotted lines, respectively. The angular position of the 22° halo maximum ($\vartheta_{\mathrm{halo,\,max}}$) is found by searching for the maximum brightness in the interval (21.0°, 23.5°). Then the angular position of the halo minimum ($\vartheta_{\mathrm{halo,\,min}}$) is determined by looking for the minimum brightness in the interval (18.0°, $\vartheta_{\mathrm{halo,\,max}}$). Another important feature is the brightness contrast of the halo. In analogy to the definition in Section 3.3.1, the HR in this section is defined as the brightness I at the scattering angle of the halo maximum $\vartheta_{\mathrm{halo,\,max}}$ divided by the brightness at the scattering angle of the minimum $\vartheta_{\mathrm{halo,\,min}}$:

$$\mathrm{HR} = I(\vartheta_{\mathrm{halo,\,max}})/I(\vartheta_{\mathrm{halo,\,min}}) \tag{3.45}$$

As an example, the values for $I(\vartheta_{\mathrm{halo,\,max}})$ and $I(\vartheta_{\mathrm{halo,\,min}})$ are displayed in Fig. 3.31 by the

Tabelle 3.3: *22° halo features, for the example of 12 May 2014 13:52 UTC (as in Fig. 3.29). The relative zenith angle (which corresponds to the scattering angle) is listed for the minimum $\vartheta_{\mathrm{halo,\,min}}$ and maximum $\vartheta_{\mathrm{halo,\,max}}$ brightness of the 22° halo together with the brightness contrast, i.e. the halo ratio (HR) for the red, green and blue image channel.*

	$\vartheta_{\mathrm{halo,\,min}}$	$\vartheta_{\mathrm{halo,\,max}}$	HR
Red	18.9°	22.0°	1.15
Green	19.4°	22.0°	1.16
Blue	19.8°	22.2°	1.14

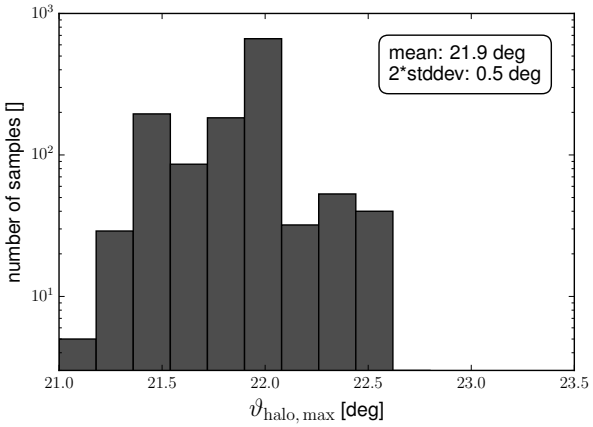

Abbildung 3.30: *Distribution of the scattering angles of the 22° halo brightness maximum $\vartheta_{\mathrm{halo,\,max}}$ in degrees for 1289 randomly chosen and visually classified images using the uppermost image segment (no. 4). The mean value amounts to 21.9° with a 2σ confidence interval of $\pm 0.5°$. Note the logarithmic scale of the y-axis.*

blue triangles pointing up (max) and down (min), respectively. For clearsky conditions and homogeneous cloud cover the brightness distribution decreases from the sun towards larger scattering angles, as shown in the example in Figs. Fig. 3.29 and Fig. 3.31. If HR < 1 the brightness at the scattering angle of the halo maximum ($I(\vartheta_{\mathrm{halo,\,max}})$) is smaller than for the minimum ($I(\vartheta_{\mathrm{halo,\,min}})$) which is representative for a monotonically decreasing, featureless curve in this scattering angle region. This is the case for clearsky conditions or homogeneous cloud cover without halo. For HR $= 1$ the brightness at the halo maximum and minimum are the same causing a slight plateau in the brightness distribution. A distinct halo peak occurs for the condition HR > 1. Thus, HR $= 1$ is assumed as lower threshold for the visibility of a halo. For the example of Fig. 3.29 the 22° halo features are compiled in Table 3.3, evaluated for the uppermost image segment. The scattering angle of the halo minimum ($\vartheta_{\mathrm{halo,\,min}}$) is smallest for the red channel and largest for the blue channel which is responsible for the reddish inner edge and the slightly blueish outer edge of the 22° halo visible in Fig. 3.20. It should be noted that in many cases the 22° halo appears rather white apart from a slightly reddish inner edge (Minnaert, 1937, Vollmer, 2006). The differences between scattering angles for the three colors are smaller for $\vartheta_{\mathrm{halo,\,max}}$ with a slightly larger value for the blue channel. The halo ratio amounts to about 1.15 averaged over all three channels and is largest for the green and smallest for the blue channel.

The angular position of the 22° halo brightness peak ($\vartheta_{\mathrm{halo,\,max}}$) can also be used to estimate the positioning accuracy of the HaloCam camera system relative to the sun. Figure 3.30 shows a histogram of $\vartheta_{\mathrm{halo,\,max}}$ for 1289 randomly selected $\mathrm{HaloCam_{JPG}}$ pictures showing a 22° halo in

the uppermost image segment. This segment was chosen since it contains the most pronounced halos. For a faint halo the peak in the brightness distribution is rather flat causing a larger uncertainty in finding the angular position of the peak. The mean value of $\vartheta_{\text{halo, max}}$ amounts to 21.9° with a 2σ uncertainty of 0.5°, which is a rough estimate of HaloCam's pointing accuracy. Since $\vartheta_{\text{halo, max}}$ and $\vartheta_{\text{halo, min}}$ are searched for within an angular interval, the pointing accuracy of ±0.5° is sufficient to detect the halo.

3.6.2 Setup and training of HaloForest

The $\text{HaloCam}_{\text{JPG}}$ long-term dataset from January 2014 until June 2016 was evaluated by applying a machine learning algorithm for the automated detection of halos. The algorithm was trained using features extracted from the $\text{HaloCam}_{\text{JPG}}$ images. Some of these features (e.g. HR, $\vartheta_{\text{halo, max}}$, $\vartheta_{\text{halo, min}}$) were already described in the previous section. As a first implementation the detection algorithm is presented here for the case of the 22° halo but it is possible to extend it to other halo types as well. The detection is performed by a classification algorithm which is trained to predict whether a $\text{HaloCam}_{\text{JPG}}$ picture belongs to the class "22° halo" or "no 22° halo". For such a binary classification a decision tree can be used to create a model which predicts the class of a data sample. Details on decision trees are explained in Appendix A.1. One major issue of decision trees is their tendency to over-fitting by growing arbitrarily complex trees depending on the complexity of the data. In this study the random forest classifier was used as described by Breiman (2001), which improves the issue of over-fitting significantly by growing an ensemble of decision trees. A description of the random forest classifier used in this study is provided in Appendix A.2. In principle, other classification algorithms could be used like artificial neural networks. The reasons why the random forest classifier was chosen are: apart from its robustness to over-fitting it does not require much pre-processing of the input data like scaling or normalizing. During the training of the individual trees the out-of-bag samples (i.e. the samples which were not in the trainings subsets) are used as test data and classification error estimates (e.g. out-of-bag error) can be calculated simultaneously (Breiman, 2001). In contrast to an artificial neural network, the basic structure and the internal threshold tests of the decision trees are simple to understand and can be explained by boolean logic. Henceforward, the algorithm applied to the classification of 22° halos will be called HaloForest.
The features used here for the classification are the 22° halo ratio, the scattering angle position of the halo minimum and maximum, and the scattering angle confining the halo peak $\vartheta_{\text{halo, end}}$, which are shown in Fig. 3.31 together with the slope of the regression line in black (solid). The halo peak is confined by $\vartheta_{\text{halo, end}}$ (dash-dotted line) which represents the scattering angle with the same brightness level as $\vartheta_{\text{halo, min}}$ in the scattering angle interval $(\vartheta_{\text{halo, max}}, 35°]$. This feature is used to ensure that the brightness for angles larger than $\vartheta_{\text{halo, max}}$ is decreasing again. The slope of the regression line serves as an estimate for the brightness gradient around the sun. For clearsky images this gradient is steeper than for overcast cases. As a measure of the separation of color in the halo, the scattering angle difference between the blue and red channel for the halo minimum ($\Delta\vartheta_{\text{halo, min}}$) and maximum ($\Delta\vartheta_{\text{halo, max}}$) are calculated, which are defined as

$$\begin{aligned} \Delta\vartheta_{\text{halo, max}} &= \vartheta_{\text{halo, max, blue}} - \vartheta_{\text{halo, max, red}} \\ \Delta\vartheta_{\text{halo, min}} &= \vartheta_{\text{halo, min, blue}} - \vartheta_{\text{halo, min, red}} \end{aligned} \tag{3.46}$$

Furthermore, the standard deviation of the brightness averaged over the image segment is used as a proxy for the inhomogeneity of the scene. These eight features are calculated for each of the six image segments separately. In order to get an impression of typical values of the training

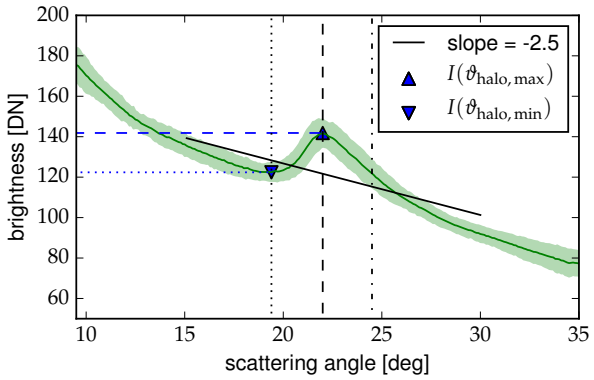

Abbildung 3.31: *As Fig. 3.29 showing the first minimum (dotted) and the maximum (dashed) of the 22° halo for the green channel. In addition, $\vartheta_{\mathrm{halo,end}}$ is indicated (dash-dot line) which represents the scattering angle of the same brightness as $\vartheta_{\mathrm{halo,min}}$ and confines the halo peak. In this example $\vartheta_{\mathrm{halo,end}}$ is located at about 24.5°. The corresponding brightness $I(\vartheta_{\mathrm{halo,min}})$ and $I(\vartheta_{\mathrm{halo,max}})$ used to calculate the HR are marked with the blue triangles pointing down (min) and up (max). The regression line of the averaged brightness distribution (solid black), which is evaluated between scattering angles of 15° and 30°, has a slope of -2.5 for this example.*

features for the two classes, Figs. 3.32a – c show 2-dimensional scatter plots of selected feature pairs for the upper image segment (no. 4). Features, which belong to the class "22° halo", are displayed in blue whereas the features of the class "no 22° halo" are represented by gray scatter points. Figure 3.32a shows the distribution of the scattering angle of the halo maximum versus minimum. The scattering angles of the halo maximum $\vartheta_{\mathrm{halo,max}}$ are confined to a smaller interval for "22° halo" compared with "no 22° halo". However, the two classes share many data points in this projection so more features are needed to generate decision boundaries in a higher, here 8-dimensional space. Figure 3.32b depicts the scattering angle difference between the blue minus the red channel for the halo maximum ($\Delta\vartheta_{\mathrm{halo,max}}$) versus minimum ($\Delta\vartheta_{\mathrm{halo,max}}$), which is positive for the "22° halo" class since the inner edge (smaller ϑ) of the 22° halo is slightly red. The HR, which is shown in Fig. 3.32c, takes values between 1 and ∼1.3 for "22° halos". Images with a low mean standard deviation of the image segment indicate rather homogeneous scenes which are present most of the time when a 22° halo is visible. Figs. 3.32a – c visualize that the two classes "22° halo" and "no 22° halo" can not be separated easily since the values of the features overlap. The lower panels of Fig. 3.32d – f display the regions which are detected as "22° halo" (blue) and "no 22° halo" (gray) by the trained algorithm.

For each of the six image segments an individual classifier was trained using a dataset of visually classified $\mathrm{HaloCam_{JPG}}$ images which were chosen randomly from the dataset. The performance of the classifiers was tested using a random selection of 30% of the dataset which was excluded from training. This procedure was repeated 100 times to get statistically significant results for the performance of the classifier. Table 3.4 shows the confusion matrix for the classifier of the segments directly above (no. 4) and below the sun (no. 1) which represent the two extreme cases of the performance of the six different classifiers: the upper part of the 22° halo has a higher brightness contrast compared to the lower part which is often obstructed by the horizon. For the training of HaloForest 1289 samples with a 22° halo and 5181 samples without 22° halo were used for the uppermost segment (no. 4). The lowermost segment (no. 1) was trained with 296 and 3370 samples of the classes 22° halo and no 22° halo, respectively. The lines of the confusion matrix indicate the true class labels of the samples ("22° halo" and "no 22° halo"), whereas the columns contain the predicted class labels. The number of true positive

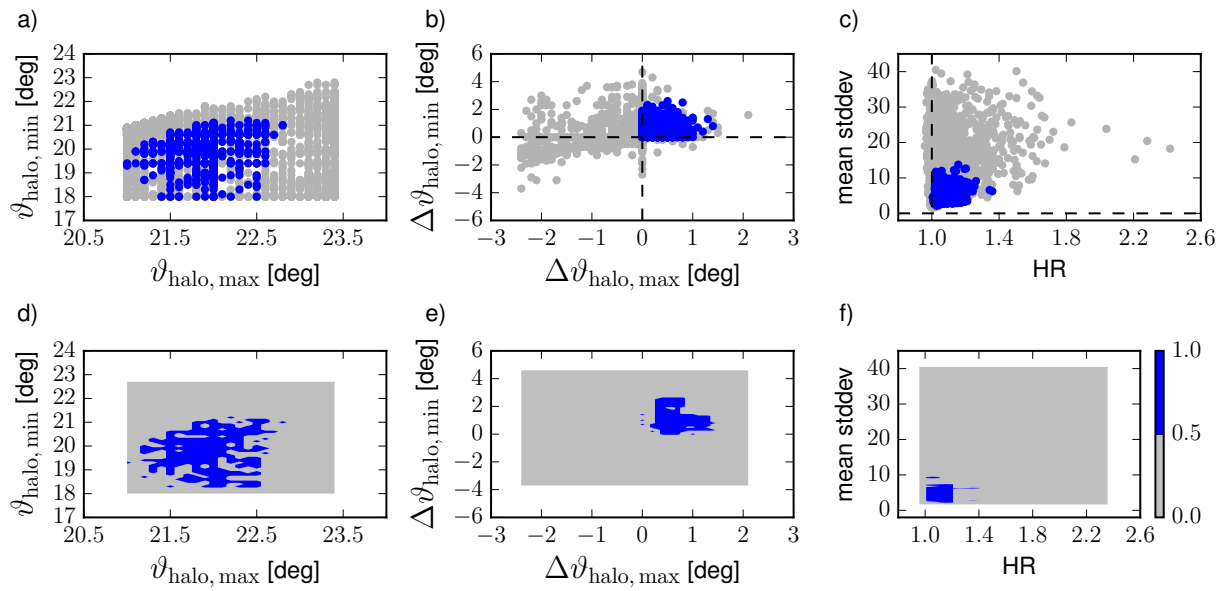

Abbildung 3.32: *Panels a) – c): scatter plots of selected pairs of the 8 features used for training HaloForest. Training samples with(out) 22° halos are represented in blue (gray). Panels d) – f): decision boundaries of the random forest classifier for the respective feature pair. The predicted probability used for separating the classes "22° halo"* ($p > 0.5$) *and "no 22° halo"* ($p \leq 0.5$) *is displayed in blue and gray, respectively.*

and negative (in bold) as well as false positive and negative classifications are evaluated and provided with a 2σ confidence interval. The correct classification of "22° halo" is maximum for the uppermost image segment (no. 4) with about 98% and minimum for the lowermost segment with about 89%. The correct classification of "no 22° halo" is overall higher than 99%, so the HaloForest algorithm seems to be able to separate the two classes well. The performance of the other four segments ranges between the results of the upper and lowermost segments.

Tabelle 3.4: *Confusion matrix for HaloForest for the uppermost (no. 4) and lowermost (no. 1) image segments. The label "Predicted" refers to the class which was predicted by HaloForest whereas "True" labels the visually identified class. The true positives (correctly classified "22° halo") are printed in bold font. False positives ("no 22° halo" classified as "22° halo") and false negatives are listed on the other diagonal. The results are provided with a 2σ confidence interval.*

		Predicted	
	Segment 4:	22° halo	no 22° halo
True	22° halo	**(97.3 ± 1.9) %**	(0.4 ± 0.3) %
	no 22° halo	(2.7 ± 0.9) %	**(99.6 ± 0.2) %**

	Segment 1:	22° halo	no 22° halo
True	22° halo	**(88.5 ± 7.1) %**	(0.5 ± 0.5) %
	no 22° halo	(11.5 ± 3.5) %	**(99.5 ± 0.2) %**

3.7 RICO – Retrieval of Ice Crystal prOperties

The preceding section presented the halo detection algorithm HaloForest which can be used to automatically evaluate the large HaloCam dataset for the frequency of 22° halos. Cirrus clouds featuring a halo display contain at least a certain amount of smooth hexagonal ice crystals. Thus, the frequency of "halo-producing" cirrus clouds provides a first estimate of the minimum fraction of smooth hexagonal ice crystals in cirrus clouds.

More detailed information about ice crystal properties can be obtained by analyzing the brightness contrast and with of the 22° halo as discussed in Section 3.3. The slope of the radiance distribution around the 22° halo contains information about the cirrus optical thickness (COT) and ice crystal effective radius. To obtain the maximum information content of the 22° halo regarding the ice crystal optical and microphysical properties, all parameters have to be considered simultaneously. This can be achieved by comparing radiance measurements of the 22° halo with radiative transfer simulations. To determine the optical and microphysical properties which best match the observations, a look-up table (LUT) was compiled by performing radiative transfer simulations with DISORT. The LUT comprises different ice crystal habits, surface roughness, effective radius, COT, and AOT. Furthermore, the LUT is calculated for different SZAs and observation geometries. For the surface albedo, aerosol type, atmospheric profile and cloud height, fixed parameters were used for the LUT. Then the LUT elements are compared with the radiance measurements to find the best matching LUT element by minimizing the root mean squared error (RMSE). LUT and observations have to be compared on the same angular grid. Maximizing the scattering angle range, which is used for this comparison, provides more information. On the other hand, for a large angular region inhomogeneities in the cirrus optical and microphysical properties become important. To optimize this trade-off, a scattering angle range between $16° \leq \Theta \leq 35°$ was chosen. Taking the measurement error into account, all LUT elements with a RMSE within the 2σ confidence interval are solutions for the cirrus optical and microphysical properties. The LUT element with the minimum RMSE is considered the best match. In the following this retrieval method will be referred to by the acronym RICSHA, which stands for "Retrieval of Ice Crystal Size rougHness and shApe".

3.7.1 Ice crystal shape and roughness models

For the retrieval 3 different models of ice crystal optical properties were used:

- YANG: optical properties based on Yang et al. (2013) for 9 different habits: droxtals, solid columns, hollow columns, plates, 8-element columns, 5-element plates, 10-element plates, solid bullet rosettes, and hollow bullet rosettes. Since this parameterization provides only three different roughness levels (smooth, moderately roughened, and severely roughened), the optical properties of smooth and severely roughened ice crystals were mixed linearly to achieve a continuous distribution of roughness levels. Different fractions of smooth and rough ice crystals were mixed via their extinction coefficient in the radiative transfer simulations. The smooth crystal fraction (SCF) ranges between $0 \leq \mathrm{SCF} \leq 1$, resulting in a rough crystal fraction (RCF) of $\mathrm{RCF} = 1 - \mathrm{SCF}$.

- $\mathrm{YANG}_{\mathrm{RND}}$: optical properties based on a random mixture of the Yang et al. (2013) optical properties. All habits 9 were considered, each with a smooth and a severely roughened version. The SCF was chosen randomly between 0% and 100% in steps of 5% for each combination of a smooth and rough habit. Likewise, the effective radius was chosen randomly for each habit between 5 and 90 µm with steps of 5 µm. The random sampling was performed similar to Wang et al. (2014) and the optical properties were mixed by their extinction coefficients as for YANG.

- GO: optical properties were calculated using the geometric optics raytracing code (Macke et al., 1996). Solid hexagonal ice crystals were assumed with aspect ratios ranging from 0.02 (thin plates) to 50 (long columns). Ice crystal roughness was parameterized by a Weibull distribution taking values between $0 \leq \sigma \leq 0.3$. As for the YANG optical properties, the different SCFs were achieved here by mixing the optical properties for smooth ($\sigma = 0$) with rough crystals ($\sigma = 0.3$) via their extinction coefficients.

3.7.2 Sensitivity studies

In the following the sensitivity of RICSHA on the retrieved SCF is tested for different scenarios using the YANG model for the ice crystal optical properties. LUTs assuming slightly different atmospheric or ice cloud parameters are matched against synthetic measurements simulated with DISORT. The tests are performed for the ice crystal habit, AOT, the aerosol type, surface albedo, and atmospheric profile. The synthetic measurements were simulated for a wavelength of 500 nm and a solar zenith angle of 45° in the almucantar plane, i.e. for varying azimuth angles at the same zenith angle as the sun. The SCF is varied between 0 and 1 in steps of 0.05, whereas the cirrus optical thickness ranges between 0.1 and 3. The effective radius is treated as a free parameter (i.e. neither constrained nor retrieved) and ranges from 10 µm to 90 µm in steps of 10 µm. Unless stated differently, ice clouds with different mixtures of smooth and severely roughened solid columns with an aerosol-free atmosphere assuming the U.S. standard atmospheric profile (Anderson et al., 1986) were used for the radiative transfer simulations.

First, the retrieval error is estimated by applying the retrieval to simulated test cases using LUTs with slight deviations in the assumed atmospheric condition, e. g. surface albedo, AOT, aerosol type. In order to investigate the stability of the retrieval for different ice clouds, simulations were performed for a range of COTs and SCFs for one ice crystal habit population. The retrieval error is evaluated for the difference of the true and retrieved SCF defined by

$$\Delta\mathrm{SCF} = \mathrm{SCF}_{\mathrm{Retrieved}} - \mathrm{SCF}_{\mathrm{True}} \,. \tag{3.47}$$

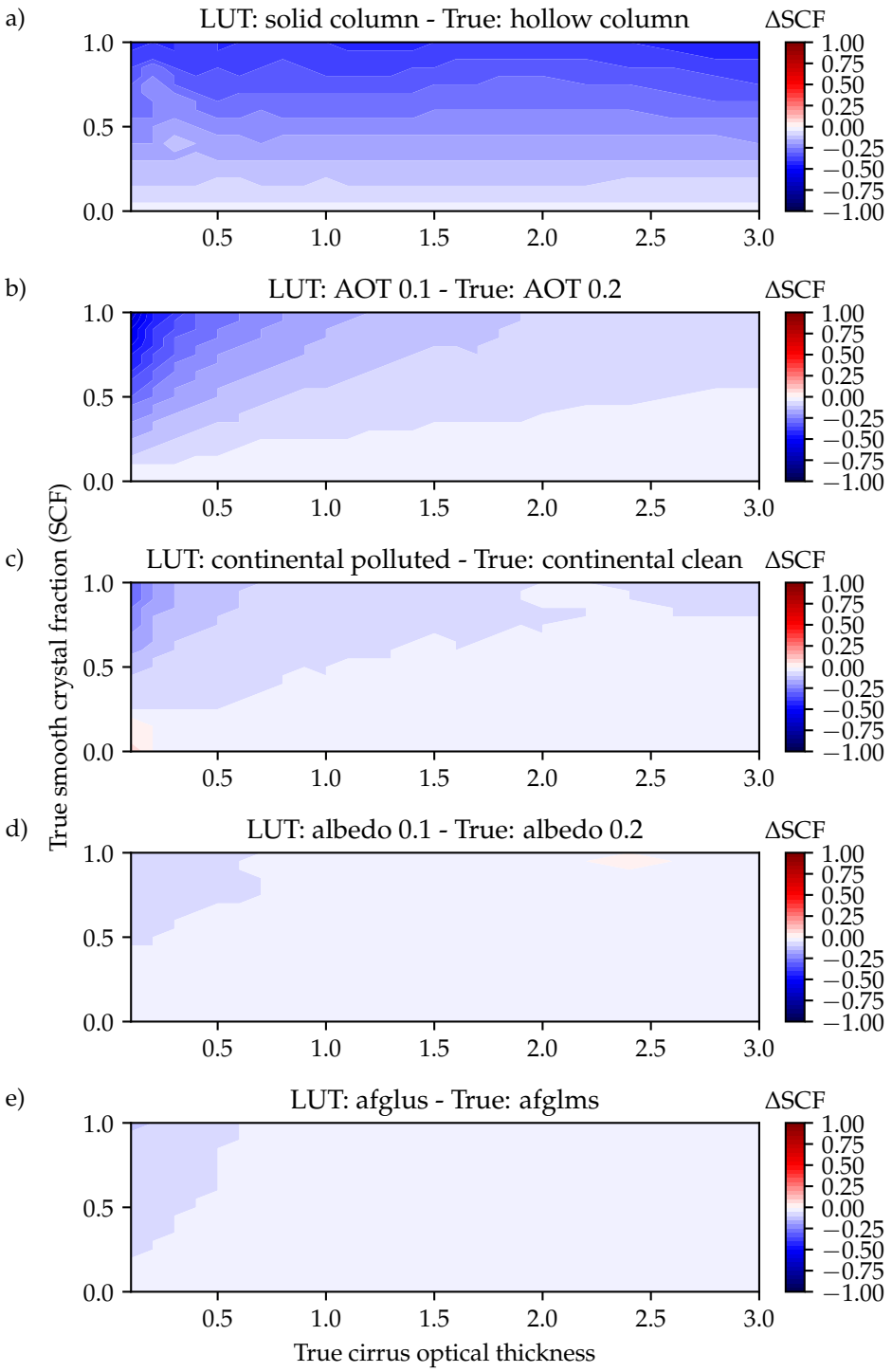

Abbildung 3.33: *Sensitivity of RICSHA regarding 5 different LUT parameters: a) ice crystal habit, b) AOT, c) aerosol type, d) surface albedo, e) atmospheric profile. A LUT was matched against synthetic measurements, simulated with DISORT, at a wavelength of* 500 nm *and a SZA of* 45° *in the almucantar plane, i.e. for varying azimuth angles at the same zenith angle as the sun. Synthetic measurements for different COTs and SCFs were calculated and are considered as "truth". The LUTs were calculated for slightly different parameter values or parameterizations for the different tests (a–e) while all other LUT parameters were correct. The panels a) – e) show contour plots of the resulting difference between the true and retrieved smooth crystal fraction* $\Delta\mathrm{SCF} = \mathrm{SCF}_{\mathrm{Retrieved}} - \mathrm{SCF}_{\mathrm{True}}$*. Blue indicates an underestimation* ($\mathrm{SCF}_{\mathrm{Retrieved}} < \mathrm{SCF}_{\mathrm{True}}$) *and red an overestimation* ($\mathrm{SCF}_{\mathrm{Retrieved}} > \mathrm{SCF}_{\mathrm{True}}$) *of the true SCF.*

Figure 3.33a demonstrates the effect of assuming a wrong ice crystal shape. All other LUT parameters are correct. The surface albedo is zero and an aerosol free atmosphere is assumed. Figure 3.33a shows a contour plot of the difference of the retrieved smooth crystal fraction ΔSCF, whereas blue colors indicate underestimation ($SCF_{Retrieved} < SCF_{True}$) of the true SCF and red colors represent overestimation ($SCF_{Retrieved} > SCF_{True}$) of the true SCF. Calculating the LUT for solid columns and applying it to a cirrus cloud consisting of hollow columns causes a tendency to underestimate the retrieved fraction of smooth ice crystals. This is due to the fact that solid columns produce a brighter halo than hollow columns. Therefore a smaller fraction of smooth ice crystals is needed in case of the solid columns to produce an equally bright halo. The error of the retrieved fraction of smooth ice crystals is almost independent of the COT but increases with SCF. A maximum error of $\Delta SCF = -0.45$ occurs for COT = 2.8 and SCF = 0.8. In Fig. 3.33b the sensitivity of the retrieved smooth crystal fraction is tested for an error in the assumed AOT. For this test the surface albedo is set to zero and the "continental clean" aerosol mixture from the OPAC library was chosen. Underestimating the AOT leads to an underestimation of the SCF, especially for very small COTs. The 22° halo in the LUT is brighter than in the true data due to the lower AOT, especially for low COTs for which the aerosol scattering features dominate over the halo features. Therefore, a lower SCF is retrieved to get a halo of the same brightness as the truth. When the COT becomes larger than the AOT the retrieval error tends to decrease. For this test the largest error of the retrieved SCF amounts to $\Delta SCF = -0.65$ for a COT of 0.1 and a SCF of 0.9.

A similar effect but much less pronounced occurs for an error in the assumed aerosol type, demonstrated in Fig. 3.33c. For the LUT the "continental polluted" OPAC aerosol optical properties were used whereas the truth is "continental clean" with a constant AOT of 0.2 and surface albedo zero. In this case the SCF is overestimated for very small COTs. The maximum difference between retrieved and true SCF amounts to $\Delta SCF = -0.3$ at a COT of 0.1 and a fraction of 0.7. The results of these two sensitivity studies demonstrate that especially for ground-based remote sensing it is crucial to have a good representation of aerosol type and optical thickness in the model setup in order to retrieve information about ice cloud optical properties.
An error in the assumed surface albedo of 0.1 instead of 0.2 (Fig. 3.33d has a significantly weaker effect on the retrieved smooth crystal fraction with a maximum error of $\Delta SCF = -0.05$ for a COT of 0.1 and a SCF of 0.1. For these simulations an aerosol free atmosphere was assumed.
The last sensitivity study Fig. 3.33e investigates the effect of a different atmospheric profile. This results in a slightly different humidity profile which in turn affects the aerosol optical properties. For this experiment the LUT assumes the U.S. standard atmospheric profile whereas the true profile is the mid-latitude summer atmosphere with higher relative humidity values in the lower layers (Anderson et al., 1986). The results show that for very thin cirrus there is a small difference between true and retrieved smooth crystal fraction of $\Delta SCF = -0.1$ for COT of 0.1 and a SCF of 0.8. In general the introduced error is negligible compared to the errors caused by a wrong representation of the aerosol optical properties.

Figure 3.34 shows the same sensitivity studies as Fig. 3.33 but assuming measurements with unknown radiometric response (Eq. (3.12)). So for finding the best match in the LUT the radiometric response of the measured radiance is a free parameter. The sensitivity test of assuming a wrong ice crystal shape, shown in Fig. 3.34a, yields almost the same results as the study with the calibrated measurements. The underestimation of the SCF is larger for a brighter halo if solid columns are assumed instead of hollow columns with a maximum error of the retrieved SCF of $\Delta SCF = -0.4$ for a COT of 2.2 and a SCF of 0.85. Figure 3.34b shows that uncalibrated measu-

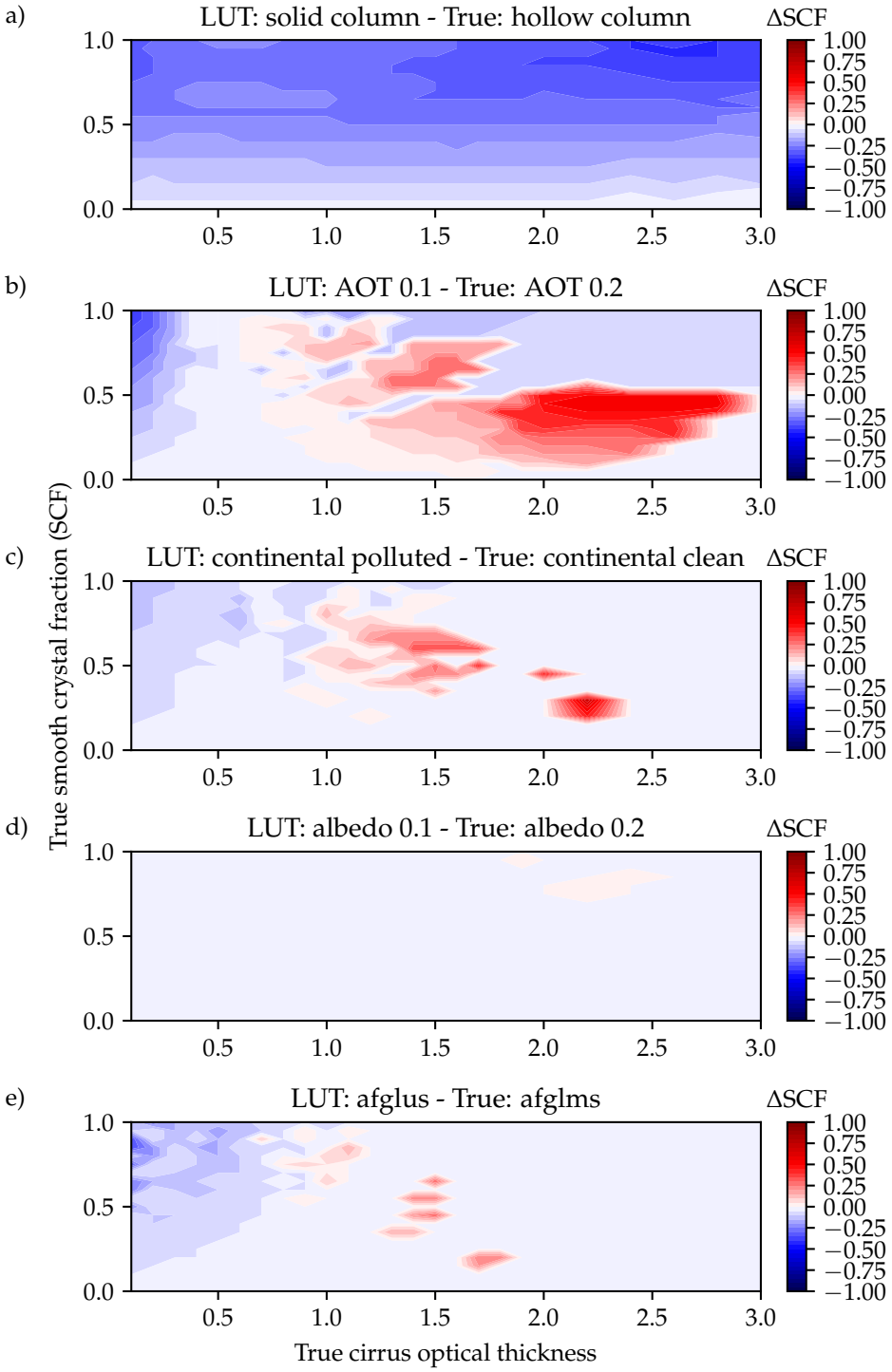

Abbildung 3.34: *Sensitivity studies for RICSHA as in Fig. 3.33 assuming uncalibrated measurements by treating the radiometric response as a free scaling parameter in the retrieval.*

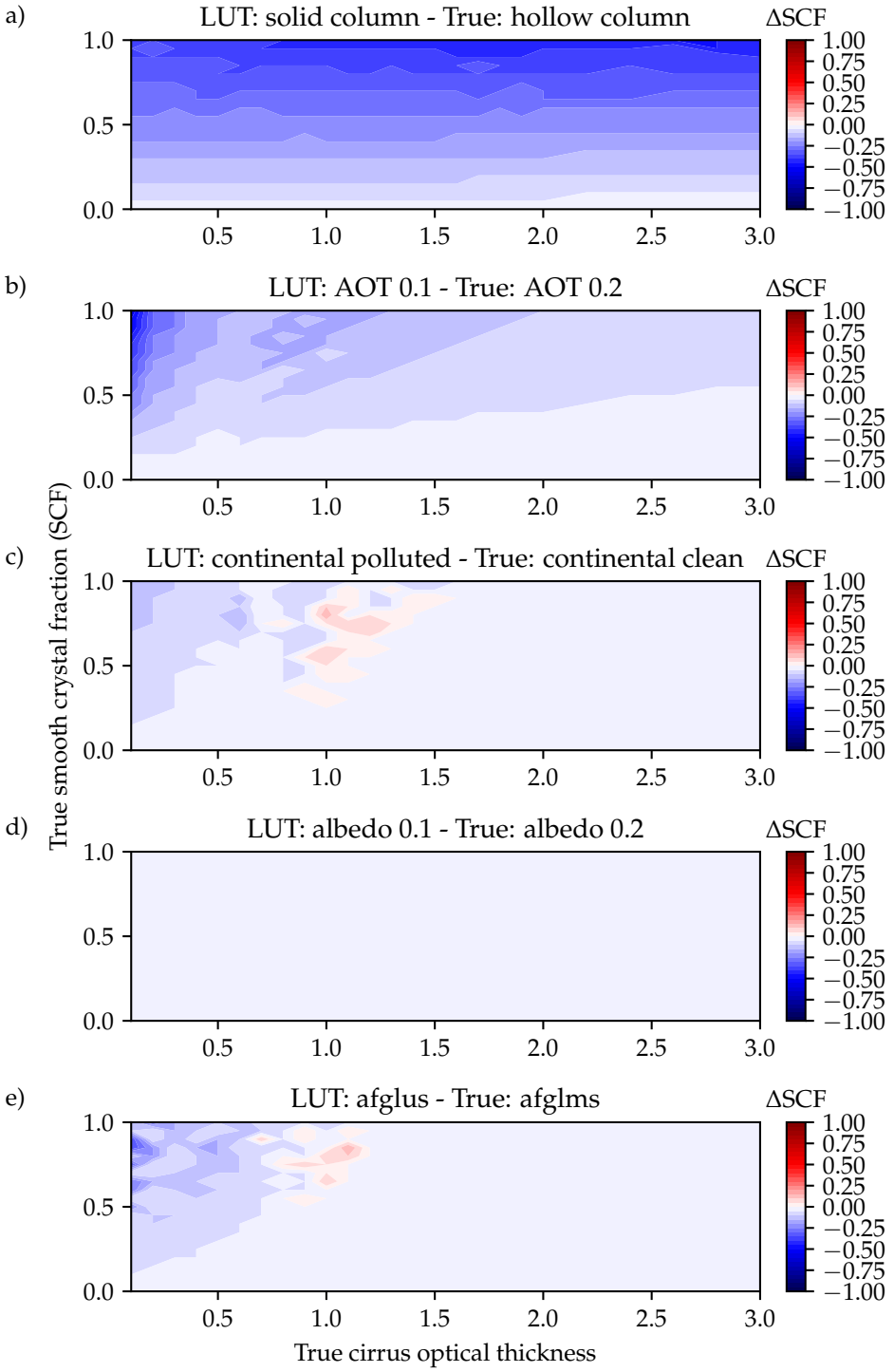

Abbildung 3.35: *Sensitivity studies for RICSHA as in Fig. 3.33 assuming a radiometric calibration error of 25%. This is achieved by using the radiometric response as free scaling parameter within the boundaries of ±25%, i.e. $R \in [0.75, 1.25]$ for the synthetic measurements simulated with DISORT.*

rements can lead to large errors of the SCF ranging from an underestimation of $\Delta\text{SCF} = -0.4$ for small COTs to overestimation up to $\Delta\text{SCF} = 0.55$ for COT> 1 for an error in the assumed AOT of 0.1. A similar behavior can be observed for the sensitivity test of the aerosol type in Fig. 3.34c which results in a maximum underestimation of the SCF of $\Delta\text{SCF} = -0.15$ for small COTs and an overestimation of the SCF up to $\Delta\text{SCF} = 0.7$ at a COT of 1.5 and a SCF of 0.5. The tendency to underestimate the retrieved SCF for small COTs and a high SCF remains almost the same as for calibrated measurements. The sensitivity studies of the retrieval on wrong assumptions of the surface albedo (Fig. 3.34d is almost negligible with a maximum error of $\Delta\text{SCF} = 0.05$ in the retrieved SCF. An error in the assumed atmospheric profile (Fig. 3.34e) results in a maximum error of the retrieved SCF between $\Delta\text{SCF} = -0.35$ and $\Delta\text{SCF} = 0.3$ at a COT of 0.1 and 0.9, respectively. This study demonstrates that for uncalibrated measurements the retrieval uncertainties can deviate up to 70% in the retrieved SCF from the errors of the calibrated measurements.
Another test was performed for calibrated measurements with an error of the radiometric response of 25%, which corresponds to the largest error for $\text{HaloCam}_{\text{RAW}}$ (B-channel) (cf. Section 3.5.3). Figure 3.35 shows the results for the same sensitivity studies as in the previous cases (Fig. 3.33 and Fig. 3.34). The results of the ice crystal habit and AOT test in Fig. 3.35a and Fig. 3.35b are very similar to the calibrated measurements assuming no error for the radiometric response (cf. Fig. 3.33a and Fig. 3.33b). A slight overestimation of the retrieved SCF occurs for the aerosol type and atmospheric profile test (Fig. 3.35c and e) compared to the sensitivity of the calibrated measurements assuming no error of the radiometric response. For the aerosol type test (Fig. 3.35c) the error of the retrieved SCF ranges between $\Delta\text{SCF} = -0.15$ and $\Delta\text{SCF} = 0.15$, whereas for the atmospheric profile test (Fig. 3.35e) ΔSCF varies between [-0.35, 0.15]. The error of the retrieved SCF for the albedo test (Fig. 3.35d) amounts to $\Delta\text{SCF} = 0$ which occurs most likely since errors in the assumed LUT parameters are transferred to the radiometric calibration factor to some extent.
These sensitivity studies demonstrate that the largest retrieval errors occur for wrong assumptions of the ice crystal habit and the AOT. Thus, for the compiled LUTs all available ice crystal habits for the YANG optical properties are considered. Under the assumption that the optical properties represent the variability of ice crystals in natural cirrus clouds, the retrieval error for the ice crystal habit is negligible. The AOT is varied in the LUT assuming typical values for Munich. For the remaining LUT table parameters, i.e. aerosol type, surface albedo, and atmospheric profile, "best guess" fixed values or parameters are chosen. The procedure how the LUT parameters are selected will be presented in the following sections.

Depending on the temperature regime of the cirrus and its evolution phase, the cloud can contain supercooled water droplets alongside the ice crystals. Hu et al. (2010) investigated the occurrence frequency, liquid water content, liquid water path, and temperature dependence of supercooled water droplets globally using CALIOP depolarization measurements and backscatter intensity measurements. These observations were combined with temperature information from the collocated infrared imaging radiometer (IIR) measurements and collocated MODIS measurements to derive cloud water paths. This study considers clouds with layer-integrated attenuated backscatter greater than $0.01\,\text{sr}^{-1}$, or optical depths greater than 0.4. Hu et al. (2010) confirmed the findings of Hogan et al. (2004) who state that supercooled water clouds are rarely found below $-35\,^{\circ}\text{C}$. According to Hu et al. (2010) the probability of water phase occurring in a cloud is almost 0% for $T \leq -35\,^{\circ}\text{C}$ and increases rapidly to almost 100% at about $-10\,^{\circ}\text{C}$.
Since water droplets cannot form halo displays due to their spherical shape, they have in prin-

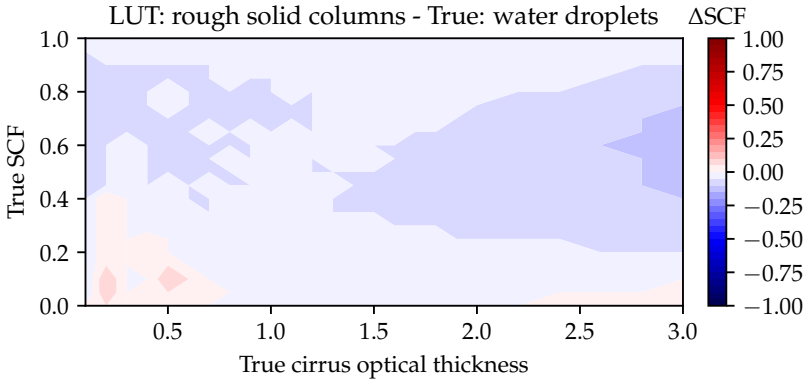

Abbildung 3.36: *Sensitivity studies for RICSHA as in Fig. 3.33 for measurements assuming mixtures of smooth ice crystal columns with supercooled water droplets.*

ciple a similar effect on halo displays as rough ice crystals in smoothing out the halo displays. Water droplets might therefore not be distinguished from rough ice crystals by passive ground-based observations in the visible spectral range. To investigate the effect of supercooled water droplets on the retrieved smooth crystal fraction, synthetic measurements were simulated with DISORT for different mixtures of smooth ice crystal columns and water droplets. Similar as for the 2-habit LUTs, the fraction of water droplets was increased from 0 for a cloud consisting entirely of smooth solid columns to 1 for a pure water cloud. The water cloud optical properties were calculated with the Mie tool described in Wiscombe (1980). A gamma size distribution was assumed with $\alpha = 7$ which corresponds to an effective variance of $\nu_{\text{eff}} = 1/(\alpha + 3) = 0.1$. It is assumed that all cloud particles (water droplets and ice crystals) have the same effective radius which was varied between 10 and 90 µm in steps of 10 µm. A LUT assuming different mixtures of smooth and rough ice crystal columns was matched against these synthetic measurements. The retrieved SCF is displayed in Fig. 3.36. The error of the retrieved SCF ranges in the interval [-0.1, 0.1]. This means that water droplets indeed have a very similar effect on the 22° halo as rough ice crystals and introduce an error of the retrieved SCF of ±0.1.

Furthermore, it was tested whether it is sufficient to perform radiative transfer simulations for a representative wavelength rather than integrating over the full spectral sensitivity curves of $\text{HaloCam}_{\text{RAW}}$. Figure 3.37 shows the results of radiative transfer simulations using libRadtran for realistic conditions including a cirrus cloud with 40% smooth crystals and a typical AOT of 0.2. The geometry was chosen in the principal plane above the sun (SZA = 45°) for scattering angles between 10° and 50°. The solid line represents spectral simulations integrated over the spectral sensitivity functions of the red green and blue channel of $\text{HaloCam}_{\text{RAW}}$. The dashed lines display the same simulation but for only one wavelength which is equal to the weighted average of the respective camera channels. The averaged relative differences are overall smaller than 2.1%. Considering the large uncertainties of the unknown aerosol type let alone the variability of the ice crystal shape, this uncertainty is considered small enough to allow for monochromatic radiative transfer simulations at the wavelengths representative for each camera channel. The representative wavelengths for $\text{HaloCam}_{\text{RAW}}$ are 618 nm for the red, 553 nm for the green, and 498 nm for the blue channel.

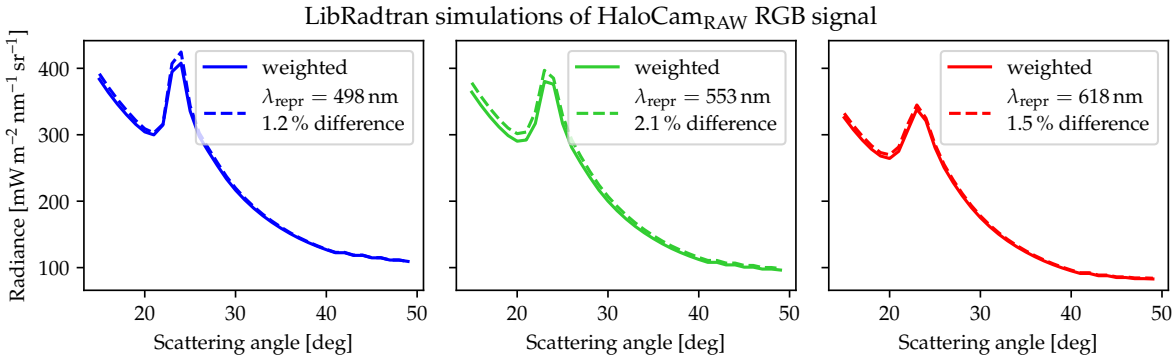

Abbildung 3.37: *Radiative transfer simulations performed with libRadtran for the HaloCam$_{RAW}$ red, green and blue channel in the principal plane above the sun with a* SZA = 45°. *A cirrus cloud with COT = 1 (at a wavelength* 550 nm*),* r_{eff} = 50 µm *and a mixture of 40% smooth and 60% severely roughened solid columns. The continental average aerosol mixture from OPAC was chosen with AOT = 0.2 at* 550 nm.

3.7.3 Additional look-up table parameters

This section discusses additional parameters which have to be considered for compiling the LUTs and explains the methods which were used to define the range of the required parameters. The sensitivity of the cloud height and thickness as well as the atmospheric profile on the 22° halo radiance distribution was tested. The tests were performed for the HaloCam$_{RAW}$ R-, G-, and B-channel. Varying the cloud base height between 6 km and 10 km, both with a geometrical thickness of 1 km resulted in differences of $\ll 1\,\%$. Similar results were obtained for the depth of the cloud which was varied between 1 km and 4 km. Also the choice of the atmospheric profile is negligible in this spectral range: the difference between a simulations using the U.S. standard atmosphere and the mid-latitude summer atmosphere was $\ll 1\,\%$. Both atmospheric profiles are defined in Anderson et al. (1986). Unless otherwise stated the LUT simulations were performed using the U.S. standard atmospheric profile and a cirrus cloud between 10 km to 11 km height.

Aerosol optical thickness

The aerosol optical thickness was derived from the AERONET AOT product (Holben et al., 1998) for the observation site on the MIM rooftop platform. This additional data could be used whenever clearsky periods occurred before of after the cirrus clouds appeared. According to the study of Schnell (2014) typical AOT values for Munich during the period from 2007 to 2010 amount to 0.269 ± 0.014 based on AERONET data for a wavelength of 500 nm and ranged between 0.12 – 0.17 at 532 nm for measurements with MULIS. Analyzing the AERONET aerosol optical thickness values (version 2, level 1.5) between September 2015 and April 2017 the mean AOT at a wavelength of 500 nm amounts to 0.18 as displayed in Fig. 3.38. AOTs > 1 are most likely due to thin, homogeneous cloud layers which are not filtered out by the AERONET cloud-screening algorithm. To cover the most frequently observed values for Munich, which are displayed in Fig. 3.38b, the LUTs were calculated for AOTs ranging between 0.0 and 0.5 in steps of 0.05. Schnell (2014) also studied the typical aerosol type over Munich using CALIPSO data. Evaluated in geometrical layer depth, the dominant aerosol type was smoke, followed by polluted dust. In autumn the clean continental aerosol type was the second largest fraction. Other observed aerosol types were dust and continental polluted aerosol. Between 2007 and 2010 no maritime aerosol was observed. Unless otherwise stated, the aerosol type chosen for

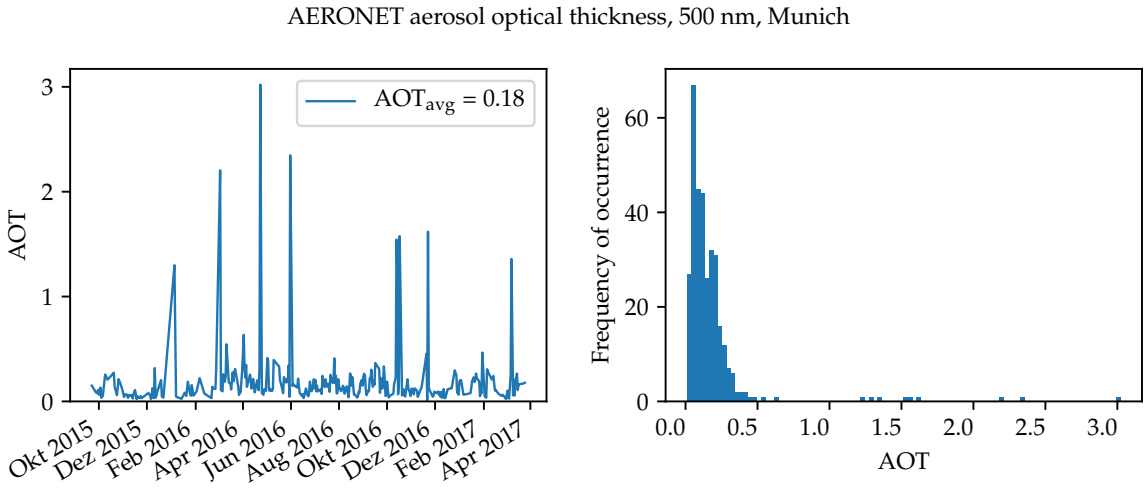

Abbildung 3.38: *AERONET aerosol optical thickness at* 500 nm *wavelength for the time range between September 2015 and April 2017 for which the LUTs are calculated. The average AOT during this time range amounts to about 0.18 (left panel). The histogram in the right panel shows that the most frequent AOTs range between 0 and 0.5. Events with* AOTs > 1 *are most likely thin, homogeneous cloud layers which are not filtered out by the AERONET cloud-screening algorithm.*

the LUT simulations was the "continental average" mixture from the OPAC database which is described in Hess et al. (1998). To constrain the AOT in the retrieval the daily mean value from AERONET was used within a 2σ confidence interval.

Cirrus optical thickness

The COT has a strong influence on the brightness contrast of the halo and has to be constrained as much as possible to retrieve ice crystal shape and roughness. For this retrieval the COT is derived from sunphotometer measurements using the SSARA instrument (Toledano et al., 2009, 2011). The SSARA instrument provides direct sun measurements with a temporal resolution of 2 s which is much more suitable for the observation of the highly variable cirrus clouds than the AERONET data which has a temporal resolution of 15 min (Holben et al., 1998). The COT is derived by calculating the total optical thickness from the SSARA direct sun measurements. The previously estimated AOT is then subtracted and a correction parameter is applied to account for the diffuse radiation measured additionally due to the increased forward scattering of the large ice crystals. Similar to the procedure presented in Reinhardt et al. (2014) the concept of the apparent optical thickness is used as in Shiobara and Asano (1994), Guerrero-Rascado et al. (2013), and Segal-Rosenheimer et al. (2013).

According to Bouguer-Beer-Lambert's law (cf. Eq. (2.17)) the solar radiance L traveling through the atmosphere with a slant path optical thickness τ_s can be denoted as

$$L = L_0 \exp(-\tau_s) \,,$$

where L_0 is the solar radiance at the top of the atmosphere. Any detector with a finite FOV which is pointing towards the sun will measure both the direct solar radiance and the diffuse radiance produced by scattering particles and molecules in the atmosphere. The total radiance entering the instrument FOV can be considered as an apparent radiance L' representing the

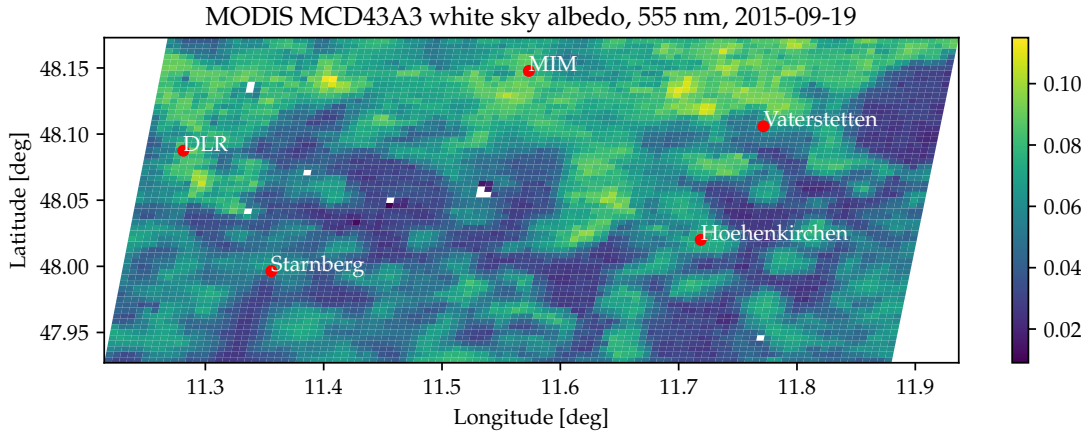

Abbildung 3.39: *MODIS MCD43A3 white sky albedo from 19 September 2015 at a wavelength of* 555 nm *displayed for the region covered by the projected* 22° *halo in the course of the day. The Meteorological Institute of LMU in Munich is marked by a red dot and labeled with "MIM". Some more locations, e.g. the DLR in Oberpfaffenhofen, are marked to provide additional geographic information. At this wavelength albedo values range between about 0.015 and 0.12 with lower values for regions with lakes (e.g. south of Starnberg) and woods (e.g. between DLR and MIM).*

direct and the diffuse part together. The apparent radiance is defined as

$$L' = L_0 \exp(-\tau_{\text{app}}) = L_0 \exp(-k\,\tau_{\text{s}})\,. \tag{3.48}$$

with the apparent optical thickness τ_{app}. The apparent optical thickness can be related with the slant-path optical thickness τ_{s} by introducing the correction factor k

$$\tau_{\text{app}} = k\,\tau_{\text{s}}\,, \tag{3.49}$$

which accounts for the difference between direct and apparent radiance due to the additional diffuse part and takes values between $[0, 1]$. Using Eq. (3.49) the slant-path optical thickness τ_{s} can be calculated by

$$\tau_{\text{s}} = \ln\left(\frac{L_0}{L'}\right)/k\,. \tag{3.50}$$

As discussed in Reinhardt et al. (2014), for optical thicknesses $\tau_{\text{s}} < 3$ the correction factor k is most sensitive to the detector FOV, the effective particle radius and shape but is almost independent of τ_{s} itself. For the ice crystal property retrieval the k-factors were calculated according to this procedure for the SSARA FOV of 1.2° (Toledano et al., 2009) assuming a COT of 1.5 as proposed by Reinhardt et al. (2014). The k-factors were tabled for all ice crystal habits, surface roughness values, and effective radii used in the LUT. The COTs derived from the SSARA direct sun measurements using the presented method, are used as an additional constraint in the retrieval.

Surface albedo

The surface albedo is another parameter which affects the transmission measured at the ground. With increasing surface albedo more radiation is reflected by the ground which is scattered again by the clouds. However, for an error of 0.1 in the assumed surface albedo the errors in the retrieved SCF are significantly smaller ($|\Delta\text{SCF}| \leq 0.05$) than for a wrong assumption of the

aerosol type ($|\Delta SCF| \leq 0.3$) or AOT ($|\Delta SCF| \leq 0.65$) (cf. Fig. 3.33). For estimating the surface albedo during the time of the measurements, the MODIS white-sky albedo product MCD43B3 (Strahler et al., 1999) was used. The procedure how the geographic coordinates of the surface albedo are calculated is described in Appendix B. The MODIS white sky albedo product is available for 7 wavelength bands centered at 469, 555, 645, 858, 1240, 1640 and 2130 nm. To obtain spectrally continuous data, the ASTER spectral library (Baldridge et al., 2009) is applied to interpolate the MODIS albedo data similar to the procedure described in Hausmann (2012). A linear combination of the spectral albedo of deciduous and conifer trees, grass, shingle and concrete is used to represent the MODIS white sky albedo. Figure 3.40 shows the MODIS white sky albedo measured at the 7 wavelengths with black dots. The black line represents the linear combination of the single ASTER spectral albedos which provides the best match of the MODIS measurements. The single spectral albedos with the corresponding weighting coefficients are depicted in different colors. To obtain the albedo measured e.g. by $\text{HaloCam}_{\text{RAW}}$, the fitted

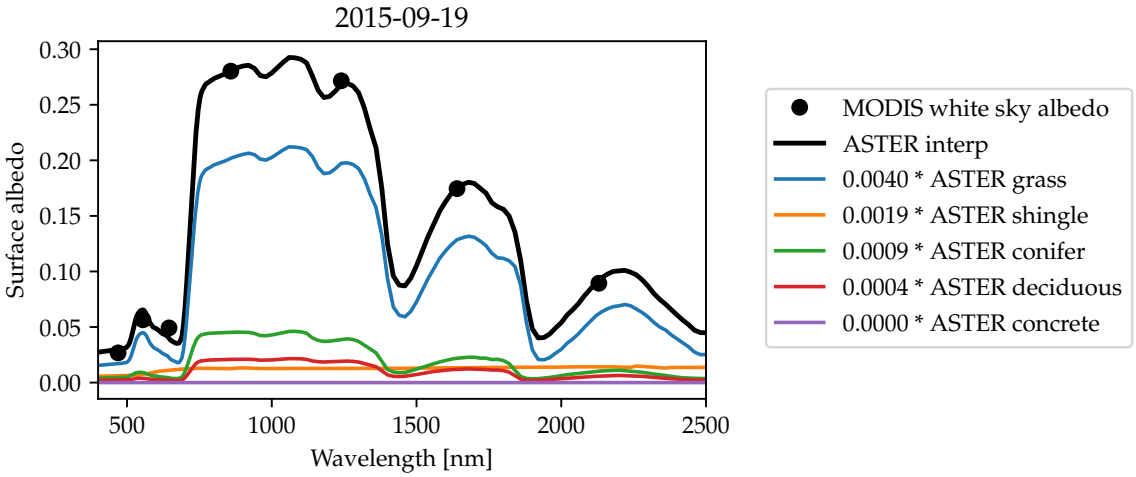

Abbildung 3.40: *Spectral albedo data from the ASTER library provided with a resolution of* 2 nm *for grass (blue), shingle (orange), conifer (green) and deciduous trees (red) as well as concrete (purple). A linear combination for the different ASTER albedo types is determined which represents best the averaged MODIS data from Fig. 3.39 by applying the least-squares method. The weighting factors for 19 September 2015 are provided in the legend of the figure. The resulting mixture of ASTER albedo data is then used to obtain an approximation of the MODIS albedo product for high spectral resolution, which is displayed by the black solid line.*

spectral albedo from the ASTER library (cf. black line in Fig. 3.40) is integrated over the spectral sensitivity of the respective camera channel. In the case of $\text{HaloCam}_{\text{RAW}}$, integrating the spectral albedo over the red, green, and blue channel yields the albedo values displayed in Fig. 3.41 with the respective line color. For this figure the MODIS white sky albedo values were evaluated between Nov 2015 and Apr 2017. Values larger than 0.1 were excluded since it is likely that they are affected by snow. Averaging over the whole period yields mean albedo values for the red, green, and blue channel of 0.065, 0.063, and 0.050 respectively. The red and green channel show higher values than the blue channel since the surface South of Munich is dominated by green grass and trees. Comparing the red and the green channel, a slight difference between winter and summer can be noticed which is very likely due to the vegetation period. During summer the deciduous trees increase the albedo in the part of the spectrum covered mostly by the green channel, whereas in the winter the red channel measures a slightly higher albedo.

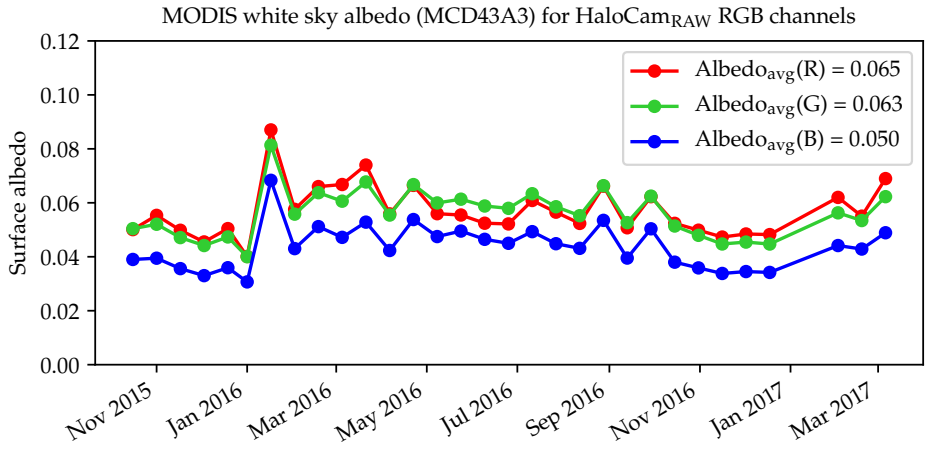

Abbildung 3.41: *Surface albedo between October 2015 and March 2017 for the HaloCam$_{RAW}$ RGB channels. The data are obtained by weighting the spectrally high-resolution parameterization of the MODIS albedo data (cf. Fig. 3.40 black curve) with the spectral response of the RGB channels (cf. Fig. 3.26). The surface albedo for the HaloCam$_{RAW}$ channels averaged over this period amounts to 0.065 (R), 0.063 (G), and 0.050 (B).*

3.8 CrystalTrace – a raytracing algorithm for oriented ice crystals

For radiative transfer simulations it is usually assumed that the scattering particles are randomly oriented within the cloud or the atmosphere. This allows to parameterize the scattering process in a simplified way: the scattering phase function depends only on the scattering angle and the relative azimuth angle of the incident and outgoing light can be selected randomly. In most cases the assumption of randomly oriented particles is realistic, but in case of cirrus clouds oriented ice crystals have frequently been observed by space-borne and ground-based observations. Noel and Sassen (2005) studied the orientation of ice crystals in cirrus and mid-level clouds using scanning polarization lidar observations. Chepfer et al. (1999) and Noel and Chepfer (2004) observed oriented ice crystals in more than 40% of ice clouds by analyzing POLDER bidirectional polarized radiances for specular reflection above optically thick ice clouds. Noel and Chepfer (2010) analyzed CALIOP backscatter and depolarization ratio for thin ice clouds and found oriented crystals in about 6% of all ice cloud layers. Zhou et al. (2012) retrieved the frequency of oriented ice crystals by simulating the CALIOP backscatter and depolarization ratio with help of a 3D Monte Carlo model.

Also certain halo displays, e.g. sundogs and upper tangent arcs, can only be explained by the presence of oriented ice crystals (e.g. Wegener (1925), Tricker (1970), Tape (1994), Tape and Moilanen (2006)). One objective of this study is to investigate the effect of ice crystal orientation on halo displays and to explore possibilities to infer the fraction of oriented ice crystals from the brightness contrast of halo displays formed by oriented crystals and randomly oriented crystals. When the ice crystals are oriented the single-scattering properties are not only a function of the scattering angle but depend also on the azimuth of the scattering plane (Liou and Yang, 2016). To allow for radiative transfer simulations of oriented ice crystals the optical properties have to be stored which implies an increased amount of data by a factor of 360 for a resolution of 1°. This can be avoided by using the geometric raytracing method to calculate the radiance field caused by the refraction and reflection of sunlight by ice crystals. This study focuses on the visible spectral range (400 nm to 700 nm), where the wavelength is much smaller than the crystal size

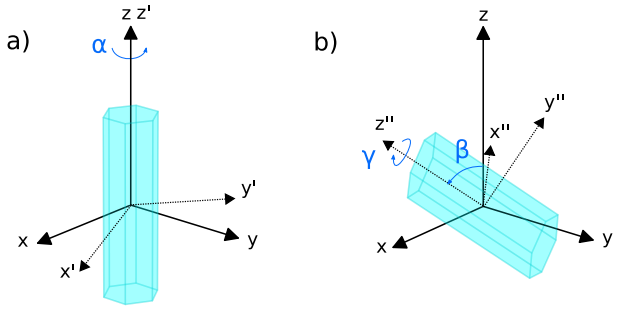

Abbildung 3.42: *Ice crystal geometry and definition of Euler angles as used for CrystalTrace. (a) Original geometry of the ice crystal rotated by the Euler angle α_{Euler} around its z-axis. The updated coordinate system of the ice crystal is now denoted by x', y', and z'. Subsequently, the ice crystal is rotated by β_{Euler} around the x'-axis, which results in the crystal orientation shown in (b). The updated coordinate system after the 2nd rotation is denoted by x'', y'', and z''. Finally, the third rotation is performed around the z''-axis indicated by γ_{Euler} in (b).*

resulting in size parameters of the order of 100. For large size parameters the geometric-optics approach can be used as an asymptotic approximation of fundamental electromagnetic theory (Liou and Yang, 2016). As another advantage geometric raytracing can be simulated using the Monte Carlo method and can thus be easily implemented in the existing MYSTIC code of libRadtran. The procedure of the raytracing method and how it is implemented in MYSTIC will be explained in the following.

The raytracing method was first developed by Wendling et al. (1979) for hexagonal ice crystal columns and plates. Several authors advanced the method by using more complex particles and including absorption and polarization: Pattloch and Tränkle (1984), Muinonen et al. (1989), Takano and Liou (1990) and later Macke (1994), Takano and Liou (1995), Hess (1996), Macke et al. (1996), Yang and Liou (1998), and Prigarin (2009).

For large size parameters the incident light can be considered as a bundle of parallel rays that undergo reflection and refraction outside and inside the ice crystal with propagation directions determined by Snell's law (cf. Eq. (2.37)) at the surface. Starting with the direction of the incident ray $\mathbf{x_0}$, the crystal's orientation is calculated by randomly choosing three Euler angles α_{Euler}, β_{Euler} (angle of crystal c-axis) and γ_{Euler}. For randomly oriented crystals the new orientation is determined by drawing random numbers r between [0, 1)

$$\alpha_{\text{Euler}} = 2\pi\, r\,, \tag{3.51}$$

$$\beta_{\text{Euler}} = \arccos(1 - 2r)\,, \tag{3.52}$$

$$\gamma_{\text{Euler}} = 2\pi\, r\,. \tag{3.53}$$

If the crystals are oriented, the tilt of their vertical axis is parameterized by a Gaussian distribution with mean value $\mu_{\beta,\text{Euler}}$ and standard deviation $\sigma_{\beta,\text{Euler}}$

$$\beta_{\text{Euler}} = \frac{1}{\sqrt{2\,\sigma^2_{\beta,\text{Euler}}\,\pi}} \exp\left(-\frac{(r - \mu_{\beta,\text{Euler}})^2}{2\,\sigma^2_{\beta,\text{Euler}}}\right)\,. \tag{3.54}$$

The standard deviation of the Gaussian orientation distribution will be referred to as *orientation parameter* in the following. Ice crystal plates orient with their c-axis vertically which implies $\mu_{\beta,\text{Euler}} = 0°$. Ice crystal columns instead have aerodynamically stable orientations with their c-axis horizontal and thus $\mu_{\beta,\text{Euler}} = 90°$. Using the rotated ice crystal coordinates, an intersection

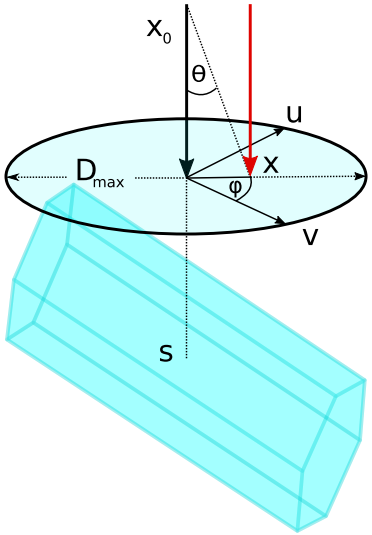

Abbildung 3.43: *Method to determine initial point x of the incident ray x_0. The red arrow denotes the incident direction of the ray with starting point x. The intersection point with the ice crystal x is determined by drawing random angles θ and ϕ in a circle centered around the barycenter s with diameter $D_{\max}$, the maximum dimension of the ice crystal. The vectors u and v are auxiliary vectors which are perpendicular to x and to each other.*

between the direction of the incident ray $\mathbf{x_0}$ and the plane of a crystal face is determined at a randomly chosen point. This procedure is illustrated in Fig. 3.43: a circle is defined in the plane perpendicular to $\mathbf{x_0}$ and centered around the geometric center of the ice crystal $\mathbf{s}$. The radius is determined by the maximum diameter $D_{\max}$ of the ice crystal. Within this circle a point is chosen by drawing random numbers for the zenith (θ) and azimuth angle (ϕ). The resulting vector is denoted by a red arrow in Fig. 3.43 and is calculated by

$$\mathbf{x} = \mathbf{s} - \mathbf{x_0} \cdot D_{\max}/2 + (\cos\phi\,\mathbf{u} + \sin\phi\,\mathbf{v})\,\sqrt{\theta} \cdot D_{\max}/2\,. \tag{3.55}$$

Random points are repeatedly selected until an intersection is found between the plane of an ice crystal face and the vector of the incident ray $\mathbf{x}$. Once an intersection is found, the photon ray is traced through the ice crystal by refraction and reflection using the Monte Carlo method. The direction of the reflected and transmitted rays can be calculated using Snell's law Eq. (2.41) and their intensity with the Fresnel reflection coefficient $R = (R_\mathrm{l}^2 + R_\mathrm{r}^2)/2$ using Eq. (2.39) and Eq. (2.38). The photon is reflected if the chosen random number $r < R$, otherwise it is transmitted. Total reflection occurs if the angle of refraction $\theta_\mathrm{t} > \arcsin(1/n_\mathrm{Re})$. This procedure is repeated until the photon escapes from the crystal.

This raytracing method allows performing radiative transfer simulations without explicit knowledge of the scattering phase function. In fact, the scattering phase function results from the raytracing procedure which is represented by the number of scattered photons collected per unit solid angle ($2\pi\,\sin\theta\,\Delta\theta$) (Liou and Yang, 2016). Liou and Yang (2016) point out that "geometric optics is the only approach in light scattering that will provide physical explanations of the features that occur in the phase function computed from "exact" solutions (e.g., the Lorenz-Mie theory) or numerical methods (e.g., finite-difference time domain method)." Furthermore, the raytracing technique is computationally fast compared to other methods like T-matrix or DDA (Flatau and Draine, 2014) which is an important advantage for the use of radiative transfer simulations. These advantages are accompanied by some drawbacks of the raytracing method as described by Liou and Yang (2016):

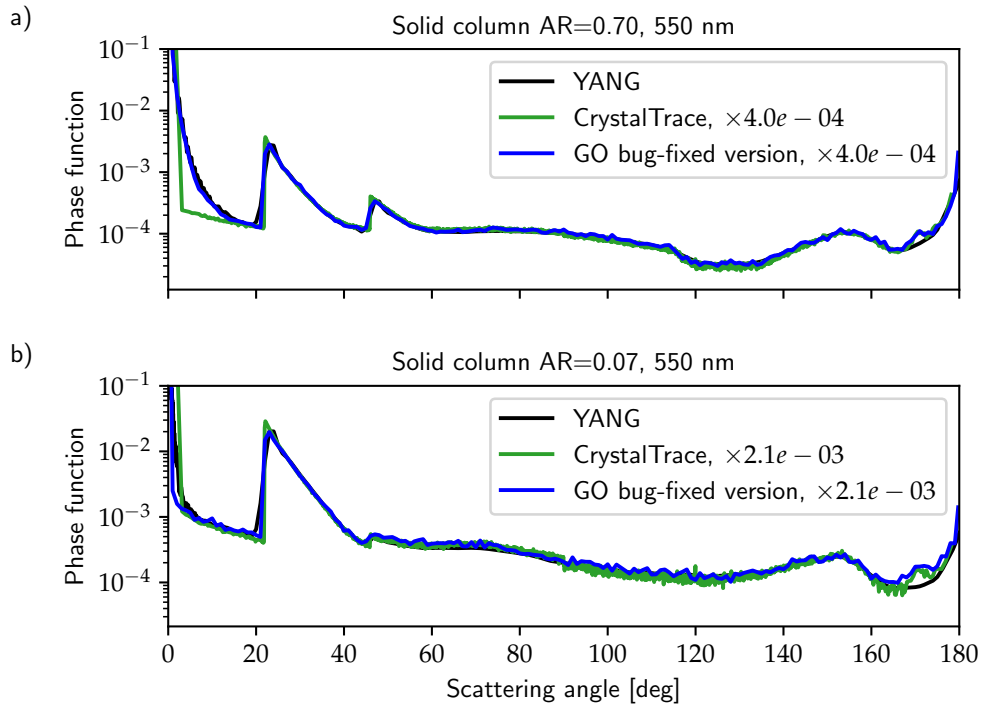

Abbildung 3.44: *Comparison of the scattering phase functions calculated with YANG (black), CrystalTrace (green) and the bug-fixed version of GO (blue) at wavelength of* 550 nm. *(a) Scattering phase functions for a solid ice crystal column with* AR = 0.7 *and* $D_{\max} = 65\,\mu\text{m}$ *and (b) for* AR = 0.07 *with* $D_{\max} = 1 \times 10^4\,\mu\text{m}$. *Both the GO and CrystalTrace phase functions were scaled to allow for a comparison of the results for scattering angles excluding the forward scattering peak. The results compare well apart from the forward scattering region for the smaller ice crystal (a) due to diffraction which is not accounted for by CrystalTrace.*

1. Assume that rays can be localized on the ice crystal surface.

2. Assume that the energy attenuated by the scatterer may be decomposed into equal extinction from diffraction and from Fresnel rays.

3. If the diffraction is accounted for by the Fraunhofer formulation the vector property of electromagnetic fields is not accounted for.

4. Direct calculations of the far field by raytracing will produce a discontinuous distribution of the scattered energy, such as the delta-transmission (Takano and Liou, 1989).

To obtain physically more realistic results, a lot of effort has been made to incorporate these effects which are discussed in Liou and Yang (2016).

The raytracing method developed for this study is called CrystalTrace and allows to perform radiative transfer simulations of mixtures of different ice crystal shapes each with an individual degree of orientation. The current implementation does not account for the polarization state of the photon, diffraction, ice absorption and ice crystal roughness which could be incorporated in the future. To study ice crystal orientation and its effect on the brightness of halo displays in the visible spectral range, this is considered a suitable setup for basic sensitivity studies. CrystalTrace was validated by comparing the scattering phase functions for ice crystals with different aspect ratios with the raytracing code of Macke et al. (1996), which is referred to as GO raytracing code.Figure 3.44 shows the comparison of the phase functions calculated with CrystalTrace (green) and the GO raytracing code (blue) for a hexagonal ice crystal with aspect

ratios 0.7 (a) and 0.07 (a) at a wavelength of 550 nm. The corresponding phase function of the YANG database (black) is shown as a reference. The results compare well apart from the forward scattering region where CrystalTrace shows smaller values than GO and YANG. This is due to diffraction which is not accounted for by CrystalTrace. Due the coarser scattering angle resolution in the case of the GO phase functions the peaks of the 22° and 46° halos are not as pronounced as for CrystalTrace.

To perform simulations of realistic ice clouds with multiple scattering in combination with molecules and aerosol particles, CrystalTrace is implemented in libRadtran's MYSTIC solver. MYSTIC solves the radiative transfer equation by using the Monte Carlo method to trace single photons through the atmosphere as described in Section 3.1.1. This is a perfectly suited framework for implementing CrystalTrace. When a scattering process takes place at an ice crystal, the photon is traced through the ice crystal and the new direction is directly calculated by CrystalTrace instead of using the stored scattering phase functions. Furthermore, no delta-scaling is needed since photons refracted by two parallel crystal faces escape the crystal and are traced further through the atmosphere, i.e. are treated as unscattered. To account for the varying projected ice crystal area for different orientations in the CrystalTrace extension implemented in MYSTIC, the photons can be assigned with a weight. The simulations shown in this study were performed with a version of MYSTIC and CrystalTrace, which does not yet account for this effect. However, the simulations with MYSTIC and CrystalTrace are only used for qualitative analyses throughout this study. Furthermore, the ice crystal aspect ratios used here are 2.5 for solid columns and 0.5 for plates, which are compact enough that this effect is almost negligible. Figure 3.45 shows the radiance distribution simulated with MYSTIC and CrystalTrace for a cirrus of optical thickness 0.8 in an aerosol-free atmosphere with non-reflective surface. A solar zenith angle of 60° and an azimuth angle of 270° was chosen. The ice cloud consists of 40% oriented ice crystal plates with their c-axis oriented vertically, 40% hexagonal columns which their c-axis oriented horizontally, and 20% randomly oriented hexagonal columns. The oriented plates are responsible for the sundogs visible on each side of the sun, whereas the oriented hexagonal columns produce the upper and lower tangent arcs visible above and below the sun in Fig. 3.45. The 22° halo forms due to the presence of randomly oriented hexagons. The oriented crystals have a standard deviation of $\sigma_{\beta,\mathrm{Euler}} = 1°$. For this simulation 1×10^7 photons were used. For the implementation of CrystalTrace, MYSTIC has to be used in the "forward mode" (cf. Section 3.1.1 and Fig. 3.2a), which has a similar computational time as the backward mode if both hemispheres are simulated. The runtime for 1×10^5 photons amounts to about 12 s for a setup as in Fig. 3.45 using an Intel Xeon E5-2650 processor with 2 GHz clock frequency.

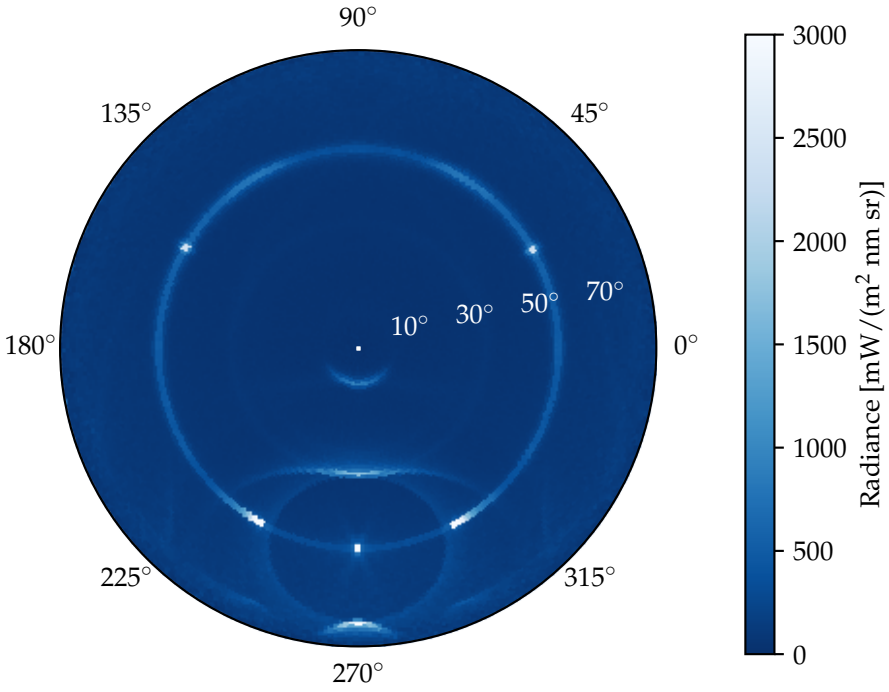

Abbildung 3.45: *Raytracing simulation with MYSTIC and CrystalTrace showing the radiance distribution in a polar projection for the upper hemisphere using* 1×10^7 *photons. The zenith angle* θ *ranges from* $0°$ *to* $90°$ *at the horizon, whereas the azimuth angle* ϕ *ranges from* $0°$ *to* $360°$*. The sun is located at a SZA of* $60°$ *at an azimuth angle of* $\phi_0 = 270°$*. The simulation was performed for a wavelength of* 550 nm *and an ice cloud of optical thickness 0.8. The cirrus cloud contains 40% oriented ice crystal columns (c-axis horizontal), 40% oriented ice crystal plates (c-axis vertical), and 20% randomly oriented ice crystal columns. For both oriented crystal populations an orientation parameter of* $\sigma_{\beta,\mathrm{Euler}} = 1°$ *was chosen.*

Kapitel 4

Results

Sections 4.1 and 4.2.1 contain parts of the publication by Forster et al. (2017):
Forster, L., M. Seefeldner, M. Wiegner, and B. Mayer, 2017: Ice crystal characterization in cirrus clouds: a sun-tracking camera system and automated detection algorithm for halo displays. *Atmospheric Measurement Techniques*, **10 (7)**, 2499–2516, 10.5194/amt-10-2499-2017, `https://www.atmos-meas-tech.net/10/2499/2017`.

4.1 Information content of the 22° halo in a real atmosphere

In Section 3.3 the information content of the 22° and 46° halo regarding ice crystal aspect ratio, surface roughness, and size was investigated based on single scattering properties. This section discusses the influence of multiple scattering on the visibility and brightness contrast of halo displays exemplary for the frequently observed 22° halo.

4.1.1 The halo ratio of the 22° halo

The effect of varying cloud optical thickness on the visibility of halo displays was already investigated by Hess (1996), Kokhanovsky (2008), Gedzelman and Vollmer (2008), Gedzelman (2008) using radiative transfer simulations. Kokhanovsky (2008) performed simulations of the brightness contrast of the 22° halo as a function of the cirrus optical thickness using the radiative transfer model SCIATRAN neglecting molecular and aerosol scattering. The results show a linear decrease of the halo contrast with increasing optical thickness. Gedzelman (2008) and Gedzelman and Vollmer (2008) used the model HALOSKY for radiative transfer simulations of halos with varying cloud optical thickness. HALOSKY considers single scattering by air molecules, aerosol particles and cloud particles assuming homogeneous, plane-parallel atmospheric layers. Multiple scattering is calculated only within the cloud by a Monte Carlo subroutine. Gedzelman and Vollmer (2008) show results for radiance simulations of the 22° halo in the principal plane below and above the sun. They found that the radiance at the bottom of the halo reaches a maximum value for a smaller COT (≈ 0.25) than the radiance at the top of the cloud (≈ 0.63). Hess (1996) found that the a 22° halo is visible if the COT is larger than the Rayleigh optical thickness and AOT together and depends on the SZA.

In this study, radiative transfer simulations were performed using the libRadtran radiative transfer package and the DISORT solver, which were explained in Section 3.1. Radiative transfer simulations of a cirrus cloud were performed assuming a homogeneous ice cloud layer with optical

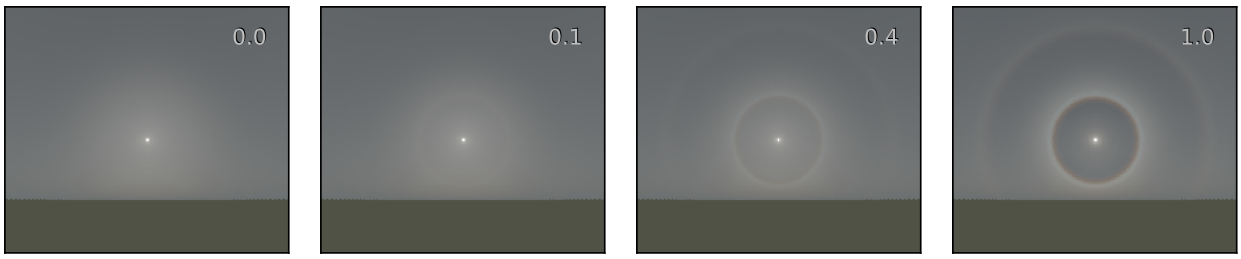

Abbildung 4.1: *Sky radiance simulations with libRadtran (Mayer and Kylling, 2005) using the DISORT solver for a solar zenith angle of 60°, a viewing azimuth angle range of 0° – 160° and for viewing zenith angles from 10° – 110° (i.e. from the zenith to 20° below the horizon). The simulations were performed for a spectral range of 380 – 780 nm (5 nm steps), weighted with the spectral sensitivity of the human eye. A homogeneous cirrus cloud layer with optical thickness of 1 was assumed. Solid column ice crystal optical properties of Yang et al. (2013) with an effective radius of* 80 µm *were used. Aerosol scattering was not considered. The four panels show radiative transfer simulations with different fractions of smooth solid columns ranging from 0% to 100%, as indicated by the labels. A background of severely roughened solid columns is assumed with fractions changing from 100% to 0%, accordingly.*

thickness 1 (at 550 nm) at a height between 10 – 11 km. Figure 4.1 shows simulations using different fractions of smooth solid columns (0%, 10%, 40%, 100%) and assuming a background of severely roughened solid columns. All ice crystals have an effective radius of 80 µm. The optical properties were chosen from the database by Yang et al. (2013). The sun is located at a zenith angle of 60°. Sky radiance was calculated for an angular range between 0° – 160° in the azimuth direction and 10° – 110° (i.e. from 10° off-zenith to 20° below the horizon) in the zenith direction, which corresponds to the view of a wide-angle camera. The simulations were performed for a spectral range of 380 – 780 nm (5 nm steps) and the results were weighted with the spectral sensitivity of the human eye according to CIE 1986, as implemented in specrend (http://www.fourmilab.ch/documents/specrend/).

Aerosol scattering was not considered and a spectral surface albedo of grass was chosen (Feister and Grewe, 1995). For 0% (first panel of Fig. 4.1) all ice crystals are rough and thus no 22° or 46° halo is visible. For a fraction of 10% smooth crystals the 22° halo starts to form which is in agreement with the findings of van Diedenhoven (2014). The 46° halo becomes visible for a fraction of 40% smooth crystals. For 100% smooth crystals both 22° and 46° halo reach a maximum brightness contrast for the respective cirrus optical thickness.

Figure 4.2 depicts the sensitivity of the halo brightness contrast, represented by the halo ratio as a function of the smooth ice crystal fraction (a), the aerosol optical thickness (b), the cirrus optical thickness (c) and the surface albedo (d) for a wavelength of 550 nm. As in Fig. 4.1 a SZA of 60° was chosen and the ice cloud was defined between 10 – 11 km. The halo ratio was determined in the principal plane above the sun. The dashed lines indicate a halo ratio of 1, which was defined as threshold for the visibility of halo displays. Figure 4.2a shows clearly that for SCF >10% the halo ratio exceeds 1 and the 22° halo is visible. An increasing aerosol optical thickness causes a decrease of the HR, which is displayed in Fig. 4.2b. For a typical value of AOT= 0.2 the HR is reduced by ∼10% compared to an aerosol free atmosphere. Figure 4.2c illustrates how the HR is determined by the optical thickness of the cirrus cloud (COT) itself. A maximum value for COT∼1 can be observed. For a very thin cirrus Rayleigh and aerosol scattering become dominant resulting in a small HR. Only when COT is larger than the optical thickness of the background (here Rayleigh and aerosol), the HR approaches its maximum

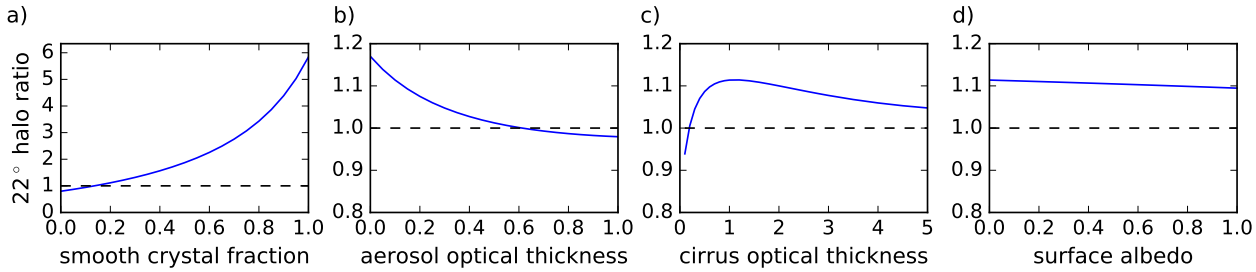

Abbildung 4.2: *Sensitivity studies of the 22° halo ratio at 550 nm (as defined in Eq. (3.45)) as a function of SCF, aerosol optical thickness (AOT), cirrus optical thickness (COT), and surface albedo (from left to right). The radiative transfer simulations were performed with libRadtran assuming an ice cloud between 10 – 11 km using ice crystal optical properties as in Fig. 4.1 for a solar zenith angle of 60°. The dashed line indicates* HR = 1*, which marks the threshold for the visibility of a halo display. The default parameters, i.e. if not varied, are 20% smooth solid columns,* AOT = 0.2*,* COT = 1.0*, and* albedo = 0.0*.*

value. For large COT, multiple scattering reduces the contrast of the halo feature and the HR decreases, similar to the findings of Kokhanovsky (2008). However, as Gedzelman and Vollmer (2008) point out, the halo peak might still be visible up to an optical thickness of ~ 5 due to the pronounced maximum in the scattering phase function.
A higher surface albedo causes longer photon paths through the atmosphere and thus a higher chance of multiple scattering (Fig. 4.2d). Reflected photons therefore cause a higher "background" brightness. It is evident that a brighter background causes a weaker brightness contrast of the halo display. In general, the effect of the surface albedo on the HR is small compared with the effect of AOT or COT. Halo displays are a geometric optics phenomenon, which means that they emerge only when the particle size is much larger than the wavelength (Fraser, 1979, Mishchenko and Macke, 1999, Garrett et al., 2007, Flatau and Draine, 2014) which also depends on the aspect ratio of the crystals (Um and McFarquhar, 2015). The solar zenith angle (SZA) affects the halo brightness contrast indirectly by increasing the photon path length through the atmosphere for large SZAs and thus increasing the amount of multiple scattering (not shown). This effect is the same for different viewing zenith angles which explains the fact why the 22° halo is always brightest at the top (directly above the sun) and faintest below the sun.

4.1.2 The FWHM of the 22° halo

In Section 3.3.2 the power spillover index and the FWHM of the 22° halo were investigated as an estimate of the ice crystal size using scattering phase functions. It was demonstrated that the power spillover index well suited to estimate the ice crystal size based on scattering phase functions but it depends strongly on the COT in a real atmosphere. In this section the FWHM of the 22° halo will therefore be investigated as an estimate of the ice crystal size. To determine the FWHM of a 22° halo in the atmosphere a method was developed to correct the radiance distribution for multiple scattering and to fit a Gaussian distribution to the 22° halo peak. The method is visualized in Fig. 4.3. Figure 4.3a shows the radiance distribution of a 22° halo formed by solid columns with an effective radius of 20 µm and a SCF of 30%. The blue curve represents the fit of the background brightness distribution which is produced by multiple scattering. The fit function for the background is defined by

$$L_{\text{background}} = a\,\exp(b\,\Theta) + c\,\cos(\Theta) + d\,\Theta + e\,, \tag{4.1}$$

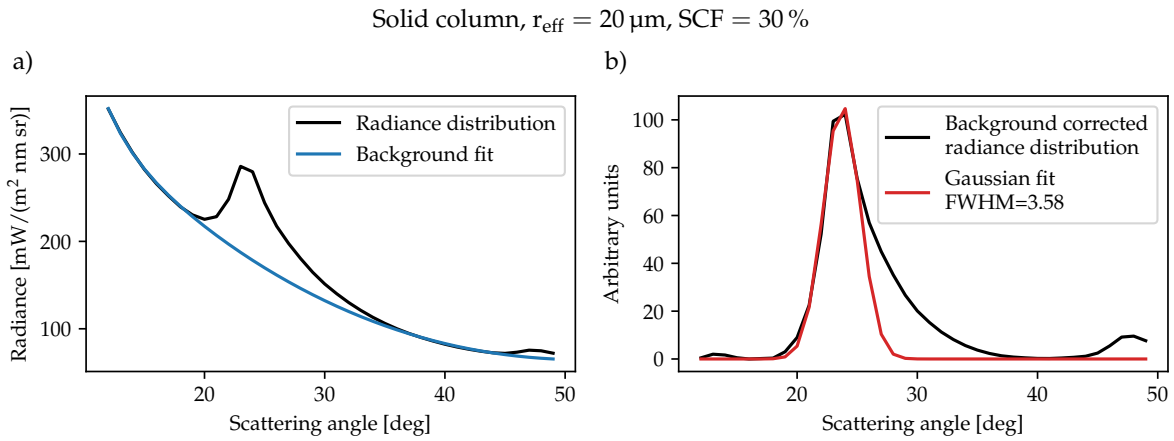

Abbildung 4.3: *Visualization of the method to estimate the FWHM of the 22° halo with multiple scattering. a) shows the original radiance distribution across the 22° halo (black) and the background fit (blue). b) displays the background-corrected radiance distribution (black) and the Gaussian fit (red). It is important to note that the background fit was performed for scattering angles $\Theta \leq 19°$ and $35° \leq \Theta \leq 45°$ and the Gaussian fit was performed for $20° \leq \Theta \leq 25°$. The original radiance distribution was simulated with libRadtran using the DISORT solver for solid ice crystal columns with $r_{eff} = 20\,\mu m$ and a SCF of 30% at a wavelength of 550 nm.*

with the scattering angle Θ and the 5 fit coefficients a, b, c, d, and e. For the background fit scattering angles $\Theta \leq 19°$ and $35° \leq \Theta \leq 45°$ were considered. In the next step the background $L_{\text{background}}$ was evaluated for all scattering angles and subtracted from the radiance distribution which results in the black curve in Fig. 4.3b. Finally, a Gaussian distribution was fitted to the background-corrected curve which is illustrated by the red curve in Fig. 4.3b. For the Gaussian distribution the following fit function was used

$$G = A \exp((\Theta - \mu)^2/(2\sigma^2)) \,, \tag{4.2}$$

with the amplitude A, the expectation value μ, and the standard deviation σ as fit coefficients. For fitting the Gaussian distribution to the background-corrected radiance distribution scattering angles in the range $20° \leq \Theta \leq 25°$ were used. The FWHM of the 22° halo is then calculated by

$$\text{FWHM} = 2\sqrt{2\log 2} \cdot \sigma \,. \tag{4.3}$$

Figure 4.4a shows the FWHM of the 22° halo calculated for different ice crystal effective radii ranging from 5 µm to 90 µm and for a COT of 0.5 (black), 1.0 (gray), and 3.0 (light gray). In the atmosphere, variations of the COT changes the HR of the 22° halo which was shown in Section 4.1.1. The sensitivity of the FWHM to variations of the COT, however, is negligible as depicted in Fig. 4.4a. Figure 4.4b shows that ice crystal habit and SCF slightly changes the FWHM. This effect is still smaller than the sensitivity of the FWHM to the ice crystal effective radius. Figure 4.5 shows the FWHM of the 22° halo as a function of the ice crystal effective radius. The mean FWHM is indicated by the blue curve and the light blue shading represents the minimum and maximum FWHM at the respective radius, which accounts for the different ice crystal habits and all SCFs between 10% and 100%. All habits were considered except for droxtals which do not produce a 22° halo.

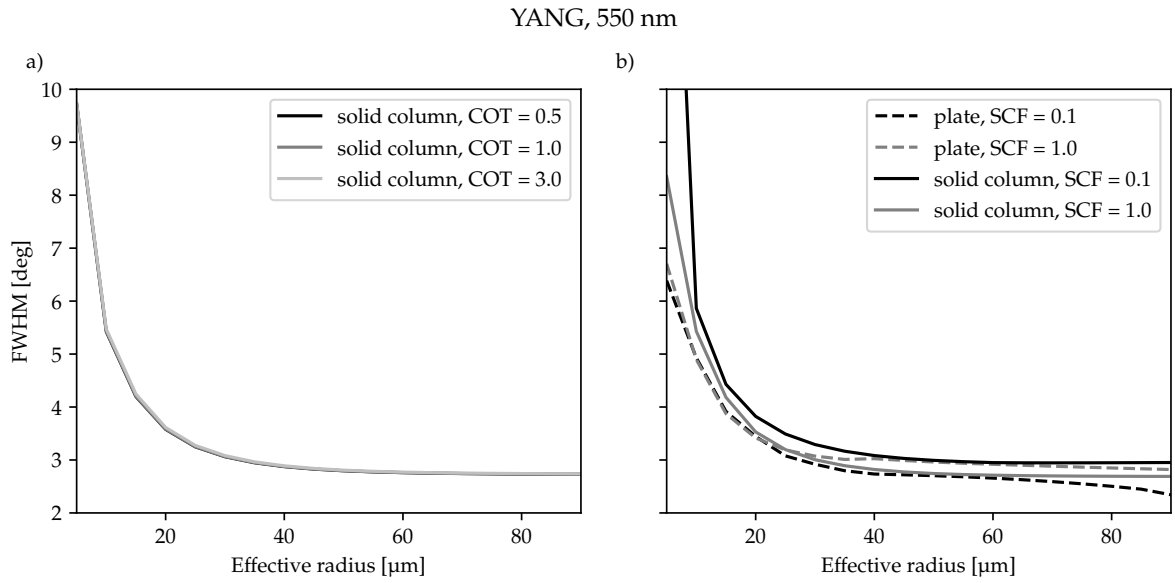

Abbildung 4.4: *Sensitivity tests of the 22° halo FWHM to a) COT and b) ice crystal habit and SCF. Panel a) demonstrates that the sensitivity of the FWHM to variations of the COT is negligible. Panel b) shows the FWHM for ice crystal plates (dashed) and solid columns (solid) for a SCF of 10% (black) and 100% (gray). This effect is not negligible but still smaller than the sensitivity to the ice crystal effective radius.*

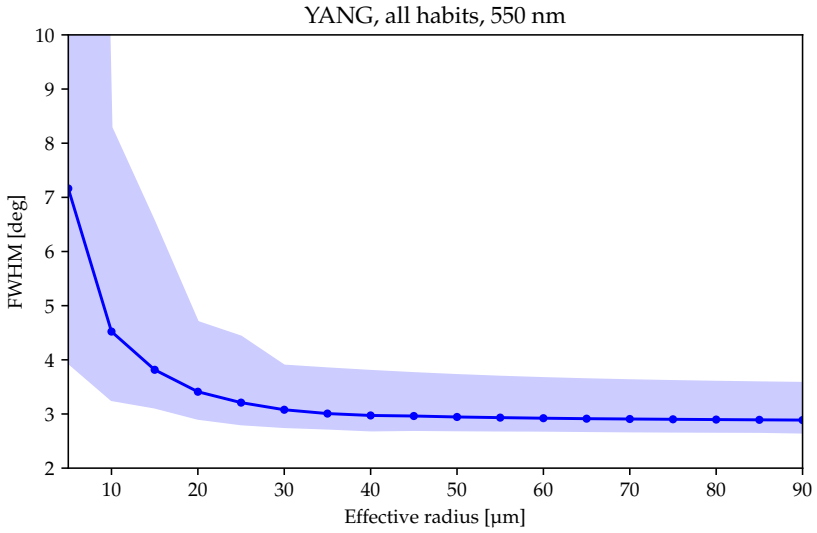

Abbildung 4.5: *FWHM of the 22° halo as a function of the ice crystal effective radius. The blue curve shows the mean FWHM and the light blue shading represents the minimum and maximum FWHM values for the respective ice crystal effective radius due to the different ice crystal habits and SCFs ranging between 10% and 100%.*

4.2 Halo display statistics

HaloCam has been operated in Munich (Germany) since Sept 2013 where it provides continuous measurements including contributions to the ML-CIRRUS campaign in March and April 2014 (Voigt et al., 2016). Only during the ACCEPT campaign (Analysis of the Composition of Clouds with Extended Polarization Techniques, Myagkov et al. (2016)) in October and November 2014 it was installed in Cabauw (The Netherlands). In the following sections the HaloCam datasets collected during the ACCEPT campaign and in Munich will be evaluated regarding the frequency of halo displays and halo-producing cirrus clouds.

4.2.1 Halo display statistics during ACCEPT

A first visual evaluation of the halo display frequency during the ACCEPT campaign (10 October until 14 November 2014) was performed. The results are displayed in Fig. 4.6 as Venn-diagram (Venn, 1880). The occurrence of each different halo type is visualized by a circle. The radius of each circle scales with the total observation time for the respective halo type. Cross sections between the circles indicate instances where two or three halo displays were visible at the same time. The observation time is given in hours. The total time of HaloCam observations, which were collected during daytime only, amounts to about 344 h. With about 30 h, halo displays were observed in almost 9% of the time. The presence of cirrus clouds within the HaloCam field of view was evaluated visually and amounts to about 110 h. Thus, about 27% of the cirrus clouds produced a visible halo display. The 22° halo (complete or partial) occurred in 16.2%, the sundogs in 19% and the upper tangent arcs in 7.8% of the time when cirrus clouds were present. Circumscribed halos were not observed during the campaign due to the low solar elevations. As

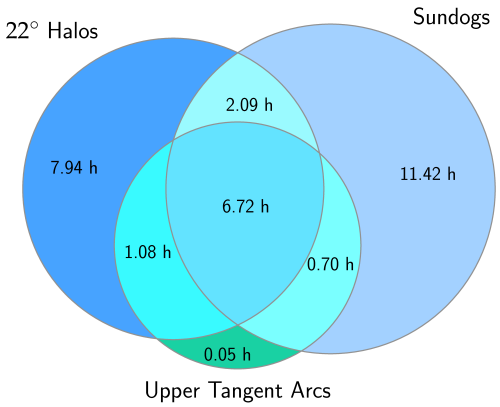

Abbildung 4.6: *Halo display statistics from HaloCam observations during the ACCEPT campaign 10 Oct – 14 Nov 2014. The observation times of 22° halo, sundogs and upper tangent arc are provided in hours and are represented by the radii of the three circles. Cross sections of circles indicate time periods when two or three halo displays were visible simultaneously. The total observation time amounts to* 344 h.

illustrated in Fig. 4.6, sundogs were observed more often than 22° halos with about 21 h vs. 18 h. Thus, sundogs occurred in 70% and 22° halos in 60% of the total halo observation time (30 h). Upper tangent arcs occurred in total for about 9 h (30%) and were accompanied most of the time by 22° halos and sundogs. Thus, the majority of the halo displays were produced by oriented ice crystals.
Compared to the findings of Sassen et al. (2003b) the relative fraction of 22° halos is roughly

similar with 50%, but sundogs with 12% and upper/lower tangent arcs with about 15% were far less frequent than observed during ACCEPT. The AKM observed the left and right sundogs with a relative frequency of 18% each, compared to 36% for the 22° halos. Although the frequency of simultaneous occurrence of the left and right sundog is unknown (from the AKM database), one can deduce that the relative frequency of sundogs is at least 18% and thus larger than the result of Sassen et al. (2003b). The reasons for the differences in the observed halo frequencies could be manifold: one main reason might be that a statistical evaluation over six weeks is compared to a database of 10 (Sassen et al., 2003b) and 30 years (AKM). It is possible that the observation time during ACCEPT was not long enough to yield representative results for the frequency of the different halo displays. Another factor could be the observation site. The mountains in the East of Salt Lake City, the observation site of Sassen et al. (2003b), could obscure the sun during periods with low solar elevation which are favorable for the formation of sundogs. So it is possible that on average fewer sundogs could have been observed in Salt Lake City than in Cabauw which is surrounded by a rather flat landscape. Also differences in the dominating weather patterns forming cirrus clouds in Salt Lake City and Cabauw could have an impact on halo formation as discussed in Sassen et al. (2003b). For the AKM and the HaloCam dataset, information about dominating weather patterns for different halo displays is not available. Furthermore, the observation period during the ACCEPT campaign from October until mid-November was dominated by low solar elevations which implies a higher chance for observing sundogs. Long-term observations have to be evaluated to obtain representative results of the frequency of the different halo types.

4.2.2 Long-term halo statistics in Munich

In Munich HaloCam has collected a dataset of more than 2 years between January 2014 and June 2016. This long-term dataset was evaluated automatically with the halo detection algorithm HaloForest (cf. Section 3.6.2). HaloForest is based on a random forest classifier and a separate classifier is trained for each of the 6 image segments shown in Fig. 3.20b. To ensure a high classification accuracy, only the classifiers for the upper image segments (3, 4, and 5) were used (cf. Table 3.4). A HaloCam image was assigned to the class "22° halo" if at least one of the image segments 3, 4, or 5 predicts a 22° halo. Applying a probability threshold of $p > 0.5$, 22° halos were detected in 152 h. Relative to the total observation time during daylight of 7345 h, 22° halos occurred in about 2.1% of the time.

As an additional test, the classification accuracy of HaloForest was checked for 470 randomly chosen HaloCam images for the "22° halo" and "no 22° halo" class within this long-term observation period in Munich. The confusion matrix for this test is provided in Table 4.1 for the image segments no. 3, 4, and 5 together. More than 88% of the 22° halos are classified correctly and less than 12% are classified incorrectly as 22° halos. Images were incorrectly classified as 22° halo predominantly due to small bright clouds or contrails in a blue sky, or structures in overcast conditions which happen to cause a peak in the averaged brightness distribution at a scattering angle of 22°.

Based on these results the fraction of cirrus clouds which produced a halo during this time period was investigated. The total frequency of occurrence of cirrus clouds was determined by independent data of co-located CHM15kx ceilometer observations (Wiegner and Geiß, 2012). To guarantee consistent observational conditions, only ceilometer measurements in the absence of low-level clouds were considered. Proprietary software of the ceilometer automatically provides up to three cloud base heights with a temporal resolution of 15 s. The detection is based on the

Tabelle 4.1: *Confusion matrix as in Table 3.4 for 470 randomly selected HaloCam images between Jan 2014 – Jun 2016, evaluated for segments 3, 4, and 5.*

		Predicted	
		22° halo	no 22° halo
True	22° halo	**88.8 %**	2.8 %
	no 22° halo	11.2 %	**97.2 %**

fact that in case of clouds backscatter signals are significantly larger than the background noise. The sensitivity of the ceilometer is sufficient to even detect clouds near the tropopause during daytime. Since ceilometers, however, do not provide depolarization information, the discrimination between water and ice clouds was made by means of the cloud base temperature T_{base}. Sassen and Campbell (2001) state that cirrus cloud base temperatures ranged between −30 °C and −40 °C during the 10-year observation period at the FARS observation site. As a temperature threshold is not an unambiguous criterion for the existence of ice clouds, the frequency of occurrence for three different temperatures was calculated: −20 °C, −30 °C, and −40 °C. If T_{base} is lower than the given temperature threshold, the cloud is considered a "cirrus cloud". The temperature profiles were obtained from routine radiosonde ascents of the German Weather Service at Oberschleißheim (WMO station code 10868), which is located about 13 km north of the HaloCam site. During the time period from January 2014 until June 2016 a fraction of 5.6% cirrus clouds was detected for a cloud base temperature of $T_{base} < -20$ °C. Towards lower cloud base temperatures the amount of detected cirrus clouds decreases to 3.5% for $T_{base} < -30$ °C and 1.9% for $T_{base} < -40$ °C.

Due to the different pointing directions of the ceilometer (towards zenith) and HaloCam (towards sun) the instruments observe different regions of the sky. This is accounted for by prescreening the data for 1-h time intervals when the ceilometer detected a cirrus cloud, subject to data availability for both instruments. The subsequent analysis of cirrus fraction and halo frequency of occurrence is based on the full temporal resolution of 15 s and 10 s, respectively. Relative to the amount of detected cirrus clouds about 25% occurred together with a 22° halo for the image segments 3, 4, and 5. This fraction does not change much for the different cloud base temperatures (26.4% for $T_{base} < -20$ °C and 24.5% for $T_{base} < -40$ °C) since the fraction of detected clouds decreases together with the detected halos for lower temperatures. According to the confusion matrix in Table 4.1, 88.8% of the detected "22° halos" are real halos, while 2.8% of the "no 22° halos" are actually "22° halos". Correcting the result for the estimated false classifications, the fraction of "halo-producing" cirrus clouds amounts to about $25\% \cdot 88.8\% + 75\% \cdot 2.8\% \approx 24\%$. The comparison of the ceilometer and HaloCam data implies that about 25% of the cirrus clouds contain some fraction of smooth, hexagonal ice crystals. Sassen et al. (2003b) observed a fraction of 37.3% cirrus clouds which produced a 22° halo within 1-hour time intervals. The results most likely differ because the observations originate from different locations which might be dominated by different mechanisms for cirrus formation. It has to be noted however, that the evaluation method is very sensitive to the sampling strategy of the observations: the fraction of "halo-producing" cirrus clouds increases to more than 50%, if the HaloCam observations are binned to 1-hour intervals, which are counted as containing a halo regardless of their duration.

For comparison, the fraction of cirrus clouds producing a halo display was evaluated visually for the HaloCam observations during the ACCEPT campaign and amounts to about 27% in-

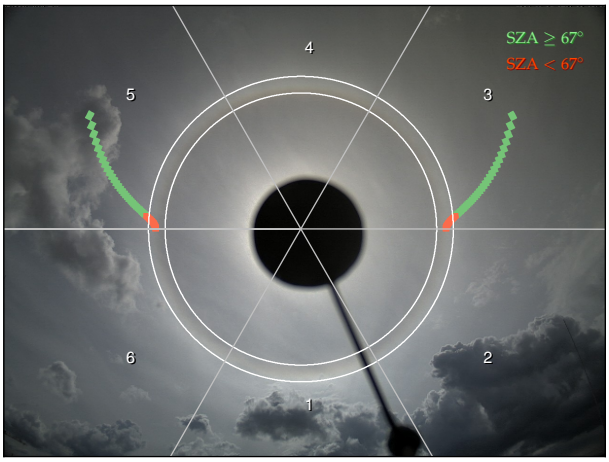

Abbildung 4.7: *HaloCam image as in Fig. 3.20b. The red and green squares indicate the minimum scattering angle of the sundogs as a function of the solar zenith angle (SZA). The SZA ranges between 90° and 35° with 1° resolution. The mask used to search for the 22° halo peak is displayed by the two white circles and covers scattering angles between 21.0° and 23.5°. Sundog positions located within this mask might be mis-classified as 22° halo and are marked as red. These positions correspond with SZAs between 90° and 67°. For smaller SZAs (higher solar elevations) the sundogs are located outside the mask and cannot be mis-classified as 22° halo by the algorithm.*

cluding 22° halos, sundogs and upper/lower tangent arcs (cf. Section 4.2.1). This value is also lower than the result provided by Sassen et al. (2003b) who observed any of the three halo types in about 54% of the 1-hour periods with cirrus.

The current version of HaloForest discriminates only between the two classes "22° halo" and "no 22° halo". Thus, interference with other halo types as sundogs or upper/lower tangent arcs and circumscribed halos might occur at certain solar elevations. The position of sundogs relative to the sun depends on the solar zenith angle (SZA) and can be calculated analytically as described in Wegener (1925), Tricker (1970), Minnaert (1993), Liou and Yang (2016). The sundogs are located at scattering angles close to the 22° halo for large SZAs and occur at larger scattering angles for small SZAs, i.e. high solar elevations. Figure 4.7 shows the same HaloCam image with the azimuth segments as Fig. 3.20b. In addition, the minimum scattering angle of the sundogs are calculated as a function of the SZA and represented by the red and green squares. The SZAs range between 90° and 35° with a resolution of 1°. The two white circles centered around the sun at scattering angles of 21.0° and 23.5° indicate the mask which is used to find the scattering angle of the 22° halo peak. For SZA $\leq$ 67° the sundog positions are located outside this mask and cannot be mis-classified as 22° halo (green squares). The red squares represent sundog positions which are located within this mask and might therefore be mis-classified. This is the case for SZAs between 90° and 67°. To obtain an estimate of the fraction of sundogs which are mis-classified as 22° halo 1000 randomly selected HaloCam images were counter-checked visually. It revealed that only 6 images showing sundogs without 22° halo in the segments (3–5) were mis-classified as 22° halo, which is $<$ 1%. Upper tangent arcs could be detected by the uppermost image segment (no. 4) and might be mis-classified as 22° halo. For very small SZAs (high solar elevations) the tangent arcs merge to form the circumscribed halo which could be detected in the segments 3 and 5 as well. The same procedure was repeated for these halo types: 1000 randomly selected images were checked for the presence of tangent arcs and circumscribed halos without 22° halo yielding 28 images or 2.8%. However, if only a fragment of a halo is visible

in the uppermost segment, it is generally difficult to discriminate between an upper tangent arc or circumscribed halo and a 22° halo.

The halo classification algorithm was presented for 22° halos, but it is possible to include training data for other halo types as well. With the current version of HaloForest and the co-located ceilometer observations the fraction of cirrus clouds producing a halo display was estimated to about 25% for Munich between Jan 2014 and Sept 2016. Extending HaloForest for the detection of other halo types, as sundogs for example, the fraction of "halo-producing" cirrus clouds could easily exceed 25%. In principle, HaloCam could also be equipped with a wide-angle lens to observe halo displays in a larger region of the sky, however at the expense of the spatial resolution.

With the knowledge of Section 4.1 further implications of the fraction of "halo-producing" cirrus clouds can be discussed in more detail. HaloCam observations showed that ∼25% of the cirrus clouds, which were visible from the ground, produced a 22° halo. It can be argued that these cirrus clouds contained a certain amount of smooth, hexagonal ice crystals. By analyzing ice crystal single scattering properties van Diedenhoven (2014) showed that a minimum fraction of 10% smooth hexagonal ice crystal columns is sufficient to produce a 22° halo. In case of ice crystal plates the minimum fraction of smooth crystals for a visible halo is much larger with about 40%. Thus, if the exact ice crystal habits of the cirrus cloud are unknown, which is typically the case, the minimum amount of smooth ice crystals probably lies in a range of 10% to 40%. This implies that even for a large fraction of irregular or small ice crystals a halo might still be visible. A larger fraction of smooth ice crystals, however, could well be possible for halos with larger HR, i.e. increased brightness contrast. Multiple scattering of the cirrus cloud or atmosphere was not considered by van Diedenhoven (2014). This study revealed that during the ∼2.5 years of HaloCam observations in Munich about 75% of the cirrus clouds did not produce a 22° halo. For favorable atmospheric conditions, i.e. COT∼1 and negligible aerosol scattering, the maximum fraction of rough ice crystals ranges between 60% and 90%. Thus, it is possible that the majority of cirrus clouds during the observation period in Munich contain a large fraction of rough ice crystals. This would support the hypothesis of e.g. Knap et al. (2005), Baran and Labonnote (2006), Baran et al. (2015) who found that on average rough ice crystals better reproduce remote sensing radiance measurements than assuming crystals with smooth surface. However, if multiple scattering by cirrus clouds or aerosol is accounted for, the minimum fraction of smooth crystals could be much larger in the case of halo-producing cirrus clouds. A more detailed analysis of the actual fraction of smooth ice crystals in halo-producing cirrus clouds will be presented in the following sections. For this analysis the halo observations need to be complemented by radiative transfer simulations and additional measurements of aerosol and cirrus optical thickness and surface albedo.

4.3 Retrieval of ice crystal properties

To retrieve more detailed information about the ice crystal properties in halo-producing cirrus clouds, the RICO retrieval (cf. Section 3.7) was applied to calibrated radiance observations from specMACS and $\text{HaloCam}_{\text{RAW}}$. Both the relative and absolute radiometric calibration of specMACS could be performed in the laboratory and the absolute radiometric uncertainty was estimated to about 5% (Ewald et al., 2015). The absolute radiometric calibration of $\text{HaloCam}_{\text{RAW}}$ however had to be performed using specMACS as reference which yields a much higher un-

certainty of about 15%. Thus, to investigate the potential and the limitations of the RICO retrieval, it was first applied to two case studies with specMACS measurements on 24 March and 22 September 2015.

4.3.1 Case study of 24 March 2015

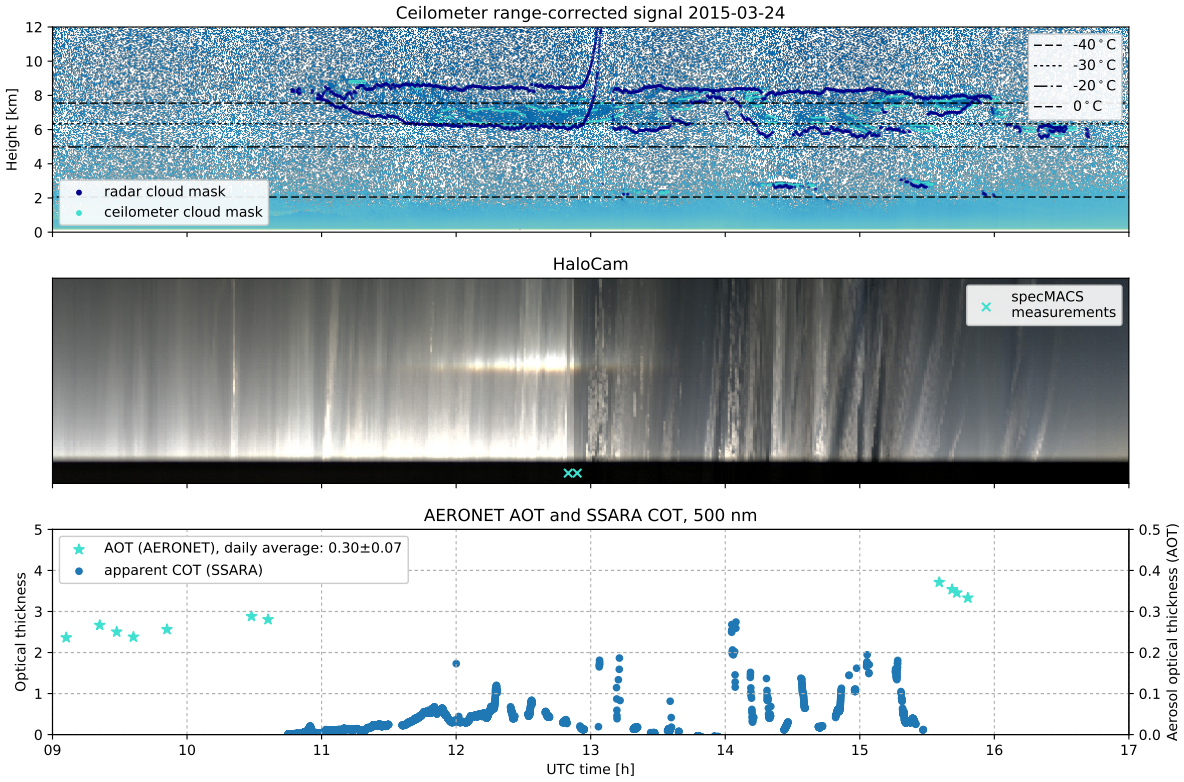

Abbildung 4.8: *Overview of observations on 24 March 2015. Top: ceilometer range-corrected signal with cloud base and top (turquoise dots) and cloud base and top from cloud radar reflectivity (dark blue dots). Temperature contour lines of 0 (dashed), -20 (dash-dotted), -30 (dotted), and −40 °C (dashed) interpolated from radiosonde data. Center: time line of* $HaloCam_{JPG}$ *pixel slices above the sun. The black region at the bottom is the sun shade. The upper part of the 22° halo or upper tangent arc is visible as a bright line in the center of the panel. The times of the specMACS measurements are indicated by the turquoise crosses around noontime. Bottom: AERONET AOT (turquoise stars) and apparent COT derived from SSARA direct-sun measurements (blue) at a wavelength of* 500 nm.

On 24 March 2015 cirrus clouds formed in an airmass between a ridge and a trough at the 500 hPa pressure level. Cirrus clouds were present between 11:00 UTC until 15:30 UTC with clearsky conditions in the morning and afternoon.

Figure 4.8 shows an overview of the co-located ceilometer, HaloCam and sunphotometer observations. When comparing the data it should be kept in mind that both the radar and the ceilometer are pointing to the zenith whereas HaloCam and the sunphotometer are following the sun, so the observed regions of the sky are not the same. The presence of a complete 22° halo requires relatively homogeneous cloud cover which allows a comparison between the data with a time shift. Assuming a westerly flow, which is typical for the observations site in Munich, the sun-tracking instruments, which are pointing to the East or South-East in the morning, detect the clouds later in their field of view than the zenith-pointing instruments. In the afternoon the sun-tracking instruments are pointing to the West and clouds approaching from this direction are

detected earlier than by the zenith-pointing radar and lidar. Simultaneous radar measurements with a MIRA-35 cloud radar (Görsdorf et al., 2015) and lidar measurements with a CHM15kx ceilometer (Wiegner and Geiß, 2012, Wiegner et al., 2014) provided information about the cirrus top and bottom height. Figure 4.8 (top) shows the range-corrected ceilometer signal and the detected cloud base and top height as turquoise dots. The ceilometer detected the cloud base height at 6.5 km and cloud top height at 7.5 km between 12 – 13 UTC. Thus, the cloud base and top height derived from radar observations are used in addition and are displayed with purple dots. Cloud top and base height are derived from the equivalent radar reflectivity factor (Ze) of hydrometeors at the boundaries of the cloud. The estimated cloud base height of the radar observations (dark blue dots) is similar to the ceilometer. Large differences, however, are visible for the estimated cloud top height which is significantly larger for the radar data at about 9 km. This effect is due to attenuation of the ceilometer signal which is more sensitive to the particle number concentration. The radar signal is able to reach the cloud top and is more sensitive to the size of the particles. To obtain the best estimate of the cloud base and top height both observations are combined using largest height of both instruments for cloud top and the smallest height for cloud base.

The study focuses on cirrus clouds, which consist of ice crystals, and have a cloud base height at temperatures below freezing point. Thus, only height levels below 0 °C are indicated. The temperature profile is obtained from radiosonde ascents at Oberschleißheim. In addition, the temperature levels at −20 °C, −30 °C and −40 °C are indicated by dash-dot, dotted, and dashed lines, respectively. At cloud base (6.5 km) the temperature was between −24 °C and −28 °C, whereas at cloud top (10 km) the temperature amounts to about −50 °C.

The HaloCam data (Fig. 4.8 center) is visualized by a time series of pixel lines, which are extracted from each image (every 10 s) in the principal plane above the sun, i.e. extending from the center of the circular shade to the image top. The image slices were stacked together showing the upper part of a 22° halo, upper tangent arc or circumscribed halo as a line approximately at the middle of the figure. The change in the HaloCam image brightness shortly before 13 UTC was due to a restart of the camera system which was necessary due to an earlier power outage. The power outage caused a reset in the automatic exposure settings of the camera which is the reason for the overexposed pixels in the halo region between 12 – 13 UTC. The HaloCam observations show cirrus clouds from around 11 UTC until 15:30 UTC with clear-sky in the morning and afternoon. A 22° halo together with upper and lower tangent arc were visible from 11 UTC until around 14 UTC with faint sundogs between 13 and 14 UTC. The “halo-line” appears slightly reddish at the lower (inner) edge and sometimes even slightly blueish at the upper (outer) edge. Low-level water cloud started to form at around 13 UTC which obstructed the visibility of the halos at times. The 22° halo and the bright upper and lower tangent arcs indicate the presence of smooth hexagonal columns which were partly oriented. The sundogs are produced by smooth ice crystal plates which are oriented with their c-axis horizontally.

The sunphotometer observations in Fig. 4.8 (bottom) show the aerosol optical thickness (AOT) from AERONET version 2, level 2.0 (cloud screened) for 500 nm (turquoise stars). Clear-sky in the morning until 10:30 UTC and in the evening from about 15:30 UTC allowed to estimate the AOT. Since the structure of the aerosol in the boundary layer, which is visible in the backscatter signal of ceilometer in the lowest 2 km, does not change much in the course of the day, the AOT during the time of the specMACS measurements is estimated by the daily mean of 0.30 ± 0.07 within a 2σ confidence interval. The apparent cirrus optical thickness is derived from SSARA sunphotometer measurements explained in Section 3.7.3. During the time when the halo displays were observed a maximum apparent optical thickness of 1.5 was measured. The values

specMACS scan time	cloud top (base) height	cloud top (base) temperature	apparent COT	COT
12:50 UTC	9 km (6 km)	−50 °C (−30 °C)	0.1 to 0.4	0.6 to 1.6
12:54 UTC	9 km (6 km)	−50 °C (−30 °C)	0.1 to 0.4	0.5 to 1.4

Tabelle 4.2: *Cloud properties during the times of the specMACS scans on 24 March 2015.*

for the times of the specMACS measurements are compiled in Table 4.2 and are used to define the range of the LUT parameters for AOT and COT and to define the height and depth of the cirrus cloud layer for the radiative transfer simulations.

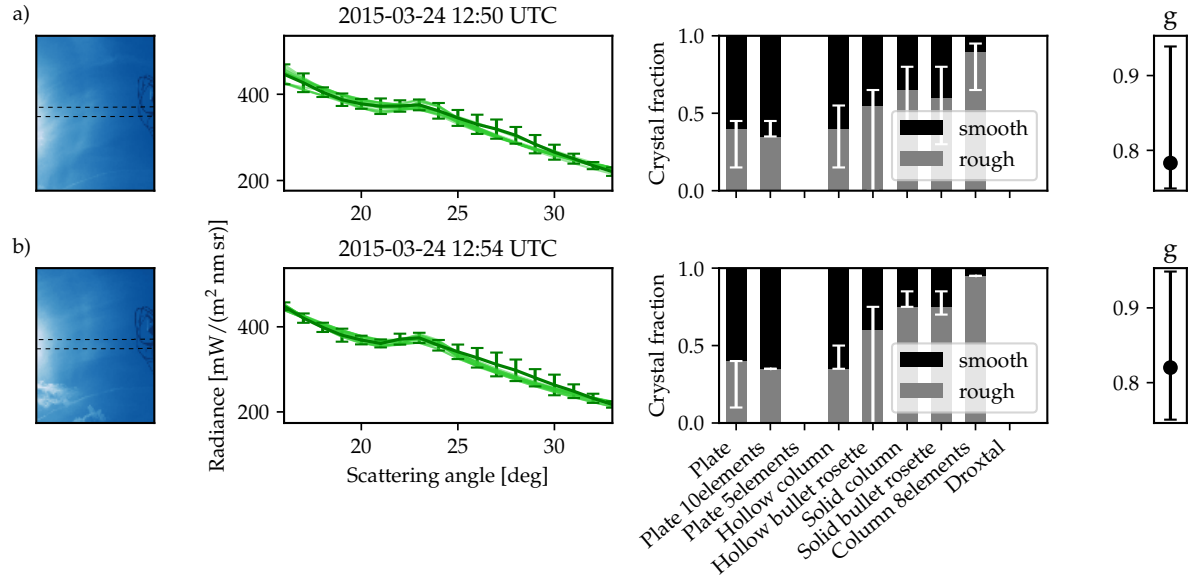

Abbildung 4.9: *Retrieval of specMACS observations on 24 March 2015 using the YANG optical properties. The first panel displays the specMACS scan across the right side of a 22° halo at a wavelength of 550 nm. The black dashed lines indicate the region which was used to extract the radiance distribution shown in the second panel (dark green) as a function of the scattering angle. The light green lines in the second panel represent matching LUT radiance distributions with the minimum and maximum SCF for each habit. The third panel shows the fraction of smooth (black) and rough (gray) crystals for all 9 habits. The white errorbars, which are centered around the SCF of the best-matching LUT element, indicate the spread of all possible solutions. The fourth panel shows the asymmetry factor (g) of the best-match (black dot) and the errorbars indicate the minimum and maximum value for all matching LUT elements of all 9 habits. a) shows the results for the specMACS scan at 12:50 UTC and b) for 12:54 UTC.*

Figure 4.9 shows specMACS measurements at 12:50, and 12:54 UTC as slices of the right hand side almucantar at a wavelength of 550 nm. The almucantar plane is used for the retrieval to avoid interference with the upper tangent arc which contains light scattered by oriented ice crystals. Sundogs were not observed. The data is displayed in green with errorbars representing the propagated measurement uncertainty, as explained in Section 3.4 within a 2σ confidence interval. The left side of the panel shows the part of the specMACS scan which was used to extract the almucantar measurements. The almucantar measurements are obtained by averaging the radiance within a mask of 2° width into bins with 0.1° resolution scattering angle bins to obtain an almucantar data slice.

LUTs were calculated for all measurement times separately and for all 9 ice crystal habits

of the YANG database. The cirrus cloud is assumed to consist of one habit with a mixture of smooth and severely roughened ice crystals with smooth crystal fractions varying between 0% and 100% with 5% resolution. Ice crystal effective radii range from 5 µm to 90 µm in 5 µm steps. The AOT values in the LUT ranged from 0.05 to 0.5 with increments of 0.05 whereas the COT values were varied between 0.05 and 6 with a resolution of 0.05 up to a COT of 2, a resolution of 0.1 up to 3, 0.2 up to 4 and 0.5 up to 6. For the aerosol optical properties the OPAC "continental average" mixture was chosen. The simulated radiance distributions in the LUT and the specMACS almucantar measurements are compared by calculating the RMSE between the curves. A match is found if the condition RMSE $\leq 2\sigma_{\mathrm{L,specMACS}}$ is fulfilled. The light green curves in the second column of Fig. 4.9 represent matching LUT elements, for reasons of visualization displayed only for the maximum and minimum retrieved smooth crystal fraction of each habit. The 3rd column of Fig. 4.9 shows a bar chart of the smooth (black) and rough (gray) ice crystal fraction for each habit corresponding to the best match, i.e. the minimum RMSE, between LUT and measurement. Error bars in white are centered at the best match crystal fraction and range between the retrieved minimum and maximum values for each habit. The 4th column of Fig. 4.9 shows the retrieved asymmetry factors as an error bar at the value corresponding to the best match and ranging between retrieved minimum and maximum value. The y-axis ranges between 0.747 and 0.951, which are the minimum and maximum value the asymmetry factor can take if all habits, smooth crystal fractions and effective radii are considered. In this first retrieval step no additional measurements are used to constrain the LUT parameters, so the results shown in Fig. 4.9 are only based on a comparison of measured and simulated radiances for AOTs, COTs, and effective radii which can take any value available in the LUT.
At 12:50 UTC (Fig. 4.9a) and 12:54 UTC (Fig. 4.9b) the specMACS measurements in the almucantar plane on the right side of the sun are evaluated. A faint 22° halo is visible which is caused by a thin cirrus cloud. The specMACS radiance distributions in the second column exhibit larger error bars in the scattering angle range from 25° to 30° which is due to spatial inhomogeneity of the cirrus. All habits, except for 5-element plates and droxtals, match the measurements with different smooth crystal fractions. However, it can be observed that for the column-like crystals a higher fraction of rough crystals than for the plate-like crystals match the observations. This can be explained with the different aspect ratio between columns and plates which causes a much brighter halo in the case of columns compared to plates. Therefore, a much higher fraction of smooth crystals is needed in the case of plate-like habits to produce the same halo brightness as for columns. The asymmetry factor of the best match amounts to about 0.78 (12:50 UTC) and 0.83 (12:54 UTC) but the 22° halo is not pronounced enough to constrain the asymmetry parameter without additional information.

The retrieval was repeated with additional constraint on the LUT using the daily mean AOT from AERONET and the apparent COT derived from the SSARA direct sun measurements. Both optical thicknesses were interpolated to 550 nm. The actual COT was derived from the apparent COT according to Eq. (3.49) by using the k-factors for the respective ice crystal habit. For each habit the k-factors were calculated for all different effective radii and SCFs available in the LUT. The minimum and maximum k-factors were used to estimate the lower and upper boundary of the true COT. Since plate-like crystals exhibit a very large variation of the k-factors due to their large asymmetry factors especially for large effective radii, the retrieval was performed iteratively: the retrieved effective radii from the first run are used to constrain the k-factors in the second run using the mean effective radius with a 2σ uncertainty. A time interval of ±5 min was chosen to account for the different direction of the direct sun measurements to derive the COT and the 22° halo. The LUT was constrained using the average over this

10 min time interval with the lower boundary being the minimum observed COT within this interval and the upper boundary determined by 2 standard deviations of the COT. The AOT in the LUT was constrained using simply the daily average within a 2σ confidence interval. Figure 4.10 shows the retrieval results for the same measurements and LUTs as in Fig. 4.9 but

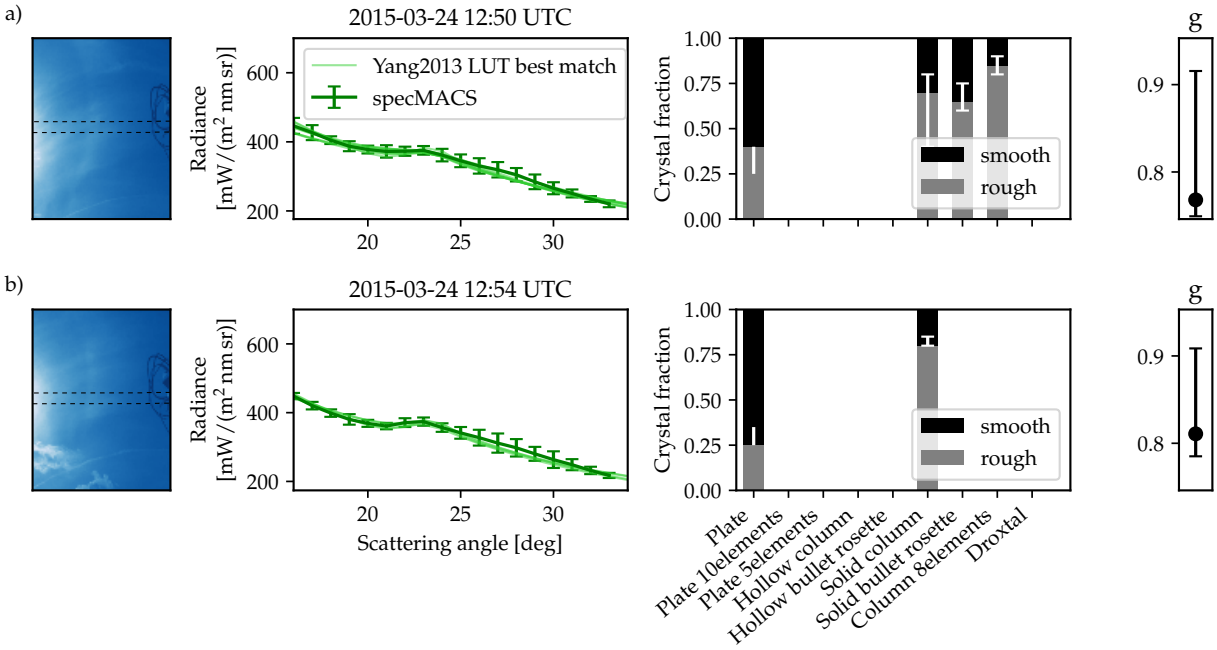

Abbildung 4.10: *As Fig. 4.9 but constraining AOT and COT from sunphotometer observations.*

with additional constraints on the possible AOT and COT values in the LUT. Now, only few ice crystal habits match the observations. At 12:50 UTC plates, solid columns, solid bullet rosettes, and 8-element columns match the observations, whereas at 12:54 UTC only plates and solid columns are retrieved. The best-match SCFs associated with the respective ice crystal habits are similar as in Fig. 4.9. Constraining the aerosol and cirrus optical thickness also helps to slightly constrain the asymmetry factor. Although the results confirm that plate-like crystals with larger SCF can produce an equally bright 22° halo as columnar crystals with smaller SCF, their asymmetry factors are quite different (cf. Fig. 3.12). Thus, as long as both plate-like and columnar crystals match the observations, the asymmetry factor can not be reliably constrained.

As a test, the retrieval was performed using random mixtures of all 9 ice crystal habits from the YANG database for the 12:54 UTC case. The best-match phase function consists of 50% smooth and 35% rough 10-element plates, 8% smooth droxtals, and 5% rough solid columns. The remaining habits sum up to 2%. The mean effective radius of the corresponding radiance distribution has an effective radius of about 70 µm and an asymmetry factor of 0.855 at a wavelength of 500 nm. However, several different mixtures of ice crystal habits match the observations. Clearly, allowing for arbitrary mixtures of multiple ice crystal habits, surface roughness, and size might yield a mixture which better represents the observations than using a single habit with smooth and rough crystal fraction. However, it should be kept in mind that the retrieved habit mixtures are "radiatively equivalent effective shapes", as stated by McFarlane and Marchand (2008) and Cole et al. (2013). Retrieving ice cloud properties from halo displays using ground-based remote sensing is a complex task which is not well constrained. Thus, allowing more freedom for arbitrary mixtures of ice crystal properties does not necessarily increase the information gain.

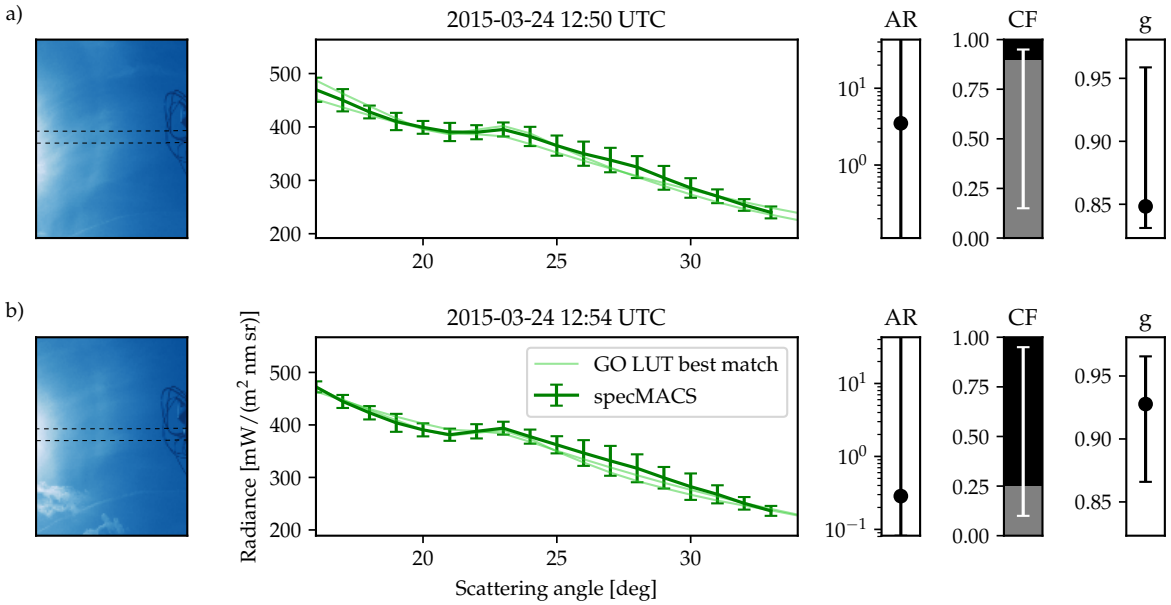

Abbildung 4.11: *Retrieval results for 24 March 2015 using GO optical properties. The first panel displays the specMACS scan across the right side of a 22° halo at a wavelength of* 550 nm. *The black dashed lines indicate the region which was used to extract the radiance distribution shown in the second panel (dark green) as a function of the scattering angle. The light green lines in the second panel represent matching LUT radiance distributions with the minimum and maximum SCF for each ice crystal AR. The results of all matching ARs, crystal fractions (CF) and asymmetry factors (g) are displayed as errorbars in the last three panels. Note the logarithmic y-scale of the AR panel. For the AR and asymmetry factor the best-match values are represented by a black dot. The best matching CF is displayed by a bar plot with black representing the smooth and gray the rough crystal fraction.*

Figure 4.11 presents the results of the retrieval applied to the same specMACS measurements as in Fig. 4.9 using the optical properties of the GO database for different ice crystal aspect ratios ranging from 0.02 (thin plate) over 1 (compact crystal) to 50 (long column). The LUT for this retrieval was generated assuming a mixture of smooth and rough crystals as for the YANG database. Here, roughness parameters of $\sigma = 0$ and $\sigma = 0.3$ were chosen for the smooth and rough crystals respectively. The results show that the LUT contains combinations of AR and SCF which yield a matching radiance distribution for all ARs. The best-match between specMACS measurements and simulations at 12:50 UTC was achieved for ice crystal columns with AR = 3.5, a SCF of 10% and an asymmetry factor (g) of 0.848. For the specMACS observations from 12:54 UTC the best match was found for ice crystal plates with AR = 0.3, a SCF of 75% and an asymmetry factor of 0.928. However, for both times combinations of AR and SCF exist which match the observations. Compared to the YANG ice crystal model, the GO model allows to vary the ice crystal AR independently from ice crystal size. This is an advantage for investigating 22° halos since the halo ratio, i.e. the brightness contrast, of the 22° halo is mainly determined by ice crystal aspect ratio and surface roughness (cf. Fig. 3.10). However, the conventional geometric optics method to calculate ice crystal optical properties has several shortcomings for smaller pristine ice crystals with random orientation which form the 22° halo (Bi Lei and Yang Ping, 2014, Yang et al., 2015).

Thus, for the following analysis the YANG optical properties will be used and each ice crystal habit will be treated separately.

4.3.2 Case study of 22 September 2015

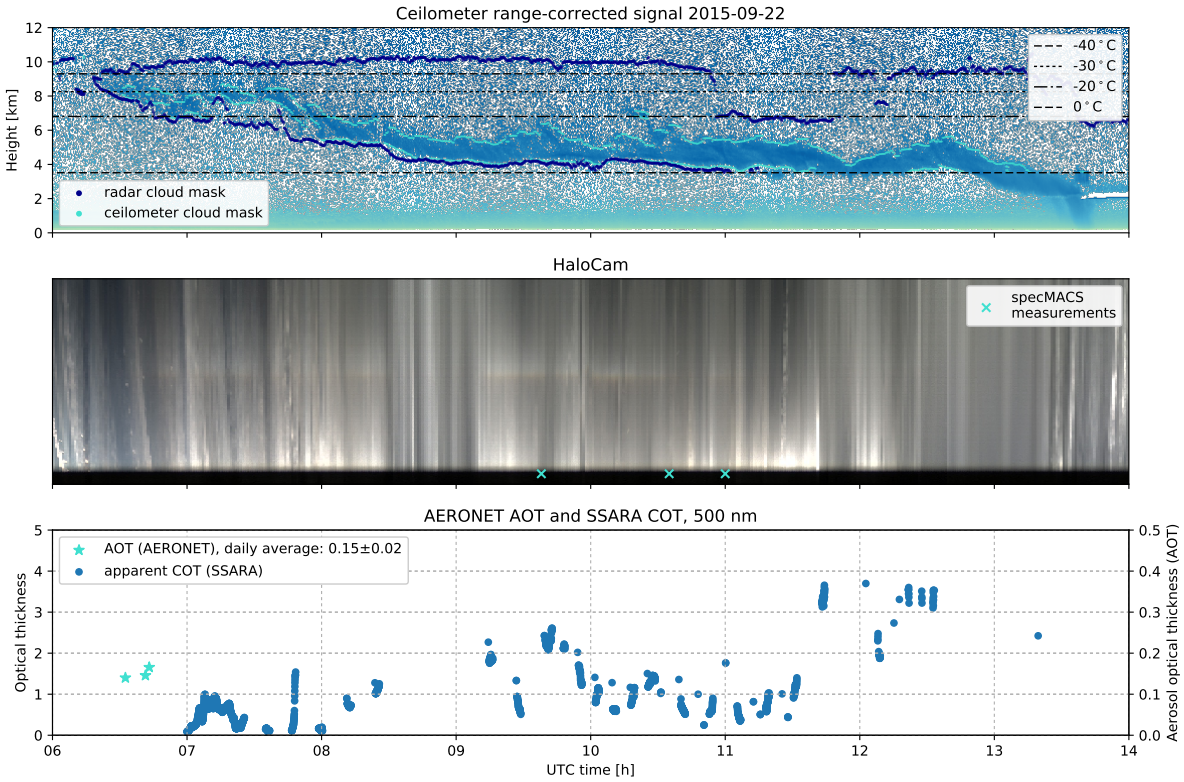

Abbildung 4.12: *Overview of observations on 22 September 2015. Displayed observations as in Fig. 4.8.*

On 22 September 2015 cirrus clouds formed on the leading edge of a warm front approaching from the West. After clearsky conditions in the early morning the first cirrus clouds formed around 7:00 UTC.

Figure 4.12 shows an overview of the ceilometer and radar observations (top), HaloCam (center), and sunphotometer (bottom) observations between 6:00 and 14:00 UTC. As explained in the previous section it is important to keep in mind that the zenith-pointing instruments (radar and ceilometer) observe different regions of the sky than the sun-tracking instruments (HaloCam and sunphotometer). For homogeneous cloud cover, which can be assumed for halo displays visible for more than 1 h, the data can be compared with a time shift. The height of the cirrus cloud base and top can be derived from ceilometer (lidar) and radar measurements. Figure 4.12 (top) shows the range-corrected ceilometer signal. As in Fig. 4.8 the detected cloud base and top height derived from the ceilometer measurements are represented by turquoise dots whereas the cloud base and top height from the radar measurements are marked with dark blue dots. Similar to Fig. 4.8 (top) the cloud top height derived from the radar measurements is significantly larger than for the ceilometer measurements. As already discussed in the previous section, the best estimate for cloud base and top height is achieved by combining both observations using the cloud base height from the ceilometer and the cloud top height from the radar measurements. This results in a cloud top height which is almost constant at 10 km between 6:30 and 11:00 UTC. Between 11:00 and 12:00 UTC the cloud top height drops to about 7 km. The cloud base height decreases in the course of the day from about 8 km at 6:30 UTC to about 4 km around 10:00 UTC where it remains until the onset of rain, which is visible in the backscatter signal of the ceilometer at

around 13:30 UTC. As in Fig. 4.8 the temperature levels at 0 °C, −20 °C, −30 °C and −40 °C, which are derived from radiosonde measurements at Oberschleißheim, are indicated by dashed, dash-dot, dotted, and dashed lines, respectively.
As in Fig. 4.8 the HaloCam data (Fig. 4.12 center) is represented as a time series of pixel lines in the principal plane above the sun with a temporal resolution of 10 s. The 22° halo observed between 7:00 to 11:00 UTC with interruptions between 8:30 to 9:00 UTC is visible as a line approximately at the middle of the figure which appears slightly red at the lower (inner) edge and sometimes even slightly blueish at the upper (outer) edge.
The sunphotometer observations in Fig. 4.12 (bottom) show the aerosol optical thickness (AOT) from AERONET version 2, level 2.0 (cloud screened) marked with turquoise stars, which could be measured in the morning at around 6:30 UTC before the first clouds of the approaching warm front formed. Since the structure of the aerosol in the boundary layer, which is visible in the backscatter signal of ceilometer in the lowest 2 km, does not change much in the course of the day, the AOT during the time of the specMACS measurements is estimated by the daily average of 0.15 ± 0.02 within a 2σ confidence interval. The apparent cirrus optical thickness is derived from SSARA sunphotometer measurements, which are available every 2 s (AERONET every 15 min), are derived as explained in Section 3.7.3. During the time when the halo display was observed a maximum apparent optical thickness of about 2 was measured. The values for the times of the specMACS measurements are compiled in Table 4.3 and are used to define the range of the LUT parameters for AOT and COT and to define the height and depth of the cirrus cloud layer for the radiative transfer simulations.
Figure 4.13 shows the specMACS measurements at 9:38, and 10:35 UTC as slices of the left

specMACS scan time	cloud top (base) height	cloud top (base) temperature	apparent COT
09:38 UTC	10 km (4.5 km)	−45 °C (−5 °C)	0.9 to 3.1
10:35 UTC	10 km (4.5 km)	−45 °C (−5 °C)	1.0 to 1.3
11:00 UTC	10 km (4.5 km)	−45 °C (0 °C)	0.3 to 2.0

Tabelle 4.3: *Cloud properties during the times of the specMACS scans on 22 September 2015.*

hand side almucantar and at 11:00 UTC the region around the almucantar at the right side of the sun at a wavelength of 550 nm. As in the previous case study the almucantar plane is used for the retrieval to avoid interference with the upper tangent arc which contains light scattered by oriented ice crystals. Sundogs were not observed. The data is displayed in green with errorbars consisting of the standard deviation of the averaged radiance and the propagated measurement uncertainty, as explained in Section 3.4. The LUT is calculated for the same parameters as for the case study of 24 March 2015. The simulated radiance distributions in the LUT and the specMACS almucantar measurements are compared by calculating the RMSE between the curves. A match is found if the condition $\text{RMSE} \leq 2\sigma_{\text{L,specMACS}}$ is fulfilled. The light green curves in the second column of Fig. 4.13 represent matching LUT elements, for reasons of visualization displayed only for the maximum and minimum retrieved smooth crystal fraction of each habit. The 3rd column of Fig. 4.13 shows a bar chart of the smooth (black) and rough (gray) ice crystal fraction for each habit corresponding to the best match between LUT and measurement with error bars spreading between the retrieved minimum and maximum values for each habit. The 4th column of Fig. 4.13 shows the retrieved asymmetry factors as an error bar at the value

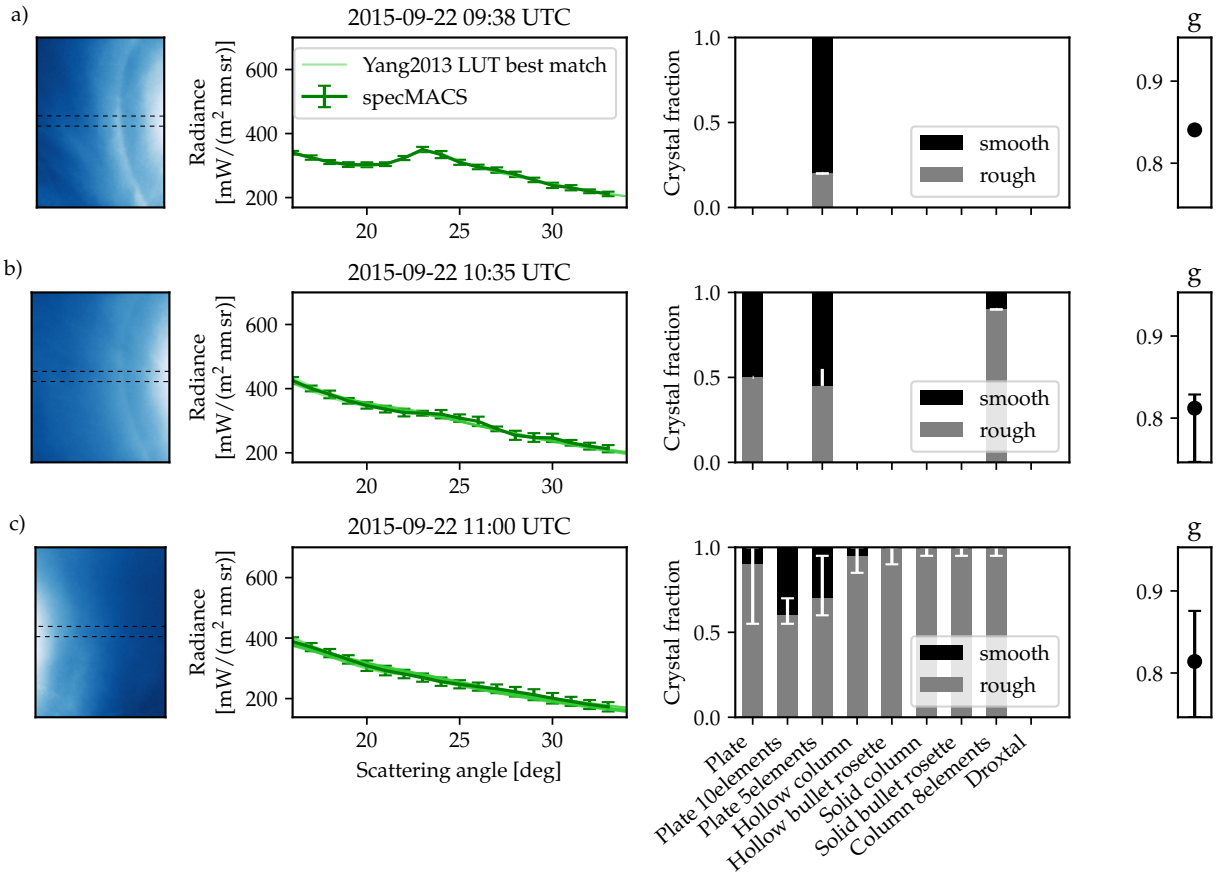

Abbildung 4.13: *Retrieval applied to specMACS observations of 22 September 2015 using the YANG optical properties. For a detailed description see Fig. 4.9.*

corresponding to the best match and ranging between retrieved minimum and maximum value. The y-axis ranges between 0.747 and 0.951, which are the minimum and maximum value the asymmetry factor can take if all habits, smooth crystal fractions and effective radii are considered. As in the previous case study the results shown in Fig. 4.13 do not consider information of additional measurement of AOT or COT.

At 9:38 UTC (Fig. 4.13a) a pronounced 22° halo is visible which constrained the LUT parameters to only a few matches for 5-element plates. The retrieved smooth crystal fraction is large with 80% varying between 75% and 90%. In this case also the asymmetry factor can be constrained to 0.84. The 22° halo at 10:35 UTC is less pronounced but helps to constrain possible combinations of ice crystal habit and surface roughness. Matching habits are plates, 5-element plates and one matching radiance distribution with 8-element columns. For the plates the smooth crystal fraction ranges between 40% and 50%, whereas 5% smooth crystals are sufficient in the case of the 8-element columns to reproduce the measured halo. For the 10:35 UTC case, the asymmetry factor can be constrained to values smaller than 0.84. The third measurement at 11:00 UTC was taken at the time when the 22° halo just disappeared as visible in Fig. 4.12 (center) and shows a featureless curve. Almost all habits match the measurements with different amount of smooth ice crystals. In this case the smooth crystal fraction is very low and rough ice crystals are dominating. Although no pronounced halo is visible, the asymmetry factor could be slightly constrained to values lower than 0.91.

Tabelle 4.4: *HaloCam$_{\mathrm{RAW}}$ 22° halo days between 22 September 2015 and 31 December 2016.*

Date	Start time	End time	Number of images
2015-09-22	6:38 UTC	11:14 UTC	1054
2015-11-08	10:00 UTC	10:37 UTC	198
2015-11-10	9:00 UTC	10:23 UTC	88
2016-01-20	9:36 UTC	11:37 UTC	544
2016-02-02	8:00 UTC	14:00 UTC	1029
2016-02-06	12:00 UTC	15:20 UTC	724
2016-04-21	11:34 UTC	13:52 UTC	770
2016-11-04	10:27 UTC	10:40 UTC	78

4.3.3 Application to long-term HaloCam observations

To obtain representative results for ice crystal properties of halo-producing cirrus clouds, long-term observations are required. However, specMACS measurement can only be performed on demand since the instrument is not waterproof. Therefore, the weatherproof automatic camera HaloCam$_{\mathrm{RAW}}$ was installed in September 2015 on the rooftop platform of MIM. Between 22 September 2015 and 31 December 2016 HaloCam$_{\mathrm{RAW}}$ recorded scenes with a 22° halo on 52 days with a temporal resolution of 10 s. Additional sunphotometer measurements are required to constrain AOT and COT. As demonstrated in Section 4.3.1, the better these two parameters can be constrained the more information about the ice crystal microphysical properties can be gained from the observations. As described in Section 3.7.3, the AOT is derived from the AERONET database and the mean and standard deviation over the whole day is used as an estimate for the AOT during the halo event. The apparent COT is derived from the SSARA sunphotometer measurements with a temporal resolution of 2 s. The retrieval is applied to the R-channel of HaloCam$_{\mathrm{RAW}}$ with a central wavelength of 618 nm to minimize the relative contribution of Rayleigh and aerosol scattering compared to the scattering by ice crystals.

Simultaneous measurements of the SSARA sunphotometer and AERONET data together with HaloCam$_{\mathrm{RAW}}$ observations are available for only 8 days which are listed in Table 4.4. Figure 4.14 shows an example of the AOT and apparent COT derived from sunphotometer measurements on 8 November 2015. The AOT is obtained from the AERONET dataset and is represented by the turquoise stars. The daily average AOT amounts to about 0.04 ± 0.01 at 618 nm, the central wavelength of HaloCam$_{\mathrm{RAW}}$'s R-channel. The blue dots in Fig. 4.14 indicate the apparent COT derived from SSARA sunphotometer measurements, which is below 1 throughout the day. The lower panel of Fig. 4.14 shows slices of the HaloCam images along the principal plane above the sun. Presence of 22° halos and UTAs appears as a bright line in the middle of the panel with a reddish inner, i.e. lower, edge from 9:30 until 10:30 UTC and between 14:00 and 14:30 UTC.

The automated halo detection algorithm HaloForest was used to filter the HaloCam$_{\mathrm{RAW}}$ images for 22° halos. The HaloCam$_{\mathrm{RAW}}$ data were geometrically and radiometrically calibrated as described in Sections 3.5.2 and 3.5.3. To use as much information as possible from the HaloCam$_{\mathrm{RAW}}$ images, the radiative transfer simulations for the LUT were performed for all the image pixels. To reduce the file size of the LUT, both the simulated and the measured images

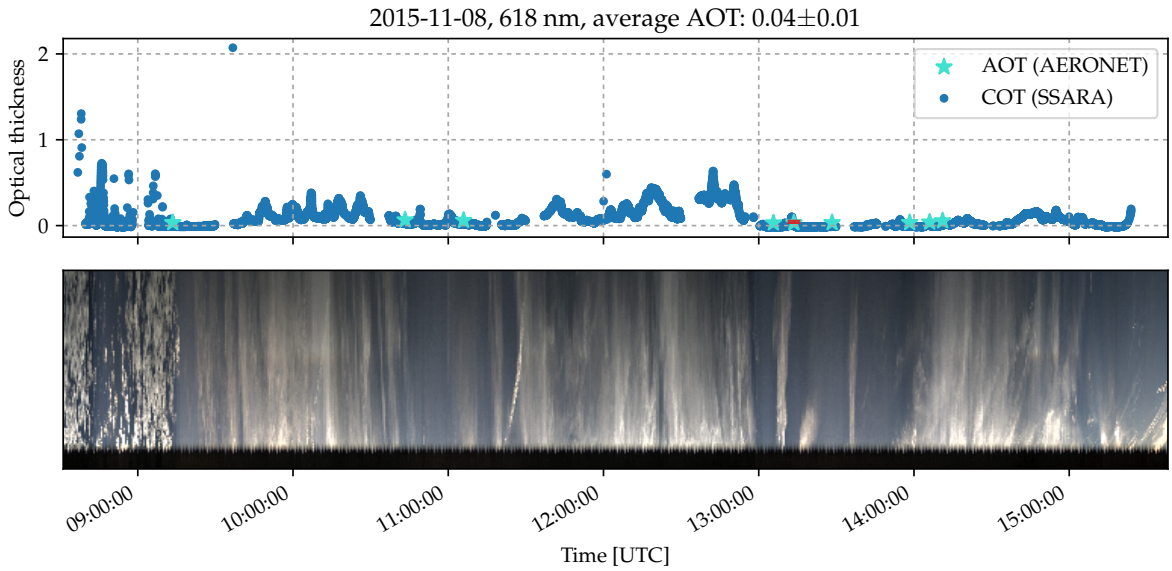

Abbildung 4.14: *Top: AERONET AOT (turquoise stars) and apparent COT derived from SSARA measurements (blue dots) for a wavelength of* 618 nm. *Bottom: time line of HaloCam*$_{\mathrm{JPG}}$ *pixel slices above the sun as described in Fig. 4.8.*

were averaged over 5 segments in the direction of the relative azimuth angle φ for the retrieval (cf. Section 3.5.2 and Fig. 3.21).

The retrieval was performed as follows: For each HaloCam$_{\mathrm{RAW}}$ image the LUT was interpolated to the respective SZA and constrained to the previously determined AOT within a 2σ confidence interval. To constrain the COT of the applied LUT, a 10 min time interval centered at the time of the HaloCam$_{\mathrm{RAW}}$ image was chosen to account for the slightly different pointing direction of $\Theta = 0°$ (sunphotometer) and $\Theta = 22°$ (halo display) in combination with the unknown wind direction. The corresponding COT was obtained by correcting the apparent COT with the k-factors of the respective ice crystal habit in the LUT according to Eq. (3.49). Then, each of the 5 averaged radiance distributions measured with HaloCam$_{\mathrm{RAW}}$ was compared to the LUT element with the respective geometry. Measurements and LUT were compared on a scattering angle grid between 18° and 24.5° with an angular resolution of 0.5°. The angular grid was optimized for the retrieval to account for the vicinity of the 22° halo in addition to its peak while keeping the angular region as small as possible to avoid inhomogeneities of the cirrus optical and microphysical properties. The best matching LUT element was determined by minimizing the RMSE between LUT and observations

$$\mathrm{RMSE}^2 = \overline{L_{\mathrm{HaloCam_{RAW}}} - L_{\mathrm{LUT}}}\,. \tag{4.4}$$

The previous case studies demonstrated that multiple configurations of ice crystal habit, SCF, effective radius, COT and AOT matched the specMACS radiance distributions within the 2σ errorbars. Here, the goal is to investigate which ice crystal habit and SCF best matches the observed radiance distributions across 22° halos. Sampling over many scenes should provide a good estimate of the average ice crystal properties of halo-producing cirrus clouds.

For 8 November 2015, 974 samples (5 segments per image) were selected and matched against the LUT after it was interpolated to the respective SZA of 65.7° and after constraining AOT and COT. For each image segment the best matching radiance distribution of the LUT was chosen.

Tabelle 4.5: *HaloCam$_{\mathrm{RAW}}$ retrieval best match results for each of the 8 days.*

Date	habit	SCF	Effective radius
2015-09-22	8-element column	24 %	28 µm
2015-11-08	plate	77 %	20 µm
2015-11-10	solid column	59 %	10 µm
2016-01-20	plate	80 %	29 µm
2016-02-02	solid column	39 %	24 µm
2016-02-06	plate	88 %	26 µm
2016-04-21	plate	75 %	16 µm
2016-11-04	5-elements plate	80 %	13 µm

The results were filtered for HR > 1 to ensure that only samples with 22° halo are considered. Also results with RMSE $> 2\sigma_{\mathrm{L}}$ were filtered out.

Figure 4.15a shows the histograms of the LUT parameters assuming solid columns as dominating ice crystal habit. The SCF shows a peak below 50% with a mean value of 35.9% which implies that the 22° halo on the HaloCam$_{\mathrm{RAW}}$ images is represented best by a larger fraction of rough solid columns mixed with smooth solid columns. The COT values are below 1 with a mean value of 0.36, whereas the AOT is constrained to 0.05. The ice crystal effective radii peak at smaller values with a mean of 31.1 µm. The mean asymmetry factor amounts to about 0.792.

Figure 4.15b shows the results for the LUT assuming ice crystal plates. In this case a larger SCF is required to match the brightness contrast of the 22° halo on the HaloCam$_{\mathrm{RAW}}$ images with a mean value of 77.2%. The average COT amounts to 0.73 with some values larger than 1. The COTs of the best match radiance distributions are significantly larger for plates than for solid columns. This is due to the extreme k-factors for ice crystal plates causing a larger spread in the possible COT values. The mean effective radius with 19.3 µm is smaller than for the solid columns. Assuming plates as dominating ice crystal habit causes a larger asymmetry factor on average with 0.876. Since the uppermost segment (no. 3 in Fig. 3.21) could contain signatures of the upper tangent arc, the retrieval results for this image segment were filtered out as a test for all 8 days but the retrieved SCF, effective radius, AOT, COT and asymmetry factor did not change significantly. Sundogs appear in the left and right image segments (no. 1 and 5) only for SZA $< 45°$ at scattering angles of $\Theta > 29°$ which does not interfere with the 22° halo (cf. Fig. 4.7).

Figure 4.16 shows the results of the retrieval applied to the 8 days of halo observations with HaloCam$_{\mathrm{RAW}}$. The upper panel presents the average SCF over the whole day for the 8 habits: plates (turquoise), 10-element plates (blue), 5-element plates(dark blue), hollow columns (pink), hollow bullet rosettes (purple), solid columns (light green), solid bullet rosettes (green) and 8-element columns (dark green). The droxtal habit was not considered for the this analysis since they do not produce a 22° halo. By grouping the ice crystal habits into columnar (green), hollow (pink), and plate-shaped crystals (blue) the SCF clusters with ∼30%, ∼60%, ∼80%. Despite the differences in the retrieved SCF there is better agreement on the effective radius among the ice crystal habits (second panel of Fig. 4.16) which ranges between 5 µm and 30 µm with a mean value of 20 µm. This confirms that the width of the 22° halo is primarily determined by ice crystal size while shape and surface roughness play a minor role which confirms the findings of Section 4.1.2.

Tabelle 4.6: *HaloCam$_{\mathrm{RAW}}$ retrieval results evaluated over all 8 days.*

Habit	RMSE	SCF [%]	Effective radius [µm]	Asymmetry factor
plate	3.93	80 ± 10	22.3 ± 11.5	0.880 ± 0.021
solid column	4.03	40 ± 20	23.8 ± 13.4	0.788 ± 0.008
8-element column	4.29	30 ± 20	22.3 ± 17.6	0.752 ± 0.001
5-element plate	4.37	70 ± 10	17.9 ± 10.2	0.838 ± 0.005
10-element plate	4.39	80 ± 10	14.3 ± 13.0	0.876 ± 0.004
solid bullet rosette	4.48	30 ± 10	20.8 ± 13.2	0.781 ± 0.014
hollow column	4.51	60 ± 20	21.8 ± 11.2	0.813 ± 0.006
hollow bullet rosette	5.08	60 ± 20	19.2 ± 12.6	0.821 ± 0.009

Tabelle 4.7: *HaloCam$_{\mathrm{RAW}}$ retrieval results sensitivities.*

Date	Aerosol type			
	spectral sensitivity	continental clean	continental polluted	urban
2015-09-22	solid column	8-element column	solid column	solid column
2015-11-08	plate	5-element plate	plate	plate
2015-11-10	hollow column	hollow column	hollow column	solid bullet rosette
2016-01-20	plate	plate	plate	plate
2016-02-02	solid column	solid column	solid column	solid column
2016-02-06	plate	plate	plate	plate
2016-04-21	plate	plate	plate	plate
2016-11-04	5-elements plate	5-element plate	5-elements plate	plate

The results in Table 4.5 show that on 5 of the 8 days plate-like crystals represent the best matching habit. In 6 of the 8 analyzed cases ice crystal optical properties with a SCF $> 50\,\%$ on average best match the observations.

The results in Table 4.6 are sorted by the RMSE starting with the smallest value. As shown in Table 4.6 ice crystal plates have the overall smallest RMSE and thus seem to match the observations better than the other 7 habits of the YANG database. The best-matching LUT elements of ice crystal plates have a SCF of $(80 \pm 10)\,\%$, an effective radius of $(22.3 \pm 11.5)\,\mu\mathrm{m}$ and an asymmetry factor of 0.880 ± 0.021. In terms of best-matching habit the plates are followed by the solid columns with a SCF of $(40 \pm 20)\,\%$, an effective radius of $(28.8 \pm 13.4)\,\mu\mathrm{m}$ and an asymmetry factor of 0.788 ± 0.008. Hollow columns and bullet rosettes have the largest mean RMSE.

To investigate the stability of the retrieval, tests were performed by multiplying the LUT radiance distributions with a slope to simulate the effect of using the representative wavelength of the camera channel instead of the spectral sensitivity or a different aerosol type. The slopes used to modify the LUT were determined similar to Fig. 3.37. The mean relative errors due to the assumption of the aerosol type or representative wavelength were overall smaller than 2%.

The LUTs were calculated assuming the continental average aerosol mixtures from the OPAC database. Table 4.7 shows the results of the best-matching habit for each day retrieved with the modified LUT. The best-matching habit slightly changed for the different modifications of the LUT but the ice crystal plates remained the overall best-matching habit. Changes of the best-matching habit occurred only within the plate-like or column-like crystal groups.

To test how representative the averaged retrieved LUT parameters are for the whole scene, the averaged $\text{HaloCam}_{\text{RAW}}$ image of each day was compared to a DISORT simulation for the same viewing geometry and resolution as the image. The results are displayed in **??** and **??** for the 8 November 2015. Interestingly, the best matching radiance distribution both for solid columns and plates exhibits a 46° halo which is not visible in the averaged $\text{HaloCam}_{\text{RAW}}$ images. It should be noted that the reason for the sharper 22° halo in the $\text{HaloCAM}_{\text{RAW}}$ measurement than in the simulation is most likely due to the coarse resolution of the scattering phase function of the YANG database of 1° in the region of the 22° halo. It could be argued that the missing 46° halo in the observations is owing to the inhomogeneity of the cirrus clouds. However, the 974 samples are consecutive images during one hour. This suggests that if ice crystals forming a 46° halo were present in the cirrus cloud, it should be visible in the averaged image. Thus, the absence of the 46° halo could be used to further constrain the ice crystal microphysical properties. This was tested by filtering out all LUT elements which show a 46° halo. The average over all habits of the SCF, effective radius and asymmetry factor did not change significantly. However, the habit with the overall smallest RMSE, i.e. the best-matching habit in this case is the solid column followed by the 8-element column. Ice crystal plates only represent the observations with larger effective radii of about 50 µm on average. This occurs due to the relationship between ice crystal AR and size for the Yang et al. (2013) optical properties. Small ice crystal plates have AR ≈ 1 (cf. Fig. 3.7) which is effective for the formation of 46° halos as shown in Fig. 3.10. Since the overall mean effective radius for all habits except for plates did not change significantly compared to the results in Fig. 4.16, it seems that the plate habit with its prescribed AR parameterization does not represent well the observations.

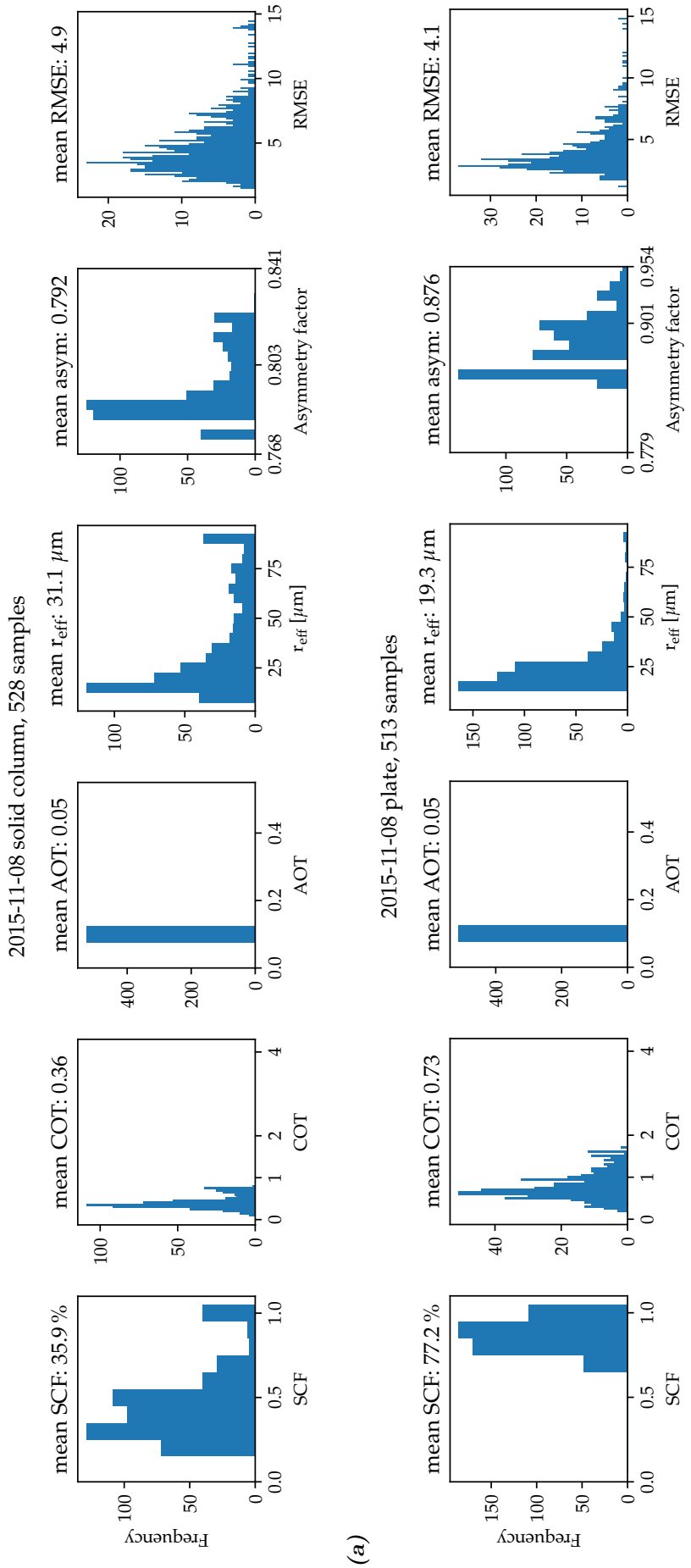

Abbildung 4.15: *Results of retrieval applied to the R-channel of the HaloCam$_{\mathrm{RAW}}$ images for 8 November 2015 using the YANG optical properties for (a) solid columns and (b) plates. The different panels show the frequency of occurrence for the LUT parameters as histograms for the SCF, COT, AOT, effective radius, asymmetry factor (from left to right) and the RMSE between LUT and measurement (rightmost panel). The results were filtered for* HR > 1 *to ensure that only image slices with 22° halo were analyzed.*

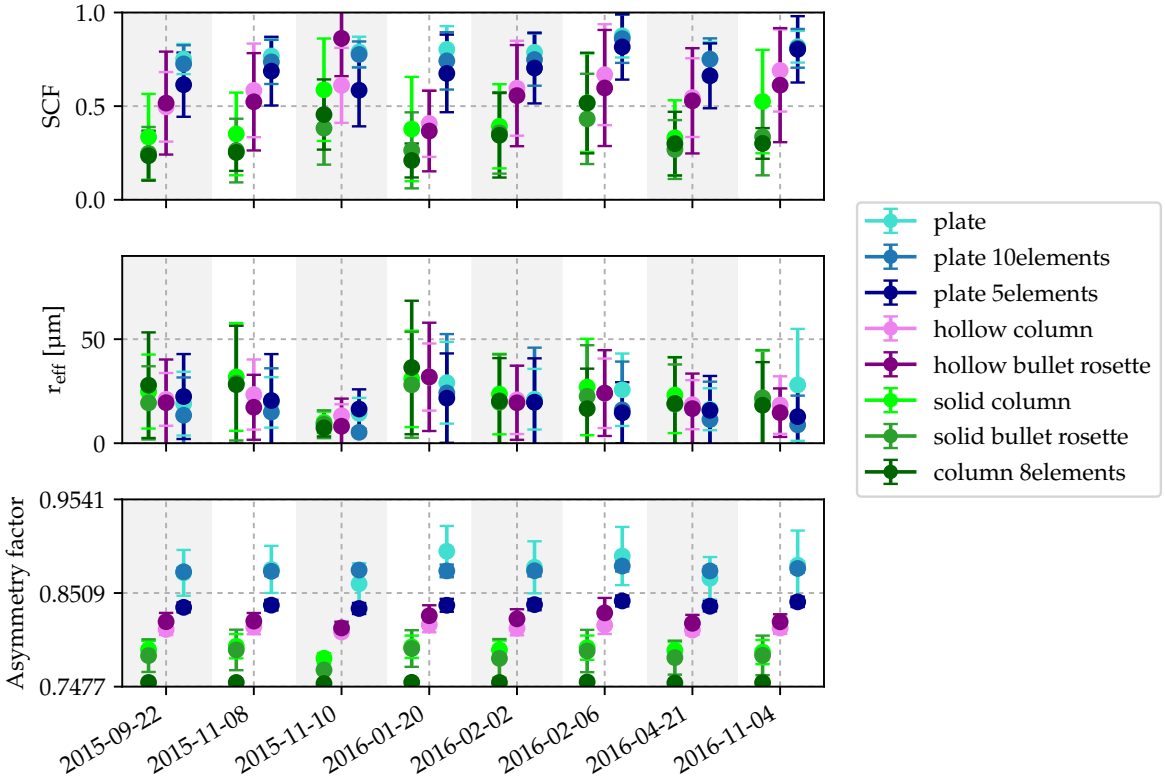

Abbildung 4.16: *Retrieval results for all 8 days listed in Table 4.4 and 8 habits of the YANG optical property database. Results are shown for the SCF (top), effective radius (middle), and asymmetry factor (bottom). The errorbars indicate the mean value with a 2σ uncertainty. The colors are grouped into blue, pink and green to highlight the plate-like, hollow, and columnar ice crystals, respectively. Darker colors refer to more complex crystals.*

Abbildung 4.17

4.4 Considerations on ice crystal orientation

A significant fraction of cirrus clouds contains oriented ice crystals (Noel and Sassen, 2005, Noel and Chepfer, 2010, Zhou et al., 2012). The statistics of halo displays during the ACCEPT campaign (Section 4.2.1) revealed that the majority of halo displays was caused by oriented ice crystals: sundogs and upper tangent arcs, which are formed by oriented plates and columns, were observed in 70% and 30% of the total observation time, respectively. 22° halos, which are caused by randomly oriented hexagonal crystals, were observed in 60% of the time. Furthermore, 22° halos, sundogs, and upper tangent arcs often occured simultaneously with a frequency of about 22% relative to the total observation time. This section presents first results of the observations during the ML-CIRRUS campaign (Voigt et al., 2016) with halo displays formed by oriented ice crystals. Using CrystalTrace, two methods are proposed to derive the fraction of oriented ice crystal plates and columns from simultaneous observations of 22° halos and sundogs or upper tangent arcs.

4.4.1 Observation of oriented ice crystals during ML-CIRRUS

During the ML-CIRRUS campaign (Voigt et al., 2016) between March and April 2014 the novel High Altitude and Long Range Research Aircraft (HALO) was probing cirrus clouds in Europe with a unique set of instruments to characterize microphysical, optical, and radiative properties of the cirrus clouds and the atmospheric conditions. Based at and flying off the German Aerospace Center (DLR) in Oberpfaffenhofen, southern Germany, several overpasses of the HALO research aircraft could be performed over the Meteorological Institute of the LMU in Munich. During the campaign continuous measurements were performed with several instruments on the MIM rooftop platform: HaloCam was operating at this time with $\text{HaloCam}_{\text{JPG}}$ and simultaneous with a Canon Powershot G12 to record images in the uncompressed and unprocessed "raw" format. Additional measurements were performed with the specMACS imaging radiometer. Continuous observations of the MIRA cloud radar are available both for zenith pointing measurements and scans. Moreover, lidar measurements were performed with the Portable Lidar System (POLIS, Heese et al. (2004)) and continuous sunphotometer measurements are available both from the AERONET Cimel and the SSARA instruments.

On 1 April 2014 halo displays formed in a very homogeneous cirrus layer over Munich showing a 22° halo simultaneously with an upper tangent arc and sundogs which lasted for about 4 h. These halo displays were accompanied with a high aerosol load of Saharan dust (Voigt et al., 2016). Figure 4.18 (left) shows the recorded $\text{HaloCam}_{\text{JPG}}$ image from 8:25 UTC on 1 April 2014. The right side of Fig. 4.18 displays the same image but applied with an unsharp mask filter to highlight the optical features in the image. Besides the 22° halo and the upper tangent arc, the concave Parry arc on top of the tangent arc is clearly visible and was present for some minutes. The Parry arc is named after W. E. Parry who first described this type of halo display between 1819 and 1820 (e.g. (Pernter and Exner, 1910, Tricker, 1970, Greenler, 1980)). This halo display is very rare and is formed by double-oriented ice crystal columns. The ice crystal columns are oriented with their c-axis horizontally as for the upper tangent arc. In addition their rotation around the c-axis, i.e. γ_{Euler} (cf. Eq. (3.53)), is also fixed. CrystalTrace was used to perform a radiative transfer simulation of the scene in Fig. 4.18 for the corresponding SZA of 57° at a wavelength of 500 nm which is shown in Fig. 4.19. As an estimate of the AOT the daily average provided by AERONET was assumed which amounts to 0.48 at a wavelength of 500 nm. The desert aerosol from the OPAC database was chosen as dominating aerosol type. The simulation was performed for a COT of 1 and an ice crystal mixture of 45% randomly oriented columns

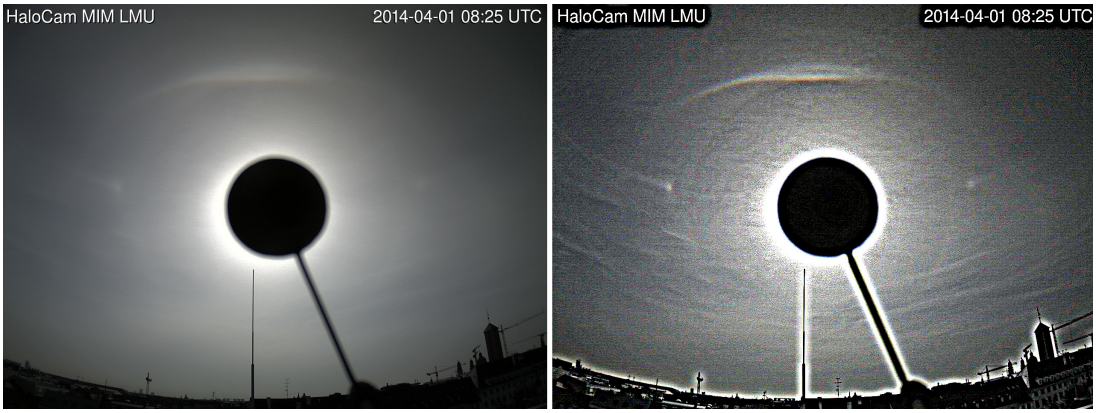

Abbildung 4.18: *HaloCam$_{\mathrm{JPG}}$ image from 1 April 2014 during the ML-CIRRUS campaign. The left panel shows the original HaloCam$_{\mathrm{JPG}}$ image with a faint 22° halo, both sundogs, an upper tangent arc and a concave Parry arc on top. The right panel displays the same image with an unsharp mask filter applied to better highlight the optical features. On the right image the Parry arc is clearly visible and even a faint circumhorizontal arc can be noticed which extends from the left sundog.*

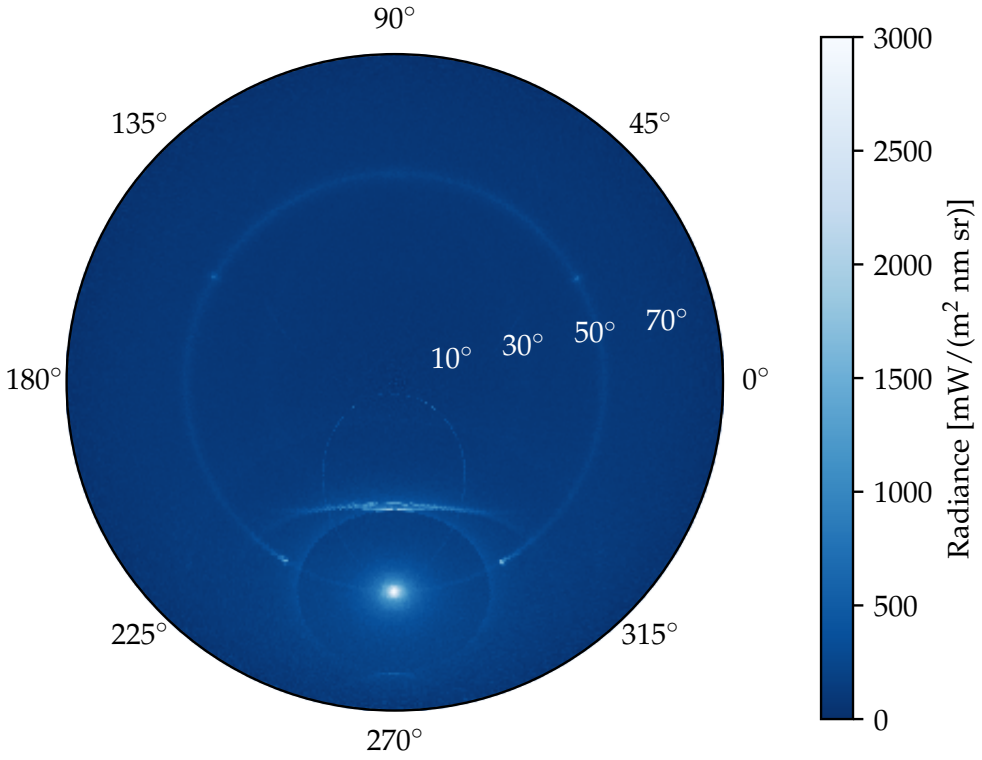

Abbildung 4.19: *CrystalTrace simulation from 1 April 2014 8:25 UTC at an SZA of 57° and a wavelength of 500 nm. The simulation was performed for 45% randomly oriented columns which form the 22° halo, 10% oriented plates which cause the sundogs, 35% oriented columns which are responsible for the upper and lower tangent arcs, and 10% Parry-oriented columns which form the upper Parry arc. A cirrus optical thickness of 1 was chosen and the aerosol was parameterized by the OPAC desert dust mixture with an AOT of 0.48 at 500 nm, which is the daily mean provided by AERONET.*

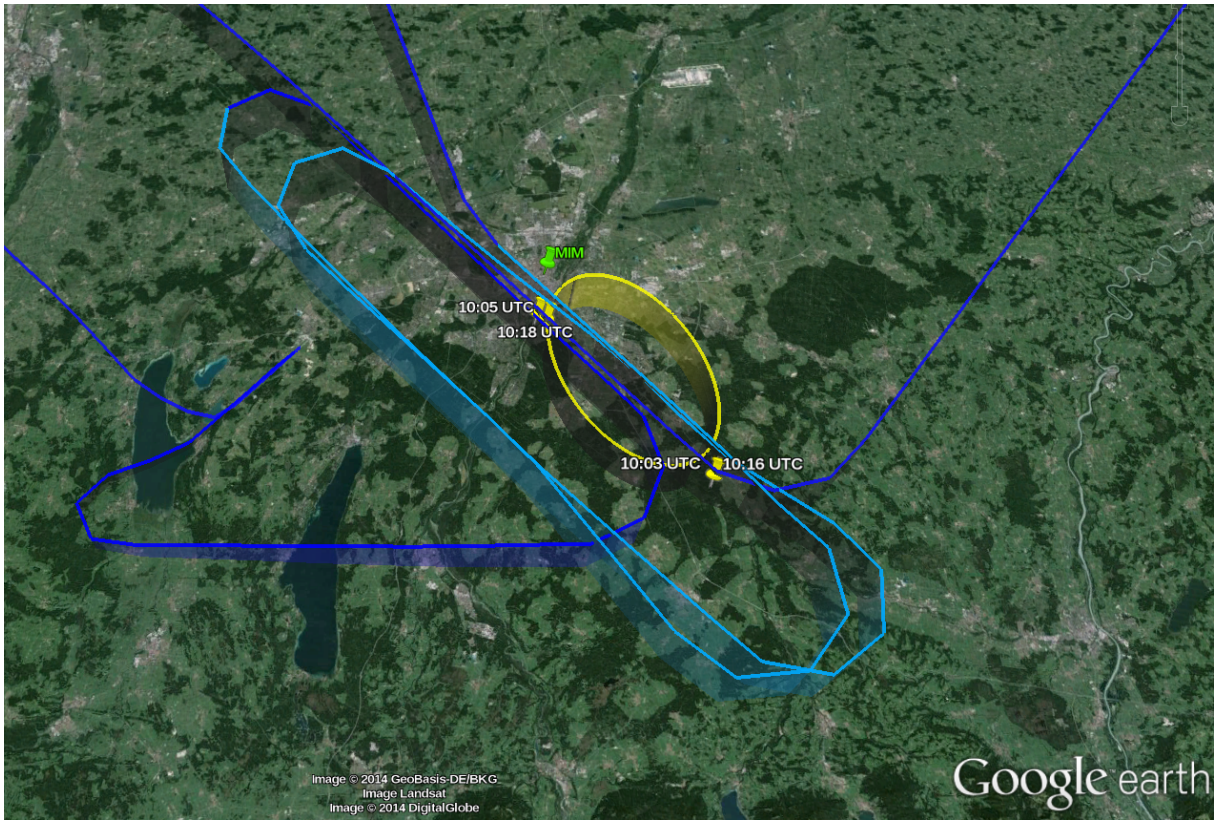

Abbildung 4.20: *Flight path of the HALO research aircraft on 1 April 2014 during the ML-CIRRUS campaign displayed in blue. The Meteorological Institute in Munich (MIM) is indicated by a green pin. The 22° halo visible from MIM is represented by the yellow ellipse, which was calculated using the equations described in Appendix B. The coordinates of the 22° halo were calculated for the respective position of the sun and the height of the cirrus cloud base, which was derived from radar measurements. The light blue sections of the HALO flight path indicate the location of the aircraft within the cirrus cloud with two overpasses over MIM at around 10:04 UTC and 10:17 UTC.*

which form the 22° halo, 10% oriented plates which cause the sundogs, 35% oriented columns which are responsible for the upper and lower tangent arcs, and 10% Parry-oriented columns which form the upper Parry arc. The relative fraction of the different ice crystal components was estimated to qualitatively reproduce the different halo displays and their relative brightness as visible in Fig. 4.18. As in Fig. 4.18 the lower Parry arc in Fig. 4.19 is not visible due to the large AOT and the long path through the atmosphere due to the low viewing zenith angle. Compared to Fig. 3.45 which was simulated for an aerosol-free atmosphere, Fig. 4.19 shows a strong forward scattering signal in the solar aureole region and the brightness of the halo displays is significantly reduced. It should be noted that diffraction and the simulation of ice crystal roughness is yet to be implemented in CrystalTrace before a quantitative retrieval of the ice crystal optical and microphysical properties as well as ice crystal orientation is possible.

On this day the HALO research aircraft could probe the cirrus clouds above the institute and could fly two legs in different heights crossing the cirrus clouds exactly where the halo displays were visible at MIM. For these two overpasses of the HALO aircraft on 1 April 2014 the measurements of the Small Ice Detector Mark 3 (SID3) was evaluated by Martin Schnaiter and Emma Järvinen from KIT Karlsruhe (personal communication). The SID3 instrument is described in Ulanowski et al. (2014) and can measure ice crystals in a size range of 5 to 50 µm. SID3 allows to resolve single particle light scattering patterns which can be used to derive ice crystal complexity (Schnaiter et al., 2016). The SID3 measurements during the first and lower leg (10:04 UTC) contained 83 well-exposed images. Of these images 16.9% showed a halo feature and 3.6% had signatures of hexagonal crystals together with a halo feature. In the second and higher leg 59 images were well-exposed and 27.1% showed a halo feature whereas 8.5% showed indications of hexagonal crystals with a halo feature. This is another indication that already a small fraction of smooth and hexagonal ice crystals is sufficient to produce a visible halo display.

To investigate whether and how the fraction of oriented ice crystals can be derived from observations of halo displays, simulations were performed using the CrystalTrace algorithm. The presented method assumes the presence of a 22° halo as a reference since it is formed only by randomly oriented ice crystals. Then, the fraction of oriented plates can be derived by comparing the brightness of the sundogs with the brightness of the 22° halo. An estimate of the fraction of oriented columns can be retrieved by comparing the brightness contrast, i.e. the HR, of the upper tangent arc with the 22° halo. The fraction of oriented plates can be estimated by comparing the HR of the sundogs with the 22° halo.

4.4.2 Information content of sundogs

Figure 4.21 shows simulations with CrystalTrace for different fractions of randomly and oriented ice crystals. The simulations were performed for an aerosol free atmosphere at a wavelength of 550 nm, a solar zenith angle of 60° and a cirrus optical thickness of 0.8. The oriented ice crystal plates have an aspect ratio of 0.5 and are oriented with their c-axis vertically with a orientation parameter of 1°. The panels of Fig. 4.21 show polar plots of the upper hemisphere with the sun located at a SZA of 60° and an azimuth of 270°. The cirrus cloud in Fig. 4.21a contains only randomly oriented plates which produce a 22° and 46° halo. A fraction of oriented crystals of 20% already shows both sundogs, the parhelic circle with the 120° parhelia and the circumzenithal arc above the sun. While the fraction of oriented crystals increases, the brightness of the sundogs and other halo types produced by the oriented crystals is increasing. Simultaneously, the brightness of the 22° and 46° halo is decreasing until the 46° halo disappears at a fraction of 60% oriented plates and the 22° halo disappears at a fraction of 100% oriented ice crystal plates. To analyze

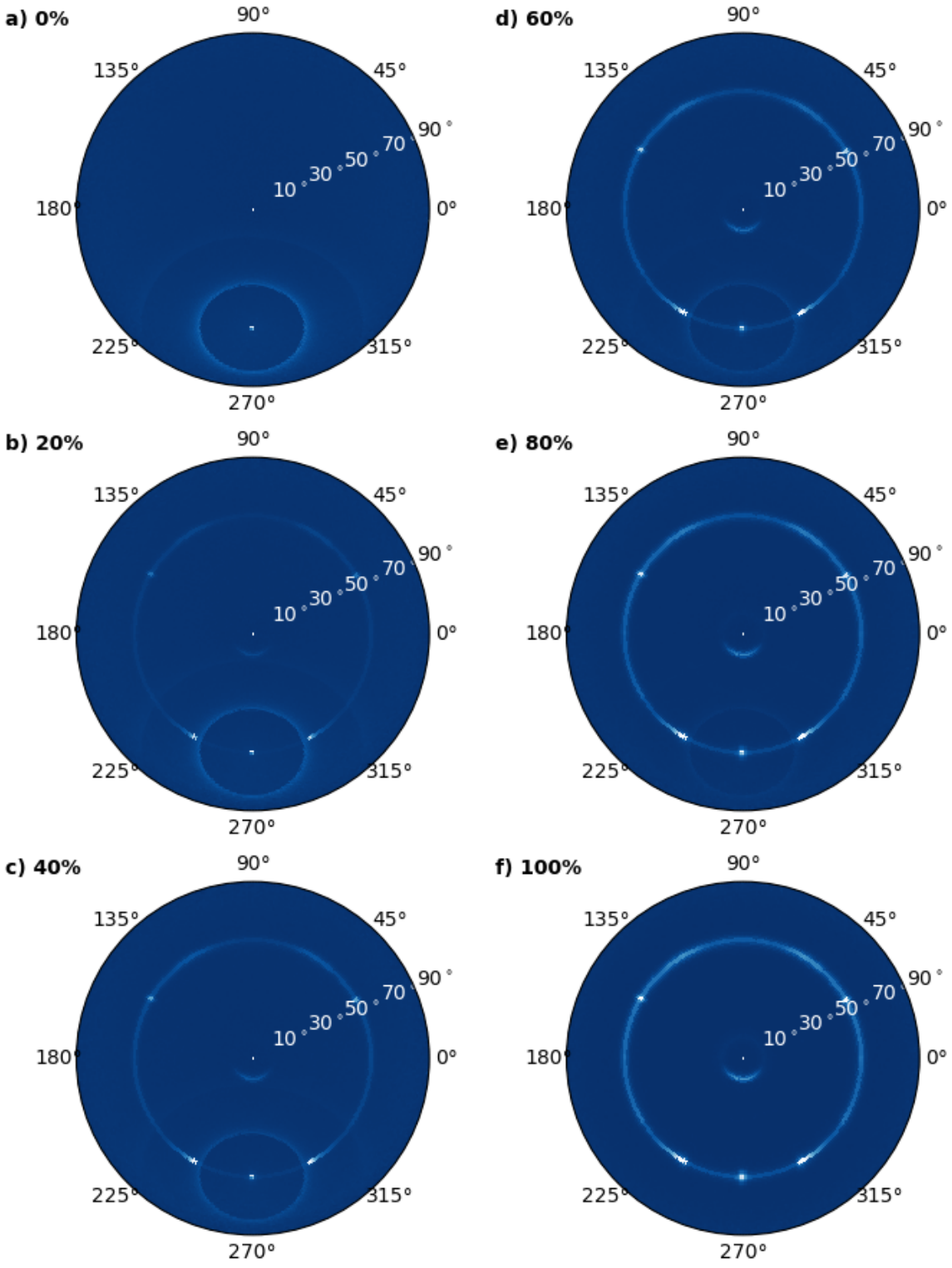

Abbildung 4.21: *Radiative transfer simulations of a cirrus cloud containing ice crystal plates using libRadtran's MYSTIC solver combined with CrystalTrace for* 10^7 *photons. A SZA of* $60°$ *and an azimuth angle of* $270°$ *was chosen. A COT of 0.8 was chosen and an aspect ratio of 0.5 was assumed for the ice crystal plates. The simulations were performed for different fractions of randomly oriented ice crystals and ice crystals oriented with the c-axis vertically with a distortion of* $1°$*. The fraction of oriented crystals is increasing from 0% in a) to 100% in f).*

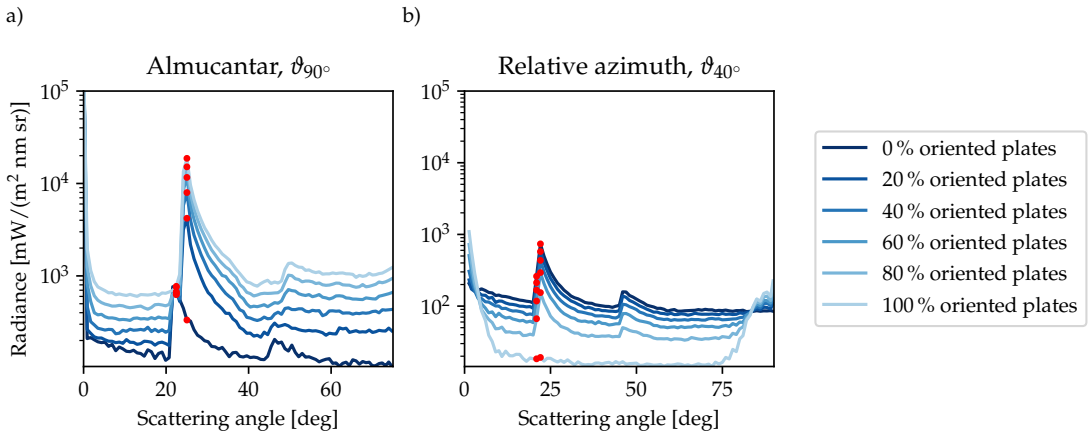

Abbildung 4.22: *Radiance distributions extracted from Fig. 4.21 in the a) almucantar plane ($\vartheta = 90°$) and b) between the almucantar and principal plane at $\vartheta = 40°$ for an increasing fraction of oriented ice crystal plates (AR = 0.5) at a wavelength of 550 nm. The radiance distribution in a) shows the cross section of the 22° halo and the right sundog, which occurs at a scattering angle of about 25°. b) Radiance distribution across the 22° and 46° halo as a function of the scattering angle. The red dots indicate the maximum and minimum of each halo display in the vicinity of the 22° halo.*

the fraction of oriented ice crystal plates the halo ratio (HR) between the 22° halo and the sundogs could be compared. For this retrieval method the HR of the sundog is evaluated in the almucantar plane, i.e. at the same zenith angle as the sun, as shown in Fig. 4.22a. The black dots represent the location of the halo minimum and maximum which are used to calculate the HR. The radiance distribution across the sundog and the brightness of the halo peak is increasing for a larger fraction of oriented plates. Figure 4.22b shows the radiance distribution across the 22° halo which is evaluated at a relative azimuth angle of $\vartheta = 40°$. The radiance distribution across the 22° halo and the brightness of the halo peak are both decreasing for a larger fraction of oriented plates. Figure 4.23 shows the HR of the sundog in the almucantar plane (a), the HR of the 22° halo at a relative azimuth angle of $\vartheta = 40°$ and the fraction of the two HRs (c). The HR of the sundog (a) is increasing for a larger fraction of oriented crystals while the HR of the 22° halo is decreasing. The fraction of $\mathrm{HR_{oriented}/HR_{random}}$ represents the factor by which the $\mathrm{HR_{random}}$ is increased due to the presence of oriented crystals. Thus, the fraction of oriented ice crystal plates could be retrieved by calculating this factor from the measurement and comparing it to a look-up table of pre-calculated factors. Besides the fraction of oriented crystals the enhancement factor depends on the ice crystal roughness, the solar zenith angle.

4.4.3 Information content of upper tangent arcs

Figure 4.24 shows simulations with CrystalTrace for different fractions of randomly and oriented ice crystal columns. The simulations were performed for a wavelength of 550 nm, a solar zenith angle of 60° and a cirrus optical thickness of 0.8. The ice crystal columns are oriented with their *c*-axis horizontally, oscillating with a standard deviation of 1°, and have an aspect ratio of 2.5. Figure 4.24 shows polar plots of the upper hemisphere with the sun located at a SZA of 60° and an azimuth of 270° similar to Fig. 4.21. The cirrus cloud in Fig. 4.24a contains only randomly oriented plates which produce a 22° and 46° halo. A fraction of oriented crystals of 20% already shows upper and lower tangent arc. As the fraction of oriented columns increases, the brightness of the upper and lower tangent arc increases and the arcs get wider. Starting from an oriented

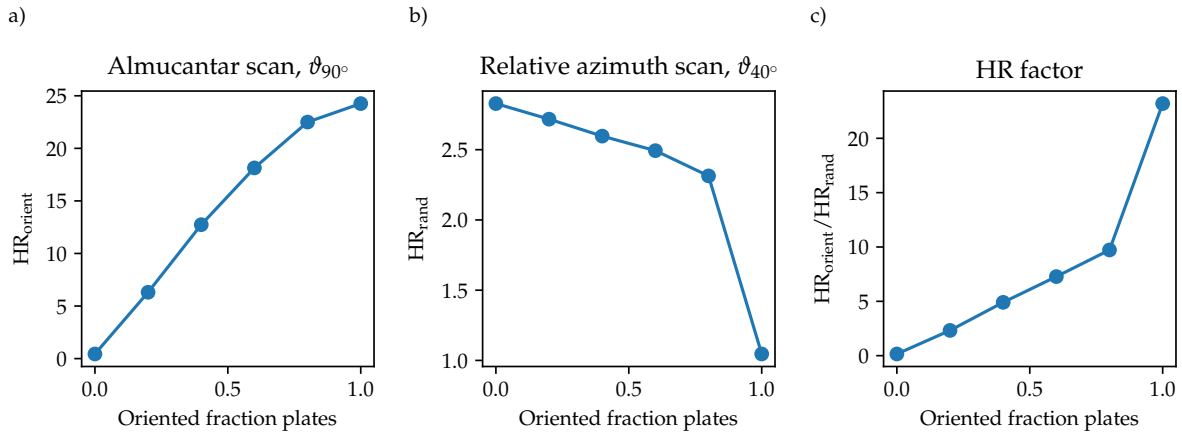

Abbildung 4.23: *Halo ratios calculated using the maximum and minimum radiance values of the halo display cross section, which are indicated by the red dots in Fig. 4.22, as a function of the oriented crystal fraction. a) Halo ratio of the 22° halo or sundogs in the almucantar plane ($\vartheta = 90°$) as a measure of the fraction of oriented ice crystal plates, denoted as HR_{orient}. b) Halo ratio of the relative azimuth scan at $\vartheta = 40°$ as a measure of the randomly oriented crystal fraction, labeled with HR_{rand}. c) Halo ratio enhancement factor, calculated by HR_{orient}/HR_{rand}.*

crystal fraction of 40% the circumhorizontal arc is visible and for fraction larger than 60% the infra- and supralateral arcs replace the 46° halo. Similar to Fig. 4.21 the 22° halo is still visible for 80% oriented columns and the upper and lower tangent arc are visible already for a fraction of 20% oriented crystals. The fraction of oriented ice crystal columns can be estimated in a similar way as for the oriented plates. Figure 4.25a shows the radiance distribution across the upper tangent arc in the principal plane, i.e. at $\phi = \phi_0$, whereas Fig. 4.25 displays the radiance distribution across the 22° halo at a relative azimuth angle of $\vartheta = 40°$. The corresponding HRs are presented in Fig. 4.26a for the upper tangent arc and in Fig. 4.26b for the 22° halo. Also for the upper tangent arc an enhancement factor of the HR can be calculated from the fraction of $HR_{oriented}/HR_{random}$ as shown in Fig. 4.26c. Similar to the case of oriented plates, the HR of the upper tangent arc increases with larger fractions of oriented crystals and the HR of the 22° halo decreases. Since the HR of the oriented crystals is much larger than HR_{random}, the enhancement factor is increasing. This approach assumes that the same ice crystals in terms of shape and aspect ratio are forming the 22° halo and the upper tangent arc or sundogs. This is not necessarily the case. When sundogs and a 22° halo is visible it might be possible that only a part of the ice crystal population is randomly oriented due to turbulence in the air. However, it is also possible that the oriented ice crystals responsible for the sundogs and tangent arcs are larger and have more extreme aspect ratios as the crystals forming the 22° halo. To account for this LUTs have to be compiled for the enhancement factor assuming mixtures of different ice crystal populations. These relative observations do not require a radiometric calibration of the camera.

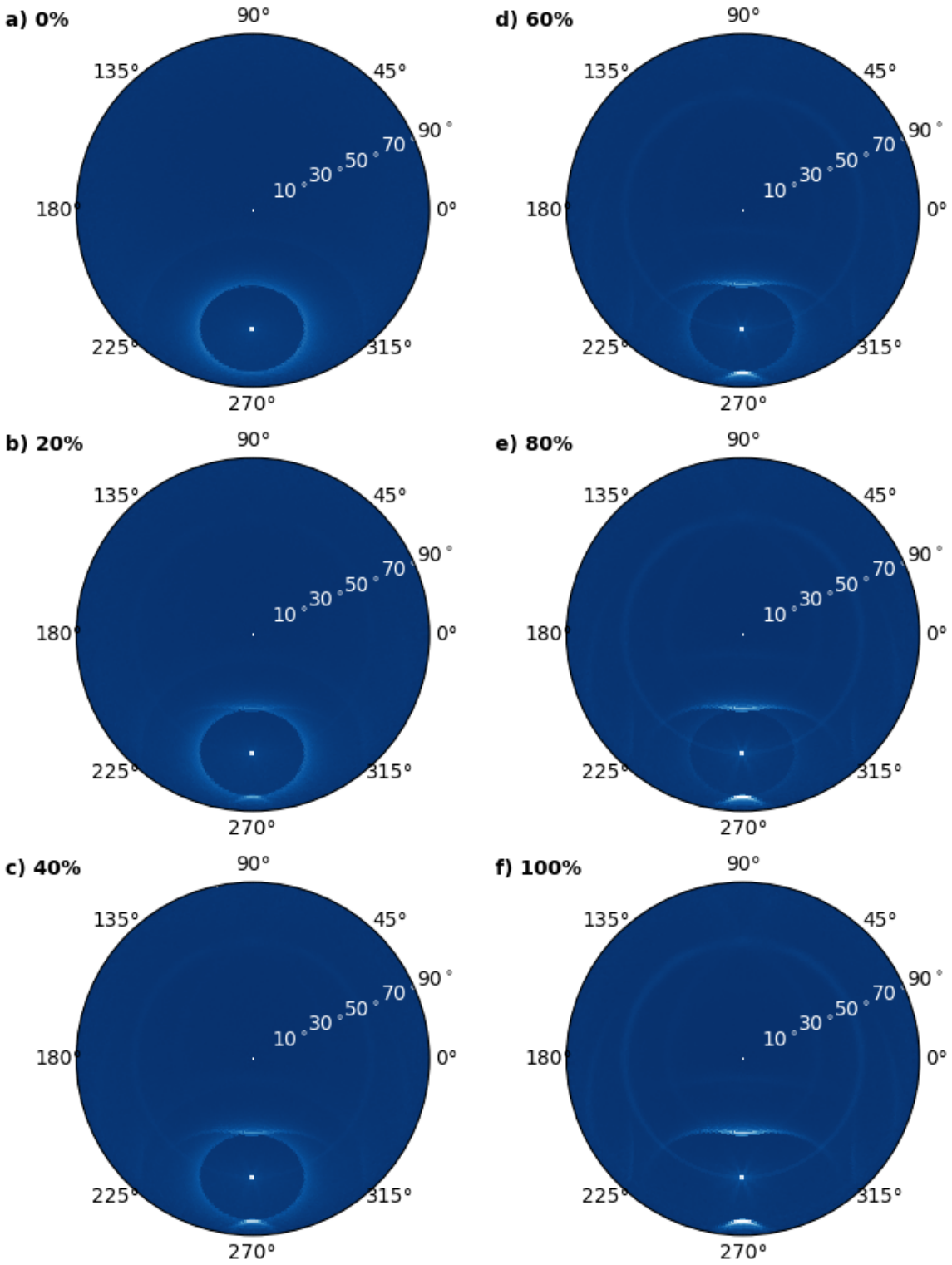

Abbildung 4.24: *As Fig. 4.21 but for ice crystal columns with an aspect ratio of 2.5. Randomly oriented columns were mixed with columns oriented with the c-axis horizontally with a distortion of 1°. The fraction of oriented crystals is increasing from 0% in a) to 100% in f).*

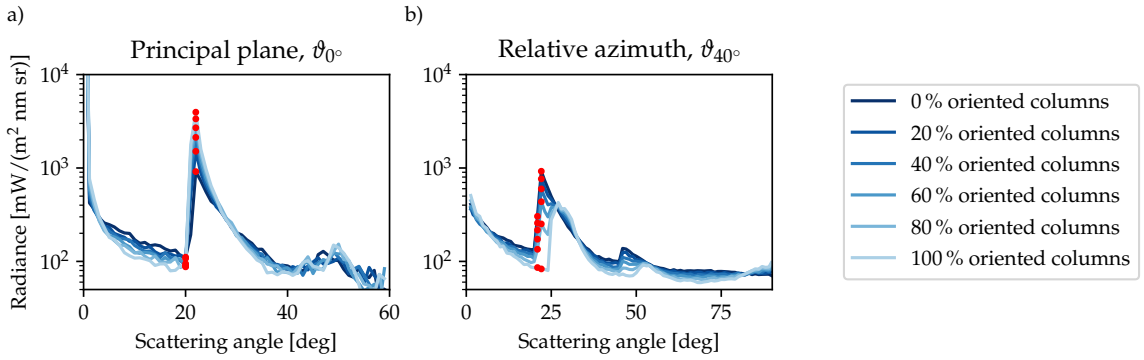

Abbildung 4.25: *Radiance distributions extracted from Fig. 4.21 in the a) principal plane ($\vartheta = 0°$) and b) between the almucantar and principal plane at $\vartheta = 40°$ for an increasing fraction of oriented ice crystal plates (AR = 2.5) at a wavelength of 550 nm. The radiance distribution in a) shows the cross section of the upper tangent arc, which occurs at the same scattering angle as the 22° halo. b) Radiance distribution across the 22° and 46° halo as a function of the scattering angle. The red dots indicate the maximum and minimum of each halo display in the vicinity of the 22° halo.*

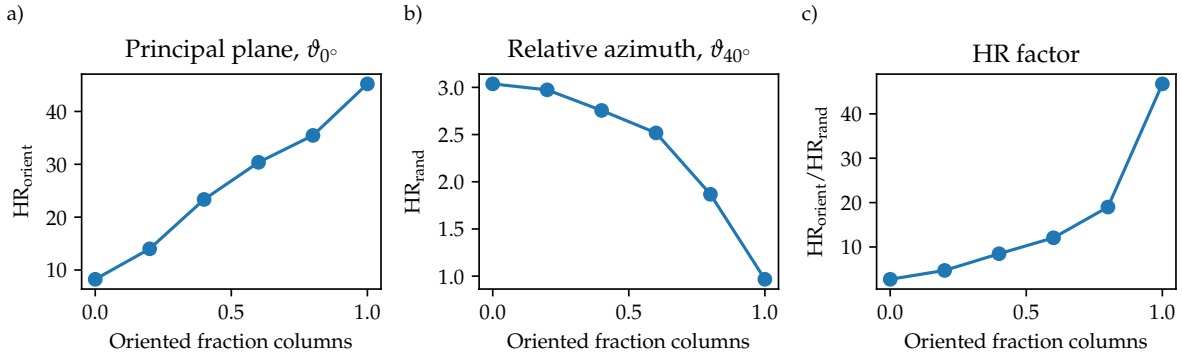

Abbildung 4.26: *Halo ratios calculated using the maximum and minimum radiance values of the halo display cross section, which are indicated by the red dots in Fig. 4.25, as a function of the oriented crystal fraction. a) Halo ratio of the 22° halo or upper tangent arc in the principal plane ($\vartheta = 0°$) as a measure of the fraction of oriented ice crystal columns, denoted as HR_{orient}. b) Halo ratio of the relative azimuth scan at $\vartheta = 40°$ as a measure of the randomly oriented crystal fraction, labeled with HR_{rand}. c) Halo ratio enhancement factor, calculated by HR_{orient}/HR_{rand}.*

Kapitel 5

Discussion

Previous studies investigating ice crystal properties such as shape, surface roughness and size are discussed in the following. The long-term HaloCam observations in Munich indicate that cirrus clouds which produce a visible 22° halo contain a SCF of about (50 ± 30) % on average. Within the measurement uncertainty of $\text{HaloCam}_{\text{RAW}}$ all habits could reproduce the observations with a different SCF. The 8 habits of the Yang et al. (2013) database clustered for columnar, hollow, and plate-like crystals with SCFs of ∼30%, ∼60% and ∼80%. In other words, smooth plates can produce an equally bright 22° halo as rough columns. This means columnar crystals are most effective in producing a 22° halo followed by hollow-ended columnar crystals and plate-like crystals. Using co-located ceilometer measurements the fraction of halo-producing cirrus clouds could be estimated to about 25%. It revealed that ice crystal plates best-match the $\text{HaloCam}_{\text{RAW}}$ observations in a scattering angle region between $19° \leq \Theta \leq 35°$ with a SCF of (80 ± 10) % and an effective radius of (22.3 ± 11.5) µm. However, the ice crystal plates of the Yang et al. (2013) parameterization produce a 46° halo for effective radii $\lesssim 50$ µm which was not visible in the evaluated $\text{HaloCam}_{\text{RAW}}$ scenes. Considering only LUT elements without 46° halo yields the solid column as best matching habit with a SCF of (40 ± 20) % and an effective radius of (28.8 ± 13.4) µm. In the following these results will be compared with the findings of other studies.

Retrievals of ice crystal habit from multi-angular satellite measurements was pioneered by Baran et al. (1998, 1999). They used radiance measurements at two different viewing angles from the Along Track Scanning Radiometer (ATSR-2) and found complex particles, such as bullet rosettes and polycrystals to best match the observations. Additional studies based on multi-angular radiance observations from the Polarization and Directionality of Earth Reflectance (POLDER) instrument, which measures the polarization state of the detected radiation in addition (Descloitres et al., 1998, Chepfer et al., 2001, Baran et al., 2001, Baran and Labonnote, 2006, Sun et al., 2006). These studies revealed that featureless phase functions better represent the measurements than phase functions of a single ice crystal habit. In general, the observed reflectances were highly variable and the retrieved ice particle shape depends on location and season. McFarlane and Marchand (2008) present a retrieval using measurements from Multi-angle Imaging Spectroradiometer (MISR) and (Moderate resolution imaging system) MODIS reflectances based on optical properties of single ice crystal habits. They state that hexagonal ice crystals (hollow columns and plate-like habits) were retrieved for 32% of the ice clouds and the remaining 68% could be represented best by complex crystals (rough aggregates and bullet rosettes). van Diedenhoven et al. (2012) retrieved rough plates with AR = 0.7 at $T < -38$ µm and AR = 0.15 AR = 0.7 at $T > -38$ µm using polarized reflectances from POLDER and PA-

RASOL during the TWP-ICE campaign. van Diedenhoven et al. (2013) retrieved rough compact and plate-like crystals with RSP polarized reflectances during the CRYSTAL-FACE campaign. Wang et al. (2014) used collocated Aqua/MODIS and CALIPSO/CALIOP observations from 2008 to retrieve optical and microphysical properties for optically thin ice clouds. They present a method to retrieve scattering phase functions based on the 1.38 µm near-IR channel and the optical thickness derived from the IR channels at 8.5 µm, 11 µm and 12 µm. A combination of roughened solid columns (55%), droxtals (35%), and smooth column aggregates (10%) was found as best-match of the inferred phase functions of cirrus clouds over ocean with an asymmetry factor of 0.778 at a wavelength of 0.65 µm. For the cirrus cases over land, however, Wang et al. (2014) state that it was difficult to find an appropriate habit mixture to fit the inferred phase function due to larger uncertainties in the derived cloud optical thickness. The best match in this case was a mixture of 76% severely roughened droxtals and 24% severely roughened solid bullet rosettes. Cole et al. (2014) used PARASOL polarization measurements to derive ice particle habit and surface roughness based on ice crystal phase functions of nine different habits and one habit mixture with 17 distinct levels of surface roughness. On a global scale, they found a compact aggregate as most commonly retrieved habit with mean roughness of $\sigma = 0.2$ and mean asymmetry factor of 0.77. Saito et al. (2017) developed an optimal estimation-based algorithm to retrieve cirrus optical thickness, cloud effective radius, fraction of (horizontally oriented) plates, and the degree of surface roughness using CALIOP and IIR (Infrared Imaging Radiometer) observations during 1 month in 2007. With an assumed ice crystal habit mixture of smooth plates and aggregates they found a bimodal distribution of surface roughness between 0 and 0.7. Since the distribution of retrieved surface roughness values peaks at both limits of the prescribed range, Saito et al. (2017) assume that the prescribed range may not be large enough. They state further the large number of retrieved aggregates with smooth surfaces is not consistent with previous studies (van Diedenhoven, 2014, Hioki et al., 2016). Possible reasons according to Saito et al. are that the column aggregate model may not be suitable for cirrus clouds and the backscattering intensity at ∼180° is underestimated with the used computing technique.

The results of this study agree with most of the discussed findings (e.g. McFarlane and Marchand (2008), Wang et al. (2014)) that the majority of cirrus clouds contain rough ice crystals. This was inferred from the long-term statistics of halo-producing cirrus clouds in Munich using HaloCam and ceilometer observations. 25% of the cirrus clouds produced a visible 22° halo indicating the presence of smooth hexagonal ice crystals. Thus 75% of the cirrus clouds which did not produce a 22° halo contained predominantly rough ice crystals. For the halo-producing cirrus clouds of the study with the $\text{HaloCam}_{\text{RAW}}$ observations, plates revealed to be the best-matching ice crystal habit in the 22° halo region followed by solid columns. However, the solid columns did not show a 46 halo in agreement with the observations for the 8 evaluated days. This result is similar to the findings of McFarlane and Marchand (2008) who found plate-like crystals and hollow columns as best-matching habits for the smooth crystal fraction. A new ice scattering model for the MODIS operational retrieval of ice cloud optical thickness and effective radius was introduced by Holz et al. (2016) which uses severely roughened aggregated columns from Yang et al. (2013) as single habit. This scattering model is used for the MODIS Collection 6 data product and has an asymmetry factor of about 0.75 in the mid-visible spectrum. According to Holz et al. (2016) this scattering model resolves the ice cloud optical thickness bias between CALIOP and MODIS observations. The results of this study also indicate that the assumption of predominantly roughened ice crystals might be justified even though 22° halos appear in about 25% of the observed cirrus clouds. When a 22° halo is present, however, a SCF of at least about

40% is required to reproduce the observations. It should be kept in mind that the results of this study were obtained from local measurements in Munich and for thin cirrus clouds, i.e. excluding tops of deep convective systems. The presented studies focus on satellite remote sensing which might be more sensitive to optically thicker ice clouds.

The retrieved effective radii in this study are, to the author's knowledge, the first statistical results for 22° halos and yield similar results for all 8 ice crystal habits with values between 5 µm and 30 µm with a mean value of 20 µm. Several studies investigated the size of halo-producing ice crystals like (Mishchenko and Macke, 1999, Fraser, 1979, Garrett et al., 2007) based on theoretical and analytical considerations. Mishchenko and Macke (1999) performed T-matrix calculations for circular ice crystal cylinders and found that a well-defined halo should be visible for ice crystal size parameters of the order of 100 and larger. Garrett et al. (2007) examined a lower and upper bound to the size of halo-producing ice crystals. They found that the minimum effective radius for crystal producing both a 22° and 46° halo amounts to about 10 µm based on an analysis of the scattering phase functions of Yang and Liou (1996) and Yang et al. (2000). They state that these results are similar to the findings of Mishchenko and Macke (1999) and the laboratory studies of Sassen and Liou (1979). An upper limit results from the criterion of random orientation which requires Reynolds numbers near unity, which occurs for compact ice crystals and $r_{\mathrm{eq}} \lesssim 100\,\mu\mathrm{m}$. Some ambiguity might occur since aggregated ice crystal such as bullet rosettes exhibit randomly oriented crystal faces while being oriented (Fraser, 1979, Sassen et al., 1994, Tape, 1994). Another indication for an upper limit are the findings of Mishchenko and Macke (1997) who found that "halo intensities erode when bubbles develop in larger ice crystals". Furthermore, Bailey and Hallett (2002) found that pristine shapes are mostly found in the laboratory for $r_{\mathrm{eq}} \lesssim 100\,\mu\mathrm{m}$. The equivalent radius is the radius of a circle with an equivalent geometric cross-section. Um and McFarquhar (2015) determined minimum size parameters for the formation of 22° halos as a function of AR resulting in 103, 90, 68, 45, 91, and 182 for ARs of 0.1, 0.25, 0.5, 1.0, 2.0, 4.0. For the 46° halo size parameters of 68, 45, 223 are required for ARs of 0.5, 1.0, and 2.0. It should be noted that the usage of the term "circumscribed halo" in Um and McFarquhar (2015) is wrong since halo displays produced by randomly oriented crystals are described, but a circumscribed halo is actually formed by horizontally oriented ice crystal columns at high solar elevations.

As discussed in Section 3.7.2 for halo-producing cirrus clouds with cloud base temperatures warmer than −35 °C the presence of water droplets cannot be completely excluded (Hu et al., 2010). However, Fig. 3.36 showed that the presence of water droplets has a small effect on the retrieved SCF since spherical water droplets act like rough ice crystals in diminishing the 22° halo.

Kapitel 6

Summary and Conclusions

This study investigates the information content of halo displays regarding ice crystal optical and microphysical properties. The main focus lies on the 22° halo which is formed by randomly oriented hexagonal ice crystals. It can be concluded that the 22° halo contains information on ice crystal shape, surface roughness, size. Analysis of scattering phase functions showed that the HR, as a measure for the brightness contrast of the halo, is primarily a function of ice crystal shape and surface roughness and depends to a minor degree on ice crystal size. However, an ambiguity exists that smooth plate-like crystals can produce an equally bright 22° halo as columnar crystals with increased surface roughness. The width of the 22° halo instead depends mainly on the ice crystal size and to a minor degree on ice crystal shape and roughness. These theoretical findings could be confirmed with the long-term HaloCam observations.

All evaluated HaloCam scenes did not show a 46° halo. The best-matching ice crystal habit for these observations is the solid column with a SCF of about $(40 \pm 20)\,\%$. Despite the large variability in habits and SCFs which reproduce the HaloCam observations, there seems to be a better agreement on effective radius among the different habits with a mean value of 20 µm and ranging between 5 µm and 30 µm.

In a first step different models of ice crystal single scattering properties were analyzed. For randomly oriented ice crystals different optical properties are available (Macke et al., 1996, Yang et al., 2013, e.g.). For this study the raytracing code of Macke et al. (1996) was used similar to van Diedenhoven (2014), however using the bug-fixed version. The bug, which was described by Konoshonkin et al. (2016), was fixed for this study by calculating the number of rays from a prescribed ray density and the respective projected crystal area instead of a fixed number of rays. This accounts for the changing projected area for different crystal orientations. This bug-fix had effects on both the 22° and 46° HR: the 22° HR is now monotonically increasing from thin plates ($AR < 1$) over compact particles ($AR = 1$) to long columns ($AR > 1$). Furthermore, the peak of the 46° halo occurred at $AR = 1$ before the bug fix and is now shifted to a slightly larger AR which can be explained with the ice crystal geometric cross section. It could be confirmed that the 22° and 46° halo ratio is determined by the ice crystal aspect ratio and surface roughness as shown in van Diedenhoven (2014). The analysis of the 22° HR revealed that the relationship between the ice crystal AR and the 22° HR is ambiguous in the sense that a smooth plate can produce an equally bright 22° halo as a roughened column.

Using the optical properties of the Yang et al. (2013) database (YANG), it was demonstrated that the power spillover index of the 22° halo is related to the size of the ice crystals as suggested by Flatau and Draine (2014). The authors also suggest that the FWHM of the 22° halo can be used as a measure of the ice crystal size. However, fitting a Gaussian distribution to the single

scattering phase functions was not stable enough to determine a reliable value for the FWHM due to the large forward scattering peak. Thus, for phase functions the power spillover index seems more suitable as an estimate of the ice crystal size.

In a second step the 22° halo ratio, power spillover index, and FWHM were investigated under multiple scattering conditions. For these sensitivity studies radiative transfer simulations were performed using libRadtran's DISORT solver and the YANG optical properties. Radiance distributions across the 22° halo were simulated for different ice crystal habits, SCFs, effective radii, COTs, AOTs, and surface albedos. Calculating the power spillover index for radiance distributions across the 22° halo showed a strong dependence on the COT. To determine the FWHM of the 22° halo peak, the background radiance distribution was subtracted before fitting a Gaussian distribution to the residual peak of the 22° halo. Applying this method to radiative transfer simulations of the 22° halo revealed that the FWHM is virtually insensitive to changes of the COT. Thus, to retrieve information about the ice crystal effective radius from 22° halo observations, the FWHM should be used instead of the power spillover index. Further sensitivity studies revealed that the FWHM primarily depends on ice crystal size while ice crystal habit and surface roughness play only a minor role. Also the HR was investigated under multiple scattering conditions. The HR depends on the COT, AOT and to a minor degree on the surface albedo. The COT introduces another ambiguity to the HR which exhibits a peak for COT ~ 1 and decreases for smaller as well as larger optical thicknesses. Thus, without additional observations the system is highly underdetermined.

In order to gain some information about ice crystal microphysical properties, the COT, AOT and surface albedo have to be determined with help of additional measurements. If these additional observations are not available, at least a lower limit for the fraction of smooth ice crystals can be derived from single scattering properties alone as stated by van Diedenhoven (2014). For a visible 22° halo, a minimum fraction of smooth crystals of 10% in case of columns or 40% in case of plates can be estimated if multiple scattering by aerosol and cloud particles is neglected. These assumptions allow to determine a minimum SCF for halo-producing cirrus clouds.

To perform long-term observations of halo displays the novel sun-tracking camera system HaloCam was developed for the automated observation of halo displays. The HaloCam system is weather-proof and consists of two cameras on a sun-tracking mount which ensures that the halo displays stay centered relative to the camera. HaloCam records pictures every 10 s after updating its position relative to the sun. The first camera, $\text{HaloCam}_{\text{JPG}}$, provides images in JPEG compression only with a sensor resolution of 1280×960 square pixels. Its lens has a field of view of 90° in the horizontal and 67° in the vertical direction. The second camera, $\text{HaloCam}_{\text{RAW}}$, provides images also in the "raw" format which is obtained directly from the sensor without compression or post-processing. $\text{HaloCam}_{\text{RAW}}$ features a lens with a horizontal FOV of 87° and a vertical FOV of 65° while the sensor has 1936×1216 square pixels. The most frequent halo displays are formed by either randomly oriented or oriented plates and columns and therefore contain the most important information about ice crystal properties. Thus, the camera setup was optimized for observing 22° halos, sundogs and upper/lower tangent arcs with high spatial and temporal resolution without loosing relevant information. The HaloCam camera system was installed in September 2013 on the rooftop platform of the Meteorological Institute in Munich, first operating $\text{HaloCam}_{\text{JPG}}$ only, followed by $\text{HaloCam}_{\text{RAW}}$ in September 2015.

In a first analysis the frequency of the 22° halo produced by cirrus clouds over Munich was investigated using more than 2.5 years of $\text{HaloCam}_{\text{JPG}}$ data. This analysis requires only a geometric calibration of the camera which allows to map the pixel coordinates to scattering angles.

For evaluating the long-term HaloCam observations in Munich an automated halo detection algorithm, called HaloForest, was developed. HaloForest is presented here for the detection of 22° halos but it can be extended for the detection of other halo types such as sundogs and upper/lower tangent arcs. The algorithm is based on a Random Forest classifier and was trained and tested against visually evaluated observations. With more than 88% of the test samples correctly classified as "22° halos" and more than 97% correctly classified as "no 22° halo", HaloForest is able to separate the two classes well. Applied to the more than 2.5 years of data, HaloForest detected 22° halos in about 2% of the total observation time during daylight.

A first estimate of ice crystal roughness was performed by evaluating the frequency of cirrus clouds that were accompanied by halo displays. For the long-term halo observations in Munich, co-located ceilometer measurements were used to evaluate the fraction of cirrus clouds. About 25% of the detected cirrus clouds in Munich occurred together with a 22° halo. These results imply that 25% of the clouds contained at least 10% smooth particles in case of columnar ice crystals and at least 40% in case of plate-shaped ice crystals. Extending HaloForest for more halo types (e.g. sundogs) would increase the fraction of "halo-producing" cirrus clouds above 25%. During the 6-weeks ACCEPT campaign the frequency of halo displays was evaluated visually and revealed that sundogs occurred in 70%, 22° halos in 60%, and upper tangent arcs in 30% relative to the total observation time. The fraction of halo-producing cirrus clouds yields about 27% for this dataset.

To further constrain the ice crystal optical and microphysical properties, multiple scattering has to be accounted for. This can be done by comparing the measured radiance distribution across the 22° halo with radiative transfer simulations assuming a range of ice crystal optical and microphysical properties. Additional observations are required to constraint COT and AOT. These can be provided by sunphotometer measurements which are available at the observation site at LMU in Munich. Look-up tables of simulated radiance distributions were compiled using the ice crystal optical properties of the YANG database for 9 different habits. To achieve continuous roughness levels, the optical properties of smooth and severely roughened ice crystals of a specific habit were mixed with SCFs ranging from 0% to 100% and RCF = 100% - SCF. Sensitivity test showed that if the retrieval is applied to uncalibrated measurements with unknown radiometric response the retrieved SCF can deviate up to 70% from the true value. If the uncertainty of the radiometric response is smaller than 25% the error in the retrieved SCF is smaller than about 15%.

This method was tested using specMACS calibrated radiance measurements of a 22° halo for two case studies on 24 March and 22 September 2015. The total measurement uncertainty of specMACS was estimated smaller than 5% (Ewald et al., 2015). Different ice crystal habits and SCFs match the observations within the measurement error showing an ambiguity between plate-shaped and columnar crystals as found from the analysis of the single scattering properties. On 24 March the AOT could be constrained to 0.30 ± 0.07 at 500 nm. During the measurements at 12:50 and 12:54 UTC the COT ranges between 0.5 and 1.6. SCFs between 10% and 90% for plates, 10-element plates, solid columns, hollow columns, 8-element columns, solid and hollow bullet rosettes matched the observations. No match was found for droxtals and 5-element plates. Considering the best match only, the SCF ranges around 40% for plates, 10-element plates and hollow columns and around 60% to 80% for the solid columns, 8-element columns and bullet rosettes.

On 22 September the AOT amounts to about 0.15 ± 0.02 and the apparent cirrus optical thickness during the scan times at 9:38, 10:35, and 11:00 UTC ranges between 0.3 and 3.1. At 9:38 UTC the 22° halo is pronounced enough to considerably constrain possible ice crystal habits

and SCFs. Only the 5-element plates match the observations with a SCF ranging from 15% to 25%. At 10:35 UTC matching crystal habits are plates and 5-element plates with a SCF of 40% to 55% and 8-element columns with a SCF of 90%. At 11:00 UTC no 22° halo is visible and the RCF is larger than about 50% for all matching habits. Of the 9 available habits a match is found for 8 habits, only the droxtals do not match the observations.

Besides the YANG optical properties the GO optical properties were tested. It revealed that for each aspect ratio a corresponding SCF could be found to represent the observations within the measurement uncertainty. A best match was retrieved for AR = 3.5 with a SCF of 10% at 12:50 UTC and AR = 0.3 with a SCF of 75% at 12:54 UTC. Compared to YANG the ice crystal aspect ratio and thus the ice crystal shape of the GO optical properties is a free parameter. This is an advantage for the analysis of 22° halos since the halo ratio, i.e. the brightness contrast, of the 22° halo is mainly determined by ice crystal aspect ratio and surface roughness. However, the conventional geometric optics method to calculate ice crystal optical properties has several shortcomings for smaller pristine ice crystals with random orientation which form the 22° halo.

Another test was performed using radiative transfer simulations of completely random mixtures of ice crystal optical properties. This test demonstrates that it is possible to match the specMACS observations with several different random mixtures. The best-match mixture consists of 50% smooth and 35% rough 10-element plates, 8% smooth droxtals, and 5% rough solid columns. The remaining ice crystal habits sum up to 2%. This test demonstrated that arbitrary mixtures of multiple ice crystal habits, surface roughness, and size might yield a mixture which better represents the observations than using a single habit with smooth and rough crystal fraction. However, the retrieved habit mixtures are "radiatively equivalent effective shapes", as stated by McFarlane and Marchand (2008) and Cole et al. (2013). Thus, allowing for arbitrary mixtures of ice crystal properties does not necessarily increase the information gain in a system which is not well constrained per se.

Since specMACS is not weather-proof, long-term observations of ice crystal optical and microphysical properties were performed using $\text{HaloCam}_{\text{RAW}}$. This camera provides the "raw" signal directly from the sensor and was geometrically and radiometrically calibrated. For the retrieval the red channel was used with a total measurement uncertainty of better than 15%. HaloForest was used to select HaloCam images with a 22° halo. For 8 days in total 22° halo observations with simultaneous sunphotometer measurements were available which are necessary to constrain both AOT and COT. In total about 4400 $\text{HaloCam}_{\text{RAW}}$ images were analyzed and compared with LUTs of radiative transfer simulations. For the LUTs the optical properties of smooth and severely roughened ice crystals of a specific habit of the YANG database were mixed as for the specMACS case studies. With this dataset the ice crystal optical and microphysical properties were retrieved which best match the observations. The results showed that ice crystal plates were the overall best-matching habit with a SCF of (80 ± 10) % and an effective radius of (22.3 ± 11.5) µm with asymmetry factors ranging between 0.880 ± 0.021. However, the ice crystal plates of the YANG database in this size range produce a pronounced 46° halo which is not visible in the evaluated HaloCam images. Filtering the LUT for elements without a 46° halo yields the solid columns as best-matching ice crystal habits with a SCF of (40 ± 20) %, effective radius of (23.8 ± 13.4) µm and asymmetry factors of 0.788 ± 0.008. For all habits the average SCF amounts to about 50% with a lower limit of 20% and an upper limit of 80% within a 2σ confidence interval. The average SCF for columnar, hollow, and plate-shaped crystals amounts to about ∼30%, ∼60%, ∼80%, which is about 30% (solid columns) to 40% (plates) larger than the minimum SCF estimated from single scattering properties. The variation of the retrieved effective radius between the ice crystal habits is much smaller than for the SCF and yields an

overall mean of about 18 µm and ranges between 5 µm and 38 µm within a 2σ confidence interval.

During the ML-CIRRUS campaign HaloCam observations on 1 April 2014 showed complex halo displays lasting for several hours with a rare Parry arc for a few minutes. Additional measurements during this campaign were performed with the MIRA-35 cloud radar, the POLIS lidar, the CHM15kx ceilometer and the Cimel and SSARA sunphotometers, as well as with the hyperspectral imaging radiometer specMACS. A unique dataset could be collected which is complemented by in situ observations during two overflights of the HALO research aircraft. A first evaluation of the SID3 images revealed a fraction of smooth crystals between 4% and 30% with the majority of ice crystals showing speckled scattering signatures on the SID3 images which indicates complex or rough ice crystals.

To retrieve the fraction of oriented ice crystals from halo displays the Monte Carlo radiative transfer model MYSTIC was extended by the raytracing algorithm CrystalTrace. The HaloCam observations of 1 April 2014 could roughly be reproduced using MYSTIC combined with CrystalTrace with the OPAC desert dust aerosol and a mixture of 45% randomly oriented columns, 10% oriented plates, 35% oriented columns and 10% columns in Parry-orientation. A method was proposed to retrieve the fraction of oriented ice crystal plates (columns) from simultaneous observation of the 22° halo and sundogs (upper tangent arc). While the HR of the 22° halo serves as a reference for the fraction of halo-producing crystals, the HR of the sundogs or upper tangent arc relative to the HR of the 22° halo should contain information about the fraction of oriented ice crystals. Since the calculation of LUT for oriented ice crystals requires the fraction of oriented crystals and the distortion width of the orientation as additional parameters together with different SCFs and different mixtures of plates and columns, the evaluation of the 1 April ML-CIRRUS case is beyond the scope of this work and should be investigated in future studies.

This study demonstrated that halo displays contain information about ice crystal properties such as ice crystal shape, surface roughness, size and orientation. By providing long-term observations of halo displays HaloCam observations can contribute to a better understanding of these ice crystal properties. Using the HaloForest this study highlights the potential and feasibility of a completely automated method to collect and evaluate halo observations. Long-term observations of 22° halos allow to estimate a minimum fraction of smooth ice crystals in cirrus clouds. Calibrated radiance observations with HaloCam compared with LUTs from radiative transfer simulations can contribute to systematically investigate ice crystal surface roughness, shape and orientation in cirrus clouds. The long-term observations in Munich indicate that about 25% of the cirrus clouds contained a SCF of about (50 ± 30) % with ice crystal effective radii of about (20 ± 10) µm regardless of the ice crystal habit. Accounting for the missing 46° halo in the HaloCam observations, solid columns reproduced best the measured radiance distributions across the 22° halo. Implemented on different sites, HaloCam in combination with the HaloForest detection algorithm can provide a consistent dataset for climatological studies. These observations might be a valuable contribution to derive ice crystal optical properties which represent typical cirrus clouds. Representative ice crystal optical properties are required for remote sensing of cirrus clouds as well as climate modeling. Furthermore, the HaloCam observations can also be used to constrain ice crystal properties for operational ground-based remote sensing of cirrus clouds.

Kapitel 7

Outlook

This study demonstrates the potential of halo displays to provide information about ice crystal shape, roughness, size and orientation. With the new automated camera system HaloCam and the halo detection algorithm HaloForest this study provides, for the first time to the author's knowledge, a framework for consistent and automated observations of halo displays. By applying the RICO retrieval to long-term observations of calibrated radiances, HaloCam allows for the first time to systematically investigate typical ice crystal properties of halo-producing cirrus clouds.

New aspects and further interesting questions occurred in the course of this work which will be explained in the following. The results of this study showed that the parameterization of ice crystal size and aspect ratio of the Yang et al. (2013) optical properties do not always reproduce the observations, especially small to medium-sized plates which always show both the 22° and 46° halo. The raytracing code of Macke et al. (1996) allows to calculate optical properties with the aspect ratio as free parameter. However, these optical properties are only valid in the Geometric Optics approximation which do not represent well ice crystal sizes less than 50 µm. Thus, for studying halo displays optical properties calculated with improved Geometric Optics methods as in Yang et al. (2013) would be necessary which provide ice crystal size and aspect ratio as independent parameters instead of ice crystal habit.

In this study a monodisperse size distribution following an exponential distribution with $\mu = 1$ was used to calculate the bulk optical properties. Baran (2012) states that the shape of cirrus particle size distributions is often bi-modal as reported by (Heymsfield and Miloshevich, 1995, Ivanova et al., 2001, Field et al., 2005, Zhao et al., 2011). Investigating different size distributions for the halo-producing cirrus clouds could reveal that the smooth ice crystals which produce the halo displays follow a different size distribution than the rough ice crystals.

Investigating the information content of the 22° halo revealed that, especially for ground-based measurements, the system depends on many parameters like the optical thickness of the cirrus and aerosol, the aerosol type, the surface albedo and of course the ice crystal shape, surface roughness, and particle size. To minimize the influence of the aerosol, the retrieval was applied to the red channel of HaloCam. Additionally the HaloCam measurements could be performed on top of a mountain, for example at the observation platform on mount Zugspitze, which is located above the boundary layer.

The HaloCam system consists of two low-cost off the shelf cameras and a suntracking mount which can easily be set-up and installed at multiple locations, as it was demonstrated during the ACCEPT campaign in the Netherlands. To constrain COT and AOT, additional sunphotometer measurements are required for the quantitative retrieval of ice crystal properties. Thus, Halo-

Cam could be installed alongside the AERONET instruments. The automated halo detection algorithm HaloForest could also be used to filter out events of homogeneous cirrus clouds in the AERONET dataset. Most 22° halos form in thin, homogeneous cirrus clouds which are difficult to filter from the sunphotometer data (Smirnov et al., 2000) and are often causing a bias in the retrieved AOT (e.g. Chew et al. (2011)).

Furthermore, HaloForest should be extended for the detection of sundogs and upper tangent arcs to obtain a long-term statistic of halo displays formed by oriented ice crystals. With help of radiative transfer simulations with MYSTIC and CrystalTrace a method was proposed to retrieve the fraction of oriented ice crystal from the simultaneous observation of the 22° halo and sundogs or the upper tangent arc. CrystalTrace needs to be extended to account for ice crystal surface roughness and diffraction. Then, the information content of halo displays produced by oriented crystals should be further investigated by sensitivity studies. Besides the ice crystal shape and surface roughness, the brightness of these halo displays depends also on the fraction of oriented ice crystals and the orientation parameter. It should be noted that the simultaneous observation of different halo displays does not necessarily constrain ice crystal shapes: although the presence of sundogs indicates ice crystal plates other ice crystal shapes could still be present in the cirrus cloud and a simultaneous 22° halo could be formed by randomly oriented ice crystal plates, columns or other hexagonal crystals. The ML-CIRRUS observations of 1 April 2014 provide a unique dataset of collocated airborne in-situ and ground-based remote sensing observations of different instruments. This dataset contains valuable measurements of several halo displays which were observed over several hours in very homogeneous conditions. Accompanied by transported Saharan dust, the evaluation of these observations is challenging but it can provide valuable insights on oriented ice crystals from a remote sensing as well as an in-situ perspective.

Besides cirrus clouds, the HaloCam observations also contain contrails and contrail cirrus which sometimes form halo displays as well. Evaluating the HaloCam observations regarding the formation of halo displays by contrails could provide further information of the ice crystals properties of these clouds which have a large influence on the global radiation budget (e.g. Schumann (2005)).

This study focused on observations of halo displays during daytime only. Sassen et al. (2003a) stated that the halo observations during night time with the moon as light source showed different cirrus properties than the daytime observations. This could be investigated by using a moon-tracking algorithm in addition to the sun-tracking algorithm.

Anhang A

Decision trees and random forest classifier

The subsequent sections provide more details on decision trees and the random forest classifier presented in Section 3.6.

A.1 Decision trees

The following description is based on Alpaydin (2010) and Raschka (2015). Decision trees start with a root node followed by internal decision nodes, branches and terminal nodes, called leaves. A typical example of a single decision tree, as used for HaloForest, is shown in Fig. A.1. For a

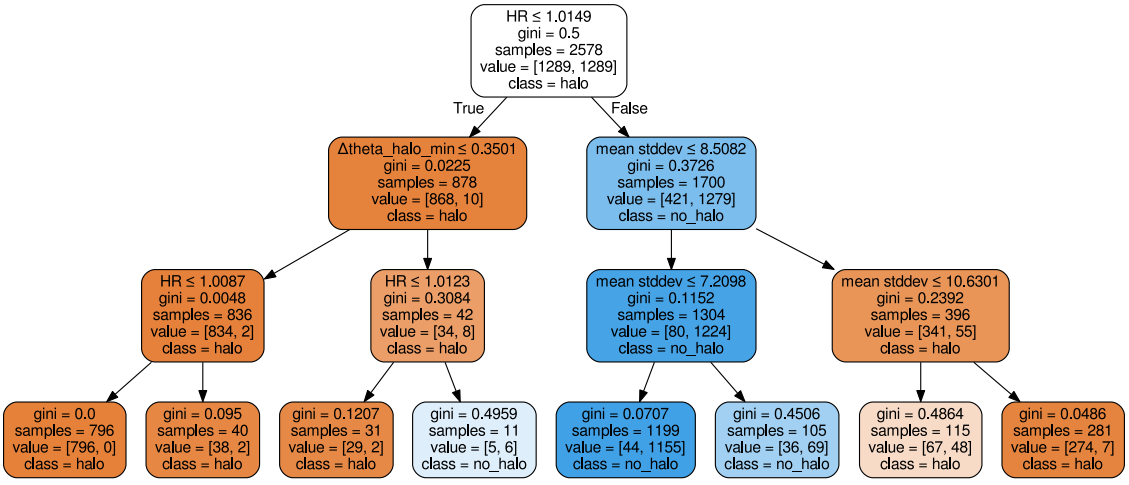

Abbildung A.1: *Example for a decision tree for a selection of three HaloCam image features confined to a maximum depth of three layers. The two classes, "halo" and "no halo" are depicted by red and blue color. The transparency of the color represents the impurity of the class.*

better visualization, the tree is grown using only three of the eight features and is pruned to a depth of three layers. The explanation provided here focuses on the structure of tree rather than the exact numbers of the threshold tests which differ from the ones used by HaloForest. The halo ratio (HR), the mean standard deviation, and $\Delta\vartheta_{\mathrm{halo,\,min}}$ are used as features in this case, which are displayed in the first line of each node box with the respective threshold test.

At each decision node a threshold test is applied to one element of the n-dimensional feature vector (here, $n = 3$) which best splits the set of samples. The metric to determine the best split in this study is the Gini impurity index, which is defined by Raschka (2015) as

$$I_G(t) = 1 - \sum_{i=1}^{c} p(i|t)^2 \,, \tag{A.1}$$

with c the number of classes and $p(i|t)$ the fraction of samples which belongs to class i at node t. The Gini index takes a minimum value for the maximum information gain (all the samples at node t belong to one class) and the index is maximum for a uniform distribution. The discrete result (here, True or False) of the threshold test decides which of the following branches is chosen. The node boxes are connected by arrows representing the branches of the tree. They are colored depending on the dominating class in the samples which is noted at the bottom of each box: red for "22° halo" and blue for "no 22° halo". The more transparent the color the higher the impurity of the classes and the larger the Gini impurity index. This splitting process is repeated recursively at each child node until a leaf node is reached. A leaf node is hit when all the samples in the subset belong to the same class, or when splitting does not add more information. By repeating this recursive decision process the n-dimensional feature space is subdivided into the pre-defined classes on a path following from the root down. Figure 3.32 shows examples of the resulting decision boundaries as 2-dimensional projections for a selection of feature pairs. The decision tree is trained using a set of labeled training samples. During training the tree grows by adding branches and leaves depending on the complexity of the data, which can lead to over-fitting. By growing an ensemble of decision trees this issue can be improved, which is the idea of random forest classifiers.

A.2 Random forest classifier implementation

In this study the random forest classifier was used, which is described by Breiman (2001) and implemented in the python module scikit-learn (Pedregosa et al. (2011), version 0.18.1). The trees are trained by applying the bootstrap aggregation (bagging) method (Breiman, 1996), i.e. by using a subset of the training samples which is chosen randomly with replacement and has the same size as the original input samples. This implementation predicts the class of a sample by averaging the probabilistic prediction of all individual decision trees instead of using the majority vote among the trees. The function call allows to define a number of parameters: the number of trees is set to 100 and a maximum number of 3 features ($\log_2(n)$ with n features) is considered for searching the best split. These parameters are chosen to minimize the out-of-bag (OOB) error, as shown in Fig. A.2. For an increasing number of estimators (trees) the OOB error stabilizes for around 100 trees and is in general smaller for a confined number of features considered at each split.

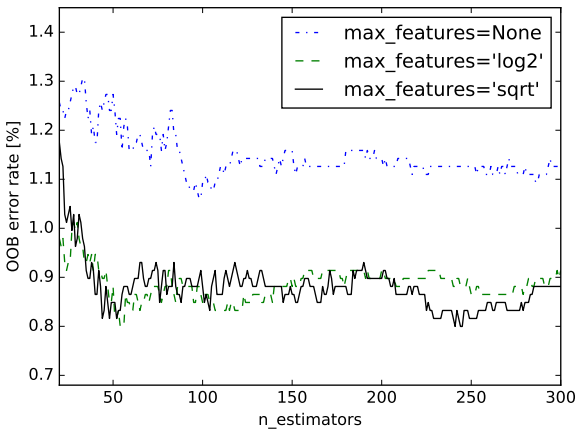

Abbildung A.2: *Out-of-bag error for different values of* n_estimators *(number of trees) for three different realizations of the random forest classifier by changing the number of features considered at each split.*

Anhang B

Projection of the 22° halo

The geographic coordinates where the albedo data has to be analyzed were determined by calculating the projection of the 22° halo a cirrus cloud layer at height z. Viewing the halo from the ground defines a cone with an opening angle of $\theta = 22°$ centered around the sun. The cross-section of this cone with a plane-parallel cirrus cloud, represented by a plane at height z, describes an ellipse with the sun in the focal point. Let the plane be located at $z = 0$. The

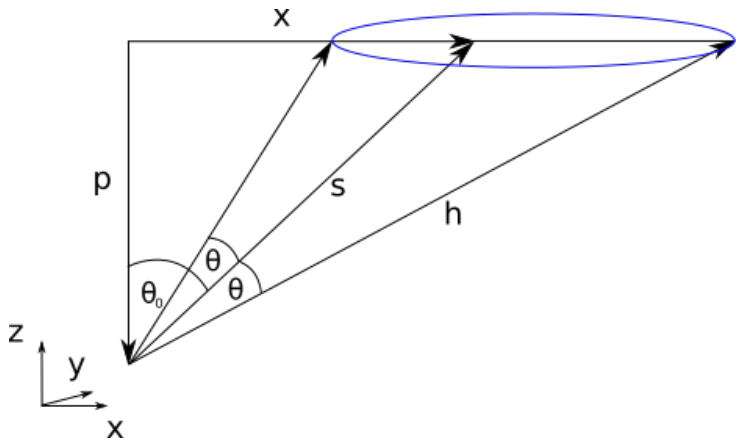

Abbildung B.1: *Geometry of the 22° halo projected onto a cloud in the x-y-plane at height $z = 0$. The projected 22° halo has the shape of an ellipse with the sun in the focal point. The position of the sun is denoted with the solar zenith angle θ_0. The observer is located at point $\overrightarrow{p}$ with $\overrightarrow{s}$ pointing into the sun and with $\overrightarrow{h}$ pointing at the 22° halo. The elliptic shape of the projected 22° halo is the result of the intersection of a cone with opening angle θ and the x-y-plane. In case of the 22° halo $\theta = 22°$ and in case of the 46° halo $\theta = 46°$, accordingly.*

coordinates of the position of the sun is

$$\overrightarrow{s} = (\sin\theta_0,\, 0,\, \cos\theta_0) = (\sin\theta_0,\, 0,\, \mu_0)\,, \tag{B.1}$$

with the solar zenith angle θ_0. The observer is located at point $\overrightarrow{p}$

$$\overrightarrow{p} = (0,\, 0,\, -p_3)\,. \tag{B.2}$$

Let $\overrightarrow{h}$ describe the points on the halo projected on the plane at $z = 0$. Then the following conditions must be fulfilled:

$$\overrightarrow{h} \cdot \overrightarrow{s} = \cos\theta = \mu\,, \tag{B.3}$$

and

$$|\overrightarrow{h}| = 1\,. \tag{B.4}$$

assuming $\overrightarrow{s}$ is already normalized. The points of the projected halo x relative to the point p can then be found by a linear combination of p and h

$$\overrightarrow{x} = \overrightarrow{p} + \alpha \cdot \overrightarrow{h}\,. \tag{B.5}$$

where $\overrightarrow{x} = (x_1,\, x_2,\, x_3)$. With $x_3 = 0$ $\overrightarrow{x} = 0$ it follows that $\alpha = \overrightarrow{p}\,/\,\overrightarrow{h} = p_3/h_3 \equiv p/h$.
Then

$$\overrightarrow{h} = \overrightarrow{x}/\alpha = \overrightarrow{x}/(\overrightarrow{p}\,/\,\overrightarrow{h})\,. \tag{B.6}$$

To fulfill $|\overrightarrow{h}| = 1$

$$|\overrightarrow{x}/(\overrightarrow{p}\,/\,\overrightarrow{h})| = 1\,, \tag{B.7}$$

which can be expressed by the vector components

$$h^2\,\frac{x_1^2}{p^2} + h^2\,\frac{x_2^2}{p^2} + h^2 = 1\,, \tag{B.8}$$

or

$$\frac{x_1^2}{p^2} + \frac{x_2^2}{p^2} + 1 = \frac{1}{h^2}\,. \tag{B.9}$$

The condition $\overrightarrow{h} \cdot \overrightarrow{s} = \mu$ can also be written as

$$h_1 \sin\theta_0 + h_3 \cos\theta_0 = \mu\,, \tag{B.10}$$

which yields

$$\frac{1}{h^2} = (\frac{x_1}{p}\sin\theta_0 + \cos\theta_0)^2/\mu^2\,. \tag{B.11}$$

Using Eq. (B.9) the vector $\overrightarrow{x}$ can be calculated by

$$x_1^2 + x_2^2 = (\frac{1}{h^2} - 1)\,p^2\,, \tag{B.12}$$

with

$$h = \mu/(\frac{x_1}{p}\sin\theta_0 + \cos\theta_0)\,. \tag{B.13}$$

Literaturverzeichnis

Allied Vision Technologies GmbH, 2015: *Manta Technical Manual*. `https://www.alliedvision.com/en/products/machine-vision-cameras/detail/Manta/G-235/action/pdf.html`.

Alpaydin, E., 2010: *Introduction to Machine Learning*. 2d ed., Adaptive computation and machine learning, MIT Press, Cambridge.

Anderson, G., S. Clough, F. Kneizys, J. Chetwynd, and E. Shettle, 1986: AFGL Atmospheric Constituent Profiles (0-120 km). Tech. Rep. AFGL-TR-86-0110, AFGL (OPI), Hanscom AFB, MA 01736.

Arnott, W. P., Y. Y. Dong, J. Hallett, and M. R. Poellot, 1994: Role of small ice crystals in radiative properties of cirrus: A case study, FIRE II, November 22, 1991. *Journal of Geophysical Research: Atmospheres*, **99 (D1)**, 1371–1381, doi:10.1029/93JD02781.

Auer, A. H. and D. L. Veal, 1970: The dimension of ice crystals in natural clouds. *J. Atmos. Sci.*, **27 (6)**, 919–926.

Bailey, M. and J. Hallett, 2002: Nucleation effects on the habit of vapour grown ice crystals from −18 to −42°C. *Quarterly Journal of the Royal Meteorological Society*, **128 (583)**, 1461–1483, doi:10.1002/qj.200212858304, `http://dx.doi.org/10.1002/qj.200212858304`.

Bailey, M. and J. Hallett, 2004: Growth rates and habits of ice crystals between -20° and -70°. *J. Atmos. Sci.*, **61**, 514–544.

Bailey, M. P. and J. Hallett, 2009: A Comprehensive Habit Diagram for Atmospheric Ice Crystals: Confirmation from the Laboratory, AIRS II, and Other Field Studies. *J. Atmos. Sci.*, **66 (9)**, 2888–2899, doi:10.1175/2009JAS2883.1, `http://dx.doi.org/10.1175/2009JAS2883.1`.

Baldridge, A., S. Hook, C. Grove, and G. Rivera, 2009: The ASTER spectral library version 2.0. *Remote Sensing of Environment*, **113**, 711 – 715.

Baran, A., P. Francis, S. Havemann, and P. Yang, 2001: A study of the absorption and extinction properties of hexagonal ice columns and plates in random and preferred orientation, using T-Matrix theory and aircraft observations of cirrus. *J. Quant. Spectrosc. Radiat. Transfer*, **70**, 505–518.

Baran, A., P. Watts, and J. Foot, 1998: Potential retrieval of dominating crystal habit and size using radiance data from a dual-view and. *Journal of Geophysical Research*, **103 (D6)**, 6075–6082.

Baran, A., P. Watts, and P. Francis, 1999: Testing the coherence of cirrus microphysical and bulk properties retrieved from dual-viewing multispectral satellite radiance measurements. *Journal of Geophysical Research*, **104 (D24)**, 31 673–31 683.

Baran, A. J., 2012: From the single-scattering properties of ice crystals to climate prediction: A way forward. *Atmospheric Research*, **112 (Supplement C)**, 45–69, doi:10.1016/j.atmosres.2012.04.010, URL `http://www.sciencedirect.com/science/article/pii/S0169809512001160`.

Baran, A. J., K. Furtado, L.-C. Labonnote, S. Havemann, J.-C. Thelen, and F. Marenco, 2015: On the relationship between the scattering phase function of cirrus and the atmospheric state. *Atmos. Chem. Phys.*, **15 (2)**, 1105–1127, doi:10.5194/acp-15-1105-2015.

Baran, A. J. and L. C. Labonnote, 2006: On the reflection and polarisation properties of ice cloud . *J. Quant. Spectrosc. Radiat. Transfer*, **100 (1–3)**, 41–54, doi:10.1016/j.jqsrt.2005.11.062, {VIII} Conference on Electromagnetic and Light Scattering by Nonspherical ParticlesVIII Conference on Electromagnetic and Light Scattering by Nonspherical Particles.

Bass, M., (Ed.) , 2010: *Handbook of Optics, Third Edition Volume I: Geometrical and Physical Optics, Polarized Light, Components and Instruments*. The McGraw-Hill Companies.

Baumgartner, A., 2013: Characterization of Integrating Sphere Homogeneity with an Uncalibrated Imaging Spectrometer. *Proc. WHISPERS 2013*, 1–4, `http://elib.dlr.de/83300/`.

Baumgartner, A., P. Gege, C. Köhler, K. Lenhard, and T. Schwarzmaier, 2012: Characterisation methods for the hyperspectral sensor HySpex at DLR's calibration home base. `http://elib.dlr.de/78685/`.

Bayer, B., 1975: Color imaging array. US Patent 3,971,065, uS Patent 3,971,065.

Bergeron, T., 1935: On the Physics of Clouds and Precipitation. *Proc. 5th Assembly UGGI*, Vol. 2, t935.

Bi Lei and Yang Ping, 2014: Accurate simulation of the optical properties of atmospheric ice crystals with the invariant imbedding T-matrix method. *J. Quant. Spectrosc. Radiat. Transfer*, **138**, 17–35, doi:10.1016/j.jqsrt.2014.01.013.

Bradski, D. G. R. and A. Kaehler, 2008: *Learning Opencv, 1st Edition*. 1st ed., O'Reilly Media, Inc., Sebastopol, CA.

Breiman, L., 1996: Bagging Predictors. *Machine Learning*, **24 (2)**, 123–140, doi:10.1023/A:1018054314350.

Breiman, L., 2001: Random Forests. *Machine Learning*, **45 (1)**, 5–32, doi:10.1023/A:1010933404324.

Buras, R., T. Dowling, and C. Emde, 2011: New secondary-scattering correction in DISORT with increased efficiency for forward scattering. *J. Quant. Spectrosc. Radiat. Transfer*, **112**, 2028–2034.

Chandrasekhar, S., 1960: *Radiative Transfer*. Dover Publications, New York, 393 pp.

Chepfer, H., G. Brogniez, P. Goloub, F. M. Bréon, and P. H. Flamant, 1999: Observations of horizontally oriented ice crystals in cirrus clouds with POLDER-1/ADEOS-1. *J. Quant. Spectrosc. Radiat. Transfer*, **63 (2)**, 521–543, doi:10.1016/S0022-4073(99)00036-9, http://www.sciencedirect.com/science/article/pii/S0022407399000369.

Chepfer, H., P. Goloub, J. Riedi, J. F. De Haan, J. Hovenier, and P. Flamant, 2001: Ice crystal shapes in cirrus clouds derived from POLDER/ADEOS-1. *Journal of Geophysical Research*, **106**, 7955–7966.

Chew, B. N., J. R. Campbell, J. S. Reid, D. M. Giles, E. J. Welton, S. V. Salinas, and S. C. Liew, 2011: Tropical cirrus cloud contamination in sun photometer data. *Atmospheric Environment*, **45 (37)**, 6724–6731, doi:10.1016/j.atmosenv.2011.08.017, http://www.sciencedirect.com/science/article/pii/S1352231011008375.

CIE, 1986: Standard on Colorimetric Observers. *Commission Internationale de l'Eclairage CIE*.

Cole, B. H., P. Yang, B. A. Baum, J. Riedi, and L. C.-Labonnote, 2014: Ice particle habit and surface roughness derived from PARASOL polarization measurements. *Atmos. Chem. Phys.*, **14 (7)**, 3739–3750, doi:10.5194/acp-14-3739-2014.

Cole, B. H., P. Yang, B. A. Baum, J. Riedi, L. C.-Labonnote, F. Thieuleux, and S. Platnick, 2013: Comparison of PARASOL Observations with Polarized Reflectances Simulated Using Different Ice Habit Mixtures. *Journal of Applied Meteorology and Climatology*, **52 (1)**, 186–196, doi:10.1175/JAMC-D-12-097.1, URL https://doi.org/10.1175/JAMC-D-12-097.1, https://doi.org/10.1175/JAMC-D-12-097.1.

Cox, C. and W. Munk, 1954: Measurement of the roughness of the sea surface from photographs of the sun's glitter. *Journal of the Optical Society of America*, **44 (11)**, 838–850.

Davis, J., T. McKee, and S. Cox, 1985: Application of the Monte Carlo method to problems in visibility using a local estimate: an investigation. *Applied Optics*, **24 (19)**, 3193–3205.

Descloitres, J., J.-C. Buriez, F. Parol, and Y. Fouquart, 1998: POLDER observations of cloud bidirectional reflectances compared to a plane-parallel model using the International Satellite Cloud Climatology Project cloud phase functions. *Journal of Geophysical Research*, **103 (D10)**, 11 411–11 418.

Eichler, H., A. Ehrlich, M. Wendisch, G. Mioche, J.-F. Gayet, M. Wirth, C. Emde, and A. Minikin, 2009: Influence of ice crystal shape on retrieval of cirrus optical thickness and effective radius: A case study. *Journal of Geophysical Research*, **114 (D19)**, n/a–n/a, doi:10.1029/2009JD012215, d19203, http://dx.doi.org/10.1029/2009JD012215.

Emde, C., R. Buras, and B. Mayer, 2011: ALIS: An efficient method to compute high spectral resolution polarized solar radiances using the Monte Carlo approach. *J. Quant. Spectrosc. Radiat. Transfer*, **112**, 1622–1631.

Emde, C. and B. Mayer, 2007: Simulation of solar radiation during a total solar eclipse: A challenge for radiative transfer. *Atmos. Chem. Phys.*, **7**, 2259–2270, doi:10.5194/acp-7-2259-2007.

Emde, C., et al., 2016: The libRadtran software package for radiative transfer calculations (version 2.0.1). **9 (5)**, 1647–1672, doi:10.5194/gmd-9-1647-2016.

Ewald, F., 2016: Retrieval of vertical profiles of cloud droplet effective radius using solar reflectance from cloud sides. Ph.D. thesis, Ludwig-Maximilians-Universität München, http://nbn-resolving.de/urn:nbn:de:bvb:19-205322.

Ewald, F., T. Kölling, A. Baumgartner, T. Zinner, and B. Mayer, 2015: Design and characterization of specMACS, a multipurpose hyperspectral cloud and sky imager. *Atmos. Meas. Tech. Discuss.*, **8 (9)**, 9853–9925, doi:10.5194/amtd-8-9853-2015.

Feister, U. and R. Grewe, 1995: Spectral albedo measurements in the UV and visible region over different types of surfaces. *Photochemistry and Photobiology*, **62**, 736–744, doi:10.1111/j.1751-1097.1995.tb08723.x.

Field, P. R., R. J. Hogan, P. R. A. Brown, A. J. Illingworth, T. W. Choularton, and R. J. Cotton, 2005: Parametrization of ice-particle size distributions for mid-latitude stratiform cloud. *Quarterly Journal of the Royal Meteorological Society*, **131 (609)**, 1997–2017, doi:10.1256/qj.04.134, URL http://dx.doi.org/10.1256/qj.04.134.

Findeisen, W., 1938: Die kolloidmeteorologischen Vorgänge bei der Niederschlagsbildung. *Meteor. Z*, **55**, 121–133.

Flatau, P. J. and B. T. Draine, 2014: Light scattering by hexagonal columns in the discrete dipole approximation. *Opt. Express*, **22 (18)**, 21 834–21 846, doi:10.1364/OE.22.021834.

Forster, L., M. Seefeldner, M. Wiegner, and B. Mayer, 2017: Ice crystal characterization in cirrus clouds: a sun-tracking camera system and automated detection algorithm for halo displays. *Atmos. Meas. Tech.*, **10 (7)**, 2499–2516, doi:10.5194/amt-10-2499-2017, https://www.atmos-meas-tech.net/10/2499/2017.

Fraser, A. B., 1979: What size of ice crystals causes the halos? *J. Opt. Soc. Am.*, **69 (8)**, 1112–1118, doi:10.1364/JOSA.69.001112.

Garrett, T. J., M. B. Kimball, G. G. Mace, and D. G. Baumgardner, 2007: Observing cirrus halos to constrain in-situ measurements of ice crystal size. *Atmos. Chem. Phys. Discuss.*, **7**, 1295–1325, doi:10.5194/acpd-7-1295-2007, https://www.atmos-chem-phys-discuss.net/7/1295/2007.

Gayet, J., O. Crepel, J. Fournol, and S. Oshchepkov, 1997: A new airborne polar Nephelometer from the measurements of optical and microphysical cloud properties. Part I: Theoretical design. *Ann. Geophysicae*, **15**, 451–459.

Gayet, J.-F., G. Mioche, V. Shcherbakov, C. Gourbeyre, R. Busen, and A. Minikin, 2011: Optical properties of pristine ice crystals in mid-latitude cirrus clouds: a case study during CIRCLE-2 experiment. *Atmos. Chem. Phys.*, **11 (6)**, 2537–2544, doi:10.5194/acp-11-2537-2011.

Gayet, J.-F., et al., 1998: In situ measurements of the scattering phase function of stratocumulus, contrails and cirrus. *Geophys. Res. Lett.*, **25 (7)**, 971–974.

Gedzelman, S. D., 2008: Simulating halos and coronas in their atmospheric environment. *Appl. Opt.*, **47 (34)**, H157–H166, doi:10.1364/AO.47.00H157.

Gedzelman, S. D. and M. Vollmer, 2008: Atmospheric Optical Phenomena and Radiative Transfer. *Bulletin of the American Meteorological Society*, **89 (4)**, 471–485, doi:10.1175/BAMS-89-4-471, http://dx.doi.org/10.1175/BAMS-89-4-471.

Gege, P., et al., 2009: A new laboratory for the characterisation of hyperspectral airborne sensors. `http://elib.dlr.de/58527/`.

Geogdzhayev, I. and B. van Diedenhoven, 2016: The effect of roughness model on scattering properties of ice crystals. *J. Quant. Spectrosc. Radiat. Transfer*, **178**, 134–141, doi: 10.1016/j.jqsrt.2016.03.001, electromagnetic and light scattering by nonspherical particles XV: Celebrating 150 years of Maxwell's electromagnetics.

Görsdorf, U., V. Lehmann, M. Bauer-Pfundstein, G. Peters, D. Vavriv, V. Vinogradov, and V. Volkov, 2015: A 35-GHz Polarimetric Doppler Radar for Long-Term Observations of Cloud Parameters - Description of System and Data Processing. *Journal of Atmospheric and Oceanic Technology*, **32 (4)**, 675–690, doi:10.1175/JTECH-D-14-00066.1.

Greenler, R., 1980: *Rainbows, Halos and Glories*. Cambridge University Press, Cambridge.

Grob, H., 2015: Characterisation and Calibration of an IR imaging spectrometer for cloud observation. M.S. thesis, Ludwig-Maximilians-Universität München.

Guerrero-Rascado, J. L., M. J. Costa, A. M. Silva, and F. J. Olmo, 2013: Retrieval and variability analysis of optically thin cloud optical depths from a Cimel sun-photometer. *Atmospheric research*, **127**, 210–220.

Hansen, J. and L. Travis, 1974: Light scattering in planetary atmospheres. *Space Sci. Rev.*, **16**, 527–610, doi:10.1007/BF00168069.

Hausmann, P., 2012: Ground-based remote sensing of optically thin ice clouds. M.S. thesis, Ludwig-Maximilians-Universität München.

Heese, B., V. Freudenthaler, M. Kosmale, M. Seefeldner, and M. Wiegner, 2004: First Results from the Portable LIDAR System Polis. *22nd Internation Laser Radar Conference (ILRC 2004)*, G. Pappalardo and A. Amodeo, Eds., ESA Special Publication, Vol. 561, 79.

Heikkilä, J. and O. Silvén, 1997: A four-step camera calibration procedure with implicit image correction. *Proceedings of IEEE Computer Society Conference on Computer Vision and Pattern Recognition*, Washington, DC, USA, 1106–1112, doi:10.1109/CVPR.1997.609468.

Hess, M., 1996: Modellierung und Messung optischer Eigenschaften von Cirren. Ph.D. thesis, Ludwig-Maximilians-Universität München.

Hess, M., P. Koepke, and I. Schult, 1998: Optical properties of aerosols and clouds: the software package OPAC. *Bulletin of the American Meteorological Society*, **79 (5)**, 831–844.

Heymsfield, A., 1972: Ice crystal terminal velocities. *J. Atmos. Sci.*, **29 (7)**, 1348–1357.

Heymsfield, A. and L. Miloshevich, 2003: Parameterizations for the cross-sectional area and extinction of cirrus and stratiform ice cloud particles. *J. Atmos. Sci.*, **60**, 936–956.

Heymsfield, A. J. and L. M. Miloshevich, 1995: Relative Humidity and Temperature Influences on Cirrus Formation and Evolution: Observations from Wave Clouds and FIRE II. *Journal of the Atmospheric Sciences*, **52 (23)**, 4302–4326, doi:10.1175/1520-0469(1995)052⟨4302:RHATIO⟩2.0.CO;2, URL `https://doi.org/10.1175/1520-0469(1995)052<4302:RHATIO>2.0.CO`, `https://doi.org/10.1175/1520-0469(1995)052<4302:RHATIO>2.0.CO;2`.

Heymsfield, A. J., C. Schmitt, and A. Bansemer, 2013: Ice Cloud Particle Size Distributions and Pressure-Dependent Terminal Velocities from In Situ Observations at Temperatures from 0° to -86°C. *Journal of the Atmospheric Sciences*, **70 (12)**, 4123–4154, doi:10.1175/JAS-D-12-0124.1, doi: 10.1175/JAS-D-12-0124.1.

Hioki, S., P. Yang, B. A. Baum, S. Platnick, K. G. Meyer, M. D. King, and J. Riedi, 2016: Degree of ice particle surface roughness inferred from polarimetric observations. *Atmos. Chem. Phys.*, **16 (12)**, 7545–7558, doi:10.5194/acp-16-7545-2016.

Hogan, R., M. Behera, E. O'Connor, and A. Illingworth, 2004: Estimate of the global distribution of stratiform supercooled liquid water clouds using the LITE radar. *Geophys. Res. Lett.*, **31**, doi:10.1029/2003GL018 977.

Holben, B., et al., 1998: AERONET - A Federated Instrument Network and Data Archive for Aerosol Characterization. *Remote Sens. of Environ.*, **66 (1)**, 1–16, doi:10.1016/S0034-4257(98)00031-5.

Holz, R. E., et al., 2016: Resolving ice cloud optical thickness biases between CALIOP and MODIS using infrared retrievals. *Atmos. Chem. Phys.*, **16 (8)**, 5075–5090, doi:10.5194/acp-16-5075-2016, `https://www.atmos-chem-phys.net/16/5075/2016`.

Hu, Y., S. Rodier, K. Xu, W. Sun, J. Huang, B. Lin, P. Zhai, and D. Josset, 2010: Occurrence, liquid water content, and fraction of supercooled water clouds from combined CALIOP/IIR/MODIS measurements. *Journal of Geophysical Research: Atmospheres (1984–2012)*, **115 (D4)**, doi:10.1029/2009JD012384.

Itseez, 2015: Open Source Computer Vision Library. `https://github.com/itseez/opencv`.

Ivanova, D., D. L. Mitchell, W. Arnott, and M. Poellot, 2001: A GCM parameterization for bimodal size spectra and ice mass removal rates in mid-latitude cirrus clouds. *Atmospheric Research*, **59 (Supplement C)**, 89–113, doi:10.1016/S0169-8095(01)00111-9, URL `http://www.sciencedirect.com/science/article/pii/S0169809501001119`, 13th International Conference on Clouds and Precipitation.

Jayaweera, K. and B. Mason, 1965: The behaviour of freely falling cylinders and cones in a viscous fluid. *Journal of Fluid Mechanics*, **22 (04)**, 709–720.

Key, J., P. Yang, B. Baum, and S. Nasiri, 2002: Parameterization of shortwave ice cloud optical properties for various particle habits. *Journal of Geophysical Research*, **107 (D13)**, 10.1029/2001JD000 742.

King, M., S. Platnick, P. Yang, G. Arnold, M. Gray, J. Riedi, S. Ackerman, and K.-N. Liou, 2004: Remote sensing of liquid water and ice cloud optical thickness and effective radius in the Arctic: Application of airborne multispectral MAS data. *Journal of Atmospheric and Oceanic Technology*, **21**, 857–875.

King, M., S.-C. Tsay, S. Platnick, M. Wang, and K.-N. Liou, 1997: Cloud retrieval algorithms for MODIS: Optical thickness, effective particle radius, and thermodynamic phase. MODIS Algorithm Theoretical Basis Document, No. ATBD-MOD-05, 1997.

Knap, W. H., L. C. Labonnote, G. Brogniez, and P. Stammes, 2005: Modeling total and polarized reflectances of ice clouds: evaluation by means of POLDER and ATSR-2 measurements. *Applied Optics*, **44 (19)**, 4060–4073, doi:10.1364/AO.44.004060.

Kokhanovsky, A., 2008: The contrast and brightness of halos in crystalline clouds. *Atmos. Res.*, **89 (1-2)**, 110–112, doi:10.1016/j.atmosres.2007.12.006.

Konoshonkin, A. V., N. V. Kustova, A. G. Borovoi, Y. Grynko, and J. Förstner, 2016: Light scattering by ice crystals of cirrus clouds: comparison of the physical optics methods. *J. Quant. Spectrosc. Radiat. Transfer*, **182**, 12–23, doi:10.1016/j.jqsrt.2016.05.006.

Kunkel, K. and J. Weinma, 1976: Monte Carlo Analysis of multiply scattered lidar returns. *J. Atmos. Sci.*, **33**, 1772–1781.

Kurucz, R., 1992: Synthetic infrared spectra. *Proceedings of the 154th Symposium of the International Astronomical Union (IAU); Tucson, Arizona, March 2-6, 1992*, Kluwer, Acad., Norwell, MA.

Lamb, D. and J. Verlinde, 2011: *Physics and chemistry of clouds*. Cambridge University Press.

Liou, K., 1992: *Encyclopedia of Earth System Sciences, Volume 1*, chap. Atmospheric radiation, causes and effects. Academic Press.

Liou, K. and P. Yang, 2016: *Light Scattering by Ice Crystals: Fundamentals and Applications*. Cambridge University Press, Cambridge.

Liou, K.-N., 1986: Influence of cirrus clouds on weather and climate processes: A global perspective. *Monthly Weather Review*, **114**, 1167–1199.

Lynch, D., K. Sassen, D. Starr, and G. Stephens, (Eds.) , 2002: *Cirrus*. Oxford University Press.

Lynch, D. K. and P. Schwartz, 1985: Intensity profile of the 22° halo. *J. Opt. Soc. Am. A*, **2 (4)**, 584–589, doi:10.1364/JOSAA.2.000584.

Macke, A., 1994: Modellierung der optischen Eigenschaften von Cirruswolken. Ph.D. thesis, Universität Hamburg.

Macke, A., J. Mueller, and E. Raschke, 1996: Single scattering properties of atmospheric ice crystals. *J. Atmos. Sci.*, **53**, 2813–2825.

Magono, C. and C. W. Lee, 1966: Meteorological classification of natural snow crystals. *J. Fac. Sci.*, **2**, 321–335.

Mayer, B., 2009: Radiative transfer in the cloudy atmosphere. *European Physical Journal Conferences*, **1**, 75–99, doi:10.1140/epjconf/e2009-00912-1.

Mayer, B. and A. Kylling, 2005: Technical Note: The libRadtran software package for radiative transfer calculations: Description and examples of use. *Atmos. Chem. Phys.*, **5**, 1855–1877, doi:10.5194/acp-5-1855-2005.

McFarlane, S. A. and R. T. Marchand, 2008: Analysis of ice crystal habits derived from MISR and MODIS observations over the ARM Southern Great Plains site. *Journal of Geophysical Research: Atmospheres*, **113 (D7)**.

McFarquhar, G. and A. Heymsfield, 1998: The definition and significance of an effective radius for ice clouds. *J. Atmos. Sci.*, **55**, 2039–2052.

Mie, G., 1908: Beiträge zur Optik trüber Medien, speziell kolloidaler Metallösungen. *Annalen der Physik, Vierte Folge*, **25 (3)**, 377–445.

Minnaert, M., 1937: *De natuurkunde van 't vrije veld. Deel I. Licht en kleur in het landschap.* W. J. Thieme, Zutphen.

Minnaert, M., 1993: *Rainbows, Halos, and Coronas*, 185–258. Springer New York, New York, NY, doi:10.1007/978-1-4612-2722-9_10.

Mishchenko, M. and A. Macke, 1997: Asymmetry parameters of the phase function for isolated and densely packed spherical particles with multiple internal inclusions in the geometric optics limit. *Journal of Quantitative Spectroscopy and Radiative Transfer*, **57 (6)**, 767–794, doi:10.1016/S0022-4073(97)00012-5, http://www.sciencedirect.com/science/article/pii/S0022407397000125.

Mishchenko, M. and A. Macke, 1999: How big should hexagonal ice crystals be to produce halos? *Applied Optics*, **38 (9)**, 1626–1629, doi:10.1364/AO.38.001626.

Mishchenko, M., W. Rossow, A. Macke, and A. Lacis, 1996: Sensitivity of cirrus cloud albedo, bidirectional reflectance and optical thickness retrieval accuracy to ice particle shape. *Journal of Geophysical Research*, **101 (D12)**, 16 973–16 985.

Mitchell, D. L. and W. P. Arnott, 1994: A Model Predicting the Evolution of Ice Particle Size Spectra and Radiative Properties of Cirrus Clouds. Part II: Dependence of Absorption and Extinction on Ice Crystal Morphology. *J. Atmos. Sci.*, **51 (6)**, 817–832, doi:10.1175/1520-0469(1994)051⟨0817:AMPTEO⟩2.0.CO;2, http://dx.doi.org/10.1175/1520-0469(1994)051<0817:AMPTEO>2.0.CO;2.

Muinonen, K., K. Lumme, J. Peltoniemi, and W. M. Irvine, 1989: Light scattering by randomly oriented crystals. *Appl. Opt.*, **28 (15)**, 3051–3060, doi:10.1364/AO.28.003051.

Myagkov, A., P. Seifert, U. Wandinger, J. Bühl, and R. Engelmann, 2016: Relationship between temperature and apparent shape of pristine ice crystals derived from polarimetric cloud radar observations during the ACCEPT campaign. *Atmos. Meas. Tech.*, **9 (8)**, 3739–3754, doi:10.5194/amt-9-3739-2016.

Nakajima, T. and M. King, 1990: Determination of the optical thickness and effective particle radius of clouds from reflected solar radiation measurements. Part I: Theory. *J. Atmos. Sci.*, **47**, 1878–1893.

Neshyba, S. P., B. Lowen, M. Benning, A. Lawson, and P. M. Rowe, 2013: Roughness metrics of prismatic facets of ice. *Journal of Geophysical Research: Atmospheres*, **118 (8)**, 3309–3318, doi:10.1002/jgrd.50357, http://dx.doi.org/10.1002/jgrd.50357.

Noel, V. and H. Chepfer, 2004: Study of Ice Crystal Orientation in Cirrus Clouds Based on Satellite Polarized Radiance Measurements. *J. Atmos. Sci.*, **61 (16)**, 2073–2081, doi:10.1175/1520-0469(2004)061⟨2073:SOICOI⟩2.0.CO;2, https://doi.org/10.1175/1520-0469(2004)061<2073:SOICOI>2.0.CO;2.

Noel, V. and H. Chepfer, 2010: A global view of horizontally oriented crystals in ice clouds from Cloud-Aerosol Lidar and Infrared Pathfinder Satellite Observation (CALIPSO). *Journal of Geophysical Research: Atmospheres*, **115 (D4)**, n/a–n/a, doi:10.1029/2009JD012365, d00H23, http://dx.doi.org/10.1029/2009JD012365.

Noel, V. and K. Sassen, 2005: Study of Planar Ice Crystal Orientations in Ice Clouds from Scanning Polarization Lidar Observations. *Journal of Applied Meteorology*, **44 (5)**, 653–664, doi:10.1175/JAM2223.1, `https://doi.org/10.1175/JAM2223.1`.

Ono, A., 1969: The shape and riming properties of ice crystals in natural clouds. *Journal of the Atmospheric Sciences*, **26 (1)**, 138–147.

Ou, S., K. Liou, M. King, and S. Tsay, 1999: Remote sensing of cirrus cloud parameters based on a 0.63-3.7 μm radiance correlation technique applied to AVHRR data. *Geophys. Res. Lett.*, **26**, 2437–2440.

Pattloch, F. and E. Tränkle, 1984: Monte Carlo simulation and analysis of halo phenomena. *J. Opt. Soc. Am. A*, **1 (5)**, 520–526, doi:10.1364/JOSAA.1.000520.

Pedregosa, F., et al., 2011: Scikit-learn: Machine Learning in Python. *Journal of Machine Learning Research*, **12**, 2825–2830.

Pekkola, M., 1991: Finnish Halo Observing Network: search for rare halo phenomena. *Appl. Opt.*, **30 (24)**, 3542–3544, doi:10.1364/AO.30.003542.

Pernter, J. M. and F. Exner, 1910: *Meteorologische Optik*. W. Braumüller, Wien.

Petty, G. W., 2006: *A first course in atmospheric radiation*. Sundog Publishing.

Platt, C., 1978: Lidar backscatter from horizontal ice crystal plates. *Journal of Applied Meteorology*, **17 (4)**, 482–488.

Prigarin, S. M., 2009: Numerical simulation of halos in crystal clouds by Monte Carlo method. *Russ. J. Numer. Anal. Math. Modelling*, **24 (5)**, 481–493.

Raschka, S., 2015: *Python Machine Learning*. Community experience distilled, Packt Publishing, Birmingham.

Reinhardt, B., R. Buras, L. Bugliaro, S. Wilbert, and B. Mayer, 2014: Determination of circumsolar radiation from Meteosat Second Generation. *Atmos. Meas. Tech.*, **7 (3)**, 823–838, doi:10.5194/amt-7-823-2014.

Rogers, R. R. and M. K. Yau, 1996: *A short course in cloud physics*. Elsevier.

Rolland, P. and K. Liou, 2001: Surface variability effects on the remote sensing of thin cirrus optical and microphysical properties. *Journal of Geophysical Research*, **106**, 22 965–22 977.

Rolland, P., K. Liou, M. King, S. Tsay, and G. McFarquhar, 2000: Remote sensing of optical and microphysical properties of cirrus clouds using Moderate-Resolution Imaging Spectroradiometer channels: Methodology and sensitivity to physical assumptions. *Journal of Geophysical Research*, **105 (D9)**, 11 721–11 738.

Saito, M., H. Iwabuchi, P. Yang, G. Tang, M. D. King, and M. Sekiguchi, 2017: Ice particle morphology and microphysical properties of cirrus clouds inferred from combined CALIOP-IIR measurements. *Journal of Geophysical Research: Atmospheres*, **122 (8)**, 4440–4462.

Sassen, K. and J. R. Campbell, 2001: A Midlatitude Cirrus Cloud Climatology from the Facility for Atmospheric Remote Sensing. Part I: Macrophysical and Synoptic Properties. *J. Atmos. Sci.*, **58 (5)**, 481–496, doi:10.1175/1520-0469(2001)058⟨0481:AMCCCF⟩2.0.CO;2.

Sassen, K., N. C. Knight, Y. Takano, and A. J. Heymsfield, 1994: Effects of ice-crystal structure on halo formation: cirrus cloud experimental and ray-tracing modeling studies. *Appl. Opt.*, **33 (21)**, 4590–4601, doi:10.1364/AO.33.004590, http://ao.osa.org/abstract.cfm?URI=ao-33-21-4590.

Sassen, K. and K.-N. Liou, 1979: Scattering of polarized laser light by water droplet, mixed-phase and ice crystal clouds. Part I: Angular scattering patterns. *J. Atmos. Sci.*, **36**, 838–851.

Sassen, K., Z. Wang, C. Platt, and J. Comstock, 2003a: Parameterization of infrared absorption in midlatitude cirrus clouds. *J. Atmos. Sci.*, **60**, 428–433.

Sassen, K., J. Zhu, and S. Benson, 2003b: Midlatitude cirrus cloud climatology from the Facility for Atmospheric Remote Sensing. IV. Optical displays. *Applied Optics*, **42 (3)**, 332–341, doi:10.1364/AO.42.000332.

Schnaiter, M., et al., 2016: Cloud chamber experiments on the origin of ice crystal complexity in cirrus clouds. *Atmos. Chem. Phys.*, **16 (8)**, 5091–5110, doi:10.5194/acp-16-5091-2016, https://www.atmos-chem-phys.net/16/5091/2016.

Schnell, F. I. J., 2014: Aerosol distribution above Munich using remote sensing techniques, http://nbn-resolving.de/urn:nbn:de:bvb:19-173683.

Schumann, U., 2005: Formation, properties and climatic effects of contrails. *C. R. Physique*, **6**, 549–565.

Seefeldner, M., A. Oppenrieder, D. Rabus, J. Reuder, M. Schreier, P. Hoeppe, and P. Koepke, 2004: A Two-Axis Tracking System with Datalogger. *Journal of Atmospheric and Oceanic Technology*, **21 (6)**, 975–979, doi:10.1175/1520-0426(2004)021⟨0975:ATTSWD⟩2.0.CO;2, http://dx.doi.org/10.1175/1520-0426(2004)021<0975:ATTSWD>2.0.CO;2.

Segal-Rosenheimer, M., P. B. Russell, J. M. Livingston, S. Ramachandran, J. Redemann, and B. A. Baum, 2013: Retrieval of cirrus properties by Sun photometry: A new perspective on an old issue. *Journal of Geophysical Research: Atmospheres*, **118 (10)**, 4503–4520.

Shcherbakov, V., 2013: Why the 46° halo is seen far less often than the 22° halo? *J. Quant. Spectrosc. Radiat. Transfer*, **124**, 37–44, doi:10.1016/j.jqsrt.2013.03.002.

Shiobara, M. and S. Asano, 1994: Estimation of cirrus optical thickness from sun photometer measurements. *J. Appl. Meteorol.*, **33**, 672–681.

Smirnov, A., B. Holben, T. Eck, O. Dubovik, and I. Slutsker, 2000: Cloud-Screening and Quality Control Algorithms for the AERONET Database. *Remote Sensing of Environment*, **73 (3)**, 337–349, doi:10.1016/S0034-4257(00)00109-7, http://www.sciencedirect.com/science/article/pii/S0034425700001097.

Stamnes, K., S. Tsay, W. Wiscombe, and K. Jayaweera, 1988: A numerically stable algorithm for discrete-ordinate-method radiative transfer in multiple scattering and emitting layered media. *Applied Optics*, **27 (12)**, 2502–2509, doi:10.1364/AO.27.002502.

Strahler, A., et al., 1999: MODIS BRDF/albedo product: algorithm theoretical basis document version 5.0. *MODIS documentation*.

Strutt, J. W., 1871: LVIII. On the scattering of light by small particles. *The London, Edinburgh, and Dublin Philosophical Magazine and Journal of Science*, **41 (275)**, 447–454.

Stubenrauch, C. J., A. Chédin, G. Rädel, N. A. Scott, and S. Serrar, 2006: Cloud Properties and Their Seasonal and Diurnal Variability from TOVS Path-B. *Journal of Climate*, **19 (21)**, 5531–5553, doi:10.1175/JCLI3929.1, `https://doi.org/10.1175/JCLI3929.1`.

Sun, W., N. G. Loeb, and P. Yang, 2006: On the retrieval of ice cloud particle shapes from POLDER measurements. *J. Quant. Spectrosc. Radiat. Transfer*, **101 (3)**, 435–447.

Takano, Y. and K.-N. Liou, 1989: Solar radiative transfer in cirrus clouds. Part I: Single-scattering and optical properties of hexagonal ice crystals. *J. Atmos. Sci.*, **46**, 1–19.

Takano, Y. and K.-N. Liou, 1990: Halo phenomena modified by multiple scattering. *Journal of the Optical Society of America A*, **7**, 885–889.

Takano, Y. and K.-N. Liou, 1995: Solar radiative transfer in cirrus clouds. Part III: Light scattering by irregular ice crystals. *J. Atmos. Sci.*, **52**, 818–837.

Tape, W., 1994: *Atmospheric halos*. Antarctic Research Series, American Geophysical Union, Washington, DC.

Tape, W. and J. Moilanen, 2006: *Atmospheric Halos and the Search for Angle X*. American Geophysical Union, Washington, DC.

Thomas, G. and K. Stamnes, 1999: *Radiative transfer in the Atmosphere and Ocean*. Cambridge University Press.

Toledano, C., M. Wiegner, M. Garhammer, M. Seefeldner, J. Gasteiger, D. Müller, and P. Koepke, 2009: Spectral aerosol optical depth characterization of desert dust during SAMUM 2006. *Tellus B*, **61 (1)**, 216–228, doi:10.1111/j.1600-0889.2008.00382.x.

Toledano, C., et al., 2011: Optical properties of aerosol mixtures derived from sun-sky radiometry during SAMUM-2. *Tellus B*, **63 (4)**, 635–648, doi:10.1111/j.1600-0889.2011.00573.x.

Tricker, R. A. R., 1970: *Introduction to Meteorological Optics*. Elsevier, New York.

Ulanowski, Z., P. H. Kaye, E. Hirst, R. S. Greenaway, R. J. Cotton, E. Hesse, and C. T. Collier, 2014: Incidence of rough and irregular atmospheric ice particles from Small Ice Detector 3 measurements. *Atmos. Chem. Phys.*, **14 (3)**, 1649–1662, doi:10.5194/acp-14-1649-2014, `https://www.atmos-chem-phys.net/14/1649/2014`.

Um, J. and G. M. McFarquhar, 2015: Formation of atmospheric halos and applicability of geometric optics for calculating single-scattering properties of hexagonal ice crystals: Impacts of aspect ratio and ice crystal size. *Journal of Quantitative Spectroscopy and Radiative Transfer*, **165**, 134–152, doi:10.1016/j.jqsrt.2015.07.001.

Urquhart, B., B. Kurtz, E. Dahlin, M. Ghonima, J. E. Shields, and J. Kleissl, 2015: Development of a sky imaging system for short-term solar power forecasting. *Atmos. Meas. Tech.*, **8 (2)**, 875–890, doi:10.5194/amt-8-875-2015, `http://www.atmos-meas-tech.net/8/875/2015`.

van Diedenhoven, B., 2014: The prevalence of the 22° halo in cirrus clouds. *Journal of Quantitative Spectroscopy and Radiative Transfer*, **146**, 475–479, doi:10.1016/j.jqsrt.2014.01.012.

van Diedenhoven, B., B. Cairns, A. M. Fridlind, A. S. Ackerman, and T. J. Garrett, 2013: Remote sensing of ice crystal asymmetry parameter using multi-directional polarization measurements – Part 2: Application to the Research Scanning Polarimeter. *Atmos. Chem. Phys.*, **13 (6)**, 3185–3203, doi:10.5194/acp-13-3185-2013, http://www.atmos-chem-phys.net/13/3185/2013.

van Diedenhoven, B., A. M. Fridlind, A. S. Ackerman, and B. Cairns, 2012: Evaluation of Hydrometeor Phase and Ice Properties in Cloud-Resolving Model Simulations of Tropical Deep Convection Using Radiance and Polarization Measurements. *J. Atmos. Sci.*, **69 (11)**, 3290–3314, doi:10.1175/JAS-D-11-0314.1, https://doi.org/10.1175/JAS-D-11-0314.1.

Venn, J., 1880: On the employment of geometrical diagrams for the sensible representations of logical propositions. *Proceedings of the Cambridge Philosophical Society*, **4**, 47–59.

Verschure, P.-P. H., 1998: Thirty years of observing and documenting sky optical phenomena. *Appl. Opt.*, **37 (9)**, 1585–1588, doi:10.1364/AO.37.001585.

Voigt, C., et al., 2016: ML-CIRRUS - The airborne experiment on natural cirrus and contrail cirrus with the high-altitude long-range research aircraft HALO. *Bulletin of the American Meteorological Society*, doi:10.1175/BAMS-D-15-00213.1.

Vollmer, M., 2006: *Lichtspiele in der Luft*. 1st ed., Spektrum Akademischer Verlag, München.

von Helmholtz, H. and A. König, 1896: *Handbuch der physiologischen Optik*. No. Bd. 1 in Handbuch der physiologischen Optik, L. Voss.

Wallace, J. and P. Hobbs, 2006: *Atmospheric Science: An Introductory Survey*. International Geophysics, Elsevier Science.

Wang, C., P. Yang, A. Dessler, B. A. Baum, and Y. Hu, 2014: Estimation of the cirrus cloud scattering phase function from satellite observations. *J. Quant. Spectrosc. Radiat. Transfer*, **138**, 36–49.

Warren, S. G. and R. E. Brandt, 2008: Optical constants of ice from the ultraviolet to the microwave: A revised compilation. *Journal of Geophysical Research: Atmospheres*, **113 (D14)**.

Wegener, A., 1925: *Theorie der Haupthalos*, Vol. 43. Aus dem Archiv der Deutschen Seewarte und des Marineobservatoriums, Hamburg.

Wegener, A., 1926: *Thermodynamik der Atmosphäre*, 156–189. Springer Berlin Heidelberg, Berlin, Heidelberg, doi:10.1007/978-3-642-90779-1_3, http://dx.doi.org/10.1007/978-3-642-90779-1_3.

Wendisch, M., P. Yang, and P. Pilewskie, 2007: Effects of ice crystal habit on thermal infrared radiative properties and forcing of cirrus. *Journal of Geophysical Research*, **112**, D08 201, doi:10.1029/2006JD007899, d08201.

Wendling, P., R. Wendling, and H. K. Weickmann, 1979: Scattering of solar radiation by hexagonal ice crystals. *Appl. Opt.*, **18 (15)**, 2663–2671, doi:10.1364/AO.18.002663, http://ao.osa.org/abstract.cfm?URI=ao-18-15-2663.

Wiegner, M. and A. Geiß, 2012: Aerosol profiling with the Jenoptik ceilometer CHM15kx. *Atmos. Meas. Tech.*, **5 (8)**, 1953–1964, doi:10.5194/amt-5-1953-2012.

Wiegner, M., et al., 2014: What is the benefit of ceilometers for aerosol remote sensing? An answer from EARLINET. *Atmos. Meas. Tech.*, **7 (7)**, 1979–1997, doi:10.5194/amt-7-1979-2014.

Wielicki, B., R. Cess, M. King, D. Randall, and E. Harrison, 1995: Mission to planet Earth: Role of clouds and radiation in climate. *Bulletin of the American Meteorological Society*, **76**, 2125–2153.

Wiscombe, W., 1980: Improved Mie scattering algorithms. *Applied Optics*, **19 (9)**, 1505–1509.

WMO, 1983: *Guide to meteorological instruments and methods of observation*, Vol. 8. Secretariat of the Worl Meteorogical Organization - Geneva - Switzerland.

Wylie, D. P. and W. P. Menzel, 1999: Eight Years of High Cloud Statistics Using HIRS. *Journal of Climate*, **12 (1)**, 170–184, doi:10.1175/1520-0442(1999)012⟨0170:EYOHCS⟩2.0.CO;2, http://journals.ametsoc.org/doi/pdf/10.1175/1520-0442%281999%29012%3C0170%3AEYOHCS%3E2.0.CO%3B2.

Yang, P., B. Baum, A. Heymsfield, Y. Hu, H.-L. Huang, S.-C. Tsay, and S. Ackerman, 2003: Single-scattering properties of droxtals. *J. Quant. Spectrosc. Radiat. Transfer*, **79-80**, 1159–1169.

Yang, P., L. Bi, B. A. Baum, K.-N. Liou, G. W. Kattawar, M. I. Mishchenko, and B. Cole, 2013: Spectrally Consistent Scattering, Absorption, and Polarization Properties of Atmospheric Ice Crystals at Wavelengths from 0.2 to 100 μm. *J. Atmos. Sci.*, **70 (1)**, 330–347, doi:10.1175/JAS-D-12-039.1, http://dx.doi.org/10.1175/JAS-D-12-039.1.

Yang, P. and K. Liou, 1996: Geometric-optics-integral-equation method for light scattering by nonspherical ice crystals. *Applied Optics*, **35 (33)**, 6568–6582.

Yang, P. and K. Liou, 1998: Single-scattering properties of complex ice crystals in terrestrial atmosphere. *Beitrage zur Physik der Atmosphare-Contributions to Atmospheric Physics*, **71 (2)**, 223–248.

Yang, P., K.-N. Liou, L. Bi, C. Liu, B. Yi, and B. A. Baum, 2015: On the radiative properties of ice clouds: Light scattering, remote sensing, and radiation parameterization. *Advances in Atmospheric Sciences*, **32 (1)**, 32–63, doi:10.1007/s00376-014-0011-z.

Yang, S., P. Ricchiazzi, and C. Gautier, 2000: Modified correlated k-distribution methods for remote sensing applications. *J. Quant. Spectrosc. Radiat. Transfer*, **64**, 585–608.

Yi, B., P. Yang, B. A. Baum, T. L'Ecuyer, L. Oreopoulos, E. J. Mlawer, A. J. Heymsfield, and K.-N. Liou, 2013: Influence of Ice Particle Surface Roughening on the Global Cloud Radiative Effect. *J. Atmos. Sci.*, **70 (9)**, 2794–2807, doi:10.1175/JAS-D-13-020.1, http://dx.doi.org/10.1175/JAS-D-13-020.1.

Zdunkowski, W., T. Trautmann, and A. Bott, 2007: *Radiation in the Atmosphere: A Course in Theoretical Meteorology*. Cambridge University Press.

Zhang, Y., W. Rossow, A. Lacis, V. Oinas, and M. Mishchenko, 2004: Calculation of radiative fluxes from the surface to top of atmosphere based on ISCCP and other global data sets: Refinements of the radiative transfer model and the input data. *Journal of Geophysical Research*, **109**, doi:10.1029/2003JD004 457.

Zhang, Z., 2000: A flexible new technique for camera calibration. *IEEE Transactions on Pattern Analysis and Machine Intelligence*, **22 (11)**, 1330–1334.

Zhao, Y., G. G. Mace, and J. M. Comstock, 2011: The Occurrence of Particle Size Distribution Bimodality in Midlatitude Cirrus as Inferred from Ground-Based Remote Sensing Data. *Journal of the Atmospheric Sciences*, **68 (6)**, 1162–1177, doi:10.1175/2010JAS3354.1, URL `https://doi.org/10.1175/2010JAS3354.1`, `https://doi.org/10.1175/2010JAS3354.1`.

Zhou, C., P. Yang, A. E. Dessler, Y. Hu, and B. A. Baum, 2012: Study of Horizontally Oriented Ice Crystals with CALIPSO Observations and Comparison with Monte Carlo Radiative Transfer Simulations. *Journal of Applied Meteorology and Climatology*, **51 (7)**, 1426–1439, doi:10.1175/JAMC-D-11-0265.1, `https://doi.org/10.1175/JAMC-D-11-0265.1`.

Zinner, T., P. Hausmann, F. Ewald, L. Bugliaro, C. Emde, and B. Mayer, 2016: Ground-based imaging remote sensing of ice clouds: uncertainties caused by sensor, method and atmosphere. *Atmos. Meas. Tech.*, **9 (9)**, 4615–4632, doi:10.5194/amt-9-4615-2016, `https://www.atmos-meas-tech.net/9/4615/2016`.

Zinth, W. and U. Zinth, 2005: *Optik. Lichtstrahlen, Wellen, Photonen.* Oldenbourg Verlag.

Acknowledgements

The radiosonde data were downloaded from http://weather.uwyo.edu/upperair/sounding.html of the University of Wyoming, College of Engineering, Department of Atmospheric Science. The halo observations during the ACCEPT campaign research received funding by the European Union Seventh Framework Program (FP7/2007-2013) under grant agreement n° 262254. We thank Markus Garhammer (LMU, Munich) and Marc Allaart (KNMI, The Netherlands) for their support during the campaign.

Lebenslauf

Sigmund Stintzing

Geburtsdatum	Geburt in Geburtsort
Schulzeit	Besuch der Schule in Ort
...	...